

# **CHEMISTRY RELATED TO THE ACTIVE SITES OF THE [Fe]- AND [FeFe]-HYDROGENASES**

A thesis submitted to the University of East Anglia

For the Degree of Doctor of Philosophy

Submitted Feb 2016

**Amanda Derry Austin Hill**

Energy Materials Laboratory

School of Chemistry, UEA

Norwich

This copy of this thesis has been supplied on the condition that anyone who consults it is understood to recognise that its copyright rests with the author and that no quotation from the thesis, nor any information derived there from, may be published without the author's prior written consent. ©

## Abstract

Hydrogenases are an important group of enzymes found in a range of microorganisms. There are three phylogenetically distinct classes of hydrogenase all of which feature iron-containing complexes. The work contained in this thesis has two main focuses: the synthesis and characterization of novel mimics of the [Fe]-hydrogenase active site, and spectroscopic studies on the interaction of iron-sulfur clusters with CO and  $\text{CN}^-$  relevant to the biosynthesis of the H-cluster of [FeFe]-hydrogenase.

The mechanism by which the [Fe]-hydrogenase functions is not fully understood, and biomimetic models currently offer limited insight. This emphasises the need to explore the fundamental organometallic chemistry of biologically relevant mono-iron complexes. Here, novel ferracyclic complexes featuring abiological ligands were synthesised, extending an existing family of mimics. Examination of the spectroscopic and electrochemical properties of these systems demonstrated that none are redox active in a range relevant to the enzyme.

The route by which microorganisms convert {4Fe4S} precursors into the {2Fe2S} assembly of the H-cluster of [FeFe]-hydrogenase is currently attracting significant scientific attention, in particular how the  $\text{Fe}(\text{CO})(\text{CN})$  moiety of the subsite is assembled. Here, the reaction of CO and  $\text{CN}^-$  with synthetic iron-sulfur clusters was used to seek out chemical precedence for the generation of this motif. It is clearly shown that  $\text{Fe}_4\text{S}_4$  clusters can be functionalised with CO and  $\text{CN}^-$  groups. Crucially, whilst good spectroscopic evidence for a complex featuring moiety **A**  $\text{Fe}(\text{CO})(\text{CN})$  was obtained this was not the case for an independent cluster featuring only moiety **B**  $\text{Fe}(\text{CO})_2(\text{CN})$ . However, there is some evidence for the formation of a cluster bearing both groups simultaneously.

## Acknowledgements

My profound thanks go to my supervisor Professor Chris Pickett for giving me the opportunity to do this Ph.D. I thank him for his enthusiastic guidance and supervision and for always making time to chat about my research.

I would also like to thank Dr Saad Ibrahim for his electrochemical expertise and Dr Graham Tizzard for his crystallographic assistance and for taking the time to prioritise some delicate samples.

A colossal thank you goes to Dr Joseph Wright for his invaluable contribution to my Ph.D., he has been a seemingly tireless source of knowledge, expertise and patience as well as being a good friend.

My sincere gratitude goes to Alistair Steele and Joshua Holmes for the hard work and considerable effort put into their undergraduate projects which have contributed to the work in this thesis.

Special thanks go to my best friends Aušra, Mark and Woody who have made my Ph.D. years exceedingly enjoyable, thank you all so much for the laughter, friendship, support and encouragement you have provided through the ups and downs of life in research.

Many thanks go to my other friends and colleagues Farhana, Irina, Lee-W., Ahmed, Khalaf, Hani, Matt, Anna and other members of the Energy Materials Laboratory past and present.

My heartfelt thanks go to my dad for sparking my interest in science at a young age and my sister Melanie for her blunt encouragement.

Finally I thank the fuzzy animals I live with, my boyfriend Lee who has been an unwavering source of love, support and delicious home-cooked meals, my dog Skye whose unbridled affection never fails to lift my spirits and my cat Luna. I love you all and thank you for being part of my little family.

***‘Who are you, who are so wise in the ways of science?’***

– Sir Bedevere, Monty Python and the Holy Grail.

***‘Huh? I... I don’t know that... aaaaaaaaaahhh’***

– Bridgekeeper, Monty Python and the Holy Grail.

# Contents

Abstract.....	i
Acknowledgements.....	ii
Acronyms.....	ix
1 Introduction.....	1
1.1 Biological aspects of hydrogen generation and uptake .....	1
1.1.1 Hydrogen: biological occurrence and role.....	1
1.1.2 The hydrogenases and nitrogenases .....	3
1.2 Metallo-sulfur clusters in biology.....	6
1.2.1 FeS-clusters structures and roles .....	6
1.2.2 Aconitase .....	9
1.2.3 CO dehydrogenase/acetyl-coA synthase (CODH/ACS) .....	10
1.2.4 Heterometallic clusters, Mo, V and Fe nitrogenases .....	11
1.2.5 Introduction to radical SAM enzymes and [FeFe]-hydrogenase structure, function and biosynthesis .....	12
1.2.6 [NiFe]-hydrogenase - structure/ function/ biosynthesis .....	26
1.2.7 [Fe]-hydrogenase- structure/ function/ biosynthesis .....	33
1.3 Chemical synthesis and functional models of metallo-sulfur clusters.....	36
1.3.1 Heteroatom –FeS clusters .....	44
1.3.2 FeMoco and P-clusters of nitrogenase (FeVco, FeFeco) .....	45
1.3.3 [FeFe]-hydrogenase active site models .....	50
1.3.4 [NiFe]-hydrogenase active site models .....	57
1.3.5 [Fe]-hydrogenase active site models .....	61
1.4 The scope of this work.....	61
1.4.1 Aims and objectives.....	61
2 Experimental methods and techniques .....	63
2.1 General synthetic methodology .....	63

2.1.1	Solvent purification .....	63
2.1.2	Handling methodology .....	63
2.1.3	Electrolyte preparation .....	63
2.1.4	Microanalysis.....	63
2.2	Background to experimental techniques.....	63
2.2.1	NMR spectroscopy .....	63
2.2.2	FTIR spectroscopy.....	65
2.2.3	FTIR spectroscopy of diatomic molecules on organometallics.....	66
2.2.4	Mass spectrometry.....	69
2.2.5	X-ray crystallography .....	70
2.2.6	Electrochemical measurements .....	72
2.2.7	Stopped-flow FTIR.....	78
2.3	Background to theoretical and simulation methods.....	79
2.3.1	Collaboration with Maurizio Bruschi .....	79
2.3.2	General introduction to density functional theory .....	79
2.3.3	Simulation of electrochemical data .....	80
3	Syntheses of analogues of the [Fe]-hydrogenase.....	81
3.1	Background to the work.....	81
3.1.1	Structure and function of the [Fe]-hydrogenase .....	81
3.1.2	Previous synthetic studies.....	81
3.1.3	Mechanistic aspects and potential intermediates in the catalytic cycle.....	93
3.1.4	Objectives of this work.....	100
3.2	Modification of the Fe-coordination sphere with donor ligands .....	101
3.2.1	Electrochemistry .....	113
3.3	Modification of the second coordination sphere .....	123
3.4	Attempts to introduce a hydride ligand .....	126
3.4.1	Conclusion.....	128

3.5	Experimental.....	130
3.5.1	Crystallography experimental.....	133
4	Reactions of $[\text{Fe}_4\text{S}_4(\text{SR})_4]^{2-}$ clusters with CO and $\text{CN}^-$ .....	136
4.1	Context of interactions of clusters with CO and $\text{CN}^-$ and the biosynthesis of the H-cluster.....	136
4.2	Earlier studies on general substitution reactions of $\{4\text{Fe}_4\text{S}\}^{2+}$ clusters .....	137
4.2.1	General electrochemical studies on $[\text{Fe}_4\text{S}_4(\text{SR})_4]^{n-}$ clusters.....	144
4.2.2	Independent interactions of $[\text{Fe}_4\text{S}_4(\text{SR})_4]^{n-}$ clusters, $n = 2-4$ with CO and $\text{CN}^-$ .....	144
4.3	Probing interactions of undifferentiated $[\text{Fe}_4\text{S}_4(\text{SR})_4]^{2-}$ (R = Et and Ph) clusters with CO and $\text{CN}^-$ as single substrates .....	146
4.3.1	Introduction to experimental techniques .....	146
4.3.2	The effect of CO on the cyclic voltammetry and stopped-flow FTIR of $[\text{Fe}_4\text{S}_4(\text{SR})_4]^{2-}$ clusters (R = Et and Ph).....	147
4.3.3	The effect of $\text{CN}^-$ on the cyclic voltammetry of $[\text{Fe}_4\text{S}_4(\text{SR})_4]^{2-}$ clusters (R = Et and Ph).....	151
4.3.4	Stopped-flow FTIR studies of the reaction of cyanide and $[\text{Fe}_4\text{S}_4(\text{SR})_4]^{2-}$ clusters (R = Et and Ph) under $\text{N}_2$ .....	161
4.4	Synergic interactions of CO and $\text{CN}^-$ with $[\text{Fe}_4\text{S}_4(\text{SR})_4]^{2-}$ clusters .....	169
4.4.1	Cyclic voltammetry experiments.....	169
4.5	Probing interactions of CO and $\text{CN}^-$ with $[\text{Fe}_4\text{S}_4(\text{SR})_4]^{2-}$ clusters, R = Ph or Et, by stopped-flow FTIR.....	176
4.5.1	Comparison of products from the reactions of $[\text{Fe}_4\text{S}_4(\text{SEt})_4]^{2-}$ and $[\text{Fe}_4\text{S}_4(\text{SPh})_4]^{2-}$ with $\text{CN}^-$ in CO saturated MeCN .....	186
4.5.2	Addition of $^{13}\text{CN}^-$ to CO saturated solution of cluster.....	188
4.5.3	Addition of cyanide to $^{13}\text{CO}$ saturated solution of cluster.....	190
4.5.4	Mass spectrometry studies.....	191
4.5.5	DFT modelling of interactions of cluster with CO and $\text{CN}^-$ .....	195
4.5.6	Attempts to isolate products .....	203

4.6	Conclusions.....	204
4.6.1	Summary of the proposed interactions of undifferentiated clusters with CO and CN <sup>-</sup> .....	204
4.6.2	Similarity to spectral data of HydG .....	207
4.6.3	Simplification of reactions – site differentiated clusters .....	209
4.7	Experimental techniques.....	210
4.7.1	Stopped-flow measurements.....	210
4.7.2	Electrochemical measurements .....	211
5	Reactions of a site-differentiated cluster with CO and CN <sup>-</sup> .....	212
5.1	Site-differentiated clusters .....	212
5.2	Probing interactions of CO and CN <sup>-</sup> by cyclic voltammetry .....	214
5.2.1	The effect of CO on the cyclic voltammetry of a site differentiated cluster ....	214
5.2.2	Spectra following mixing of CO and clusters .....	214
5.2.3	The effect of CN <sup>-</sup> on the cyclic voltammetry of a site differentiated cluster...	215
5.2.4	Probing the interaction of site differentiated cluster (8) with CN <sup>-</sup> under N <sub>2</sub> by stopped-flow FTIR .....	223
5.3	Reaction of CO and CN <sup>-</sup> with the site differentiated cluster.....	224
5.4	Probing interactions of CO and CN <sup>-</sup> by Stopped-flow FTIR.....	228
5.4.1	Addition of cyanide to CO saturated solution of “Holm cluster”.....	228
5.4.2	Addition of cyanide to <sup>13</sup> CO saturated solution of “Holm cluster” .....	230
5.4.3	Mass spectrometry studies.....	234
5.4.4	Isolation of products by crystallisation.....	236
5.4.5	Elemental Analysis .....	239
5.5	Conclusions.....	241
5.5.1	General summary of reactions .....	241
5.5.2	Relevance or otherwise to H-cluster intermediates in HydG .....	243
5.6	Experimental.....	247
5.6.1	Stopped-flow measurements.....	253

5.6.2	Electrochemical measurements .....	253
6	Summation of the work, conclusions and future work .....	254
6.1	Summary of chapter 3 .....	254
6.2	Summary of chapters 4 and 5 .....	255
7	References.....	258

## Acronyms

Ado•	5'-Deoxyadenosyl radical
ADP	Adenosine diphosphate
adt	2-Azapropan-1,3-dithiolate
ATP	Adenosine triphosphate
ATR	Attenuated total reflectance
Bdt	1,2-Bezenedithiolate
Cp*	Pentamethylcyclopentadienyl, C <sub>5</sub> Me <sub>5</sub>
CV	Cyclic voltammetry
DFT	Density functional theory
DMF	<i>N,N</i> -Dimethylformamide
DNA	Deoxyribonucleic acid
dppv	1,2-Bis(diphenylphosphino)ethylene
DTT	Dithiothreitol
ENDOR	Electron nuclear double resonance
EI	Electron ionisation
EPR	Electron paramagnetic resonance
ESI	Electrospray ionisation
EXAFS	Extended X-ray absorption fine structure
Fc	Ferrocene
FcP*	(Cp*)Fe(C <sub>5</sub> Me <sub>4</sub> CH <sub>2</sub> PEt <sub>2</sub> )
FTIR	Fourier transform infrared
GDP	Guanosine diphosphate
GP	Guanylylpyridinol
GTP	Guanosine triphosphate
HYSCORE	Hyperfine sub-level correlation
H <sub>4</sub> MPT <sup>+</sup>	Tetrahydromethanopterin

IMe	1-Methylimidazol-2-ylidene
IR	Infrared
MS	Mass spectroscopy
NMR	Nuclear magnetic resonance
NRVS	Nuclear resonance vibrational spectroscopy
odt	2-Oxapropan-1,3-dithiolate
ORTEP	Oak Ridge thermal ellipsoid program
PDB	Protein databank
pdt	Propan-1,3-dithiolate
QM/MM	Quantum mechanics/molecular mechanics
RT	Room temperature
SAM	<i>S</i> -Adenosyl-L-methionine
Tbt	2,4,6- $\{(\text{SiMe}_3)_2\text{CH}\}_3\text{C}_6\text{H}_2$
THF	Tetrahydrofuran
tRNA	Transfer ribonucleic acid
UV-vis	Ultraviolet-visible

# 1 Introduction

## 1.1 Biological aspects of hydrogen generation and uptake

### 1.1.1 Hydrogen: biological occurrence and role

The primordial atmosphere was likely to have been hydrogen rich,<sup>1</sup> thus it is conceivable that some of the first life on Earth evolved to utilise hydrogen as an energy source.<sup>2</sup> Hydrogenases are enzymes that enable cells to use dihydrogen and are present in many extant microorganisms. Some prokaryotes also have the ability to produce dihydrogen giving the remarkable potential to set up whole ecosystems based not on organic carbon and oxygen (the products of photosynthesis) but on dihydrogen.<sup>3</sup> Such communities have been observed in an active deep-sea hydrothermal field in the Central Indian Ridge where the microbial colonies are supported by abiologically derived H<sub>2</sub> and CO<sub>2</sub>.<sup>4</sup> The idea that such ecosystems can exist and survive independently of the products of photosynthesis is of great interest both in relation to the origins of life on Earth and in the search for life on other planets.<sup>5</sup> On Mars photochemical reactions have led to a high proportion of H<sub>2</sub> and CO in the atmosphere.<sup>6</sup> Both of these gases are used by a large variety of organisms on Earth. It has been demonstrated that several species of CO-oxidizing bacteria and archaea can grow autotrophically at the expense of CO with H<sub>2</sub> as an end-product.<sup>7-9</sup> Dihydrogen is an energy source for many bacteria, the greatest yield of energy being provided by the oxidation of H<sub>2</sub> by O<sub>2</sub>.<sup>2</sup> Hydrogenase enzymes are involved in both aerobic and anaerobic oxidation of H<sub>2</sub>. In the modern atmosphere there is very little dihydrogen. As it is formed by geological and biological processes it is very quickly used up by the various microbial communities that it encounters. An example of microbial uptake and use of H<sub>2</sub> in stagnant water is shown in Figure 1.

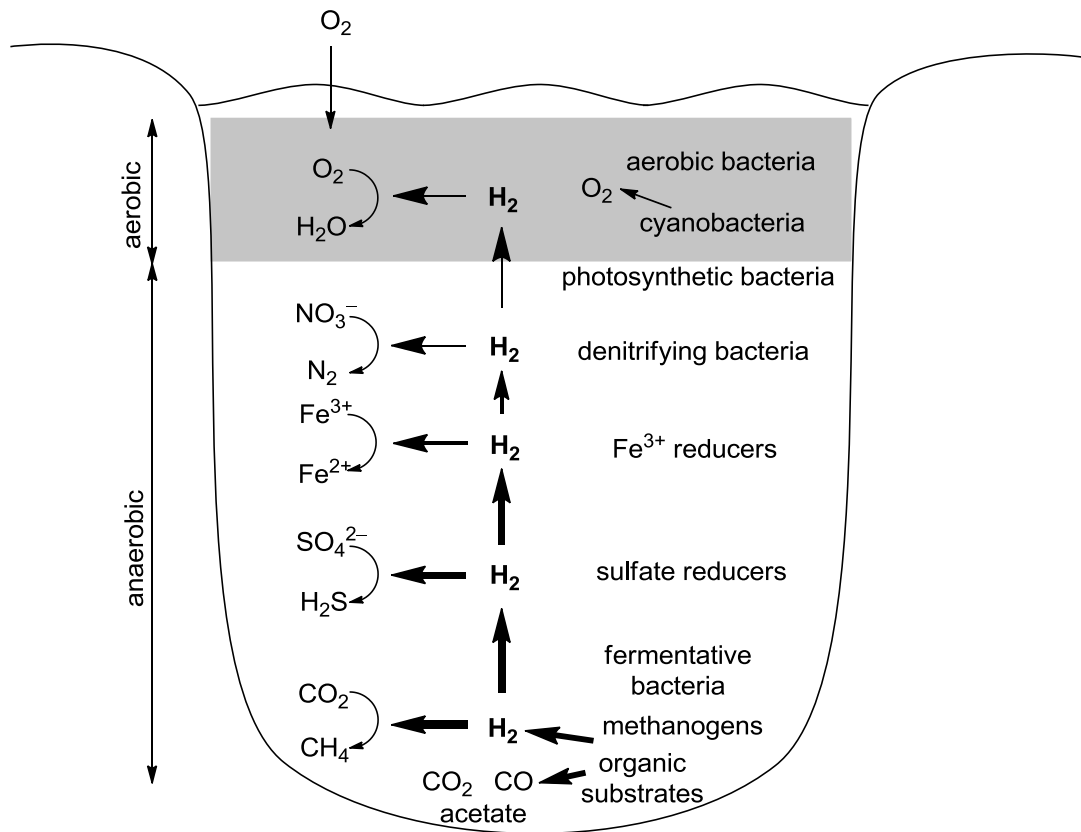


**Figure 1** Anaerobic and aerobic bacterial metabolism in an aquatic stratified system as can be found in a pond, lagoon or flooded soil. The scheme illustrates the vertical distribution of different redox reactions catalyzed by different microorganisms capable of producing or consuming H<sub>2</sub>. The redox potential, more negative at the bottom of the anaerobic fluid, increases upward and is positive in the aerobic phase near the surface of the water in contact with air. The vertical arrows emphasise the decreasing H<sub>2</sub> flux from bottom to the top of the stagnant water. Adapted from Conrad<sup>10</sup> and Cammack.<sup>11</sup>

In stagnant water H<sub>2</sub> is produced by fermentative bacteria in the sediment, there is H<sub>2</sub> flow from the site of excretion through layers of bacteria stratified according to the redox potential where they are able to oxidise H<sub>2</sub>. Clostridia bacteria in the sediment are involved in the fermentation of organic matter producing CO<sub>2</sub> and H<sub>2</sub>.<sup>10</sup> Methanogenic archaea in anoxic soils and sediments use H<sub>2</sub> in order to reduce CO<sub>2</sub> to methane. In the presence of alternative electron acceptors (sulfate, Fe<sup>3+</sup>, nitrate) the microbial structure changes. Species of

*Desulfovibrio* can use hydrogen to reduce sulfate to sulfide, such species are known as sulfate reducers. Fe<sup>3+</sup> reducers are found in a wide variety of sedimentary environments using oxides of Fe<sup>3+</sup> to oxidise H<sub>2</sub> under anoxic conditions. One family that does this is *Geobacter*, which can also use O<sub>2</sub> and nitrate as alternative electron acceptors. Fe<sup>3+</sup> reduction appears to have evolved several times in phylogenetically distinct Fe<sup>3+</sup> reducers with different Fe<sup>3+</sup> reduction mechanisms and evidence suggests that Fe<sup>3+</sup> reduction may have been the first form of microbial respiration.<sup>12</sup> Denitrifying bacteria oxidise H<sub>2</sub> using nitrate. The conditions near the surface are aerobic as oxygen from the air and oxygen from photosynthetic cyanobacteria diffuse into the water. Here aerobic bacteria use oxygen to oxidise H<sub>2</sub> to water. The energy generated from the oxidation of H<sub>2</sub> by these various oxidative processes shown in Figure 1 is captured in the form of ATP by the chemiosmotic mechanism of oxidative phosphorylation.

### 1.1.2 The hydrogenases and nitrogenases

Many different kinds of microorganisms have developed ways to utilise dihydrogen as an energy source. In nature the interconversion of H<sub>2</sub> into a proton and hydride (or protons and electrons) is catalyzed by a diverse group of metalloenzymes known as hydrogenases. Based on the metal content of the active site, hydrogenases are classified according to three phylogenetically distinct classes: [Fe]-, [FeFe]- and [NiFe]-hydrogenases. The [Fe]-hydrogenase catalyses the heterolytic cleavage of dihydrogen whereas the [FeFe]- and [NiFe]- catalyse the interconversion of dihydrogen into protons and electrons. These reactions are outlined in Equation 1.



[Fe]-hydrogenases are found only in methanogenic archaea where the enzyme catalyses part of the reaction pathway in the conversion of CO<sub>2</sub> with H<sub>2</sub> to CH<sub>4</sub>.<sup>13</sup> Expression of [Fe]-hydrogenase is upregulated under nickel deficient conditions.<sup>14</sup> The active site of this enzyme is shown in Figure 2.

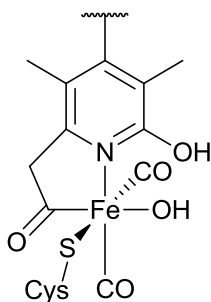


**Figure 2** Active site of [Fe]-hydrogenase.<sup>15</sup>

The [Fe]-hydrogenase was once thought to be metal-free as it is redox inactive in the accessible physiological domain of  $-1$  to  $+1$  V (redox window of water at pH 7),<sup>16</sup> and EPR (electron paramagnetic resonance) silent.<sup>17</sup> Also in contrast to the [FeFe]- and [NiFe]-hydrogenases, the [Fe]-hydrogenase contains no iron-sulfur clusters and was called “iron-sulfur cluster-free hydrogenase” to highlight this.

The [NiFe]- and [FeFe]-hydrogenases are both bi-metallic redox active hydrogenases. They both catalyse the interconversion of dihydrogen into protons and electrons. The two differ in their activity and their sensitivity to inhibition by O<sub>2</sub> and CO. The [NiFe]-hydrogenases are less sensitive to inhibition by CO and O<sub>2</sub> and their biological function involves the uptake rather than generation of H<sub>2</sub>.<sup>18</sup> The activity of [FeFe]-hydrogenase can be 10 to 100 times greater than [NiFe]-hydrogenases for both the oxidation of H<sub>2</sub> and the reduction of protons.<sup>19</sup> The active sites of the [NiFe]- and [FeFe]-hydrogenases is shown in Figure 3.

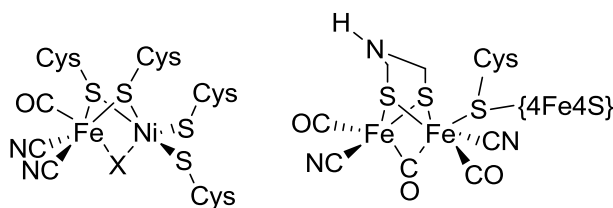
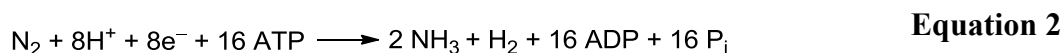


**Figure 3** Left: Active site of [NiFe]-hydrogenase (X = HOS<sup>-</sup>, HO<sup>-</sup> or H<sup>-</sup> depending on the state);<sup>20, 21</sup> Right: Active site of [FeFe]-hydrogenase (the H-cluster).<sup>21, 22</sup>

The active sites of the [FeFe]- and [NiFe]-hydrogenases both contain biologically unusual CO and CN<sup>-</sup> ligands. These ligands serve as  $\pi$ -acceptors that stabilise the low redox states of the metal ions.

Nitrogenases are enzymes that have the unique ability in nature to reduce atmospheric dinitrogen into ammonia. They are key to the biological nitrogen cycle.<sup>23</sup> Nitrogenases generate dihydrogen as an integral part of nitrogen fixation. When dinitrogen is not available nitrogenase will still catalyze the reduction of protons to dihydrogen.<sup>24, 25</sup> The general equation for the biological fixation of dinitrogen is shown below (Equation 2).



Nitrogenase enzymes are made up of two metalloprotein components, these are referred to as the Fe protein (or dinitrogenase reductase/ component II) and the molybdenum-iron (MoFe) protein (or dinitrogenase/ component I). The generation of ammonia by nitrogenase involves an intricate interaction between the protein components, ATP (adenosine triphosphate), protons and electrons.<sup>27-30</sup> The active site of nitrogenase, FeMoco, where protons and dinitrogen are reduced, is shown in Figure 4.<sup>31-33</sup>

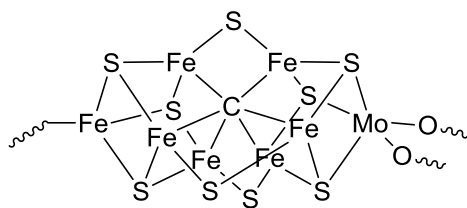


**Figure 4** The FeMo cofactor (FeMoco) of nitrogenase.<sup>31-33</sup>

The FeMoco is a complex cluster consisting of seven irons, nine sulfides and one molybdenum ion. Recent evidence suggests that the identity of the central atom is carbon.<sup>33</sup>

The P-cluster (an  $\text{Fe}_8\text{S}_9$  cluster) responsible for electron transfer to the FeMoco and found in the Fe protein of nitrogenase is shown in Figure 5.<sup>34</sup> Two states have been discovered: a reduced  $\text{P}^{\text{N}}$  state and a  $2e^-$  oxidised  $\text{P}^{\text{OX}}$  state. The  $\text{P}^{\text{N}}$  state contains a central  $\mu_6$  sulfur atom bridging six iron atoms: a remarkable bonding mode in biological iron-sulfur clusters.

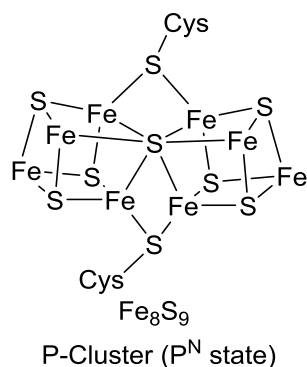


**Figure 5**  $\{8\text{Fe}7\text{S}\}$  core of the P-cluster of nitrogenase in the  $\text{P}^{\text{N}}$  state.<sup>34</sup>

## 1.2 Metallo-sulfur clusters in biology

### 1.2.1 FeS-clusters structures and roles

Iron-sulfur clusters are ubiquitous in living systems and are perhaps the most ancient of prosthetic groups. This can be recognised by their presence in the active sites of  $[\text{FeFe}]$ -hydrogenase and nitrogenase as shown previously. They are versatile and sustain many

fundamental life processes. More than 120 different enzymes and proteins have been shown to contain iron-sulfur clusters.<sup>35, 36</sup> It is speculated that iron-sulfur complexes played an imperative role in the beginnings of life on Earth.<sup>37</sup>

A major role of iron-sulfur clusters in biology is electron transport and it is their ability to delocalise electron density over their Fe and S atoms that makes them so well suited for this function.<sup>38, 39</sup> As a result, iron-sulfur clusters are the chief components of the respiratory and photosynthetic electron transport chains. Electron transport pathways in many membrane-bound and soluble redox enzymes are defined by iron-sulfur clusters. They are also the redox active centres in ferredoxins, a large class of mobile electron carriers.<sup>40</sup> Clusters involved in electron transfer can contain {2Fe2S}, {3Fe4S}, {4Fe4S}, or {8Fe7S} core units. A variety of structures of different types of iron-sulfur clusters are shown in Figure 6.

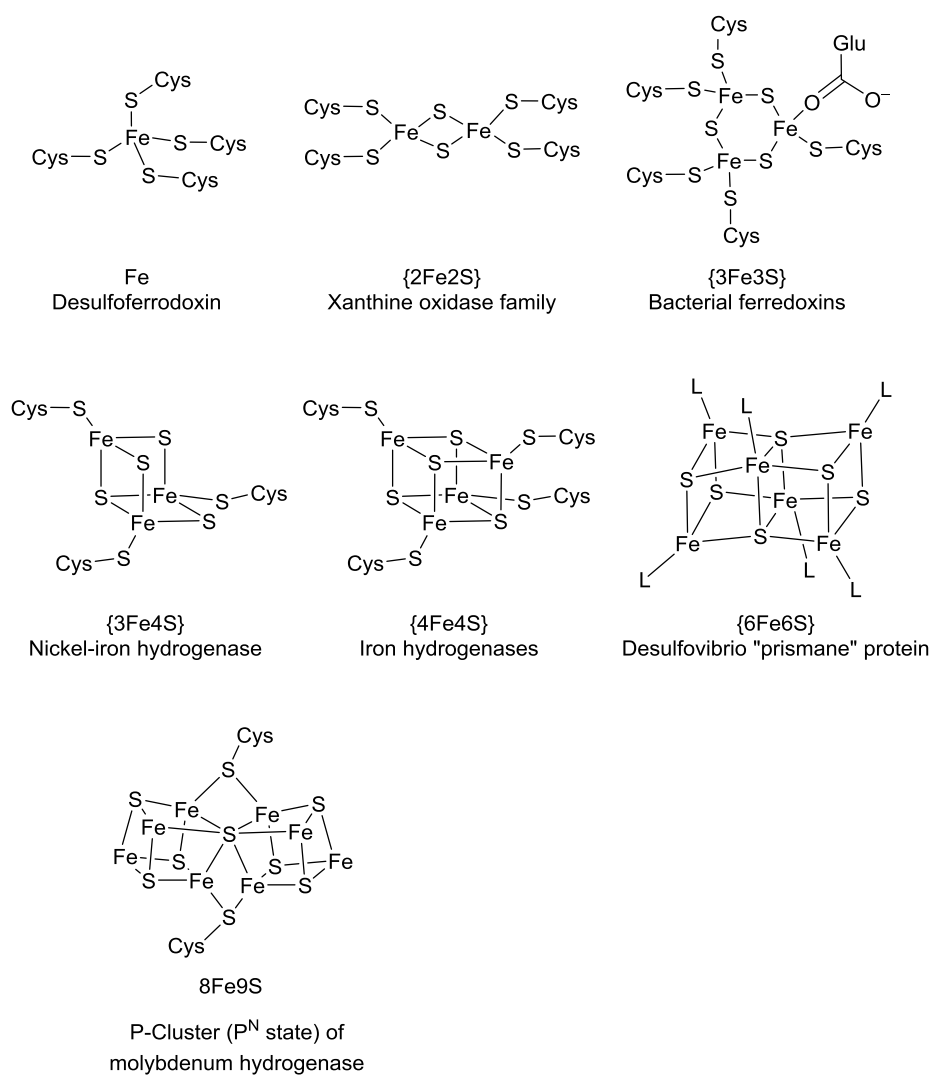


**Figure 6** The clusters in this work have been stylised as cubic structures. Crystal structures of  $\{4Fe4S\}$  clusters reveal that in reality they exhibit a distorted rhombohedral geometry.

Electron transfer is undeniably a major role of iron-sulfur clusters in biology, however, many also have a catalytic function. These include redox-active catalysts such as nitrogenase, [FeFe]-hydrogenase, carbon dioxide dehydrogenase and redox-inactive catalysts such as aconitase, endonuclease III, ferrochelatase and fumarate dehydratase. Catalytic iron-sulfur clusters generally contain  $\{4Fe4S\}$  or  $\{2Fe2S\}$  clusters that work with other metal centres such as Ni, Mo or V.<sup>43</sup> The following section will introduce important FeS cluster containing proteins.



the enzyme can be restored upon reduction of the cluster where it picks up a fourth iron reforming the  $\{4\text{Fe}4\text{S}\}^{2+}$  cluster. When nitro analogues of the natural substrates of aconitase are used activity of the enzyme is greatly inhibited. This is good evidence for the reaction catalyzed by aconitase taking place via a E1cB mechanism (elimination unimolecular conjugate base).<sup>44</sup>

### 1.2.3 CO dehydrogenase/acetyl-coA synthase (CODH/ACS)

CO dehydrogenases/acetyl-CoA synthases (CODH/ACS) are NiFeS-cluster enzymes that have a role in anaerobic carbon transformation pathways. The main function of this enzyme is to catalyze two reactions: 1) the reaction of carbon monoxide and water with an electron acceptor substrate to carbon dioxide and the reduced acceptor (Equation 3), 2) the formation of acetyl-CoA from the reaction of coenzyme A with carbon dioxide and a methyl source (Equation 4).



The CODH/ACS complex of *M. thermoacetica* has been studied extensively<sup>143</sup> and is known to be composed of an  $\alpha_2\beta_2$  tetramer where the  $\alpha$ -subunits correspond to ACS and the  $\beta_2$  dimer to CODH.<sup>144</sup> The active site of CODH/ACS holds a  $[\text{Ni}4\text{Fe}5\text{S}]$  unit known as the C-cluster. This is the site of conversion of CO to  $\text{CO}_2$ . The active site for the synthesis of acetyl-CoA is called the A-cluster, it contains a  $[\text{Ni}4\text{Fe}4\text{S}]$  unit connected via a cysteine residue to a cubic  $\{4\text{Fe}4\text{S}\}$  cluster (Figure 7).<sup>145</sup> The  $\{4\text{Fe}4\text{S}\}$  cluster in the A-cluster is likely to be the initial acceptor of electrons from the reduced CODH.

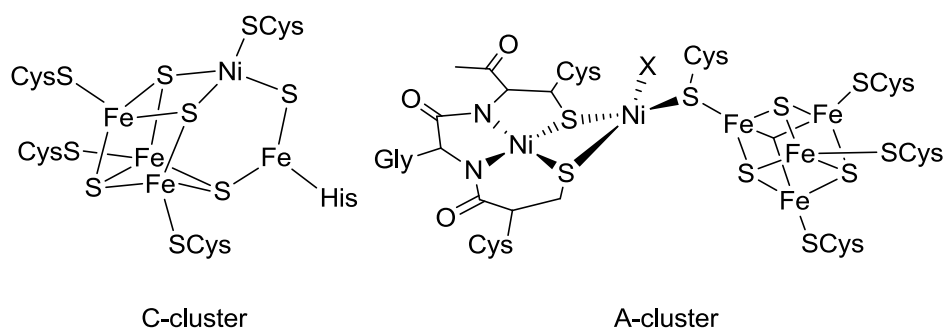


**Figure 7** The C-cluster (site of conversion of CO to CO<sub>2</sub>) (left) and the A-cluster (site of acetyl coA synthesis) (right) of CODH/ACS. X is a non protein ligand.<sup>145</sup>

### 1.2.4 Heterometallic clusters, Mo, V and Fe nitrogenases

Three homologous members of the nitrogenase family are known, the Mo-, V- and the Fe-only nitrogenase. Though similar in structure each differs by a (hetero)metallic atom in their active site. Interestingly all three exhibit nitrogenase activity with the order of greatest activity Mo > V > Fe.<sup>146</sup> Therefore activity is highest in Mo-nitrogenase but Mo is not essential for nitrogenase activity.

The Mo-nitrogenase is the most common and the best characterised. It is made up of two metalloprotein components, the Fe protein and the MoFe protein. The former contains a ferredoxin (an Fe<sub>4</sub>S<sub>4</sub> cluster) and has a role in the transfer of electrons to the MoFe protein and the hydrolysis of Mg-bound ATP. The FeMo protein contains an {8Fe9S} cluster called the P-cluster {8Fe9S} and the FeMoco {Mo7Fe9S} subsite. The P-cluster is thought to also have a role in the transfer of electrons onto FeMoco the site of N<sub>2</sub> reduction.<sup>147</sup> Like the Mo-nitrogenase, the Fe-only- and the V-nitrogenases both consist of these two component metalloproteins.<sup>148</sup>

The Fe proteins of V- and Mo-nitrogenase have been shown to share 91 % sequence identity. The VFe protein of the V-nitrogenase and the MoFe protein of the Mo-nitrogenase share approximately 33 % sequence similarity.<sup>149</sup> It has been shown that V-nitrogenase can use CO

as a substrate in addition to N<sub>2</sub>. In an experiment where both the Mo- and V-nitrogenases were in the presence of 100 % CO the generation of H<sub>2</sub> (a byproduct of nitrogenase activity) in V-nitrogenase was inhibited by 76 %, whilst Mo-nitrogenase was almost completely unaffected.<sup>150</sup> It is interesting to note that ATP hydrolysis rates in both enzymes were comparable under CO. This suggests electron flux in similar amounts in the two nitrogenases under these conditions.<sup>151</sup> These findings seem to imply that V-nitrogenase prefers CO over N<sub>2</sub> as a substrate. The dual role of the V-nitrogenase in N<sub>2</sub> and CO reduction could imply a link between the evolution of the carbon and nitrogen cycles on Earth.<sup>151</sup> In addition, it suggests that these isoelectronic substrates can be reduced by analogous reaction mechanisms.<sup>149</sup>

Fe-only nitrogenase can be formed in many nitrogenase-containing bacteria when V and Mo concentrations are very low.<sup>152</sup> The discovery of Fe-only nitrogenase showed that nitrogenase activity could be achieved in the absence of a heterometal. It seems that nitrogenase bacteria can utilise Fe-only nitrogenase as a secondary N<sub>2</sub> fixing system under Mo-deficient conditions.<sup>148</sup> A study has shown that most nitrogenase bacteria have adopted either V- or Fe-only nitrogenase as secondary way of fixing N<sub>2</sub>, whereas some species of *Azotobacter* can utilise both in addition to Mo-nitrogenase.<sup>148</sup>

### **1.2.5 Introduction to radical SAM enzymes and [FeFe]-hydrogenase structure, function and biosynthesis**

The active site of the [FeFe]-hydrogenase contains a {4Fe4S} cluster attached via a cysteine residue to a di-iron subunit. This subunit contains biologically unusual CO and CN<sup>-</sup> ligands and an azadithiolate bridge (see Figure 3) and is the centre of catalysis. Structural and conformational support is provided by the protein scaffold, allowing the active site stability in its optimal geometrical arrangements as it cycles through catalytically active states. A relay

system of {4Fe4S} clusters is held within the protein. This system assists in the fast electron transfer between the buried catalytic centre and the protein surface. The protein structure of [FeFe]-hydrogenase is shown in Figure 8.

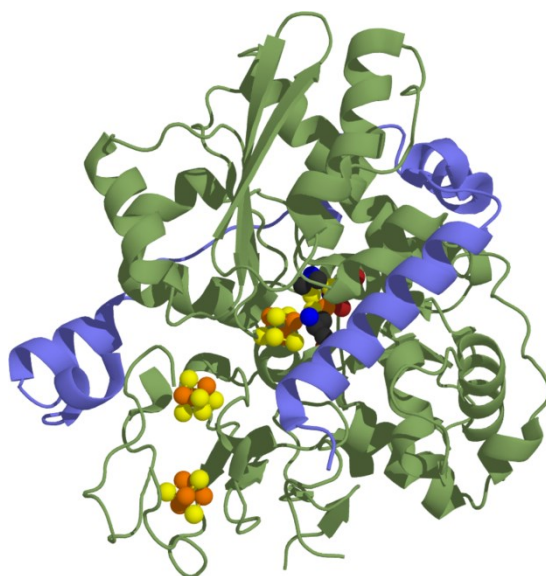


**Figure 8** *Desulfovibrio desulfuricans* [FeFe]-hydrogenase (PDB code: 1HFE):<sup>45</sup> some residues have been omitted for clarity. Reproduced with permission of the author from ref. 46.

The protein structure also incorporates hydrophobic channels forming routes for the diffusion of small gas molecules to and from the active site.<sup>45, 47</sup> These gas channels make the diffusion of consumed and produced H<sub>2</sub> into and out of the active site possible. However, the passage of other small gases is also possible leading to potential irreversible inhibition by CO and irreversible destruction by O<sub>2</sub>.<sup>48, 49</sup> This leads to the requirement to handle these enzymes very carefully and under anaerobic conditions. This gas channel is depicted below in Figure 9.

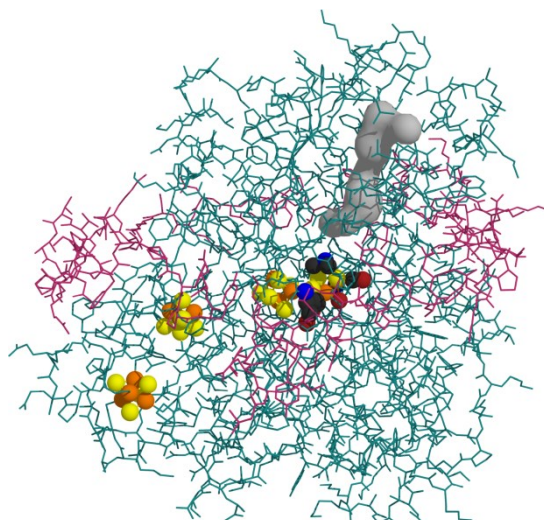
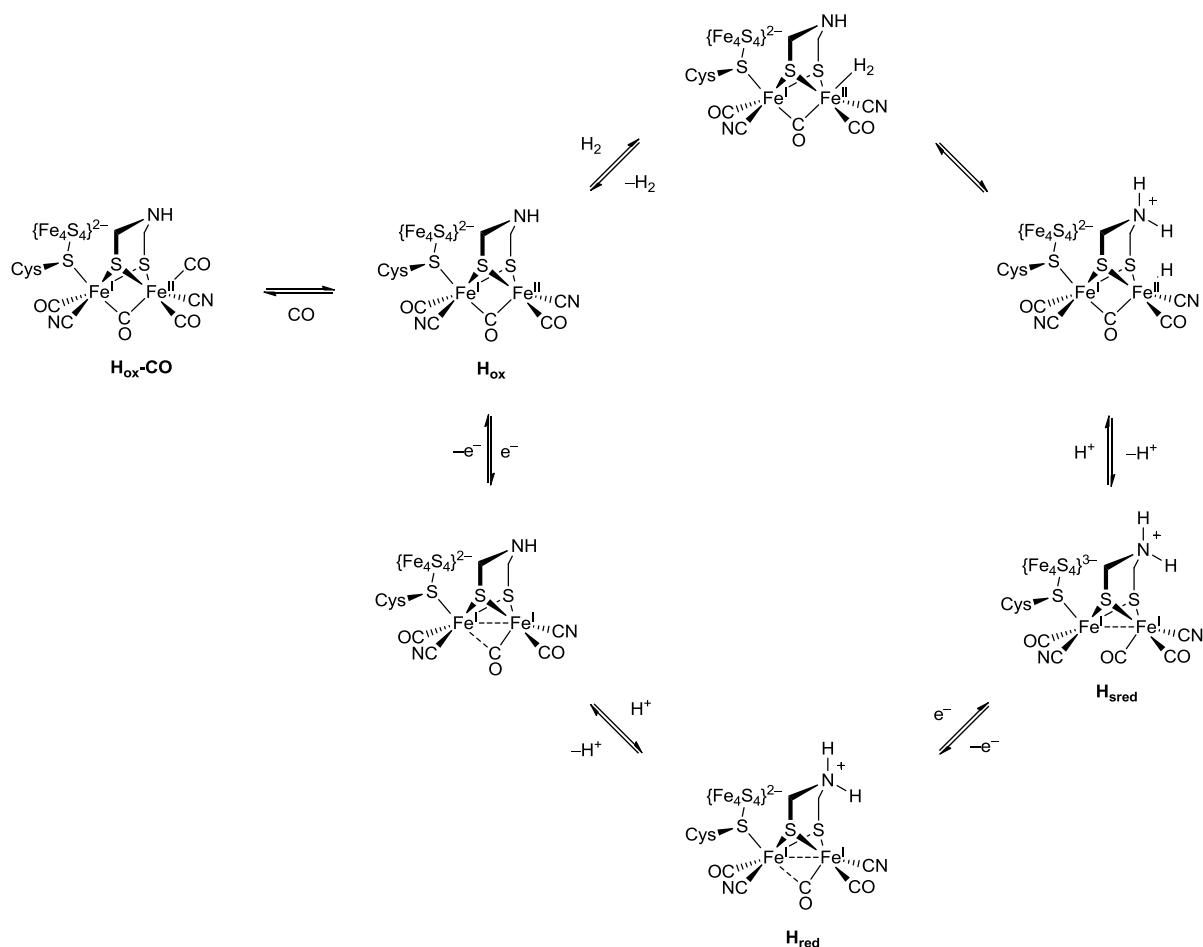


**Figure 9** structure of [FeFe]-hydrogenase from *Desulfovibrio desulfuricans* (PDB code: 1HFE);<sup>45</sup> gas channels modelled using MOLE 2.0 are depicted in grey.<sup>50</sup> Reproduced with permission of the author from ref. 46.

A combination of spectroscopic and crystallographic data has led to the current consensus view of the catalytic cycle of [FeFe]-hydrogenase (shown in Scheme 3). The species  $H_{\text{red}}$  and  $H_{\text{ox}}$  have been isolated crystallographically and characterised spectroscopically. Whilst there is EPR and FTIR evidence supporting the assignment of  $H_{\text{sred}}$  many of the other intermediates proposed in the catalytic cycle are subject to speculation.



**Scheme 3** Postulated catalytic cycle for [FeFe]-hydrogenase.<sup>51</sup>

It is proposed that H<sub>2</sub> oxidation by [FeFe]-hydrogenase occurs by H<sub>2</sub> first binding to the vacant site on the distal Fe of H<sub>ox</sub>, followed by the heterolytic cleavage of the H–H bond assisted by the amine on the bridgehead and finally the transfer of two electrons individually from the Fe bound hydride to the {4Fe4S} cluster and the distal Fe of the [FeFe] subsite. The release of protons and electrons from H<sub>sred</sub> regenerates the starting H<sub>ox</sub> state completing the catalytic cycle. Each step in the catalytic cycle is reversible and the reverse reaction the reduction of protons to H<sub>2</sub> is proposed to follow the same steps and intermediates but in the opposite direction. The following section shall discuss radical SAM chemistry and how this relates to the biosynthesis of the H-cluster.

The superfamily of radical *S*-adenosylmethionine (SAM) enzymes catalyze an extraordinarily diverse assortment of reactions ranging from the simple abstraction of hydrogen to complex multistep rearrangements and insertions. They catalyze a wide variety of biological functions, including DNA repair, tRNA modification as well as cofactor and natural product biosynthesis. The radical SAM superfamily contain a  $CX_3CX_2C$  motif that binds a {4Fe4S} cluster; conserved features that are essential for the reductive cleavage of SAM.<sup>52</sup> The {4Fe4S} cluster is bound to the motif by its three cysteines leaving one remaining iron free to bind to SAM.<sup>53</sup> The reductive cleavage of SAM into a 5'-deoxyadenosyl radical (Ado•) and methionine is a key initiating step as shown in Figure 10.

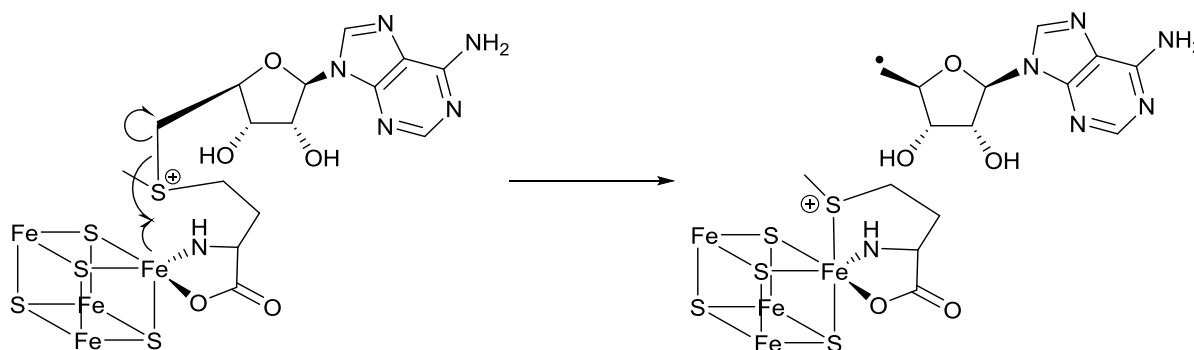


**Figure 10** General mechanism for the reductive cleavage of SAM into 5'-deoxyadenosyl radical and methionine.<sup>52</sup>

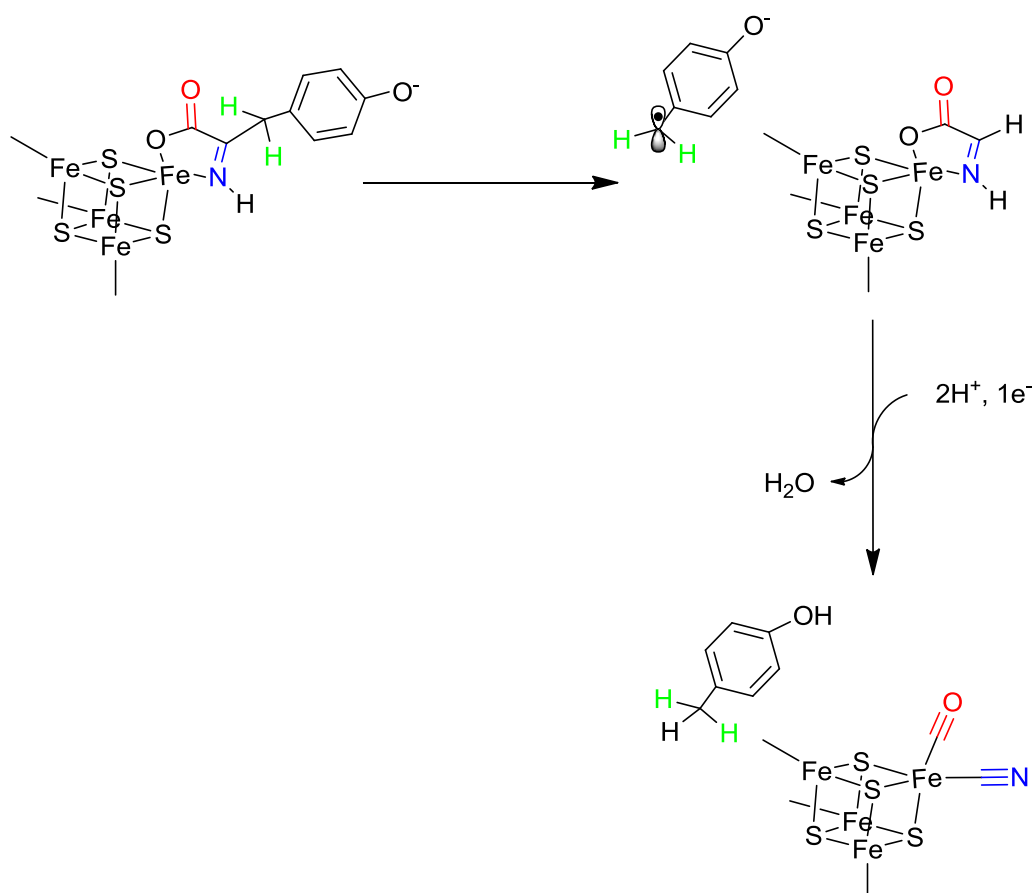
This Ado• intermediate is highly reactive and activates the substrate through stereoselective H-abstraction.<sup>54</sup> Numerous SAM enzymes have been shown to contain a second “auxiliary” {4Fe4S} cluster. In enzymes such as biotin synthase the second cluster takes part directly in the reaction: it is the source of an inserted sulfur atom.<sup>55</sup> In most other SAM enzymes with two clusters, the role of the second cluster is still uncertain, however, the possibility of the second cluster acting as an electron donor has been considered in these cases.<sup>56</sup>

The growing accessibility of crystal structures of radical SAM enzymes have allowed the identification of more conserved features of this superfamily. The position of the active site {4Fe4S} cluster within a  $\alpha_8\beta_8$  (“TIM-barrel”) fold was identified during early structural studies including those on HemN and BioB.<sup>57, 58</sup> With the increasing number of structures being revealed, a “partial”  $\alpha_6\beta_6$  was found to be a feature of many enzymes. The more open conformation of the partial TIM barrel allows the binding of larger substrates, e.g. pyruvate formate-lyase activating enzyme (PFL-AE).<sup>52</sup>

A vast amount of knowledge has been gained from the study of radical SAM enzymes since the discovery of lysine 2,3-aminomutase. However, much remains to be understood about these enzymes and the vast array and the intricacy of the reactions catalyzed. The handling difficulties connected to dealing with such oxygen-sensitive enzymes has added to the difficulty in building a complete picture. The inner workings and structure of many known radical SAM enzymes still await elucidation. Many SAM enzymes have only been identified by their sequence alignments with nothing known about their role within the enzyme, substrate or reaction catalyzed. As described below radical SAM enzymes play a key role in the maturation of hydrogenases.

The radical SAM enzymes HydE and HydG are key enzymes in the maturation of the [FeFe]-hydrogenase (HydA), an enzyme at the heart of hydrogen metabolism in certain varieties of anaerobic bacteria. The active site of HydA is composed of a {4Fe4S} cluster linked via cysteine to di-iron subsite. This subsite is known as the H-cluster and is the centre of catalysis. The H-cluster is ligated by biologically unusual CO and CN<sup>-</sup> ligands as well as an azadithiolate bridge as shown in Figure 3. Evidence suggests that the H-cluster is synthesised separately from the apoenzyme and then inserted into HydA by a mechanism involving HydE, HydF and HydG.<sup>59</sup>

HydG has high sequence similarity to biotin synthase and more is known about it than the two other H-cluster maturases (HydE and HydF). It has been shown that HydG is responsible for the synthesis of the CO and CN<sup>-</sup> ligands of the H-cluster using tyrosine as a substrate and generating *p*-cresol as a by-product (Scheme 4). HydG contains two {4Fe4S} clusters, one at the N-terminus that generates Ado• and a C-terminal cluster that is suggested to be the centre of CN<sup>-</sup> and CO production. A study has shown that disruption of the C-terminal cluster considerably reduces the enzyme's affinity for tyrosine but not for SAM. Analysis of kinetic data from iron-sulfur cluster mutants showed that the cluster at the C-terminus is not necessary for tyrosine cleavage to *p*-cresol but is needed for the conversion into CO and CN<sup>-</sup>.<sup>60</sup> Generally, it is accepted that initiation of the reaction of HydG is caused by phenolic hydrogen abstraction from tyrosine by Ado•, however, what happens following this and subsequent steps is unclear. In recent work <sup>2</sup>H, <sup>13</sup>C and <sup>15</sup>N-labelled tyrosine together with EPR spectroscopy were used to unveil reaction intermediates of HydG. From this a detailed mechanism was proposed making account of the roles of the N- and C-terminal clusters.<sup>61</sup> The findings support a mechanism in which the tyrosine radical is cleaved heterolytically to produce a 4-oxidobenzyl radical and dehydroglycine, where dehydroglycine is bound to the C-terminal cluster. The 4-oxidobenzyl radical is reduced by electron and proton transfer to *p*-cresol. Finally, via a mechanism that is still to be fully elucidated CO and CN<sup>-</sup> ligands are generated by the cleavage and dehydration of dehydroglycine as shown in Scheme 4. It is proposed that these small diatomic ligands bind in a *cis* fashion to the unique iron site of the C-terminal cluster.<sup>61</sup>



**Scheme 4** Proposed mechanisms for the generation of CN<sup>-</sup> and CO ligands from tyrosine in HydG: Tyrosine binds to the accessible iron atom at the C-terminal [4Fe-4S] cluster where the phenolic hydrogen atom is abstracted by the SAM generated 5'-deoxyadenosyl radical. Heterolytic cleavage occurs generating dehydroglycine and a 4-oxido benzyl radical. The latter species is reduced to p-cresol while dehydroglycine quickly decomposes leaving one CO and one CN ligand at the C-terminal {4Fe4S} cluster.<sup>61-63</sup>

Further work by Kuchenreuther and co-workers<sup>62</sup> involving an elegant combination of stopped-flow FTIR (Fourier transfer-infrared) and electron-nuclear double resonance (ENDOR) spectroscopies has provided evidence supporting the idea that the Fe(CO)(CN) complex is further converted by HydG to an Fe(CO)<sub>2</sub>(CN) synthon. This synthon potentially forms part of the H-cluster's active site and is proposed to be inserted into apo-HydA by the actions of HydE and HydG.

Although the structure and function of the [FeFe]-hydrogenase has been widely modelled, explored and characterised,<sup>47, 63, 64</sup> the mechanism by which it is assembled in biology is not yet fully understood. Early experiments where the gene for expression of the [FeFe]-hydrogenase enzyme, HydA was expressed in *E. coli* found that the protein obtained was inactive.<sup>65</sup> A study by Mulder showed that the subsite was missing but the cluster had been put together by *E. coli*. Therefore the genes that code for “machinery” that assembles the subsite must be separate from those that code for the enzyme. There are three accessory proteins responsible for the bioassembly of the diiron subsite and its insertion into HydA. These are known as HydE, HydF and HydG and the genes that code for them were discovered about 10 years ago.<sup>66</sup> These genes are conserved in all species that produce [FeFe]-hydrogenase<sup>67</sup> and when expressed in *E. coli* can be used to activate apo-HydA.<sup>68</sup>

HydF contains two domains that are crucial for hydrogenase maturation, a {4Fe4S} cluster near the C-terminus with three conserved cysteines and an N-terminal GTPase domain.<sup>69, 70</sup> HydE and HydG are both radical SAM enzymes<sup>71</sup> containing a N-terminal {4Fe4S} cluster with an open binding site that can bind *S*-adenosyl methionine (SAM). HydE and HydG also contain binding motifs at the C-terminus for a second iron-sulfur cluster. Under certain preparative conditions HydE can be shown to contain a {2Fe2S} cluster.<sup>72</sup>

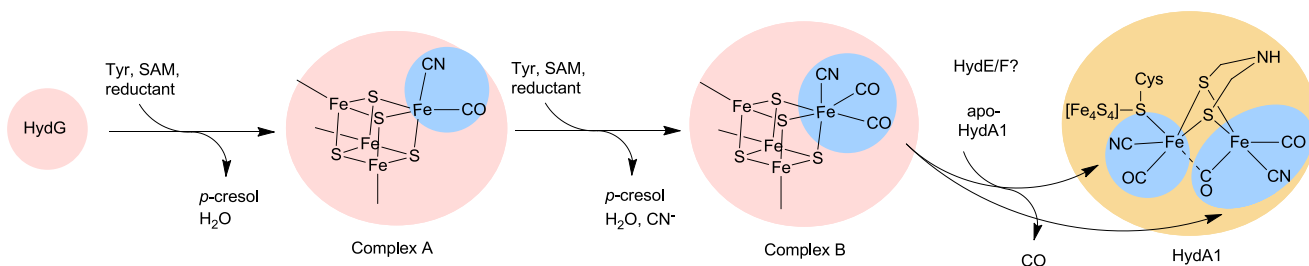
Radical SAM enzymes catalyze numerous radical reactions and it is thought that the CO, CN<sup>-</sup> and the bridging dithiolate group of the active site are all products of such reactions.<sup>63</sup> It seems plausible that the ligands of the active site are made by HydE and HydG, whilst HydF puts the subsite together. It has been shown that when purified HydF is expressed with HydE and HydG, apo-HydA can be converted into active [FeFe]-hydrogenase.<sup>73</sup> A FTIR, EPR and EXAFS (extended X-ray absorption fine structure) study on HydF from *Clostridium acetobutylicum* expressed with HydE and HydG found that a diiron species similar to the H-

cluster is present in fully “assembled” HydF.<sup>74, 75</sup> Similar results were obtained when the same genes were expressed in *E. coli*.<sup>76</sup> The data obtained for both of the experiments above were not identical but both sets of results point to a binuclear iron subsite with CO and CN<sup>-</sup> ligands. In HYSCORE (hyperfine sub-level correlation) experiments on *Clostridium acetobutylicum* HydF reduced {4Fe4S} cluster revealed coordination by a histidine ligand.<sup>74</sup> This was later identified as His352 (one of two conserved histidines).<sup>77</sup> The same HYSCORE experiment in *Thermotoga maritima* HydF did not reveal any histidine coordination.<sup>69, 78</sup> The two histidines in the [4Fe4S] binding pocket are essential for the correct maturation of HydA even though they are not necessary for the binding of the cubane cluster.<sup>77</sup> It is therefore feasible that they could play a part in stabilizing the [2Fe]<sub>H</sub> precursor in HydF perhaps through hydrogen bonding. In an EPR study photoreduced nonreconstituted *Clostridium acetobutylicum* HydF in *E. coli* (without maturases HydE and HydG) an additional EPR signal was seen and was assigned to a reduced {2Fe2S} cluster.<sup>76, 79</sup> It has been suggested that this binuclear core could serve as a scaffold onto which to assemble the CO, CN<sup>-</sup> and dithiol ligands thus forming the H-cluster [2Fe]-subsite.<sup>63</sup> Unassembled HydF seems unlikely to contain a preformed diiron scaffold prepared to accept the individual ligands. This would mean that the potentially toxic ligands would have to be released directly into the cytosol causing harm to the cell. It is therefore proposed that the ligands are received by HydF in preformed iron centred “packages”.<sup>63</sup> Further investigation into the structures and activity of HydG and HydE may provide insight into the mechanism of assembly of the diiron subsite.

In addition to a SAM binding {4Fe4S} cluster, HydG and HydE contain a binding site for a second iron-sulfur cluster at the C-terminus of the protein. The occupancy and function of these sites is still debatable. The FeS site in HydE is not required for maturation, whilst the site in HydG seems to be essential.<sup>72</sup> In solution it seems that HydE can accommodate a second {4Fe4S} cluster,<sup>71</sup> but this is not seen in available crystal structures.<sup>72, 80</sup> In structures

containing bound SAM and thiocyanide the second site is occupied by a {2Fe2S} cluster coordinated by three cysteines and one arginine or water molecule.<sup>80</sup> The design of HydE seems to suggest a metabolite pathway from the radical SAM site through a “TIM barrel” to the C-terminal {2Fe2S} cluster with analogy to what is found in BioB (a protein involved in Biotin biosynthesis).<sup>58</sup> HydE and HydG have very similar sequences, however, HydE is not known to have a substrate, while HydG uses tyrosine. It has been shown that HydG converts tyrosine into *p*-cresol, HCN and CO (Scheme 4).<sup>81, 82</sup> In experiments using labelled tyrosine the CN<sup>-</sup> and CO were shown to be derived from the C $\alpha$ -N and CO<sub>2</sub><sup>-</sup> moieties.<sup>83</sup> This reaction shows great similarity to other radical SAM proteins for example ThiH (thiamine biosynthesis) and BioB.<sup>81, 84</sup> The N-terminal cluster in HydG is extremely important for CO and CN<sup>-</sup> synthesis. When a HydG variant is produced without this cluster some CN<sup>-</sup> is still generated<sup>85, 86</sup> but this is at a rate 100 times lower than wild type HydG.<sup>61</sup> Spectroscopic and kinetic studies involving the C-terminal cluster showed that it could be involved in tyrosine binding in a mode similar to that of the SAM binding cluster.<sup>60, 61</sup> An oxido-benzyl radical intermediate was found in a rapid freeze quench study during the conversion of tyrosine by HydG.<sup>61</sup> This supports the mechanistic idea that dehydroglycine could be bound to the open coordination sphere of the C-terminal {4Fe4S} cluster during the formation of CO and CN<sup>-</sup> (Scheme 4).

Kuchenreuther and co-workers<sup>62</sup> carried out stopped-flow FTIR and ENDOR spectroscopy studies on HydG and identified the presence of two distinct spectroscopic intermediates on the pathway to generating the diiron subsite of [FeFe]-hydrogenase. They proposed a pathway for synthon formation where CO and CN<sup>-</sup> are coordinated to the corner of the {4Fe4S} cube, as outlined in Scheme 5.

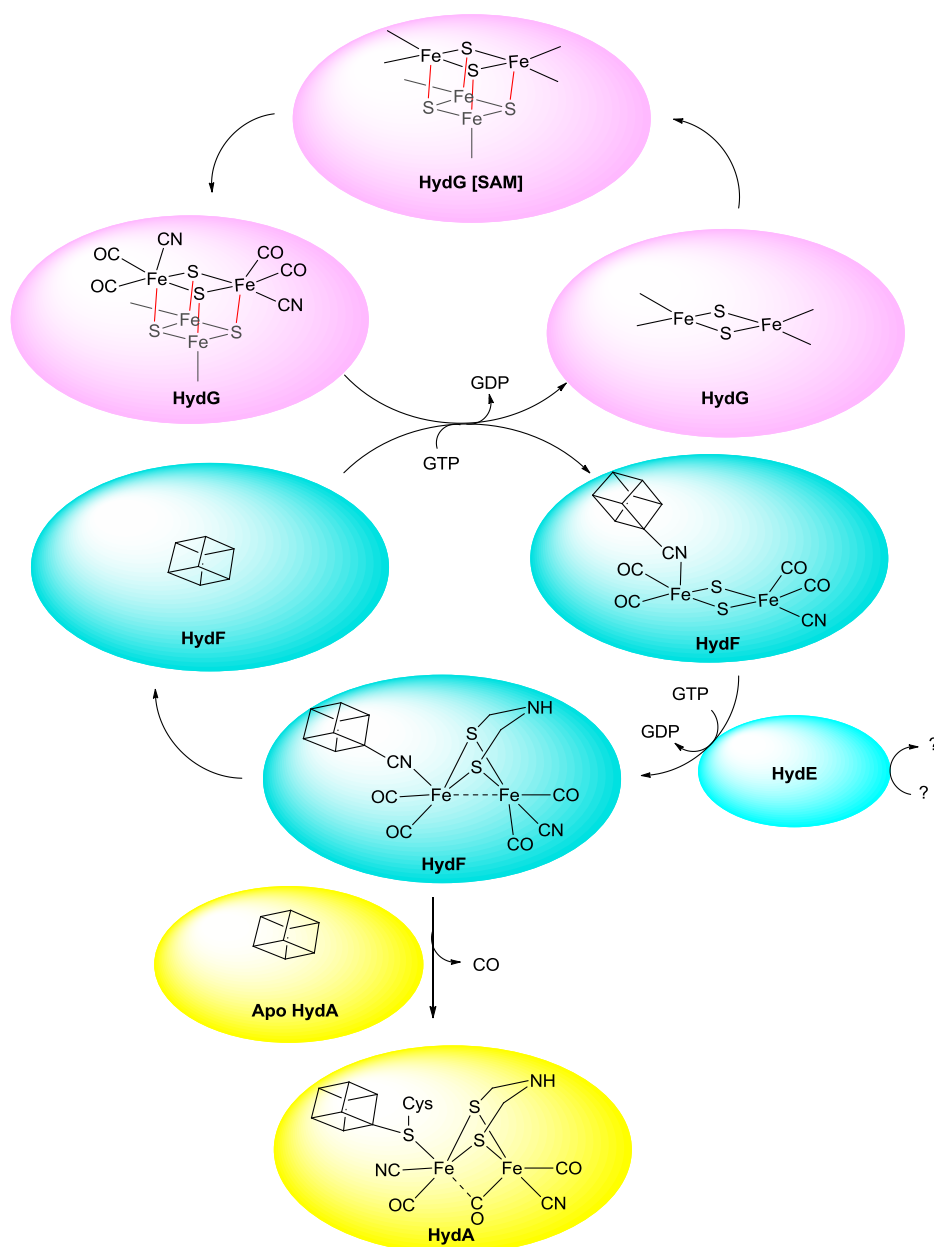


**Scheme 5** Pathway proposed by Kuchenreuther<sup>62</sup> involving the formation of two distinct intermediates on the way to formation of the diiron subsite of [FeFe]-hydrogenase.

A recent study has provided fresh insight into the structure and therefore mechanism of action of HydG.<sup>87</sup> Using high resolution crystal structure and EPR analysis it was revealed that HydG contains a [Fe<sub>5</sub>S<sub>5</sub>] cluster featuring a labile fifth Fe thought to be the centre of Fe(CO)<sub>2</sub>(CN) synthon formation.

Earlier it has been hypothesised that HydG also forms the dithiol bridging ligand, by catalyzing the conversion of tyrosine into a glycine radical which then reacts with C-terminal [4Fe-4S] cluster.<sup>88</sup> The Swartz group conducted extensive *in vitro* maturation studies<sup>89</sup> where HydA, HydE, HydG, and HydF were all individually expressed in *E. coli* and incubated in all possible combinations. This work showed that HydG seemed to be the only maturase essential for the activation of HydA. The final activity of HydA does not seem to be affected at all by exclusion of HydF during *in vitro* maturation. Maturation without HydE results in only 4 % activity. It should be noted however that these experiments took place in the presence of *E. coli* cell lysate which proved to be necessary for *in vitro* maturation. This led to the suggestion that HydA can be activated by HydG and the “housekeeping” proteins of *E. coli* alone. A recent study by Britt, George and co-workers has revealed the FTIR spectroscopic signature of potential Fe(CO)<sub>2</sub>CN “synthon” after two tyrosine turnovers of HydG.<sup>62</sup> It was proposed that this species is centred at the accessible unique iron atom of the C-terminal {4Fe4S} cluster in HydG. It was shown with <sup>57</sup>Fe ENDOR studies that HydG is

the sole source of iron for the H-cluster.<sup>62</sup> It has therefore been proposed by Swartz and co-workers that HydG acts as a protein scaffold for the H-cluster rather than HydF. This idea sees HydF acting as a transferase to store and pass the synthesised diiron subsite and all its ligands to apo HydA. It is strongly suggested that the first step in the assembly of the diiron subsite occurs on the second [4Fe-4S] cluster of HydG.<sup>63</sup> It could be speculated that after four turnovers an  $\text{Fe}_2(\text{CO})_4(\text{CN})_2$  species is formed as part of the cubane cluster. It could also be proposed that during the same process the azadithiolate bridge is formed in a mechanism such as that proposed by Pilet and co-workers.<sup>88</sup> This paints a picture of HydG being a highly multitasking enzyme which catalyses both the radical splitting of tyrosine as well as the processing of the dehydroglycine subsequently formed into CO and  $\text{CN}^-$  ligands. Although a mechanism where HydG synthesises the bridging ligand seems feasible, it could also be possible that HydE synthesises the azadithiolate bridge (further along the assembly line) as the sequence homology of HydE and HydG is high. The evidence so far is beginning to build a picture of what the maturase pathway might look like. A speculative mechanism is highlighted below (Scheme 6).<sup>63</sup>



**Scheme 6** Proposed pathway for the maturation of HydA: 1) CO and CN<sup>-</sup> ligands are derived from tyrosine in HydG and captured on the second {4Fe4S} cluster; 2) an Fe<sub>2</sub>S<sub>2</sub>(CO)<sub>4</sub>(CN)<sub>2</sub> unit is separated from this cluster and passed to HydF; 3) under GTP (guanosine-5'-triphosphate) consumption this precursor is passed to HydE which incorporates the bridging thiol through an as yet unknown mechanism; 4) the Fe<sub>2</sub>(adt)(CN)<sub>2</sub>(CO)<sub>4</sub> precursor, again under GTP conversion is finally inserted into apo-HydA yielding the native holo-enzyme, thereby releasing HydF for the next turnover. Adapted from ref. 63.

This mechanism proposes that HydG and HydE interact with HydF sequentially during *in vivo* maturation. Recent maturation expression studies support this and reveal distinct HydG-HydF and HydE-HydF interactions suggesting the separate participation of HydE and HydG in modifying the H-cluster precursor on HydF.<sup>90</sup> HydE is proposed to pick up a precursor intermediate lacking the azadithiolate bridge from HydF and this could be why no substrate conversion activity is found when looking at HydE alone. In order for activity to be seen the correct precursor is required in the FeS binding pocket. It is thought that the subsequent dissociation of HydE and HydG from HydF after transfer of intermediates may be driven by the GTPase activity of HydF.<sup>90</sup> *In vivo* maturation of HydF appears to be essential whilst *in vitro* maturation can occur in the absence of HydF, this might be related to the difference in concentration regime between *in vitro* and *in vivo* maturation.<sup>89</sup> It has been demonstrated that a synthesised chemical model of the diiron subsite of [FeFe]-hydrogenase can be introduced into HydA without any helper proteins.<sup>91</sup> During *in vitro* experiments like this the concentrations of reactants seem to be high enough for insertion to occur spontaneously, whereas in the cell, the concentrations of reactants are low and therefore transfer needs to be facilitated by transferases.

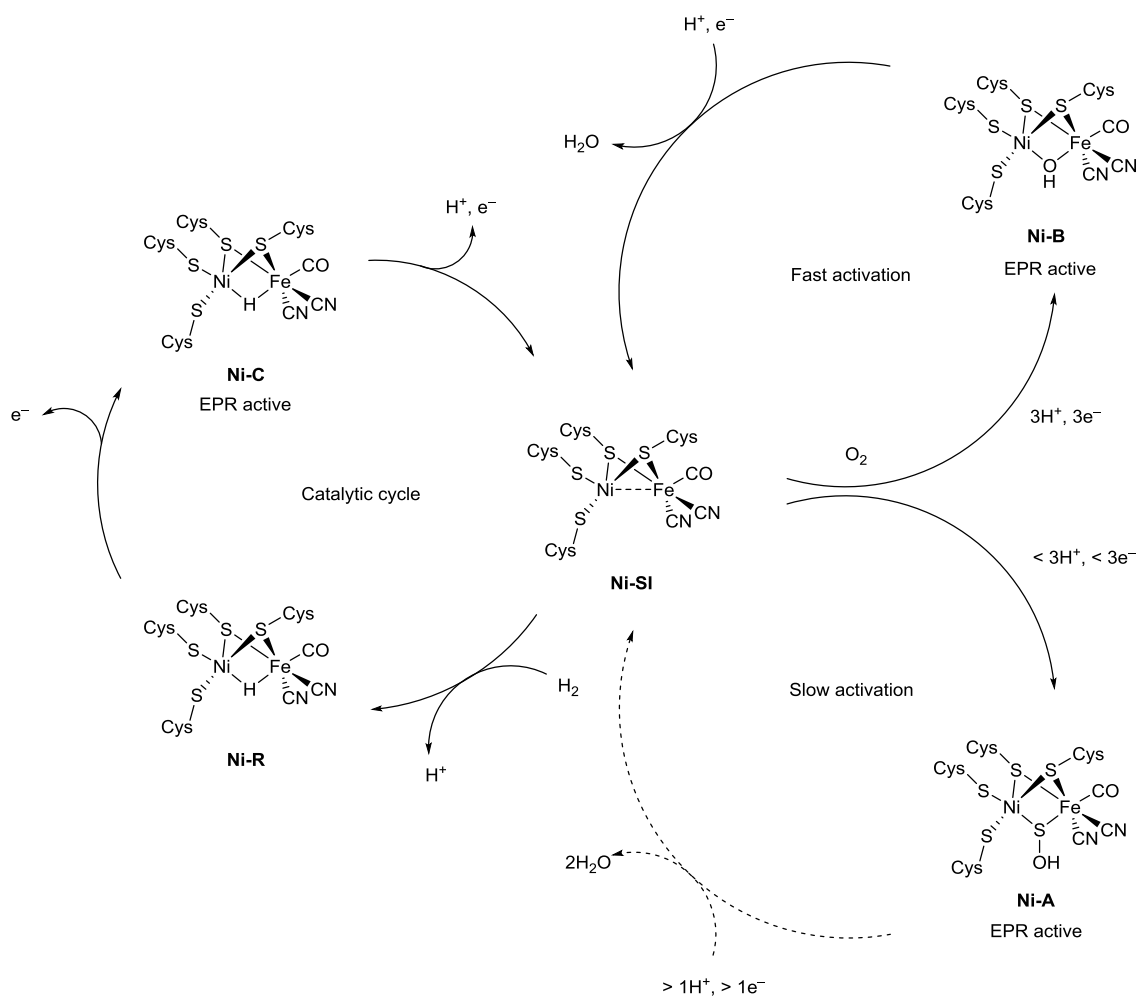
Mechanistic studies into the bioassembly of the H-cluster have provided great insight into how the diiron subsite might be put together by its maturases. However, more information and evidence is required in order to generate a complete mechanistic picture.

### **1.2.6 [NiFe]-hydrogenase - structure/ function/ biosynthesis**

The [NiFe]-hydrogenase is the most biologically abundant hydrogenase.<sup>92</sup> As with the [FeFe]-hydrogenases, [NiFe]-hydrogenase can reversibly catalyze the interconversion of H<sub>2</sub> into protons and electrons at low overpotentials, however, their physiological specialism is in hydrogen uptake.

The active site of the [NiFe]-hydrogenase as shown in Figure 3 is composed of a bimetallic core bridged by two cysteinyl ligands with two further cysteine ligands coordinated at nickel and one CO and two CN<sup>-</sup> ligands coordinated to iron. These ligands are conserved in the catalytic cycle.<sup>64, 92</sup> The nickel centre has approximate disphenoidal (“seesaw”) or distorted trigonal pyramidal geometry, whilst the iron atom has octahedral or square pyramidal geometry depending on the state of the enzyme. Inhibition of [NiFe]-hydrogenase by CO occurs at the nickel atom.<sup>93</sup>

The catalytic cycle and routes of conversion of inactive to active enzyme states of [NiFe]-hydrogenase are depicted in Scheme 7. The cycle below covers states that have been crystallographically and/or spectroscopically identified. **Ni-A** is a well characterised state is EPR-active.<sup>94</sup> This state is aerobically isolated and unlikely to be physiologically relevant as it is inactive. It can however be gradually activated under reducing conditions. It is postulated that the bridging species residing between the Ni(III) and Fe(II) in this state is a hydroperoxide ligand.<sup>95</sup> In order to convert this state into the catalytically active, EPR-silent, Ni(II)Fe(II) **Ni-SI** level, the hydroperoxide ligand must be removed and this thought to be why this process is so slow. The **Ni-B** state can be crystallographically characterised by isolation of the [NiFe]-hydrogenase under anaerobic and reducing conditions followed by controlled oxidation at low temperature. This form of the enzyme can be quickly activated to give **Ni-SI**.<sup>95</sup> The bridging ligand between the Ni(III) and Fe(II) in **Ni-B** has been shown to be an oxygen ligand (hydroxide in this case).



**Scheme 7** Overview of the known species in the catalytic and activation cycles of [NiFe]-hydrogenase.<sup>92, 94</sup>

FTIR data available on the different redox/protonation states of the [NiFe]-hydrogenase is complex. For example there are two postulated **Ni-SI** and three **Ni-R** substates.<sup>47, 64</sup> Confident assignment is given to the species in [NiFe]-hydrogenase from *Desulfovibrio gigas*.<sup>96</sup>

Assignment of available crystallographic data for the reduced states of the enzyme (e.g. EPR-active **Ni C** or EPR-silent **Ni-SI**) can be ambiguous.<sup>97</sup> The presence of a bridging hydride in **Ni-C** is shown unambiguously in spectroscopic evidence<sup>98, 99</sup> (which of course would not be difficult to detect in protein crystallography).

The active site of the [NiFe]-hydrogenase is made up of a NiFe(CN)<sub>2</sub>CO sub-unit which contains unusual biologically toxic diatomic ligands. This subsite is linked to an electron transport chain made up of three iron-sulfur clusters. The generation of this enzyme requires a complex interplay between maturation machinery including several accessory proteins (HypA, -B, -C, -D, -E, -F and others). More is known about the maturation processes involved in the biosynthesis of the [NiFe]-hydrogenase than the [FeFe]-hydrogenase and biochemical and structural studies in the last ten years have shed a lot of light on the mechanism.<sup>100-102</sup> In the maturation of [NiFe]-hydrogenase there are four accepted main steps: 1) the [NiFe] active site is assembled in four substeps: synthesis of CN<sup>-</sup>, formation of Fe-CN, insertion of CO and insertion of Ni into the apoprotein; 2) C-terminal cleavage of the large subunit; 3) delivery of the iron-sulfur clusters to the small subunit 4) the protein is translocated from the cytoplasm to the periplasm by a twin arginine translocation system.<sup>63</sup> Figure 11 depicts some of the main features in the maturase pathway of the [NiFe]-hydrogenase. HypEF generate the CN<sup>-</sup> ligands from carbamoyl phosphate.<sup>103, 104</sup> S-Carbamoylation of HypE is catalyzed by HypF via two unstable intermediates.<sup>105-108</sup> At the C-terminus of HypE a cysteine thiol forms a thiocarboxamide which is subsequently converted into thiocyanate by ATP (adenosine triphosphate)-dependent dehydration.<sup>109, 110</sup> The attached CN<sup>-</sup> is then passed on to an iron atom within the HypCD complex.

The CO ligand of the [NiFe]-hydrogenase was first thought to be synthesised from carbamoylphosphate as with CN<sup>-</sup>. It was suggested in later studies that CO is derived from a different source.<sup>111-113</sup> When *Ralstonia eutropha* is grown heterotrophically with glycerol or fructose that has been <sup>13</sup>C labelled the CO ligands were derived exclusively from <sup>13</sup>C-labelled glycerol.<sup>114</sup> In the presence of <sup>13</sup>CO gas and non-labelled glycerol-fructose medium, the CO ligand in [NiFe]-hydrogenase was <sup>13</sup>C-labelled. This leads to the postulation that CO in [NiFe]-hydrogenase is derived from ambient CO, this is not likely however as the

concentration of gas used in the labelling experiment was 130 times higher than in ambient conditions and resulted in only 50 % labelling of the CO ligand. Cell growth was delayed significantly in cells that were grown in a minimal medium under CO-limited conditions. Under these conditions it seems that gaseous CO, with an unknown biosynthetic pathway, is required. The results regarding generation of CO suggest that a different biosynthetic pathway exists to synthesise the CO ligand.

$\text{Fe}(\text{CN})_2\text{CO}$  is put together by cooperation between HypC, HypD and HypE, where HypD is used as a scaffold.<sup>115, 116</sup> The two cyanide ligands are the first to bind to iron, transferred from HypE, followed by CO (see Figure 11).<sup>117</sup> Binding of  $\text{CN}^-$  first in the HypCD-Fe complex allows the stabilization of iron in as a low spin Fe(II) thus allowing the carbonyl ligand to bind to iron.<sup>110, 118</sup> The  $\text{Fe}(\text{CN})_2\text{CO}$  is subsequently inserted into precursor large subunit before the nickel atom is inserted.<sup>63</sup> A complex of HypA and HypB together with SlyD (sensitive to the lysis of D) are involved in Ni insertion.<sup>119-122</sup> One Ni binds per HypA monomer with high affinity. In addition it has been shown that HypA can bind the large precursor subunit without the involvement of the other Hyp proteins.<sup>123</sup> Therefore the evidence suggests that HypA is responsible for Ni trafficking.<sup>124</sup> The GTPase HypB contains two metal binding sites for Ni or Zn.<sup>125</sup> Nickel migrates from the GTPase domain of HypB to HypA, this is made more efficient by the formation of a HypAB complex.<sup>126, 127</sup> SlyD (or GDP) binding to HypB can increase the rate of transfer of Ni from HypB to HypA.<sup>128, 129</sup>

There are two major steps in the biosynthesis of the iron-sulfur clusters in [NiFe]-hydrogenase: firstly the iron-sulfur clusters are constructed within a scaffold protein and secondly these clusters are trafficked to the target apoprotein.<sup>130</sup> In the construction step, L-cysteine derived sulfur is transferred to the scaffold, produced by cysteine desulfurases. Iron is derived from a source that has not yet been revealed and the iron-sulfur clusters are assembled within the scaffold. The mechanism by which this occurs is not yet understood.

The transfer step is carried out by iron-sulfur carrier proteins, in *E. coli* these are ErpA (essential respiratory protein A), IscA (iron-sulfur cluster protein A) and SufA (sulfur mobilization protein A).<sup>131</sup> It has been shown that in the maturation of the iron-sulfur clusters in *E. coli* only IscA and ErpA are essential.<sup>132</sup> The assembled [NiFe]-hydrogenase is then moved from the cytoplasm to the periplasm by a Tat protein export pathway.<sup>133</sup> The overall maturase pathway for the NiFe active site is summarised in Figure 11.

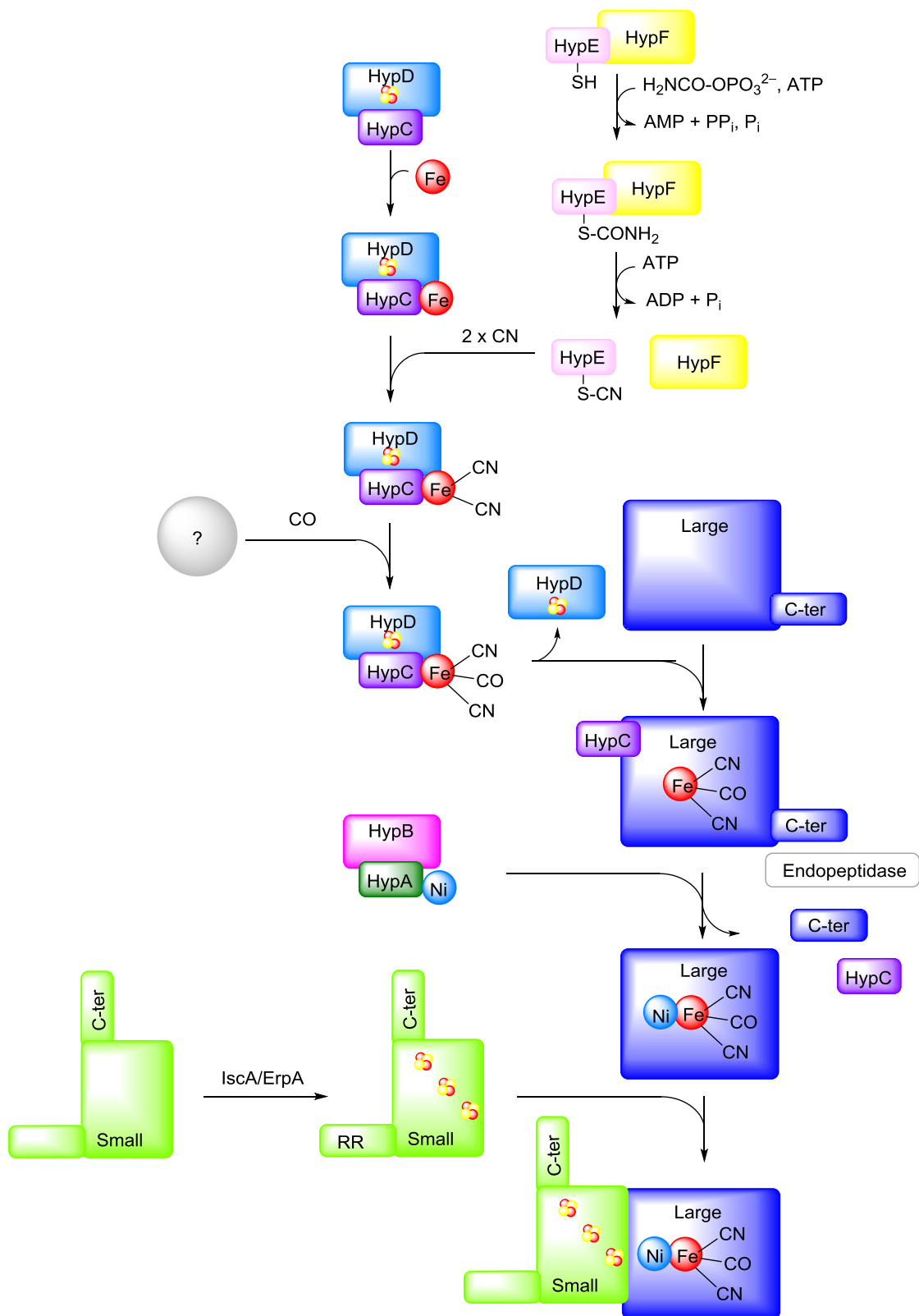
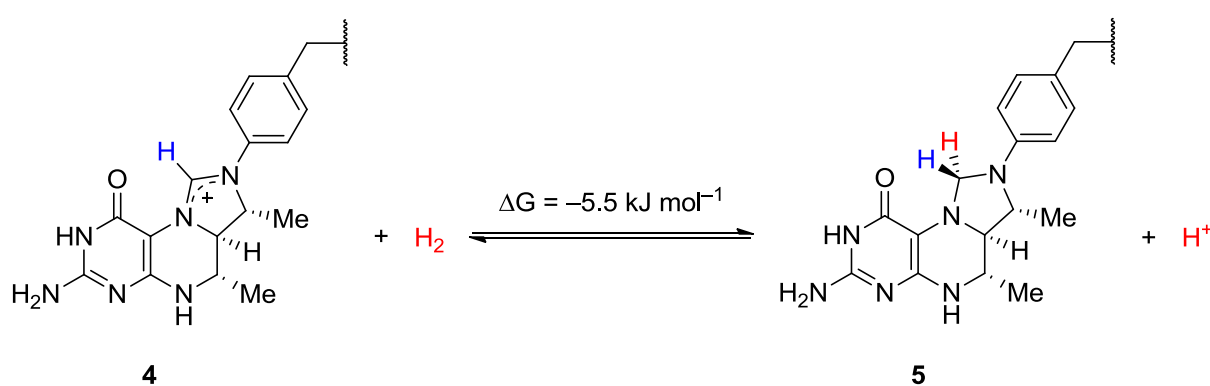


**Figure 11** Schematic representation of the maturation pathway of [NiFe]-hydrogenase in *E. coli* focusing on the generation of the subsite. Adapted from ref. 63.

### 1.2.7 [Fe]-hydrogenase- structure/ function/ biosynthesis

The [Fe]-hydrogenase is expressed by methanogenic archaea under nickel-deficient conditions.<sup>134</sup> These bacteria use dihydrogen as an energy source and the hydrogenase plays an important role in the methanogenic pathway, where it catalyses the reversible reduction of methenyltetrahydromethanopterin (methenyl-H<sub>4</sub>MPT<sup>+</sup>) to methylene-H<sub>4</sub>MPT. In this process dihydrogen is heterolytically cleaved into a proton and a hydride ion, which is transferred to the *pro-R* position of the carbocation atom shown in Scheme 8.



**Scheme 8** Stereospecific reversible hydride transfer to methenyltetrahydromethanopterin 4, catalyzed by the [Fe]-hydrogenase.<sup>135, 136</sup>

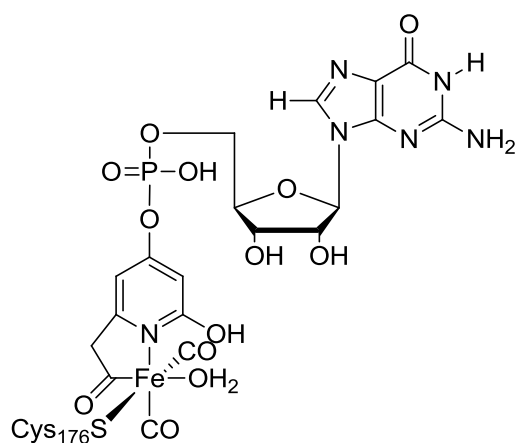


**Figure 12** [Fe]-Hydrogenase active site including guanylyl pyridinol cofactor.<sup>15</sup>

The active site of this enzyme is made up of an Fe(II) centre ligated by biologically unusual *cis* CO, cysteine and a chelating guanylyl pyridinol (GP) cofactor as shown in Figure 12. The crystal structure of this enzyme was fully revealed in 2009.<sup>15</sup> The [Fe]-hydrogenase enzyme is homodimeric and composed of three folding units. The N-terminal peripheral units are made up of Rossmann fold-like domains. The central unit is made up of an intertwined helix bundle formed from the C-terminal segments of each subunit. The active site of the [Fe]-hydrogenase is bound within the peripheral units as shown in Figure 13.<sup>137</sup>

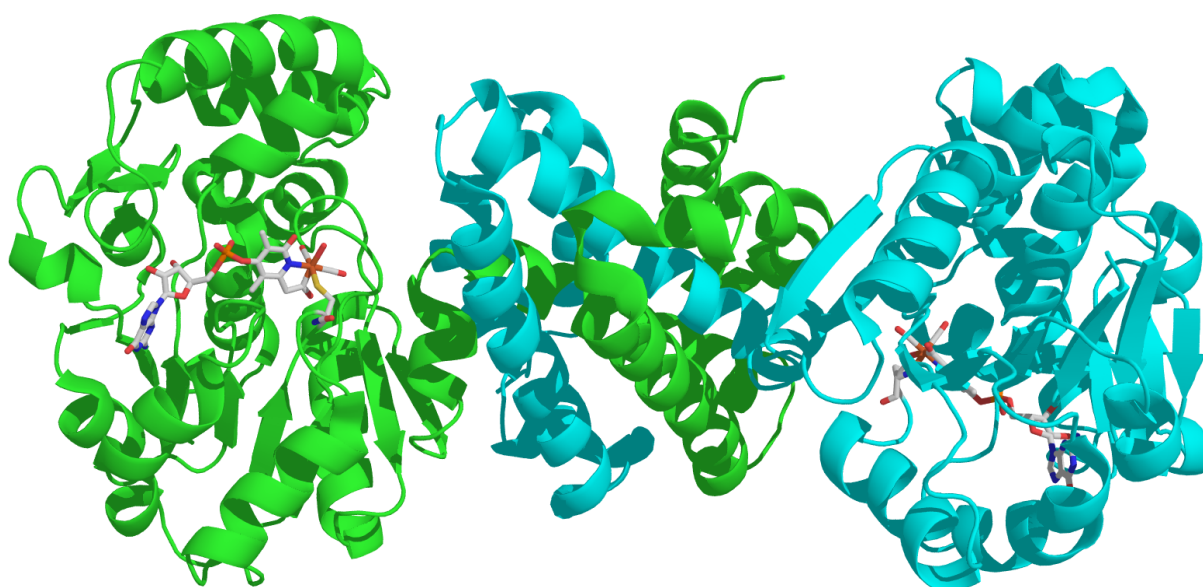


**Figure 13** Crystal structure of the wild-type holoenzyme from *Methanocaldococcus jannaschii*, showing the two protein subunits (cyan and green) and the bound Fe cofactor (grey = carbon, blue = nitrogen, red = oxygen, orange = phosphorus, yellow = sulfur, dark brown = iron).<sup>137</sup> The structure of the apoenzyme shows the same homodimer arrangement, but containing a ‘closed’ cleft between the peripheral and central units.<sup>138</sup>

The studies leading to the proposed mechanism by which the [Fe]-hydrogenase functions are discussed in section 3.1.3. The elucidation of the structure of [Fe]-hydrogenase came around a decade after the structures of the [FeFe]- and [NiFe]-hydrogenases were revealed. Thus

relatively little is known about the maturation of the active site of the [Fe]-hydrogenase. Seven accessory proteins are coded for by the HcgA-HcgG set of genes and it has been shown that each one of them is required for maturation.<sup>139</sup> The roles of each of the accessory proteins is as of yet unknown although some clues have been provided by annotation: HcgA is annotated as a radical SAM enzyme, HcgB seems to have a phosphate-binding domain and is involved in forming the guanylylpyridinol part of the cofactor,<sup>140</sup> HcgC is supposed to have a NAD(P)-binding Rossmann-like domain; HcgD is suggested to be an iron chaperone for the FeGP cofactor as shown in Figure 14;<sup>141</sup> HcgG is annotated as fibrillar-like protein but may have a SAM-binding domain.<sup>139</sup>

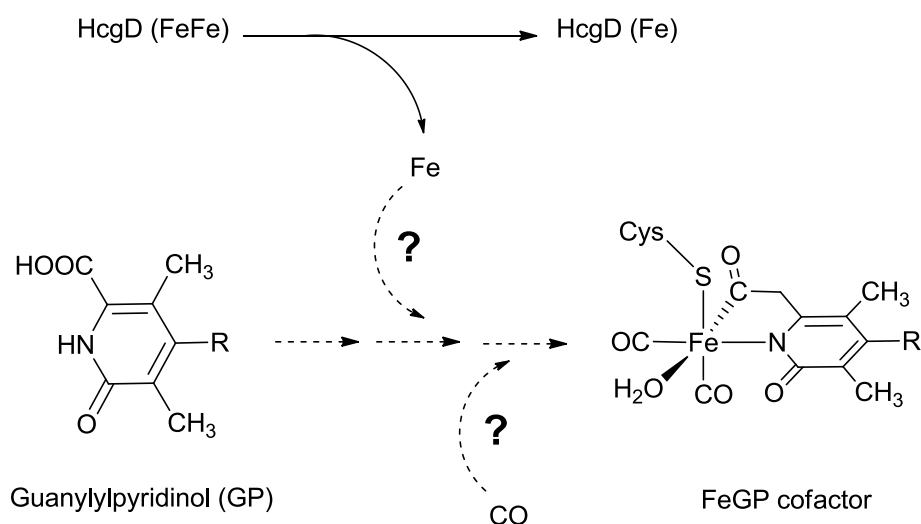


**Figure 14** A proposed function of HcgD in FeGP cofactor biosynthesis. The guanylylpyridinol precursor is converted by uncharacterised enzymes to the intact FeGP cofactor. It is proposed that one iron from HcgD could be delivered to a guanylylpyridinol precursor. Enzyme reactions for the formation of the acyl- and CO-ligands and their ligation to the iron (arrows with dashed line and “?” symbols) are not characterised yet. Adapted from ref. 141.

Little is known about the roles of these accessory proteins. HcgA has sequence similarity to HydG and was cautiously assigned to a role involving the generation of the CO ligands of the

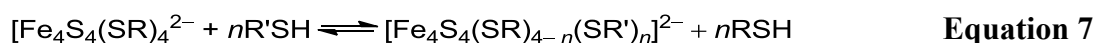
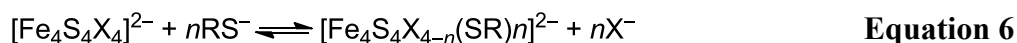
FeGP cofactor; this was debunked however by in vivo labelling studies which demonstrated that these CO ligands come from CO<sub>2</sub>.<sup>142</sup> Further work is required in order to gain a better understanding of the [Fe]-hydrogenase maturation pathway.

### 1.3 Chemical synthesis and functional models of metallo-sulfur clusters

Chemical and mechanistic insight into biological iron-sulfur cluster containing systems can be gained by studying synthetic analogues. The development of synthetic iron-sulfur clusters began in the early 1970s when the first [Fe<sub>4</sub>S<sub>4</sub>(SR)<sub>4</sub>]<sup>2-</sup> were produced.<sup>153, 154</sup> The original synthesis was achieved by a self-assembly reaction (Equation 5).<sup>153, 154</sup>



Synthetic ligand substitution reactions were subsequently devised (Equation 6).<sup>155</sup>



In mixtures of clusters with different ligands, facile redistribution reactions occur that led to statistical mixtures (Equation 8).



Altering the stoichiometry of Equation 5 to that of Equation 10 or Equation 11 leads to the formation of two different intermediates as shown in Figure 15. These reactions are some of

the few iron-sulfur cluster syntheses where the clusters are formed by the sequential formation of intermediates. In Figure 15  $\text{Fe}^{\text{III}}$  is reacted with 3.5 eq. of  $\text{RS}^-$  leading to the formation of a “ferromantane” with an adamantane-like structure. This intermediate is then reacted with 4 eq. of elemental sulfur to yield an  $[\text{Fe}_4\text{S}_4(\text{SR})_4]^{2-}$  cluster. The alternative route Equation 11 uses 5 or more eq. of  $\text{RS}^-$  giving an  $[\text{Fe}(\text{SR})_4]^{2-}$  complex. This reacts with 1 eq. sulfur yielding an  $[\text{Fe}_2\text{S}_2(\text{SR})_4]^{2-}$  cluster which goes onto react with methanol to give the final  $[\text{Fe}_4\text{S}_4(\text{SR})_4]^{2-}$  cluster.

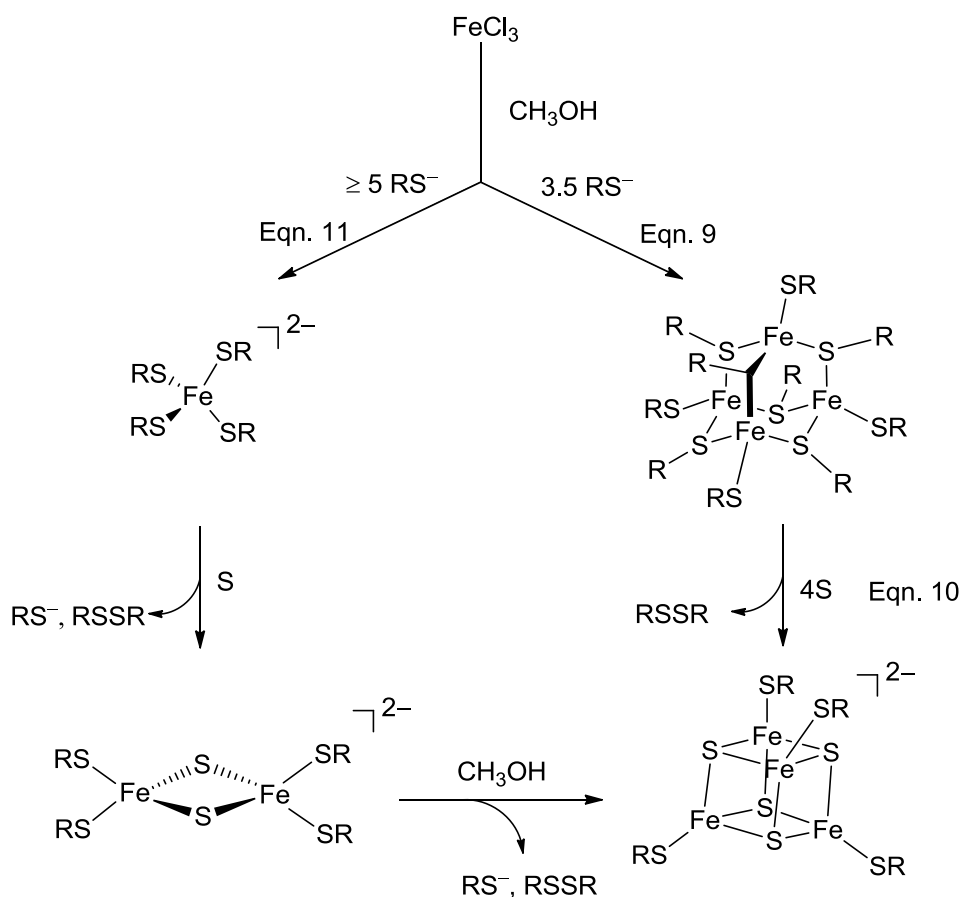
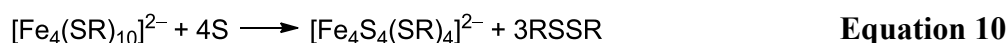


**Figure 15** Depiction of the coupled reactions leading to assembly of  $[\text{Fe}_4\text{S}_4(\text{SR})_4]^{2-}$  clusters with initial mole ratios  $\text{RS}^- : \text{Fe}^{\text{III}} : \text{S} = 3.5 : 1 : 1$  and  $\geq 5 : 1 : 1$ .

$\text{Fe}^{\text{III}}$  reacts with 3.5 eq.  $\text{RS}^-$  to form a “ferromantane” with an adamantane-like structure (Equation 9).<sup>156</sup> Subsequent reaction of this adamantane-like structure with sulfur forms an

$[\text{Fe}_4\text{S}_4(\text{SR})_4]^{2-}$  cluster (Equation 10). An alternative synthesis of an  $[\text{Fe}_4\text{S}_4(\text{SR})_4]^{2-}$  cluster can be achieved via an  $[\text{Fe}(\text{SR})_4]^{2-}$  intermediate (Equation 11).



Species like  $[\text{Fe}_4\text{S}_4(\text{SR})_4]^{2-}$  are thought to be thermodynamic sinks in Fe-S cluster synthesis as they are often the unintended by-products in many reactions that contain  $\text{Fe}^{\text{II, III}}$ , sulfide or sulfur and thiolate or other terminal ligands.

Using the reactions above a wide array of synthetic  $\{4\text{Fe}4\text{S}\}^{2+}$  clusters have been synthesised. These contain a variety of ligands which have ranged from bulky hydrophobic groups to a simple  $\text{SH}^-$  ligand, have included hydrophilic ligands, macrocyclic ligands, crown ether ligands and Cys peptide ligands. The wide variety of different  $\{4\text{Fe}4\text{S}\}^{2+}$  clusters is reviewed in ref. 157.

[1:3] Site differentiated iron-sulfur clusters, for example,  $[\text{Fe}_4\text{S}_4(\text{LS}_3)(\text{SEt})][\text{NBu}_4]_2$  **14** as shown in Figure 16, are clusters in which three of the iron sites are bound to a large tridentate ligand, leaving one site more reactive than the others. Many biological iron-sulfur clusters involved in electron transfer or catalysis are bound in a similar fashion by three cysteine residues thus making [1:3] site differentiated clusters ideal candidates for mimicking the chemistry that takes place at these unique Fe sites (see section 1.2.5). In synthetic [1:3] site

differentiated clusters substitution reactions at the unique iron site can take place with a variety of ligands including thiolates, phenolates, tertiary phosphines and cyanide.

The first example of a tridentate ligand used to generate a [1:3] site differentiated cluster was reported by Holm and co-workers where they used 1,3,5-tris[4,6-dimethyl-3-(methoxymethylthio)phenylthio]-2,4,6-tris(*p*-tolylthio)benzene (**LS<sub>3</sub>**, **7**) as shown in Figure 16.

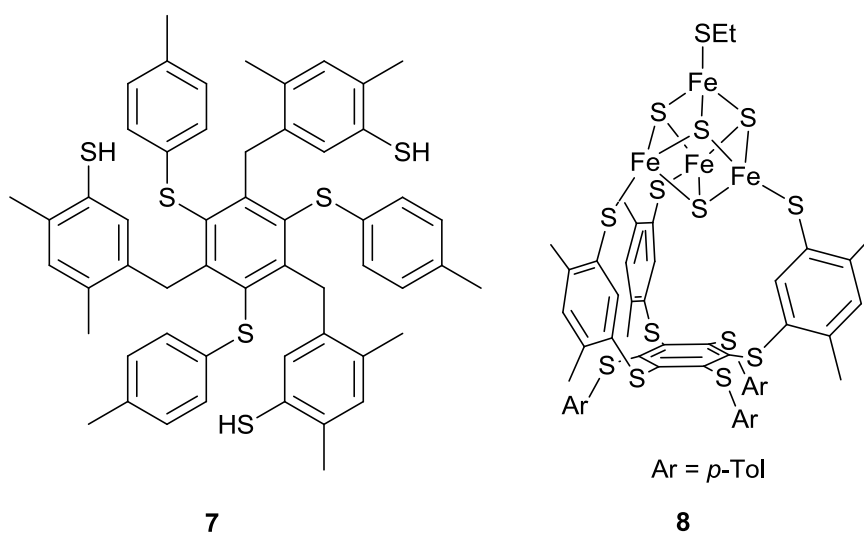
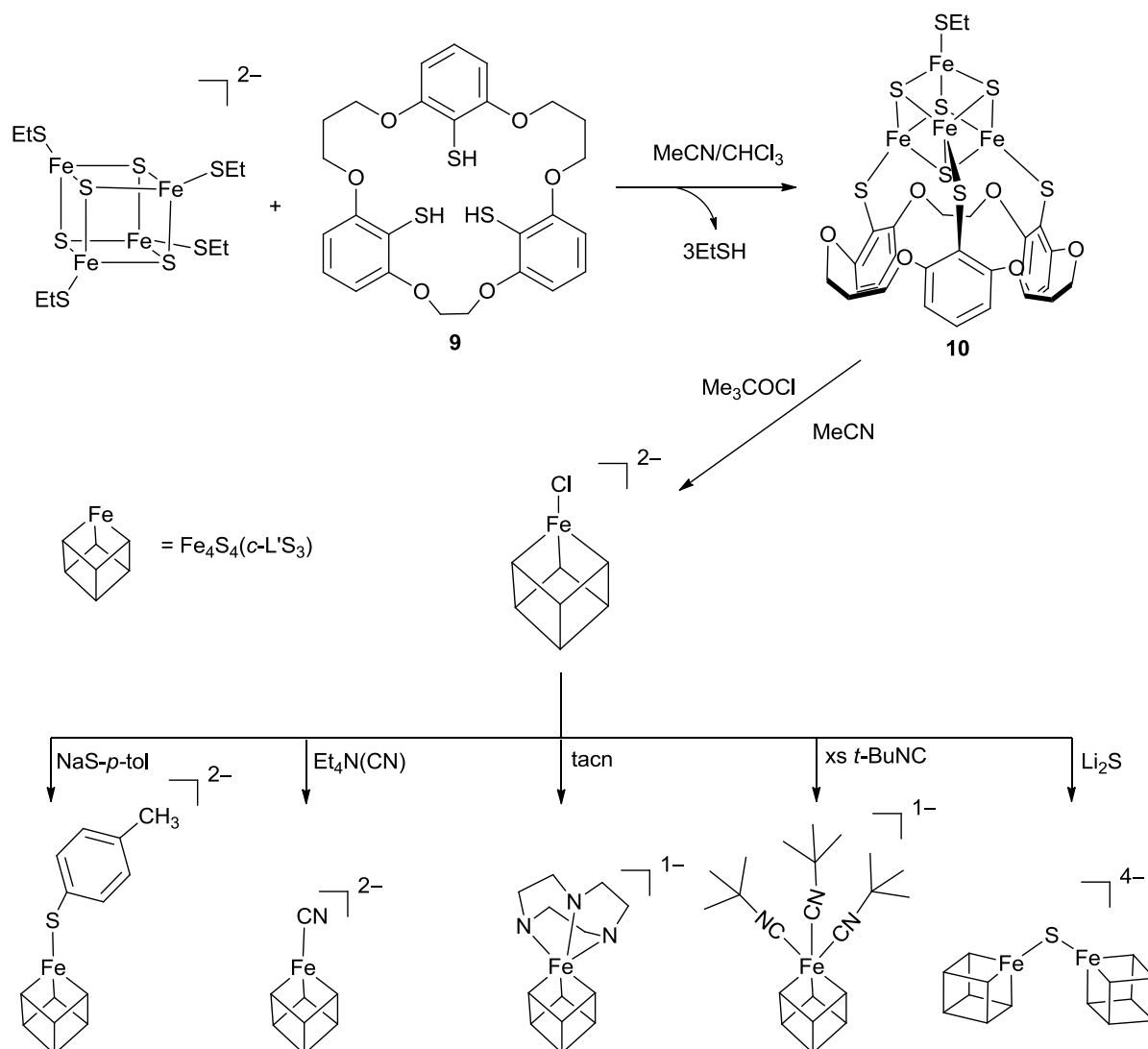


**Figure 16** 1,3,5-Tris[4,6-dimethyl-3-(methoxymethylthio)phenylthio]-2,4,6-tris(*p*-tolylthio)benzene a large tridentate trithiolate ligand (left), [1:3] site differentiated cluster **8**  $[\text{Fe}_4\text{S}_4(\text{LS}_3)(\text{SEt})][\text{NBu}_4]_2$  (right) by Holm.<sup>158</sup>

A summary of the extensive substitution reactions of this family of site differentiated clusters at the unique iron site conducted by Holm and Zhou<sup>159</sup> is shown in Scheme 9. In this study clusters  $[\text{Fe}_4\text{Q}_4(\text{LS}_3)\text{Cl}]^{2-}$  (where Q = S, Se) were used ( $\text{LS}_3 = \mathbf{7}$ ).



variety of ligands including cyanide and isocyanide affords another family of site differentiated clusters each with a different ligand at the unique iron site.



**Scheme 10** Family of site differentiated clusters using a macrocyclic polyether trithiol by Holm and co-workers adapted from ref. 160.

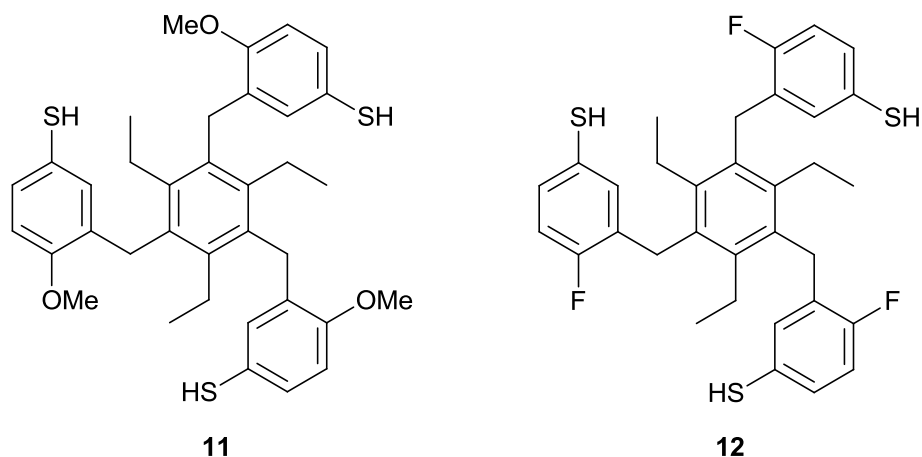


**Figure 17** Tridentate trithiolate ligands designed by Terada and co-workers.<sup>161</sup>

In 2012 Terada and co-workers extended the scope of the synthesis of site differentiated {4Fe4S} clusters by synthesizing two new tridentate trithiolate ligands **11** and **12**.<sup>161</sup> Reaction of these ligands with a synthetic iron-sulfur cluster affords **13** and **14** as shown in Figure 18.

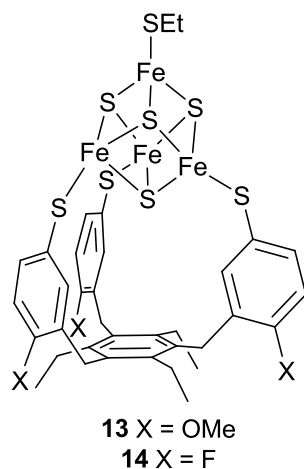


**Figure 18** [1:3] site differentiated cluster by Terada and co-workers.<sup>161</sup>

Terada and co-workers produced clusters with ethanethiolate, benzenethiolate and hydrosulfide at the unique iron site. Each complex afforded single crystals suitable for X-ray crystallography.

In 2013 Coucouvanis and co-workers developed a family of site differentiated clusters as shown in Figure 19 used to produce bio-inspired models of assimilatory sulfite and nitrite



### 1.3.1 Heteroatom –FeS clusters

Clusters containing a  $MFe_3S_4$  cubane-type core unit were first prepared in 1978<sup>163</sup> in an attempt to synthetically mimic the active site of Mo-nitrogenase (discussed further in sections 1.2.4 and 1.3.2.).

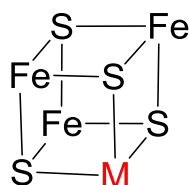


**Figure 21** A cubane-type  $MFe_3S_4$  cluster

$MFe_3S_4$  clusters have been synthesised where  $M = V, Nb, Mo, W, Re, Co$  and  $Ni$ .<sup>164</sup> So far  $MFe_3S_4$  clusters have not been detected in native proteins and there seems to be no clear biological function for the  $Fe_3S_4$  precursor.<sup>165</sup> As mentioned previously (section 1.2.2) aconitase in its inactive form contains an  $Fe_3S_4$  cluster which must take up  $Fe^{II}$  in order to restore activity.

In work attempting to mimic the C-cluster of carbon monoxide dehydrogenase (which exists as a  $NiFe_4S_5$  core) Holm and co-workers<sup>166</sup> synthesised a  $NiFe_3S_4$  with the hope of extending the structure by introducing an  $Fe^{II,III}$  site with appropriate bridges *exo* to the core. The group were not able to incorporate an extra iron but were able to mimic the square planar geometry at  $Ni$ .

$MFe_3S_4$  can also form bridged double cubane species (such as those used to model the active site of nitrogenase). Iron-sulfur clusters incorporating heterometals in their cubane structure are of interest both as potential ways to mimic the structural and electronic properties of biological clusters and in extending the known chemistry of these kinds of structures.

### 1.3.2 FeMoco and P-clusters of nitrogenase (FeVco, FeFeco)

An early nitrogenase active site analogue was synthesised in 1978 by Wolff and co-workers.<sup>163</sup> Their approach followed the “self-assembly” method seen in the generation of {4Fe4S} clusters. Anaerobic reaction of 1 eq. of (Et<sub>4</sub>N)<sub>2</sub>MoS<sub>4</sub>, 3 eq. of FeCl<sub>3</sub>, and 9 eq. each of ethanethiol and NaOMe in methanol afforded complex **17**.

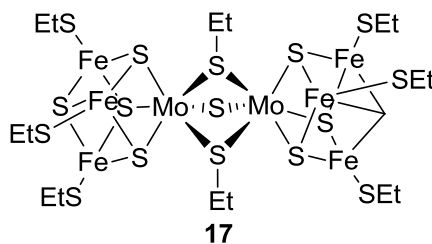
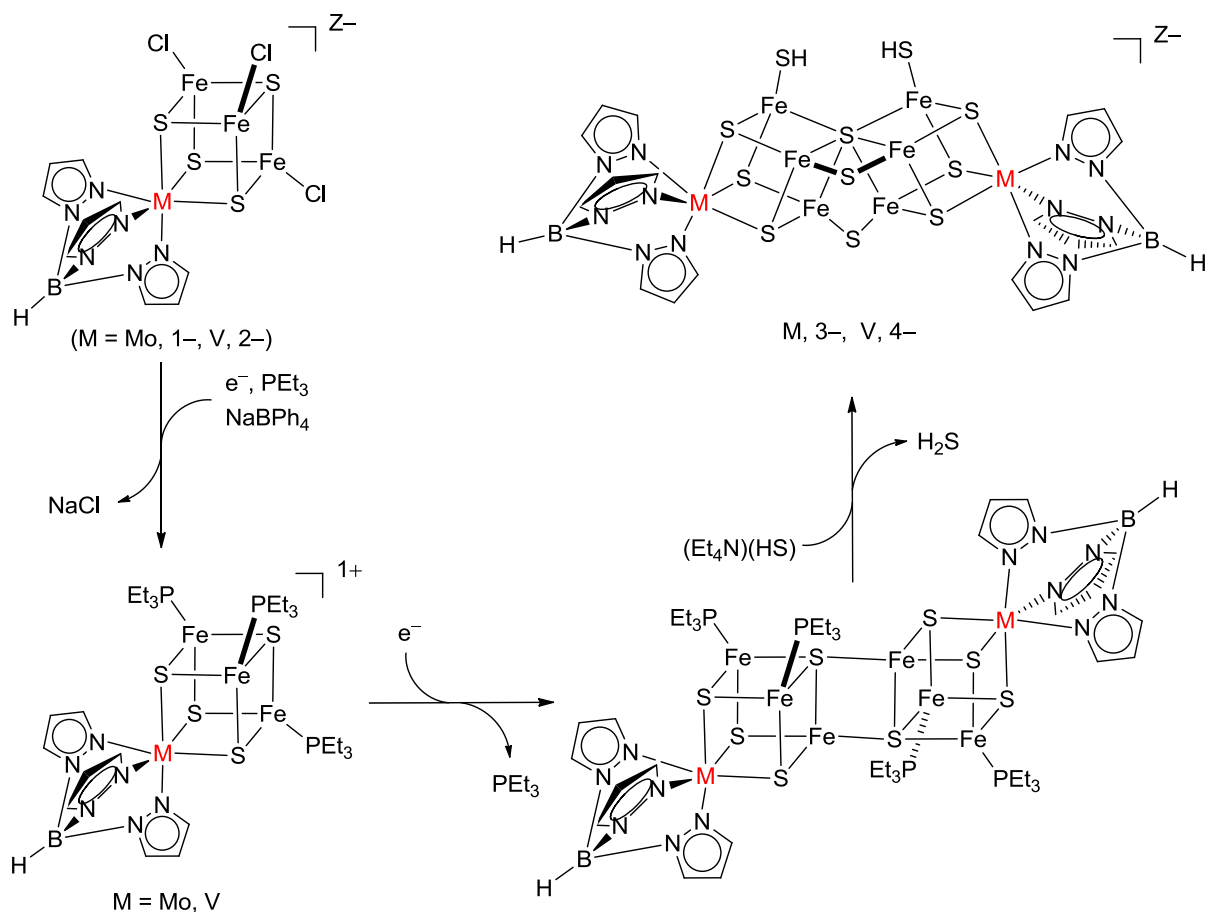


**Figure 22** Structure of [Mo<sub>2</sub>Fe<sub>6</sub>S<sub>9</sub>(SEt)<sub>8</sub>]<sup>3-</sup> an early nitrogenase mimic.<sup>163</sup>

This was at the time the closest approach to mimicking the nitrogenase active site, incorporating Mo into iron-sulfur clusters. However, it was not considered a “true mimic” as it differed in the ratio of Mo:Fe:S and in the bonding arrangement between the two clusters.

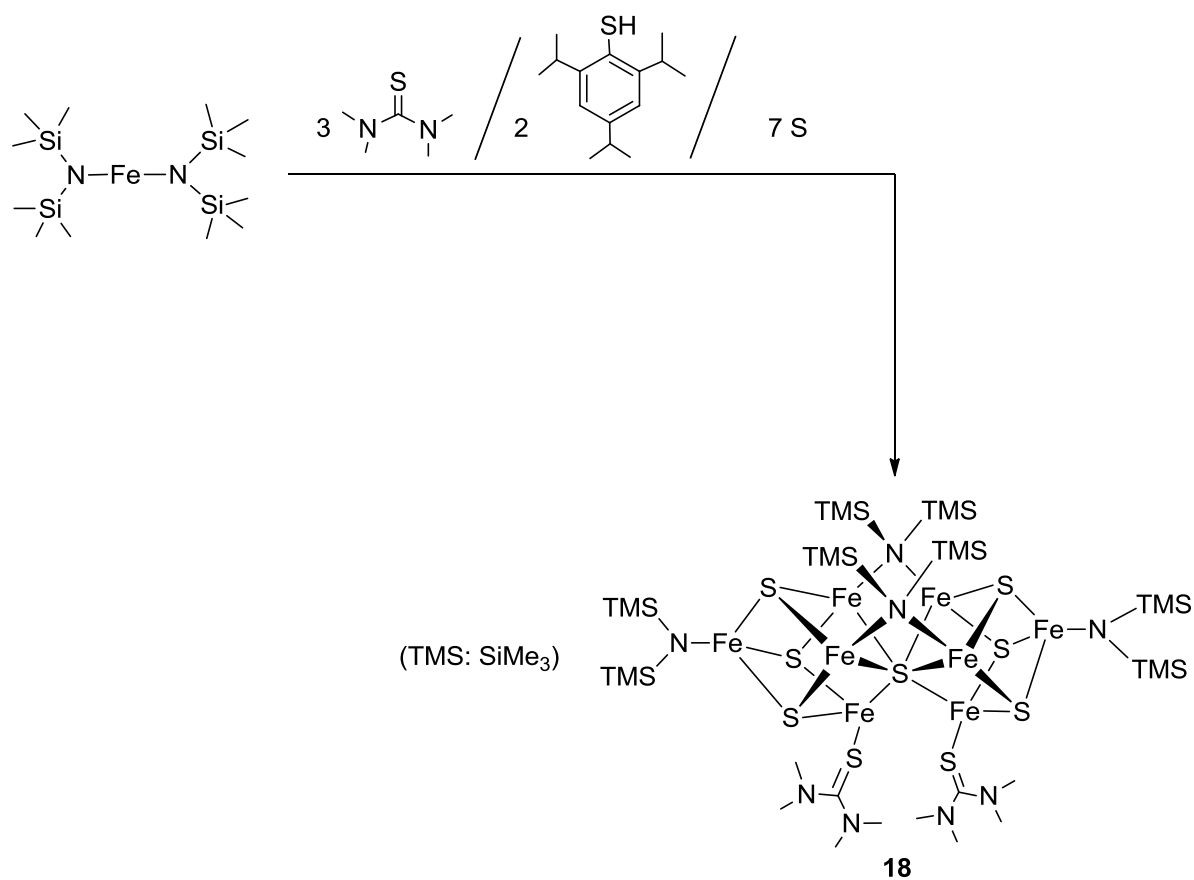
A later study by Holm and co-workers<sup>167</sup> described the use of reduced clusters in the synthesis of analogues of the active site of nitrogenase. The structures synthesised featured either Mo or V as their heterometal. Scheme 11 outlines the synthetic procedure used. The bulky ligand tris(pyrazoyl)hydroborate<sup>1-</sup> was incorporated at the heterometal site to prevent the formation of potentially isomeric products. The key result in this work is that the core shapes of their final V and Mo containing clusters are similar to that of the P<sup>N</sup> (the reduced state) cluster of nitrogenase (Figure 5). A best-fit superposition of the core of V and Mo with the Fe<sub>8</sub>S<sub>7</sub>(μ<sub>2</sub>-S<sub>Cys</sub>)<sub>2</sub> core of the P<sup>N</sup> cluster give weighted rms (root mean square) deviations of 0.33 and 0.38 Å, respectively, suggesting close topological similarity.



**Scheme 11** Synthetic procedure by Holm and co-workers generating heterometallic models similar to the P<sup>N</sup> cluster in nitrogenase.<sup>167</sup>

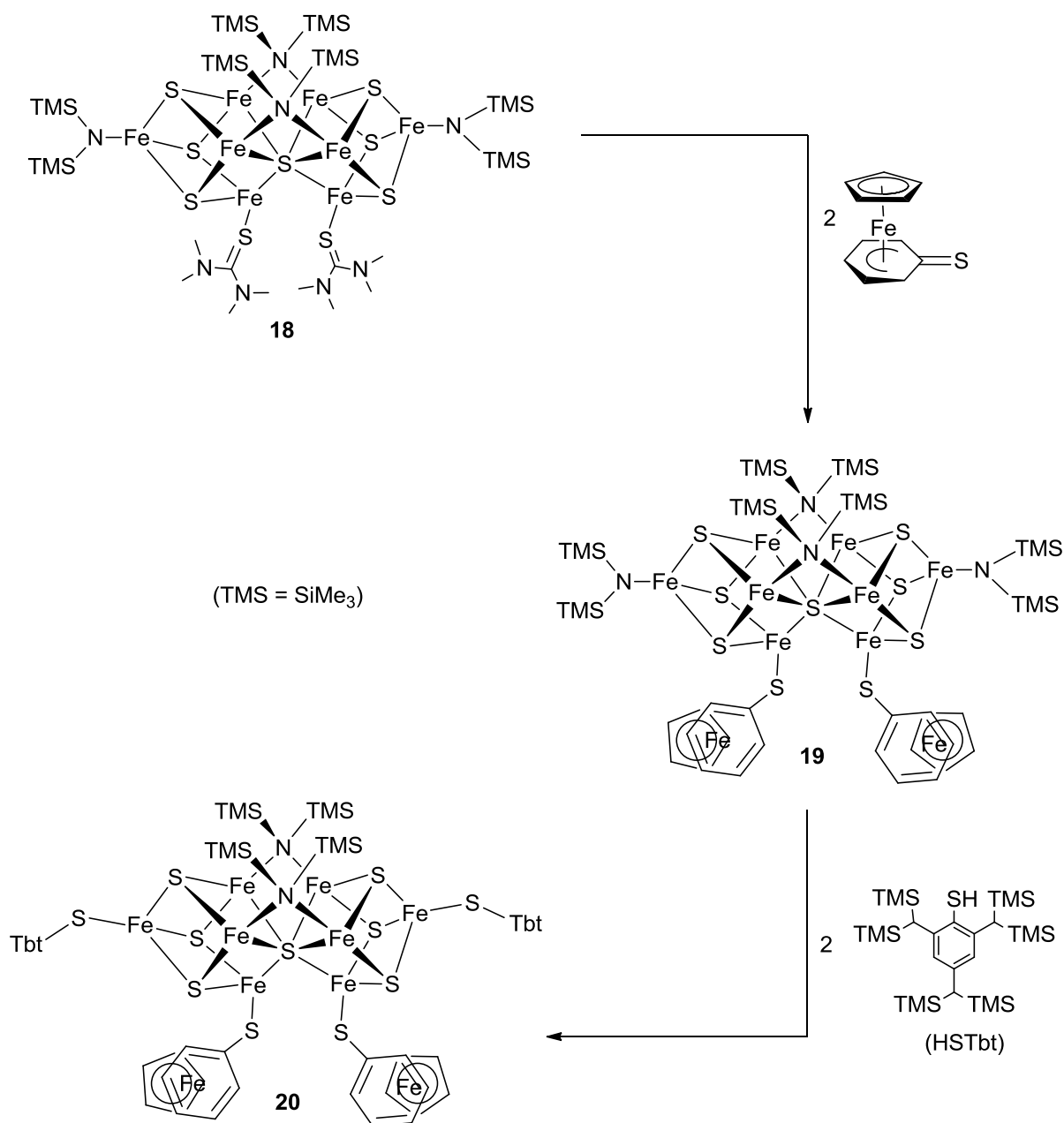
Using a different approach, recent studies by Ohki have produced further nitrogenase models that mimic the  $\mu_6$  S arrangement in the P<sup>N</sup> cluster.<sup>168</sup> These were synthesised in non-polar solvent and the Fe containing starting materials contained large hydrophobic HN(SiMe)<sub>2</sub>. [Fe{N(SiMe)<sub>3</sub>}<sub>2</sub>]<sub>2</sub> serves as a base deprotonating RSH to give the Fe-SR moiety and HN(SiMe)<sub>2</sub>. This serves as an alternative to the common synthetic route to iron-sulfur clusters starting with FeCl<sub>3</sub> in polar solvent with anionic ligand exchange of Cl<sup>-</sup> and RS<sup>-</sup>. The idea behind Ohki's research was to avoid the {4Fe4S} "thermodynamic sink" and to stabilise the formation of an {8Fe7S} cluster. The advantage of this route over the route by Holm (Scheme 11) is that this seems to be a "one pot" reaction. Ohki proposes that the use of

hydrophobic solvent stabilises the {8Fe7S} core and points to the presence of hydrophobic residues (Phe, Pro and Met) around the P-cluster in the natural system.



**Scheme 12** Synthesis of {8Fe7S} cluster by Ohki.<sup>168</sup>

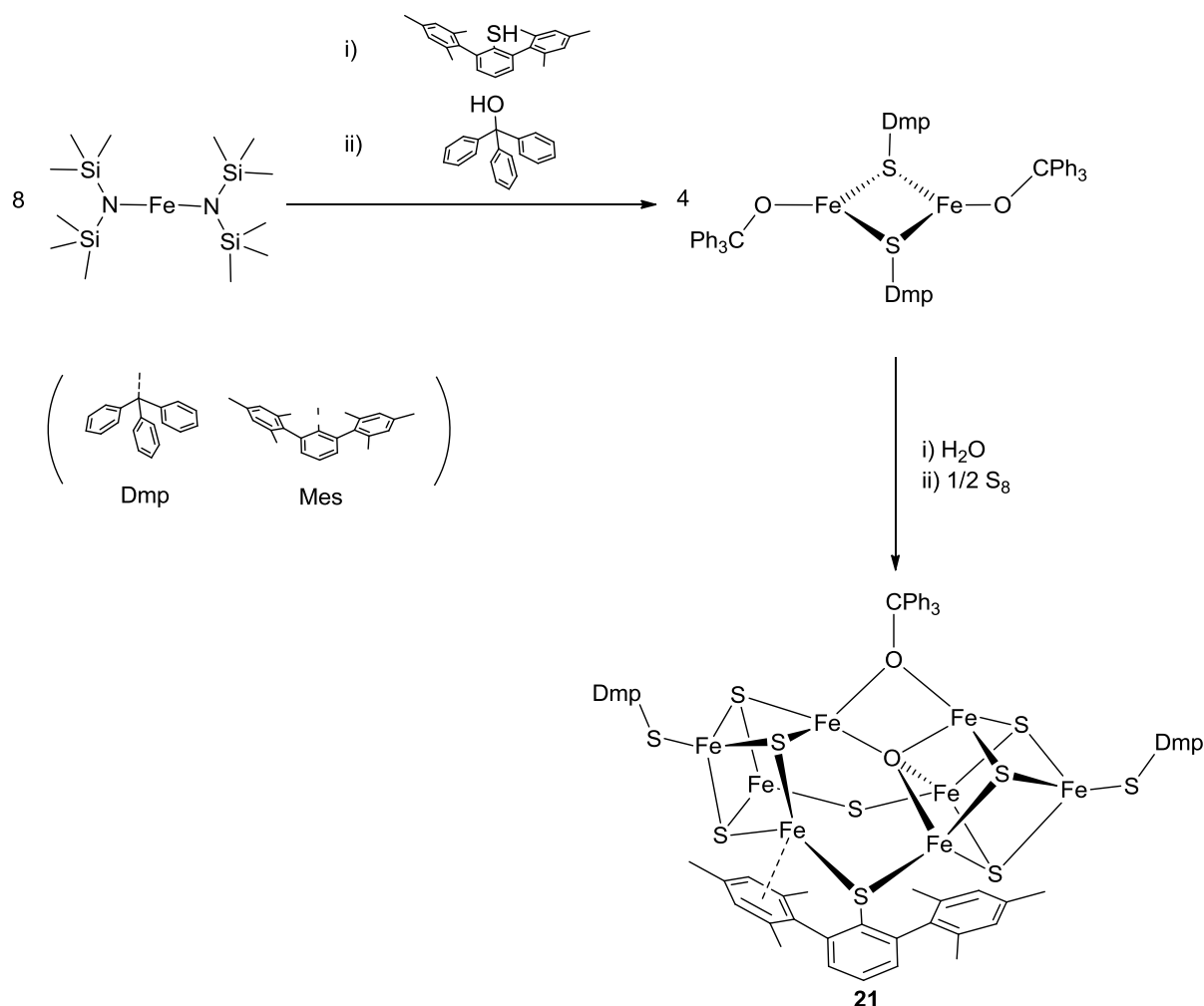
Although complex **18** shares a {8Fe7S} core with the P<sup>N</sup>-cluster of nitrogenase, the latter is coordinated by six cysteinyl thiolates whilst **18** is supported by four amides and two thiourea ligands. Ohki's subsequent efforts were targeted at introducing thiols into the ligand sphere of the synthetic {8Fe7S} complex. The most successful approach involved the use of a sandwich complex [(η<sup>5</sup>-C<sub>5</sub>H<sub>5</sub>)-Fe(C<sub>6</sub>H<sub>5</sub>S)] giving a bis-thiolate cluster followed by use of the bulky thiol HSTbt (Tbt: 2,4,6-((SiMe<sub>3</sub>)<sub>2</sub>CH)<sub>3</sub>C<sub>6</sub>H<sub>2</sub>) to yield a {8Fe7S} with four thiolate ligands.



**Scheme 13** Synthesis of thiolate coordinated {8Fe7S} cluster by Ohki.<sup>168</sup>

It is noteworthy that although **20** has higher structural analogy to the P<sup>N</sup>-cluster of nitrogenase than **18**, the use of bulky thiols means that there is no substitution of the bridging amides (bridging cysteine thiols in the P<sup>N</sup> cluster Figure 5). Attempts to add thiol ligation using less bulky ligands led to degradation of the {8Fe7S} cluster into {4Fe4S} clusters.<sup>168</sup>

In attempts to mimic the FeMoco of nitrogenase Ohki attempted the incorporation of a light atom (oxygen, but now known to be carbon in the natural system) into an  $[\text{Fe}_8\text{S}_6]$  core.

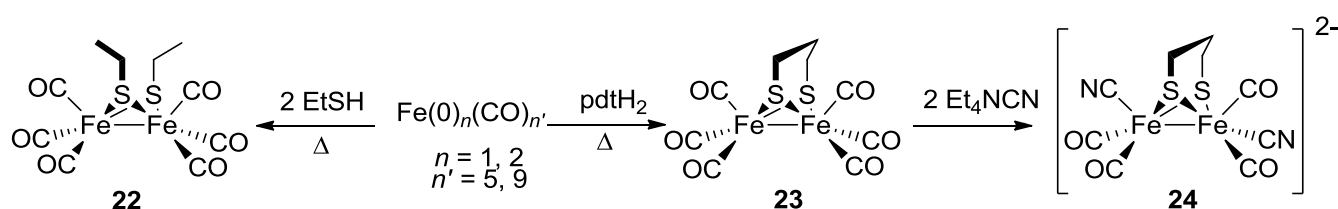


**Scheme 14** Synthesis of  $[\text{Fe}_8\text{S}_6\text{O}]$  cluster by Ohki.<sup>168</sup>

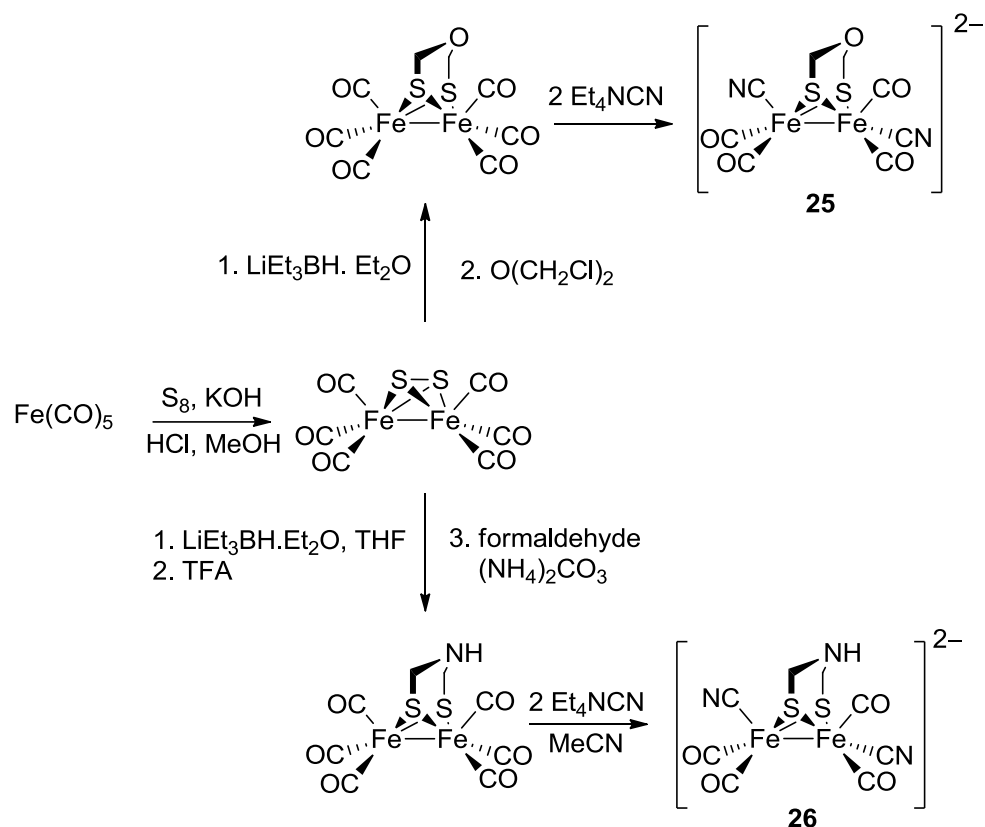
In structure **21** the central bridging oxygen is  $\mu_4$  ligated whilst the central carbon atom in FeMoco bridges six irons. Ohki suggests that this bonding mode may be relevant to the substrate-bound FeMoco. It has been suggested that the central carbon atom in FeMoco may dissociate from an inner iron atom allowing the binding of an external substrate.<sup>169</sup>

### 1.3.3 [FeFe]-hydrogenase active site models

Synthetic species analogous to the diiron subunit of [FeFe]-hydrogenase were known long before the structure of the active site was elucidated. In 1929 Reihlen and co-workers reported the preparation of bridged hexacarbonyl diiron complexes including the synthesis of  $[(\mu\text{-SEt})_2\text{Fe}_2(\text{CO})_6]$ .<sup>170</sup> When the structure of the H-cluster was revealed in 1998–1999<sup>22, 45</sup> the observation that the active site and a previously reported complex  $[(\mu\text{-pdt})\text{Fe}_2(\text{CO})_6]$  by Seyferth<sup>171</sup> were strikingly similar undoubtedly stimulated the research of the separate groups of Pickett, Darensbourg and Rauchfuss in the synthesis of a  $[(\mu\text{-pdt})\text{Fe}_2(\text{CO})_4(\text{CN})_2]^{2-}$  (Scheme 15).<sup>172-174</sup> Synthetic effort aimed at modelling and identifying the bridgehead atom (now known to be N)<sup>175</sup> led to the synthesis of related diiron compounds bearing adt (azadithiolate =  $[(\text{SCH}_2)_2\text{NR}]^{2-}$ )<sup>176</sup> and odt (oxodithiolate =  $[(\text{SCH}_2)_2\text{O}]^{2-}$ )<sup>176-178</sup> as derivatives of the pdt bridge.



**Scheme 15** Synthesis of first structural analogues of the active site of [FeFe]-hydrogenase **22**<sup>170</sup>, precursor diiron hexacarbonyl complex **23** and the first true [FeFe]-model complex  $[(\mu\text{-pdt})\text{Fe}_2(\text{CO})_4(\text{CN})_2]^{2-}$  **24**.<sup>172-174</sup>



**Scheme 16** Scheme for the preparation of [FeFe]-subsite analogues bearing naturally relevant and alternative odt.

Following the synthesis of these early models an explosion of synthetic chemistry reporting new mimics of the [FeFe]-subsite has occurred with over 300 novel structural mimics described over the past two decades.<sup>64, 179</sup> A great deal of this work has focused on producing complexes that mimic the key features of the natural active site including bridging CO,<sup>180</sup> mixed-valent Fe(II)–Fe(I) systems that reproduce the “rotated state” of the enzyme,<sup>181</sup> the isolation of biologically relevant and stable terminal hydride species<sup>182</sup> and the construction of a full H-cluster model by linking a synthetic subsite to the site differentiated cluster Fe<sub>4</sub>S<sub>4</sub> **8** (Figure 16).<sup>183</sup>

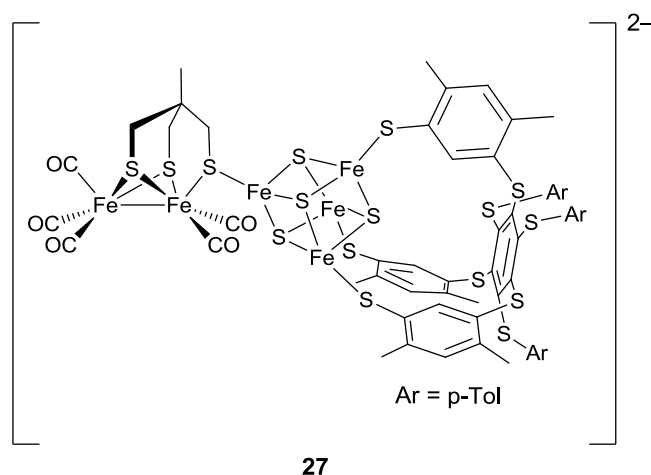


**Figure 23** H-cluster model **27** synthesised by Tard et al.<sup>183</sup>

Interest in modelling the [FeFe]-hydrogenase active site has not subsided and continues with nearly 100 new papers published in the last half a decade. Most of this work has focused on making changes to the bridging group but little success has been had in key areas such as lessening the large overpotential required for catalysis (a feature of many [FeFe]-mimics).

In order to prepare diiron mimics with redox properties closer to the thermodynamic potential for the reduction of  $H^+$ , Felton and co-workers<sup>184</sup> incorporated a suitably substituted aromatic dithiolate bridgehead. The benzene rings on these  $[(\mu\text{-bdt})Fe_2(CO)_6]$  (bdt = benzenedithiolate,  $[(S)_2C_6H_4]^{2-}$ ) type diiron systems are highly substituted with electron withdrawing groups. Studies of these and related systems showed that the potential for catalysis could be decreased by up to 150 mV when the number of electron withdrawing groups was increased but doing so lowers the catalytic efficiency in terms of turnover frequency.

There have been problems with the stability and reactivity of  $CN^-$  containing mimics where  $CN^-$  competes for protons or causes the decomposition of the complex in protonation experiments.<sup>185</sup> Thus, replacement of cyanide on model clusters with abiological phosphines, carbenes and other ligands has also been a target. These surrogate ligands are attached with the aim of being similar in electronic donating properties to  $CN^-$  but without inherent

complications and have included thioether groups, isocyanides, carbenes, amines and phosphines.<sup>186</sup> The incorporation of these ligands has allowed for many important aspects of the subsite to be modelled and accessed, such as isolation of a terminal hydride.<sup>187</sup>

So far in the literature there is only one example of an [FeFe]-hydrogenase synthetic model containing a bridging CO with support only from cyanide ligation.<sup>180</sup> There is slow conversion of this species back to a complex containing all terminal CO. A recent example of an isolatable bridging CO species is given in the work by Talmarin and co-workers, where a chelating dicarbene is coordinated to  $[(\mu\text{-pdt})\text{Fe}_2(\text{CO})_6]^{2-}$  to give  $[(\mu\text{-pdt})\text{Fe}_2(\text{CO})_4(\kappa^2\text{-Ime-CH}_2\text{-Ime})]$  (Ime = 1-methylimidazol-2-ylidene).<sup>188</sup> In the presence of  $\text{P}(\text{OMe})_3$  the diferrous, bridging CO,  $[(\mu\text{-pdt})(\mu\text{-CO})\text{Fe}_2(\text{CO})_2(\text{P}(\text{OMe})_3)_2(\kappa^2\text{-Ime-CH}_2\text{-Ime})]^{2+}$  compound was produced and isolated.

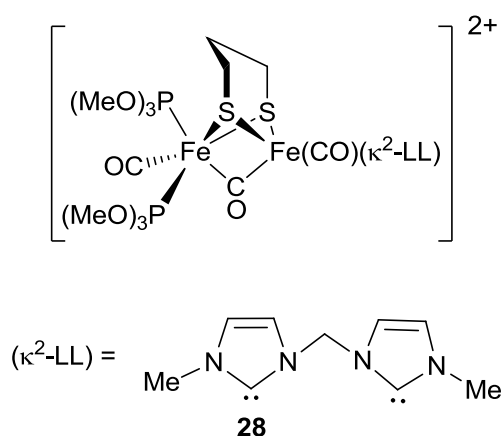
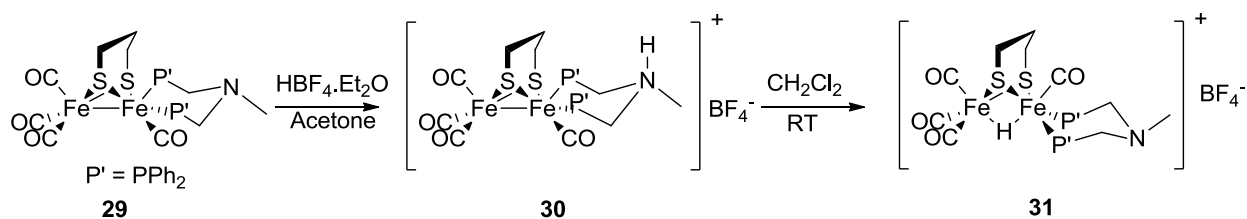


**Figure 24** Recent example of an isolable bridging CO species by Talmarin and co-workers.<sup>188</sup>

In further work by the same group Scheme 17 illustrates proton transfer behaviour by a model complex. Protonation in the natural subsite of [FeFe]-hydrogenase is thought to occur at the free coordination site of the distal Fe in the  $\text{H}_{\text{ox}}$  state of the enzyme. Features such as

the Fe–Fe bond, amino bridge, cyanide ligands, and the dithiolate bridges are also possible sites of protonation all with some supporting evidence in the literature.<sup>186</sup>



**Scheme 17** Protonation of **29** to yield ammonium salt **30**, and its subsequent isomerization that results in delivery of a proton to the metal-metal bond to form a bridging hydride **31**.<sup>189</sup>

Producing models incorporating a mixed valence Fe(II)-Fe(I) system has relied on ligation with phosphines and/or carbenes. These ligands stabilise diiron model systems in non-coordinating solvents, through their steric bulk and by increasing the electron density at Fe.<sup>64</sup> This has paved the way to synthesizing model complexes with a “rotated state”, in which an Fe centre adopts a square pyramidal geometry, with a free coordination site for substrate binding. These models are good mimics of the H<sub>ox</sub> state in the natural system. A recent example of a mixed valent model complex is found in the work by Ott and co-workers. The substitution of two CO ligands in  $[(\mu\text{-pdt})\text{Fe}_2(\text{CO})_6]^{2-}$  (**23**) by a chelating diphosphine ligand with an electron deficient carborane bridgehead provide the model complex **32** (Figure 25) with sufficient electron density to stabilise the Fe(II)–Fe(I) state. Electrochemical oxidation produces a mixed valent species that is stable on the minutes time-scale, this was characterised by a reversible oxidation process in the cyclic voltammetry (CV) and by electron paramagnetic resonance spectroscopy (EPR) and hyperfine sub-level correlation spectroscopy (HYSCORE).<sup>190</sup>

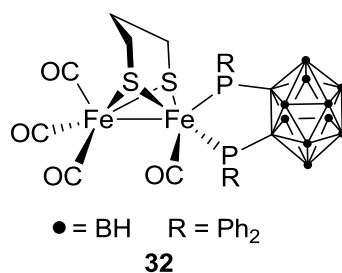


**Figure 25** [FeFe]-model that features a chelating diphosphine borane ligand.

Recent work by Rauchfuss and co-workers gives the first example of the isolation and characterization of a stable terminal hydride diiron unit achieved by low temperature synthesis and of a doubly protonated diiron unit **33** (Figure 26).<sup>191</sup> The crystal structure obtained replicates structurally relevant features such as bridging CO and demonstrates the remarkably short distance between the terminal hydride and the equatorial amino proton of 1.88(7) Å, an indication of significant hydrogen bonding. This structure supports the idea that the bridging amine has a role in the splitting of dihydrogen.

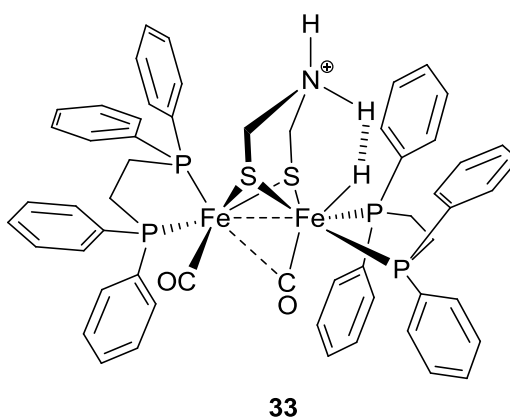


**Figure 26** Terminal hydride species isolated by Rauchfuss and co-workers.<sup>191</sup>

The ultimate goal of much of the synthetic work on modelling the [FeFe]-hydrogenase is to access models that not only replicate the structure, but also the activity of the natural active site. In 2012 Camara and Rauchfuss reported an [FeFe]-mimic bearing a functional electron transfer relay **34**  $[\mu\text{-}\{(S\text{CH}_2)_2\text{NBn}\}\text{Fe}_2(\text{CO})_3(\text{FcP}^*)(\text{dppv})]$  (dppv = 1,2-

bis(diphenylphosphino)ethylene) (Figure 27) ( $\text{FcP}^* = \text{Cp}^*\text{Fe}(\text{C}_5\text{Me}_4\text{CH}_2\text{PEt}_2)$ ) the first example of a model [FeFe]-system that performs catalytic  $\text{H}_2$  oxidation. The authors report 4 turnovers of  $\text{H}_2$  oxidation over a 5 h period ( $10^{-4} \text{ s}^{-1}$ ) a catalytic rate many orders of magnitude lower than the  $28000 \text{ s}^{-1}$  of natural system.<sup>19</sup>

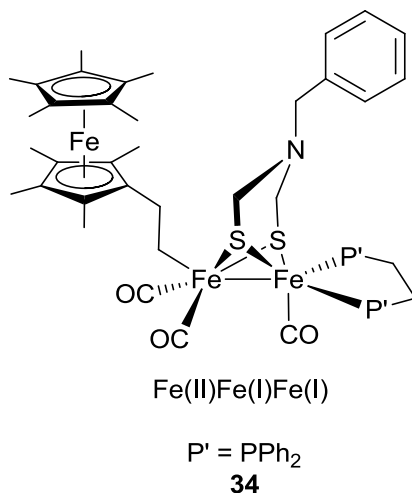


**Figure 27** [FeFe]-mimic bearing a functional electron-transfer relay by Camara and Rauchfuss.<sup>192</sup>

Complexes such as these are an important step towards mimicking [FeFe]-hydrogenase activity, though there is still a lot of progress to be made before comparable catalytic rates are seen. Overcoming this challenge is of importance if catalytic systems adequate for future practical applications are to be developed. In addition, future work on model complexes of [FeFe]-hydrogenase could reveal more information about how the natural system functions.

### 1.3.4 [NiFe]-hydrogenase active site models

Soon after the structure of the active site of the [NiFe]-hydrogenase was revealed several early structural mimics were reported **35–36** (Figure 28).<sup>193</sup> Mimicking the complex structure of the [NiFe]-active site as well as replicating its activity in model complexes has long been a challenge for chemists. Leading up to 2009 many structural mimics had been reported<sup>186, 194, 195</sup> with some featuring the all-sulfur coordination sphere around nickel, the  $\{\text{Ni}(\mu\text{-SR})_2\text{Fe}\}$  core and  $\text{CN}^-$  and CO ligation to Fe (Figure 28). However, catalytic activity was absent in all these mimics.

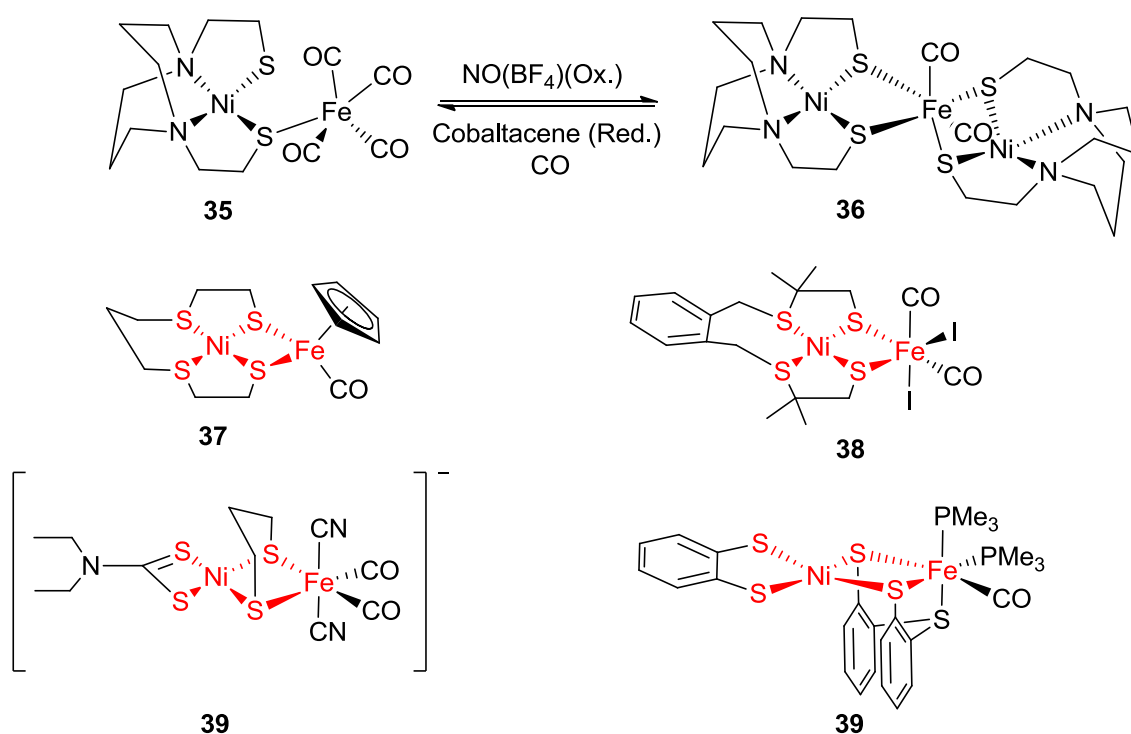
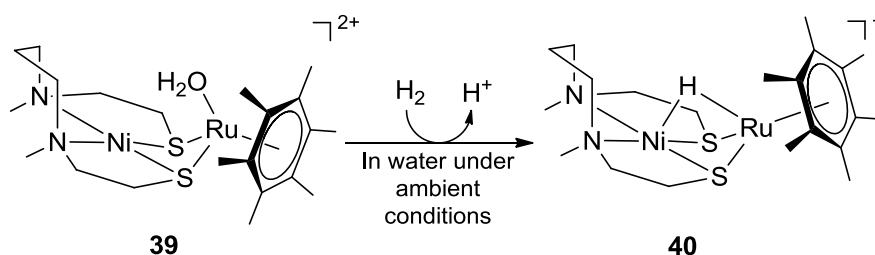


**Figure 28** Selected early [NiFe]-models with compounds **37–39** featuring the biologically relevant  $\{\text{Ni}(\mu\text{-SR})_2\text{Fe}\}$  core, coloured in red. Adapted from ref. 196.

An approach used by chemists in an attempt to replicate the catalytic activity of [NiFe]-hydrogenase is the use of ruthenium as a surrogate for iron in model complexes. Ruthenium complexes are widely used as catalysts for hydrogenation or hydride-transfer reactions<sup>197</sup> and can accommodate both hard and soft ligands (including dihydrogen and hydride). Work by

Ogo and co-workers in 2008 illustrates the use of this strategy to produce a model complex capable of catalytically oxidizing dihydrogen in the presence of Cu(II) ions as the oxidizing agents.<sup>198</sup> They showed that the H<sub>2</sub> activation by the catalyst involves the formation of a H<sup>-</sup> bridging the two metal centres (Scheme 18).<sup>199</sup>



**Scheme 18** Formation of **40** a Ni( $\mu$ -H)Ru complex obtained from the reaction of **39** with dihydrogen in water under ambient conditions (20 °C and 100 Pa).<sup>199</sup>

The geometry exhibited by the Ogo group's model is very similar to the Ni-C state of the [NiFe]-hydrogenase. The next major step for chemists in the modelling [NiFe]-hydrogenase was to produce functional mimics containing first-row transition metals. Several examples of models achieving this are reviewed in ref. 196. These models were reported to only exhibit catalytic H<sub>2</sub> evolution activity once again proceeding via a bridging hydride intermediate. One notable example of a functional [NiFe]-mimic is a recent model again by Ogo's group.<sup>200</sup> This model is able to mediate both hydrogen evolution and oxidation and so is the first model to reproduce the bidirectional activity of [NiFe]-hydrogenase at a binuclear core.

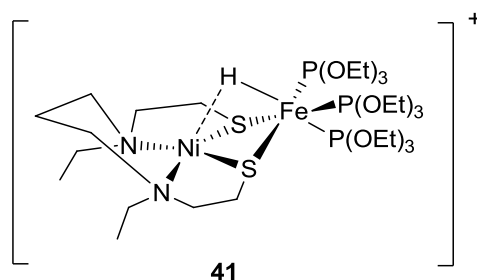
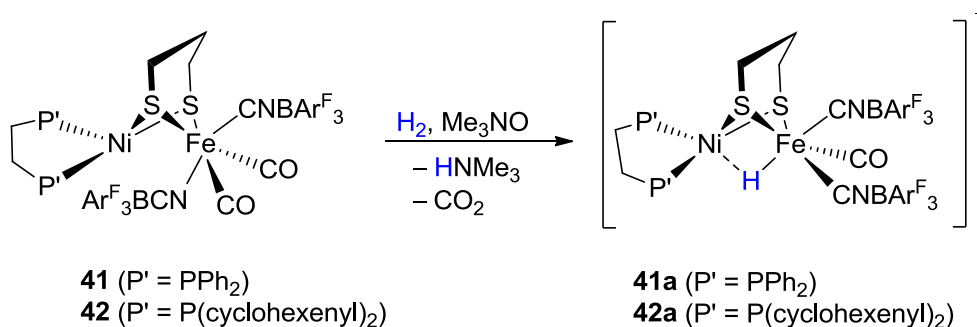


**Figure 29** Structurally relevant [NiFe]-mimic active for bidirectional conversion of protons and electrons for dihydrogen by Ogo and co-workers.<sup>200</sup>

The three triethylphosphite ( $\text{P}(\text{OEt})_3$ ) ligands on this complex modulate the electronic properties of the Fe centre allowing the coordination of dihydrogen (the first step in  $\text{H}_2$  activation). Methanolate, a strong base promotes the heterolytic splitting of  $\text{H}_2$  by capturing a proton whilst hydride remains coordinated to the Fe centre in a bridging mode. This hydride containing complex can be oxidised at mild potential by methylviologen ( $\text{MV}^{2+}$ ). The catalytic cycle is completed by release of a proton thus regenerating the starting material. There is still progress to be made however as this model only achieves one catalytic turnover with a yield of only 12 %, although a better yield (45 %) can be achieved using a stronger oxidant such as the ferrocenium ion.

Currently the closest models of biomimetic ligation of the [NiFe]-hydrogenase are seen in recent work by Manor and Rauchfuss. They report the synthesis of two  $[(\text{dxpe})\text{Ni}(\mu\text{-pdt})\text{Fe}(\text{CO})_n(\text{CNBAR}^{\text{F}_3})_2)]^-$  compounds, **41** and **42** ( $x = \text{phenyl}$  or  $\text{cyclohexenyl}$ , and  $\text{BAR}^{\text{F}_3} = \text{B}(\text{C}_6\text{F}_5)_3$ ) (Scheme 19).<sup>201</sup>



**Scheme 19** The preparation of the bridging hydride species  $[(\text{dxpe})\text{Ni}(\mu\text{-pdt})\text{Fe}(\text{CO})_n(\text{CNBAR}^{\text{F}_3})_2]^-$  which feature a bridging hydride with hydridic character akin to the Ni-C/R states of the natural enzyme.<sup>201</sup>

The isocyanide ligands  $\text{CNBAR}^{\text{F}_3}$  have the dual role of protecting the Fe centre sterically from chemical attack and providing the anionic character found in the natural system. The novel mimics **41** and **42** are able to heterolytically cleave dihydrogen giving complexes **41a** and **42a**, respectively. Similarly to the previously mentioned work by Ogo and co-workers **41a** can carry out bidirectional behaviour all be it in the presence of a strong base (diazabicycloundecene) for  $\text{H}_2$  oxidation and in the presence of  $\text{HCl}$  for  $\text{H}_2$  evolution. The latter process only occurs on a stoichiometric level. These models must be viewed with caution when compared directly to the natural system as the models appear to function via the Fe centre as opposed to the Ni centre (as is the case in the [NiFe]-hydrogenase). This conclusion was made from the observation that the difference between the oxidation potentials of **41** and **42** (20 mV) was very small even though each model contains phosphines with different basicities at the nickel centre.

### 1.3.5 [Fe]-hydrogenase active site models

The active site of the [Fe]-hydrogenase is shown in Figure 2, it contains an Fe(II) centre ligated by a chelating acyl pyridine ligand, cysteine residue, biologically-unusual *cis* CO ligands and a vacant site thought to be occupied by a solvent molecule (i.e. water). The first report of the crystal structure of the active site of the [Fe]-hydrogenases stimulated the modelling of these key features of the active site. Models have developed from simple early models mimicking only the *cis* CO arrangement<sup>202</sup> (Figure 40) to very close structural mimics<sup>203</sup> (Scheme 29) and have included models that aim to mimic the function rather than the ligand sphere<sup>204</sup> (Figure 41). A survey of the active site models of [Fe]-hydrogenase is given in Section 3.1.2.

## 1.4 The scope of this work

### 1.4.1 Aims and objectives

The work in this thesis focuses on two main areas; first the chemical properties and substitution reactions of a family of chemical models of the [Fe]-hydrogenase and second studies on the interaction of synthetic  $\{4\text{Fe}4\text{S}\}^{2+}$  clusters with CO and  $\text{CN}^-$  in relation to proposed intermediates in the biosynthesis of the H-cluster of [FeFe]-hydrogenase.

In the first area as described in chapter 1 the main objectives were 1) to investigate the substitution chemistry of a ferracyclic carbamoyl containing parent compound with more strongly donating ligands such as tertiary phosphines and to investigate the electronic properties of these products. 2) To increase the structural analogy to the natural system by extending the second coordination sphere of the parent complex by incorporation of a pyridone ligand. 3) Investigating the interaction of the parent complex with sources of hydride in an attempt to isolate biologically relevant intermediates.

In the second area the work focused on 1) The interaction of site differentiated and undifferentiated  $\{4\text{Fe}4\text{S}\}^{2+}$  clusters with CO and  $\text{CN}^-$  characterised by electrochemistry and stopped-flow FTIR. 2) Comparison of results with the proposed intermediates in the biosynthesis and with DFT (density functional theory) calculated structures. 3) Isolation of crystal structures of chemical models. These studies are presented in chapter 4 and 5.

## **2 Experimental methods and techniques**

### **2.1 General synthetic methodology**

#### **2.1.1 Solvent purification**

Solvents were freshly distilled under an inert atmosphere of dinitrogen from an appropriate drying agent using standard laboratory procedures.<sup>205</sup>

#### **2.1.2 Handling methodology**

Unless otherwise stated chemicals were handled under an inert atmosphere of dinitrogen or argon using standard Schlenk line techniques.<sup>206</sup> Chemicals (starting materials, electrode materials, solvents, specialist gases) were generally purchased from Sigma-Aldrich, Alfa Aesar or specialist suppliers without further purification.

#### **2.1.3 Electrolyte preparation**

[NBu<sub>4</sub>][BF<sub>4</sub>] was the standard electrolyte used in electrochemistry experiments. It was prepared by a standard laboratory procedure.<sup>207</sup>

#### **2.1.4 Microanalysis**

Elemental analysis was carried out at London Metropolitan University using a Thermo Scientific Flash 2000 Elemental Analyser configured for %CHN.

## **2.2 Background to experimental techniques**

### **2.2.1 NMR spectroscopy**

Nuclear magnetic resonance (NMR) spectroscopy is a technique commonly used to determine the structure of organic molecules.<sup>208</sup> In NMR spectroscopy a sample is placed in a

powerful magnetic field and irradiated with a pulse of radiowaves. This produces a signal that is then converted into an NMR spectrum. Some nuclei have a non-zero spin and NMR exploits their interaction with an external magnetic field. A spinning atom (such as a proton) generates its own magnetic field in proportion to the magnitude of the spin. When an external magnetic field is applied  $(2S + 1)$  spin states exist. For a proton  $S = 1/2$ , and therefore two spin states exist, one parallel and one antiparallel to the external magnetic field. The greater the external magnetic field applied the greater the energy difference in energy between the states. The NMR sample is irradiated with radiowaves and this causes the spin to transition from one state to the other. This transition occurs because the radiowaves absorbed have the same energy as the energy difference between the two spin states, this is known as resonance. A signal is generated from the energy released when the spin population of the nuclei returns to equilibrium. Processing of the signal leads to a peak of frequency  $\nu$  where  $\Delta E = h\nu$ .

A naïve prediction might be that we would only see one peak per kind of nucleus (e.g. C, H, B). However, nuclei of the same kind in a compound will not necessarily resonate at the same frequency. For example, protons in a compound may be in different chemical environments: this dictates the electron density around the nuclei. Electrons generate a local magnetic field which opposes the applied magnetic field. Therefore, where electron density is higher the net magnetic field will be weaker, lowering the frequency of the signal produced. The frequency of a given NMR signal is converted into a chemical shift from a given reference in ppm. This gives us a value that is independent from the magnetic field strength. Nuclei in different chemical environments will give different chemical shifts and therefore give rise to separate signals.

$$\text{chemical shift, } \delta, \text{ in ppm} = 10^6 \times \frac{\nu_{\text{resonance}} - \nu_{\text{reference}}}{\nu_{\text{reference}}}$$

In addition to the external and local magnetic field contributions, spins from neighbouring nuclei can interact with one another. This imparts a further magnetic contribution if the neighbouring nuclei have non-zero spin. A spin 1/2 nucleus can either exist as “spin up” or “spin down” and each state acts on a neighbouring nucleus to either increase or decrease the net magnetic field, respectively. This has the effect of splitting the signal seen into two peaks (or more depending on the number of neighbouring nuclei with non-zero spin). This splitting is known as the coupling constant ( $J$ ) and is reported in Hz.

The combination of chemical shift and coupling information makes NMR a powerful spectroscopic technique for the modern synthetic chemist.

### **2.2.2 FTIR spectroscopy**

In infrared spectroscopy (IR) a sample is irradiated with infrared light and certain frequencies are absorbed as bonds within molecules move to higher vibrational levels. Different types of bonds within molecules will absorb IR radiation of different frequencies. The strength of a bond can also be approximated from the frequency of IR light it absorbs. IR spectroscopy is therefore a valuable technique in characterizing functional groups within molecules.<sup>208</sup>

Sampling techniques in IR spectroscopy vary in consideration of the sample state. IR radiation has a limited transmittance depth in molecular solid samples, and to circumvent this a number of approaches are taken to produce finely dispersed solids which will give a useful signal. By far the most common approach is to produce a dilute paste of the solid by grinding with Nujol (paraffin oil). The Nujol mull is then thinly applied between single-crystal NaCl discs or a similar ionic solid that will not absorb IR radiation in the region of interest. A second approach is to intimately mix the solid with KBr and create a disc using a hydraulic press. Solid samples can also be analyzed by attenuated total reflectance (ATR). In ATR the solid is pressed against a single crystal sample head, commonly diamond. IR light is passed

through the crystal making use of total internal reflectance; a small amount of this light escapes the crystal as an evanescent wave which penetrates a short distance into the sample (typically less than one micrometre). This has the advantage of not having to add anything extra to the sample.

For liquids and solutions the absorption of the light by the sample is less problematic. Samples can be applied directly to the IR discs or an ATR, or can be injected into an IR transmission cell (for air sensitive samples).

### 2.2.3 FTIR spectroscopy of diatomic molecules on organometallics

A useful equation for predicting the wavenumber of vibration of a diatomic molecule is given by Equation 12.

$$\tilde{\nu} = \frac{1}{2\pi c} \sqrt{\frac{k_f}{\mu}} \quad \text{Equation 12}$$

where  $k_f$  is the force constant in  $\text{N m}^{-1}$ ,  $\mu$  is the reduced mass in kg, and  $c$  is the speed of light measured in  $\text{cm s}^{-1}$ . The reduced mass can be calculated by Equation 13.

$$\mu = \frac{m_1 m_2}{m_1 + m_2} \quad \text{Equation 13}$$

where  $m_1$  is the mass of atom 1 in kg and  $m_2$  is the mass of atom 2 in kg. These equations can also be useful when applied to multi-atom molecules in the context of isotopic labelling. The bond strength and therefore the IR vibrational frequency of a bond depends on the mass of the atoms that make it up. Isotopic substitution of one of the components will result in a change in the reduced mass. Therefore we can make a prediction of the size of the shift in vibrational frequency based on the equations above. This relies on the assumption that each bond behaves as an isolated diatomic.

IR spectroscopy is a particularly useful technique to probe  $\text{C}\equiv\text{N}^-$  and  $\text{C}\equiv\text{O}$  containing molecules. This is because of the dipole moment of these functional groups which give rise to strong absorptions in a region largely free of other signals. The typical range for metal-bound CO stretching frequency is  $2200\text{--}1850\text{ cm}^{-1}$  and that for  $\text{CN}^-$  is  $2100\text{ to }1800\text{ cm}^{-1}$ . In the complexes studied here labelling studies have that in any one complex bearing both  $\text{CN}^-$  and CO the former is of higher energy than the latter. In this work the units of absorbance are measured in  $\Delta$ milliabsorbances. The change in absorbance between an initial “background” scan and subsequent scans (after adding the sample or adding reactants together for stopped-flow FTIR) is measured.

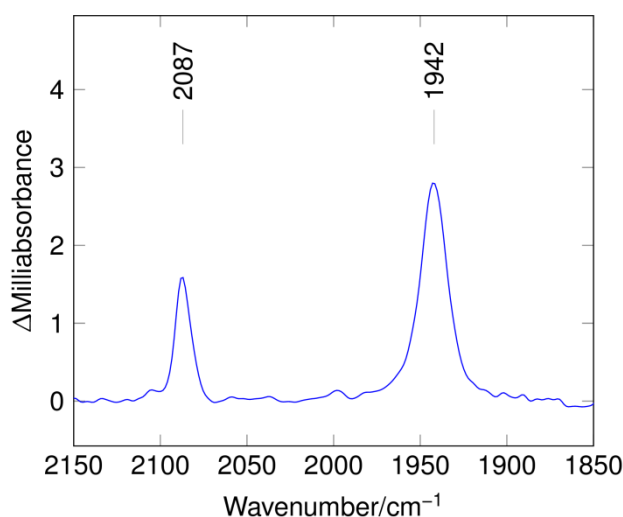


**Figure 30** Example of an IR spectrum. Two strong bands can be seen, one in the region of  $\text{CN}^-$  ( $2087\text{ cm}^{-1}$ ) one in the region of CO ( $1942\text{ cm}^{-1}$ ).

The positions of  $\text{C}\equiv\text{O}$  absorptions are characteristic of the type of  $\text{C}\equiv\text{O}$  functional group and are influenced by the electronic environment of the atom to which they are attached (particularly in metal-carbonyl complexes). In  $\text{C}\equiv\text{O}$  complexes with metals, the  $\text{C}\equiv\text{O}$  binds to the metal via  $\sigma$  donation into a vacant metal  $d$  orbital. In addition to a  $\sigma$  bond, a metal carbonyl bond is further strengthened through the overlap of antibonding  $\pi^*$  molecular orbital of  $\text{C}\equiv\text{O}$  and the  $d$  atomic orbitals of the metal (known as back-bonding). Commonly,  $\text{C}\equiv\text{O}$  in

metal carbonyl complexes vibrates at frequencies lower than that found for free C≡O. This means that the C≡O bond is weakened by binding to the metal, consistent with the idea that back-bonding between the metal and C≡O takes place.

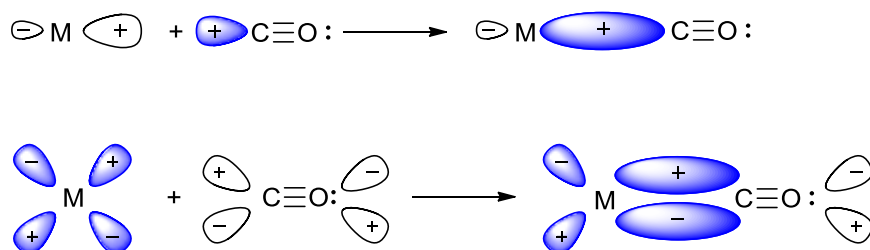


**Figure 31** Top: Bonding between the empty  $d$  orbital of a metal centre and the  $\sigma$  bonding orbital of  $\text{C}\equiv\text{O}$ . Bottom: bonding between the filled  $d$  orbital of a metal and the  $\pi^*$  unoccupied molecular orbital of  $\text{C}\equiv\text{O}$ .

The occupation of the  $\pi^*$  molecular orbital of  $\text{C}\equiv\text{O}$  with electron density leads to a destabilizing of the  $\text{C}\equiv\text{O}$  bond. The more electron-rich the metal centre to which  $\text{C}\equiv\text{O}$  is bound the greater the extent of the weakening of the  $\text{C}\equiv\text{O}$  bond. A weaker bond will vibrate at a lower frequency than a stronger bond therefore the vibrational frequency of a  $\text{C}\equiv\text{O}$  stretch can give information about the electronic environment of the metal centre. Equally, predictions of the direction of the shift in vibrational frequency can be made when altering the electron richness of the metal in a metal carbonyl by changing the ligand environment.

The number of bands observed in an infrared spectrum is related to the symmetry of the complex. This can be analysed by group theory or in current methodology by analysis of structures by DFT. Group theory will predict the number of bands only and is most useful for a molecule of higher symmetry. DFT will predict positions and intensities too, and although one can argue about accuracy, this information is often as useful as a predicted number of bands.

## 2.2.4 Mass spectrometry

Mass spectrometry is a useful analytical technique that measures the mass of an ionised molecule or fragment.<sup>208</sup> This is typically done by ionizing a chemical sample, separating the ions and fragments created according to their mass and having a means of detecting them.

The general scheme for this is shown in Figure 32.

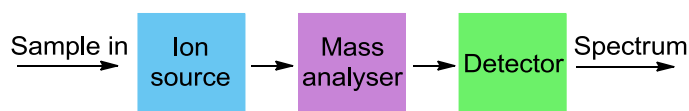


**Figure 32** Basic schematic of mass spectrometer.

This then produces a mass spectrum, a plot of ion signal as a function of mass to charge ratio. Samples are introduced into the spectrometer as a solution or solid and then vaporised under vacuum. There are a variety of techniques used to then ionise the sample. One such technique is electron ionization (EI), where high energy electrons are fired at the sample. The high energy electrons create positively charged ions by knocking off electrons from the sample. The resulting positively charged ions are then electrostatically repelled into the mass analyser. The main disadvantage of electron ionization is that direct bombardment of the sample with electrons can lead to fragmentation of ions before they reach the detector.

Electrospray ionization is now a commonly used ionization technique. In this technique the sample is made into a solution which can sometimes have added ionic compounds such as carboxylate or sodium alkoxide. This is then sprayed through a fine capillary at a potential of several thousand volts. The aerosol produced consists of charged droplets of solution. The droplets are then swept into a high vacuum, evaporating the solvent and eventually causing the droplets to explode. This gives sample molecules with ions attached. These are then accelerated into the mass analyzer.

In contrast to a classical quadrupolar analyser, the orbitrap method relies on ions trapped in a cylindrical electric field. The trapped ions orbit a central spindle-like electrode under the influence of an oscillating electric field. The frequency of orbit is dependent upon the mass of the ion in question and can be extracted by Fourier transform. As the ions are trapped during analysis it is possible to selectively extract them for hyphenated analysis. The orbitrap technique combines the soft ionization technique of ESI with the ability to obtain high-resolution results it thus becoming the standard technique for molecular identification for mass spectrometry.<sup>209</sup>

### **2.2.5 X-ray crystallography**

X-ray crystallography is the definitive technique for determining the exact structure and shape of a molecule.<sup>208</sup> Unlike spectroscopic techniques, which give qualitative data concerning functional groups and connectivity, X-ray crystallography gives a defined structure. One drawback is the need to obtain a good quality crystal of the compound of interest, which is often difficult. A crystal is composed of ions, or molecules arranged in a regular order throughout the solid forming a lattice, in which the smallest repeating subunit is called the unit cell.

In order for diffracted X-rays to be observed, there must be constructive interference between them. Figure 33 illustrates the diffraction of X-rays from lattice planes. In order to have constructive interference the path difference between these X-rays must be equal to an integer number of wavelengths.

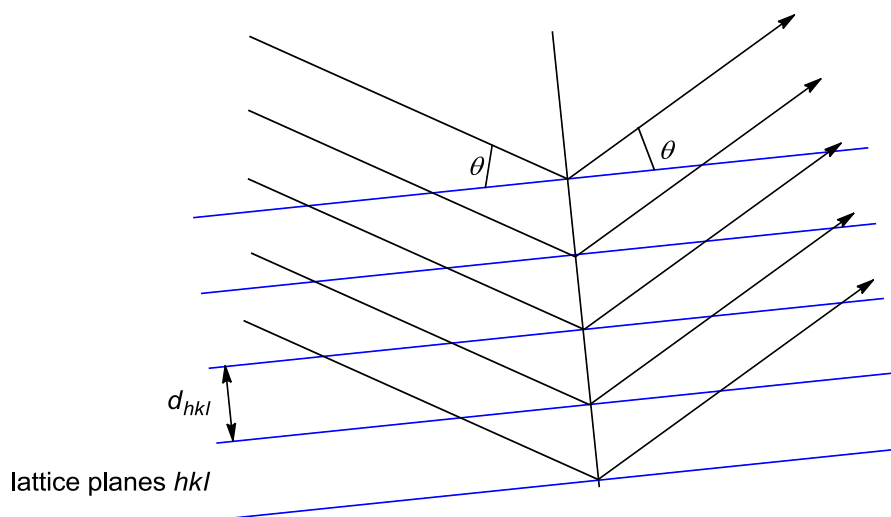


**Figure 33** Diffraction of X-rays from crystal lattice planes.

This leads onto Bragg's law

$$2d \sin \theta = n\lambda$$

where  $\theta$  is known as the Bragg angle,  $\lambda$  is the wavelength of the X-rays and  $d$  is the distance between adjacent planes in a parallel set.

Bragg's Law is a fundamental law in diffraction that gives the conditions under which a diffracted beam of radiation may be observed.<sup>210</sup> When a good quality crystal is irradiated with X-rays, the radiation will be diffracted in a regular pattern. The diffraction is strongest in regions of high electron density as it is the electrons that diffract the X-rays. The diffraction pattern is used to discern the location of the atoms in a molecule as most electron density is centred around the nuclei. It is possible to not only determine the spatial arrangement of the atoms but also how the molecules pack within the cell. To obtain this information the electron density is mapped out, with heavier atoms placed in regions of higher electron density. The experimental information is compared to a computer model of the suspected structure and refined until good agreement is obtained. One measure of the

agreement between the experimental data and the computer model is known as the *R*-factor, the smaller the *R*-factor: the better the agreement.

### 2.2.6 Electrochemical measurements

Where the chemistry of compounds involves their ability to undergo redox changes, electrochemical techniques can offer a unique insight into the intimate detail. Perhaps the most versatile electrochemical technique is cyclic voltammetry (CV). In CV a potential applied to the solution is swept over a controlled range and the current response is recorded. By varying factors such as the temperature, scan rate and potential range the analysis of a set of CV experiments can give information about the kinetics and thermodynamics of a chemical system. Cyclic voltammetry is a particularly useful technique as an experiment requires very little compound (milligrams) and is essentially non-destructive since the chemistry occurs in a small volume in the diffusion layer at the surface of the electrode, leaving the bulk concentration essentially unchanged.

During a basic CV experiment a redox active compound (the subject of the experiment) is dissolved in a solution containing a non-redox active electrolyte. The electrolyte is present to reduce resistance and allow charge to flow. Electrolytes used in non-aqueous solvents feature large ions to give good solubility and thus conductivity. For example  $[\text{Bu}_4\text{N}][\text{BF}_4]$  is a common electrolyte in a solvent such as acetonitrile. The solution of subject compound and electrolyte are contained within an electrochemical cell which typically has three chambers, each of which contains an electrode, Figure 34.

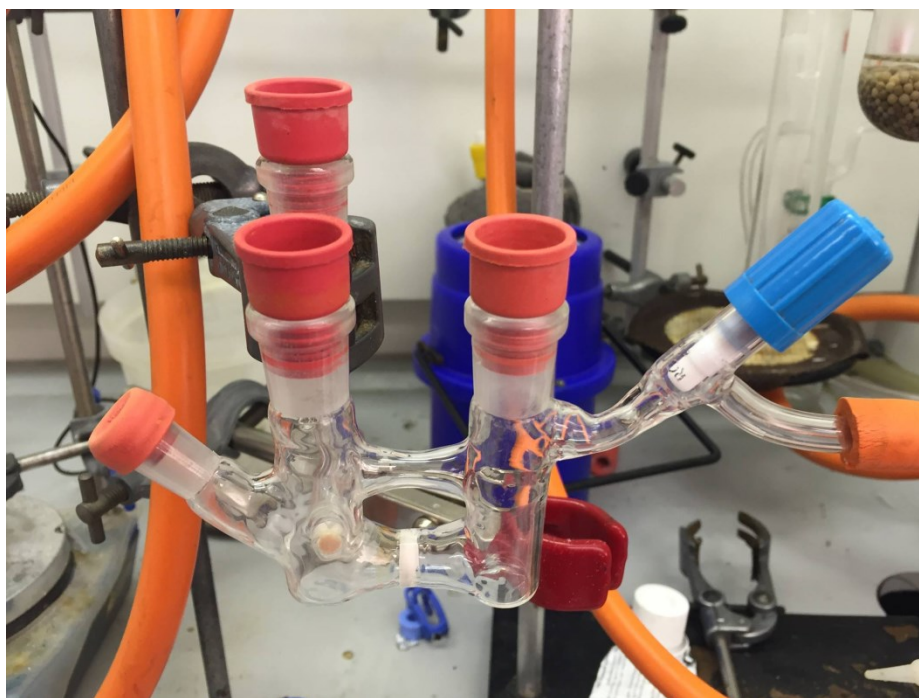


**Figure 34** Photograph of a three-chambered electrochemical cell.

A common three electrode arrangement is made up of a working electrode, typically made of vitreous carbon (platinum, gold or amalgamated gold can also be used), a secondary electrode made of platinum and a reference electrode of silver wire or Ag/AgCl.<sup>211</sup> In a cyclic voltammetry experiment there is a variable potential difference between the working and secondary electrodes and a fixed potential difference between the working and reference electrodes. Over the time-course of the experiment the variable potential difference is swept over a controlled range in the manner depicted, Figure 35.

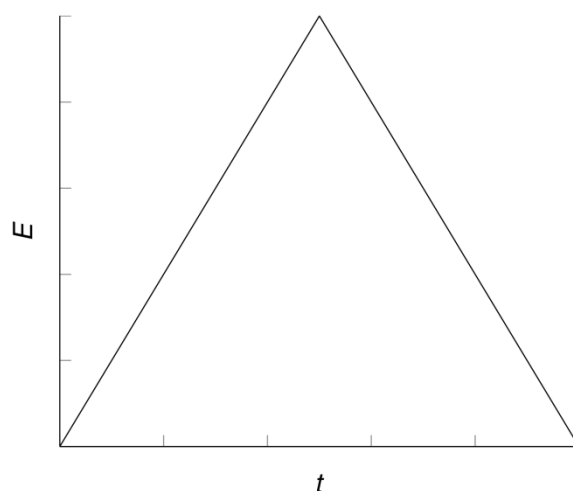


**Figure 35** The potential difference sweep during a typical CV experiment, where the slope is equal to the scan rate.<sup>212</sup>

Figure 36 below shows the key features of a typical cyclic voltammogram for a reversible couple. On the forward sweep, the current passed rises to a maximum  $i_p^{ox}$  at the oxidation potential  $E_p^{ox}$ , before falling away in the reverse direction the absolute value of the current again rises to a maximum  $i_p^{red}$  at the reduction potential  $E_p^{red}$ . The average of  $E_p^{ox}$  and  $E_p^{red}$  is  $E_{1/2}$  for the redox couple being examined. For an ideal one electron reversible couple, the difference between  $E_p^{ox}$  and  $E_p^{red}$  is close to 60 mV at room temperature (theoretically 59 mV at 25 °C), and  $i_p^{ox}/i_p^{red} = 1$ . Figure 36 illustrates the effect of scan rate on the cyclic voltammogram. For a fully reversible process, the peak positions are unaffected whilst the peak current scales linearly with the square root of the scan rate.

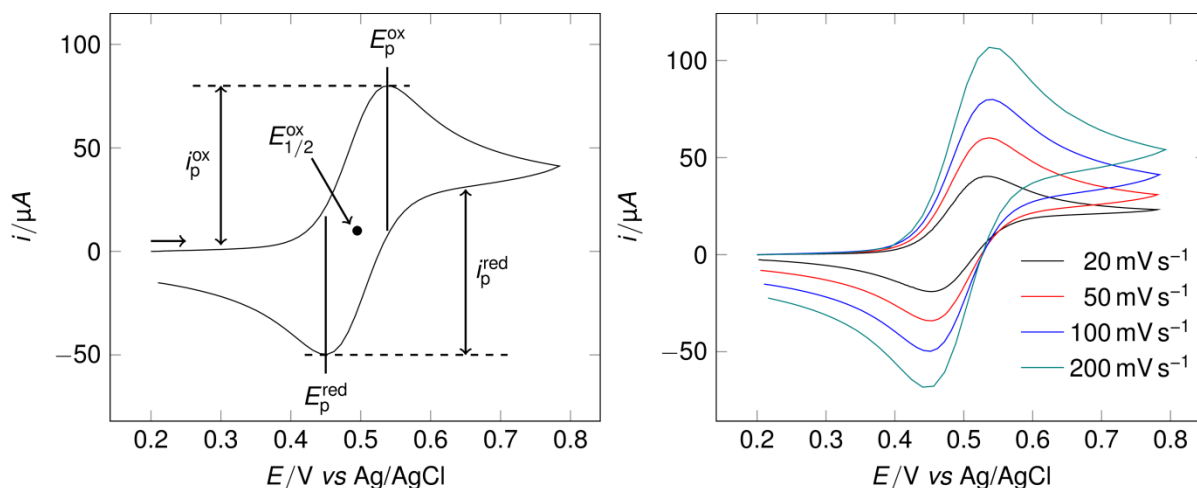


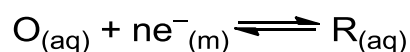
**Figure 36** Left: CV of 3.5 mM ferrocene recorded at 100 mV s<sup>-1</sup> vs Ag/AgCl in 0.1 M [Bu<sub>4</sub>N][BF<sub>4</sub>]- MeCN at 25 °C; Right: CV of 3.5 mM ferrocene recorded at various scan rates vs Ag/AgCl in 0.1 M [Bu<sub>4</sub>N] [BF<sub>4</sub>] -p MeCN at 25 °C. Reproduced with permission of the author from ref. 46.

The information contained in the cyclic voltammogram above tells us that ferrocene is a reversible, one-electron system. In addition, for a reversible system, it can be shown that the magnitude of the forward peak current is given by the Randles-Sevcik equation (Equation 14)

$$i_p = 2.69 \times 10^5 n^{3/2} A D^{1/2} C^* \nu^{1/2} \quad \text{Equation 14}$$

where  $n$  is the number of electrons associated with the oxidation or reduction step of the parent species,  $A$  is the area of the electrode in cm<sup>2</sup>,  $D$  is the diffusion coefficient of the species in cm<sup>2</sup> s<sup>-1</sup>,  $C^*$  is the bulk concentration expressed in mol<sup>3</sup> dm<sup>-3</sup>, and  $\nu$  is the potential scan rate in V s<sup>-1</sup>. A system can quickly be assessed for reversibility by plotting the peak current vs the square root of the scan rate over a range of scan rates.

For the general charge transfer reaction



it was shown by Nernst that the potential established at the electrode under equilibrium conditions is given by

$$E_e = E^\circ + \frac{RT}{nF} \ln \frac{C^{\text{ox}}}{C^{\text{red}}}$$

where the potential at equilibrium ( $E_e$ ) of the electrode results from the standard electrode potential ( $E^\circ$ ) of the reaction and the concentrations of O and R, which, under equilibrium conditions are the same as the bulk solution. Thermodynamic parameters such as free energies, entropies, enthalpies, equilibrium constants, activities and solution pH can be obtained from equilibrium electrochemical measurements.<sup>213</sup>

In this work the potential at which redox couples are reported are given as the  $E_{1/2}$  (the mid potential between  $E_p^{\text{ox}}$  and  $E_p^{\text{red}}$  as shown in Figure 36).

The Nernst equation defines the equilibrium potential  $E_e$  for a system as:

$$E_e = E^0 + \frac{RT}{nF} \ln \frac{a^{\text{ox}}}{a^{\text{red}}} \quad \text{Equation 15}$$

where  $a^{\text{ox}}$  and  $a^{\text{red}}$  are the thermodynamic activities of the redox partners and  $E^0$  is the *standard potential*. This can be re-written as:

$$E = E^0 + \frac{RT}{nF} \ln \frac{\gamma^{\text{ox}} C^{\text{ox}}}{\gamma^{\text{red}} C^{\text{red}}} \quad \text{Equation 16}$$

where  $\gamma^{\text{ox}}$ ,  $\gamma^{\text{red}}$ ,  $C^{\text{ox}}$ ,  $C^{\text{red}}$  are the respective activity coefficients and concentrations of the oxidised and reduced species. Rearranging this equation gives:

$$E = E^0 + \frac{RT}{nF} \ln \frac{\gamma^{\text{ox}}}{\gamma^{\text{red}}} + \frac{RT}{nF} \ln \frac{C^{\text{ox}}}{C^{\text{red}}} \quad \text{Equation 17}$$

Letting

$$E^{0'} = E^0 + \frac{RT}{nF} \ln \frac{\gamma^{\text{ox}}}{\gamma^{\text{red}}} \quad \text{Equation 18}$$

and defining  $E^{0'}$  as the *formal potential* we have an alternative form of the Nernst equation:

$$E = E^{0'} + \frac{RT}{nF} \ln \frac{C^{\text{ox}}}{C^{\text{red}}} \quad \text{Equation 19}$$

$E_{1/2}$  is related to  $E^{0'}$  by the expression:<sup>214</sup>

$$E_{1/2} = E^{0'} + \frac{RT}{nF} \ln \sqrt{\frac{D^{\text{red}}}{D^{\text{ox}}}} \quad \text{Equation 20}$$

The diffusion coefficients ( $D$ ) of the redox partners of systems of moderate molecular mass (>200) are usually quite similar. If we consider a case where the reduced form of the redox pair has a diffusion coefficient as much as 20 % greater than that of the oxidised species, then it can be shown that for a one electron couple:

$$E_{1/2} = E^{0'} + 2.34 \text{ mV} \quad \text{Equation 21}$$

Thus to a reasonable approximation:

$$E_{1/2} \approx E^{0'} \quad \text{Equation 22}$$

Using similar arguments for activity coefficients we can use the approximation:

$$E_{1/2} \approx E^{0'} \approx E^0$$

Equation 23

### 2.2.7 Stopped-flow FTIR

Stopped-flow is a useful technique for detecting the presence of short lived intermediates in solution and for gathering kinetic data about a reaction. In a stopped-flow experiment two syringes are used each loaded with one of two reactive partners. The two syringes are connected to a mixing chamber and then to a spectroscopic cell. At the start of the reaction the two syringes are injected simultaneously into the mixing chamber. Rapid mixing occurs and the product solution moves into the cell. The FTIR then starts scanning the mixture and follows the progress of the reaction from time zero. It can thus be seen that stopped-flow can give information about reaction rates and show the presence of any intermediates formed.<sup>215</sup> A schematic of a stopped-flow IR is shown below (Scheme 37).

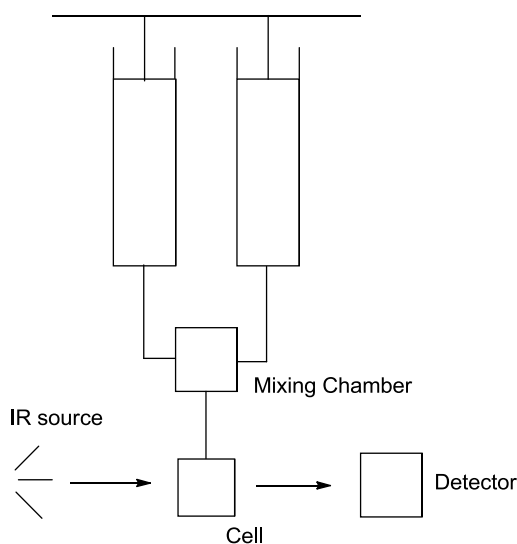


**Figure 37** Basic cross-section of stopped-flow IR.

In practice the distance between the mixing chamber and the cell needs to be minimised to reduce the “dead time”: the time interval between mixing and the first observable signal. There is also a time-scale requirement for acquisition of Fourier transform infrared data as

this involves a mechanical component (interferometer). For systems in use today the dead time of roughly 50 ms is less significant than the requirements for the acquisition of infrared data which limit time resolution to at best tens of milliseconds.

Stopped-flow IR is particularly powerful when the observed bands fall in an otherwise unpopulated region of the spectrum. Organometallic compounds that contain CO and CN bands are therefore favourable for study using this method as the distinct chromophores fall in a unique spectral window. Data obtained from absorption-time data is analyzed to provide kinetic information on the rate of consumption of starting material and growth of product(s).

## **2.3 Background to theoretical and simulation methods**

### **2.3.1 Collaboration with Maurizio Bruschi**

The detailed DFT calculations were performed by Professor Maurizio Bruschi at the University of Milan-Bicocca as these involved advanced consideration of spin states associated with the iron-sulfur clusters used in this study. The author used these results in the analysis of the likely structures of products and of their experimental spectra, specifically FTIR.

### **2.3.2 General introduction to density functional theory**

Density functional theory (DFT) is a computational modelling technique used to simulate the structure and properties of relatively small molecules. DFT has become an increasingly popular technique in the last 20 years as it has been shown to give useful information for a range of chemical systems, whilst being less computationally intensive than *ab initio* techniques. The key concept in density functional theory is to calculate the electron density of the simulated system rather than a series of wavefunctions. DFT can be used to predict a

range of spectroscopic properties particularly those for ground state electron configurations, for example infrared and Raman data.<sup>216</sup>

### **2.3.3 Simulation of electrochemical data**

There is a strong theoretical understanding of the behaviour of electroactive species in solution. Cyclic voltammograms can be simulated by calculation of the current which flows as a consequence of changing the concentrations of species at the electrode. These time dependent changes are determined by Nernstian, diffusional and chemical reactions in the diffusion layer. The equations underlying these processes can be solved analytically for the simplest of systems such as reversible electron transfer but iterative numerical simulation can be successfully applied for analysis of more complex system.<sup>217</sup>

## 3 Syntheses of analogues of the [Fe]-hydrogenase

### 3.1 Background to the work

#### 3.1.1 Structure and function of the [Fe]-hydrogenase

The structure and function of the [Fe]-hydrogenase is covered in section 1.2.7. The following sections survey chemical model studies of the enzyme active site and what is currently known about the way it functions.

#### 3.1.2 Previous synthetic studies

Looking at the ligand arrangement of the active site of the [Fe]-hydrogenase it is known that the Fe(II) centre is ligated by a chelating ortho-acyl pyridone ligand, cysteine residue, biologically unusual CO ligands in a *cis* arrangement and a vacant site thought to be occupied by a solvent molecule (i.e. water).<sup>15</sup>

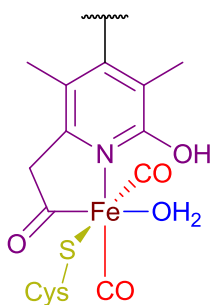


**Figure 38** Active site of the [Fe]-hydrogenase. Key features outlined in the text are highlighted in colour.<sup>15</sup>

Synthesizing chemical models that imitate this unusual ligand arrangement poses an interesting challenge and will allow better understanding of the inner workings of the enzyme as well as more fundamental chemical insight into the coordination chemistry of these systems.

Before the crystal structure of the [Fe]-hydrogenase was obtained attempts to model the structure based on spectroscopic information had already begun.<sup>94</sup> In particular it was known that the system contained an Fe centre with *cis* CO ligation and a pyridone derivative.<sup>218, 219</sup> Thus early modelling aimed to replicate these known ligands.

One of the first examples of modelling the guanyl pyridone cofactor derivative on a model [Fe]-hydrogenase system was reported by Rauchfuss and co-workers.<sup>220</sup> In model **44** (Figure **39**) 6-(carboxymethyl)-4-methyl-2-hydroxypyridine **43** is used as an analogue of the guanyl pyridone cofactor and ruthenium is a surrogate for iron. The ligand **43** does not bind to the ruthenium metal centre via  $\kappa^2$ -N,O chelation due to the stronger binding affinity of the carboxylate group.

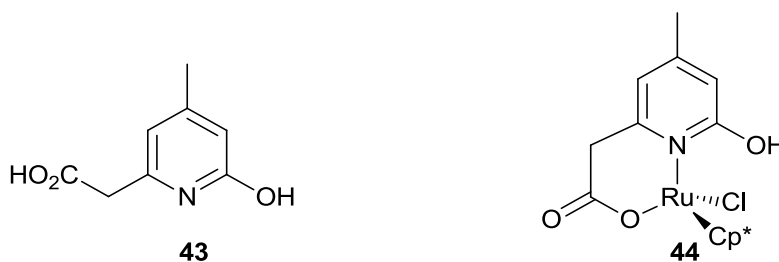


**Figure 39** Early model complex as reported by Rauchfuss (Cp\* = C<sub>5</sub>Me<sub>5</sub>).<sup>220</sup>

An early study based on EXAFS data suggested that the Fe-containing active site was low coordination number and contained two CO ligands, sulfur ligation and one or two N/O containing ligands within bonding distance.<sup>221</sup> Holland and co-workers developed a model based on this low coordination number CO containing iron centre (shown in Figure 40). The carbonyl stretches reported for the complex **45** were 1917 and 1996 cm<sup>-1</sup> not close to those for the natural system; however Holland noted the model was Fe(I) whilst the natural system is Fe(II).

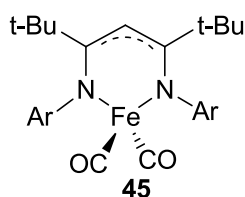
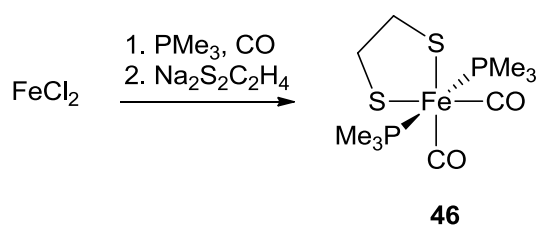


**Figure 40** Iron(I) *cis*-dicarbonyl complex reported by Holland and co-workers, (Ar = 2,6-(*i*-Pr)<sub>2</sub>C<sub>6</sub>H<sub>3</sub>).<sup>202</sup>

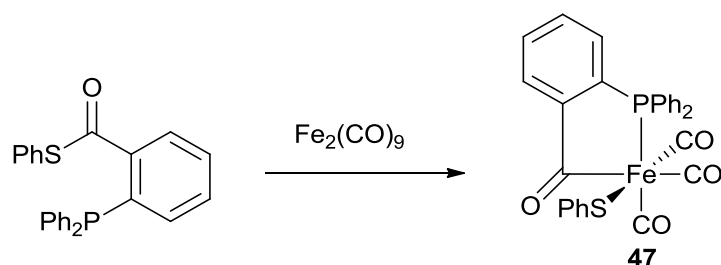
Evidence for the carbonyl ligands in the active site of the [Fe]-hydrogenase existing in a *cis* arrangement was determined by an infrared spectroscopic study before crystallographic characterization of the structure. The IR stretching frequencies of the CO bands in the active site were reported as 1972 and 2031 cm<sup>-1</sup>.<sup>218</sup> It can be shown that the angle between the two groups  $2\theta$  is related to the IR intensity ratios by the equation  $I_{\text{sym}}/I_{\text{asym}} = \cotan^2 \theta$ , where  $I_{\text{sym}}$  and  $I_{\text{asym}}$  are the infrared intensities for the symmetric and anti-symmetric stretches, respectively.<sup>222</sup> By applying this formula to the data obtained for the enzyme it can be shown that the angle between the two carbonyls is 90°.

Rauchfuss and co-workers synthesised a *cis*-CO [Fe]-hydrogenase model complex which was studied in comparison to the natural system by NRVS (nuclear resonance vibrational spectroscopy) to discover the minimal ligand arrangement for the natural system (Scheme 20).<sup>223</sup> This was found to be two *cis* carbonyls, sulfur and a light atom suggested to be the pyridyl cofactor nitrogen.<sup>223</sup> This gave CO stretches at 2011 and 1944 cm<sup>-1</sup> not especially close to the natural system: 1972, 2031 cm<sup>-1</sup>. The study reports that the bond angle between the CO ligands is 97.56°.



**Scheme 20** Synthesis of model compound for NRVS studies as reported by Rauchfuss and co-workers.<sup>223</sup>

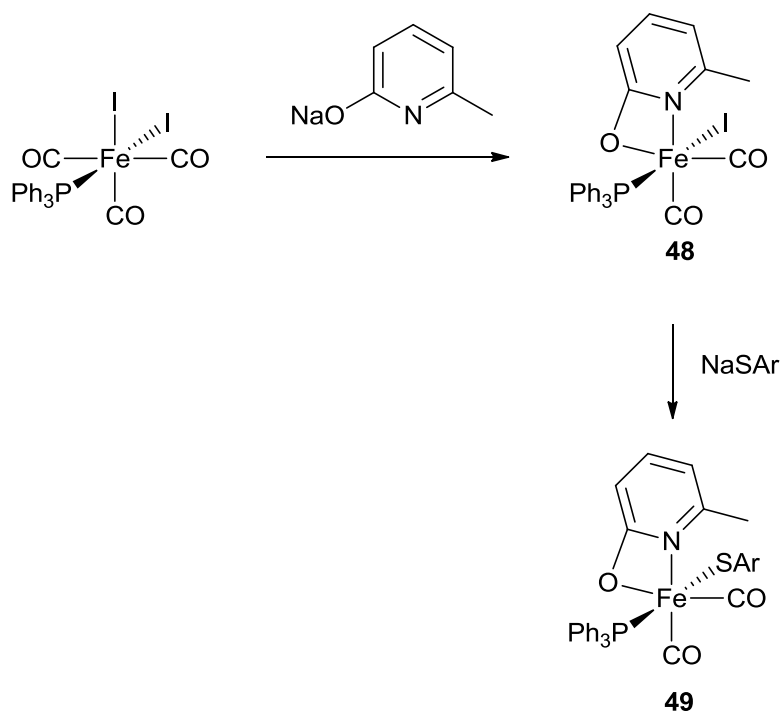
After crystallographic characterization of the active site of [Fe]-hydrogenase,<sup>15</sup> subsequent synthetic models mimicked further components of the ligand sphere. Rauchfuss and co-workers developed an active site with a phosphine-modified thioester derivative, tackling the challenge of introducing an acyl derivative (Scheme 21).<sup>224</sup> This approach replaces the amine with a tertiary phosphine moiety (an abiological ligand) and generates a heterocyclic ring where the position of the aromatic ring is not directly above the Fe centre as in the natural system.



**Scheme 21** Synthesis of model complex as reported by Rauchfuss.<sup>224</sup>

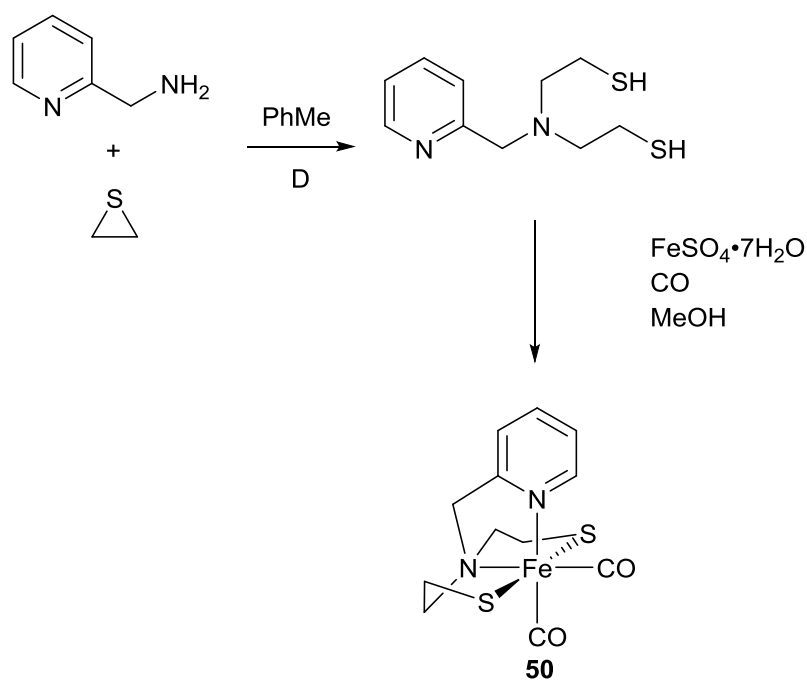
Model compounds containing a nitrogen–sulfur chelate are a useful approach to generating ligand sets with closer analogy to the natural system of [Fe]-hydrogenase than just *cis*-carbonyl arrangement. Hu and co-workers developed an [Fe]-hydrogenase model that includes a pyridone molecule in a *cis*-dicarbonyl system **48** (Scheme 22).<sup>225</sup> In the model complex by Hu, the pyridone ligand chelates to the Fe centre by the nitrogen and oxygen atoms, and the complex gives rise to IR bands at 1987 and 2032  $\text{cm}^{-1}$ . The structural analogy

of the complex to the natural system was extended by inclusion of a bulky thiol to yield complex **49** (Scheme 22).<sup>225</sup>



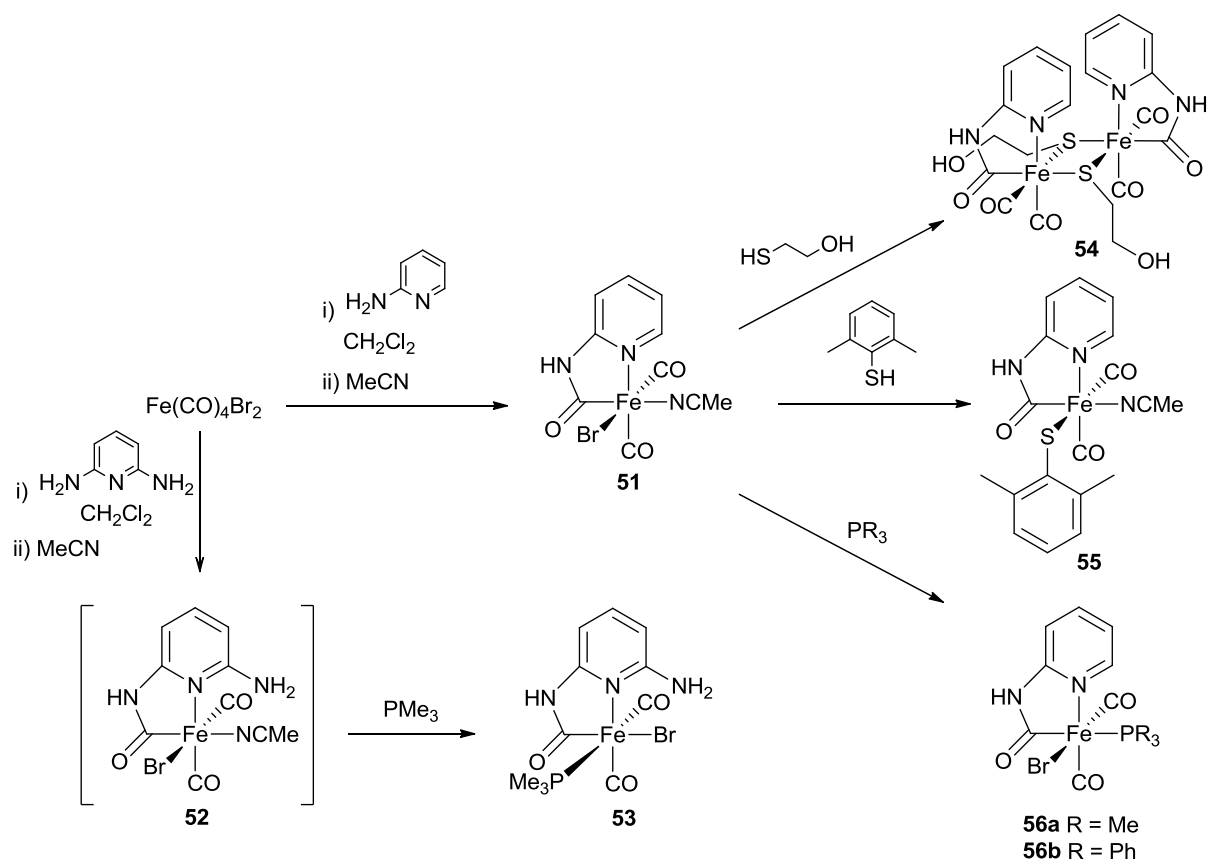
**Scheme 22** Synthesis of pyridone-containing model (Ar = 2,6-Me<sub>2</sub>C<sub>6</sub>H<sub>3</sub>).<sup>225</sup>

Pickett and co-workers synthesised a model complex containing a tetradentate ligand with both pyridine and thiolate donors (Scheme 23). This allowed the formation of a complex with pyridone, thiolate and CO ligation without the need for phosphine (an abiological ligand).<sup>226</sup> Model **50** exhibits two IR bands in the carbonyl region at 1973 and 2026 cm<sup>-1</sup>, in very good agreement with those observed in the natural system. It is important to note however, that few structurally similar complexes have given concordant IR data.



**Scheme 23** Synthesis of a phosphine-free model by Liu, Pickett and co-workers.<sup>226</sup>

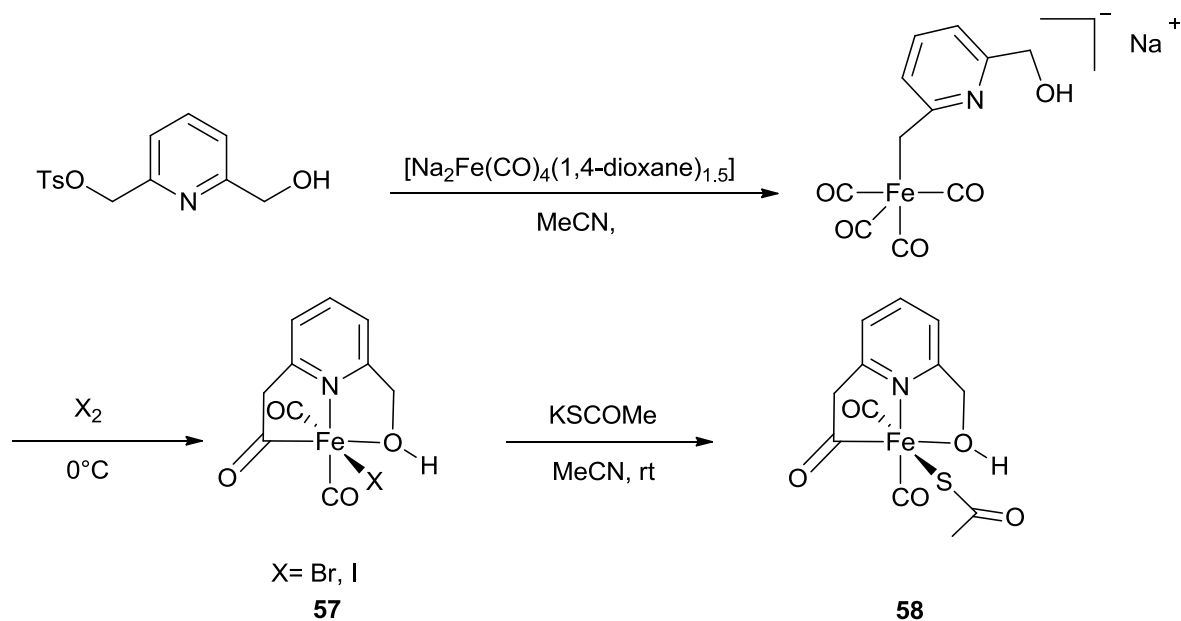
Pickett and co-workers reported a family of [Fe]-hydrogenase models with an amide group as a surrogate for the acyl of the natural system.<sup>227</sup> These models have mimicked the ligand environment of the [Fe]-hydrogenase in a variety of ways including thiol ligation and the introduction of a pendant NH<sub>2</sub> group (Scheme 24).



**Scheme 24** Synthesis of [Fe]-hydrogenase active site model complexes as reported by Pickett.<sup>16, 227</sup> Complexes **56a** and **56b** were synthesised by the author of this thesis as described in section 3.2.

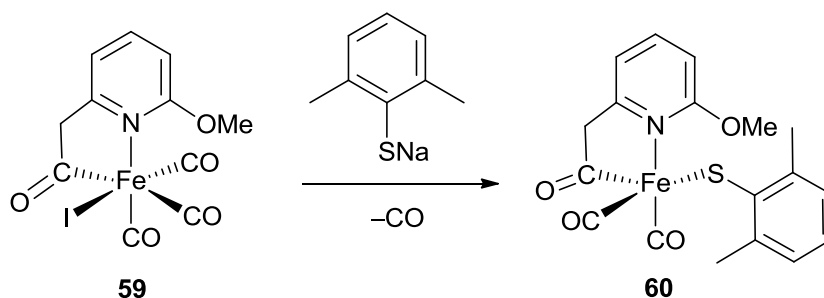
Song reported the first [Fe]-hydrogenase model to contain an acyl methyl(hydroxymethyl)-pyridine ligand (Scheme 25).<sup>228</sup> The incorporation of this ligand was thought to be an important advance on the structures reported so far. The acyl methyl(hydroxymethyl)pyridine ligand mimics the pyridone derivative of the natural system with an electronegative atom at the 6 position. It is the hydroxyl group that is thought to play an important role in the heterolytic cleavage of dihydrogen. However in this particular model system the OH is bound to a methylene group rather than directly to the pyridine ring. Thus spatially and electronically the model it is rather removed from the natural system.

The acyl methyl(hydroxymethyl)pyridine ligand is introduced to  $\text{Na}_2\text{Fe}(\text{CO})_4$  via nucleophilic substitution. The formation of model **57** proceeds via an unstable intermediate, followed by migratory insertion of CO, coordination of the hydroxyl group and oxidation by  $\text{I}_2$  or  $\text{Br}_2$ . The ligand environment of complex **57** is brought closer to the natural system by incorporation of  $\text{MeCOS}^-$  which also eliminates the halide.



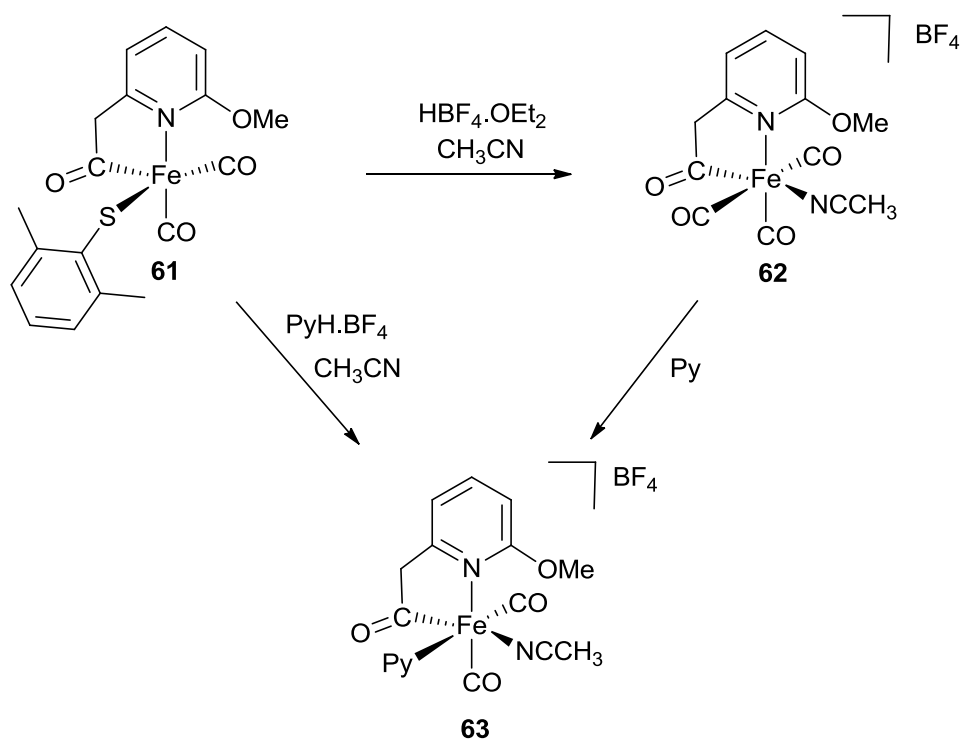
**Scheme 25** Synthesis of [Fe]-hydrogenase active site model complexes as reported by Song.<sup>228</sup>

In 2011 Hu reported a five coordinate [Fe]-hydrogenase square pyramidal model complex.<sup>229</sup> The catalytic cycle in the enzyme is believed to involve activation of the substrate by a five coordinate Fe centre. This makes the model developed by Hu an interesting starting point for studying how the [Fe]-hydrogenase enzyme works. Notably in this structure the OMe group on the heterocyclic ring is deployed in a similar fashion to the OH in the natural system.

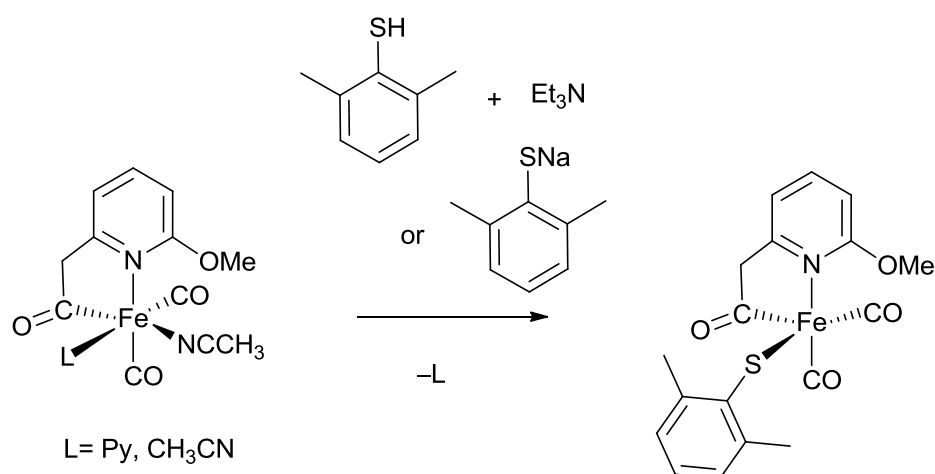


**Scheme 26** Synthesis of five coordinate [Fe]-hydrogenase active site model complexes as reported by Hu.<sup>229</sup>

In further work Hu and co-workers reported the reversible protonation of the thiolate ligand of the five coordinate model complex. They showed that the thiolate could be protonated and removed and deprotonated and reintroduced to regenerate the five coordinate complex **61** (Scheme 28). The static structures **60** and **61** are enantiomers (which is a special case of being geometric isomers). It is possible that in solution the ligands are dynamic and that will racemise the system: supporting evidence for this behaviour is seen in the THF solution IR spectrum of **51** where the bands seen suggest that isomers of the molecule exist in solution.



**Scheme 27** Protonation and loss of thiol from model complex of [Fe]-hydrogenase by Hu.<sup>230</sup>

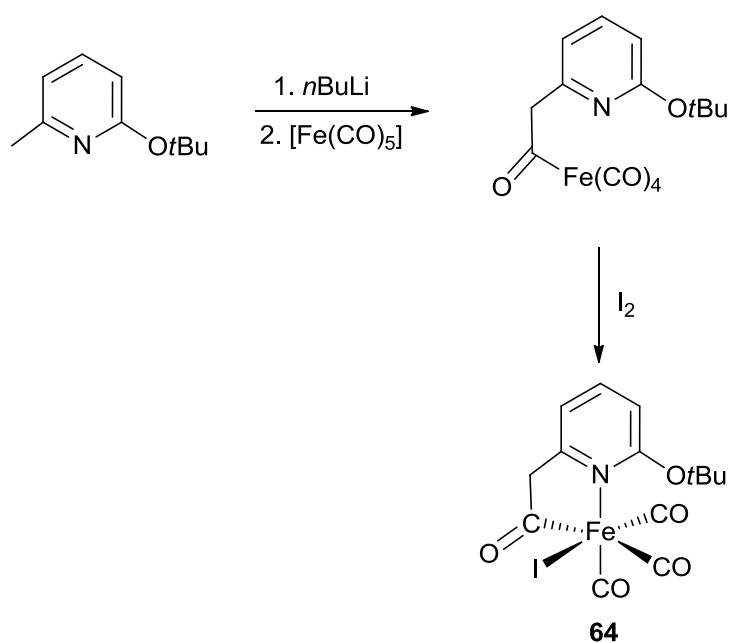


**Scheme 28** Deprotonation of thiol and regeneration of five coordinated model complex of [Fe]-hydrogenase by Hu.<sup>230</sup>

During the heterolytic cleavage of dihydrogen, a hydride (picked up by methylene- $\text{H}_4\text{MPT}^+$ ) and a proton are formed. The proton is thought to quickly exchange with the bulk solvent but the immediate proton acceptor is unknown. The cysteine residue (176), pyridonyl hydroxyl

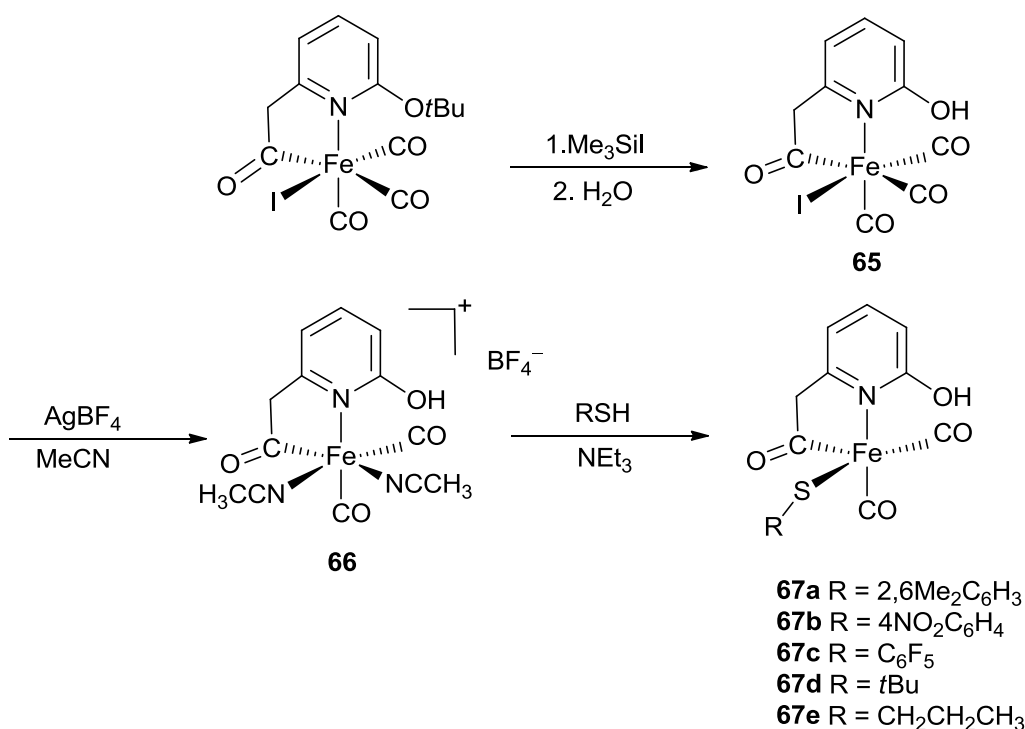
group and acyl ligand of the iron centre of the natural system could all function as the internal base. The protonation reactions of Hu's model indicate that the cysteine thiolate could be a viable proton acceptor for [Fe]-hydrogenase.

The latest work by Hu and co-workers<sup>203</sup> reported a model with an iron centre featuring an acylmethylpyridinol ligand (Scheme 29). Direct reactions of iron carbonyls with acylmethylpyridinol ligands and derivatives have so far not been reported in the literature as a successful strategy due to the reactivity of the OH group. Therefore Hu and co-workers followed a strategy where the hydroxyl group was protected before reaction with an iron centre and subsequently deprotected.



**Scheme 29** Coordination of protected ligand to generate [Fe]-hydrogenase model complex.<sup>203</sup>

They showed that their acylmethylpyridinol containing [Fe]-hydrogenase model could be coordinated with a variety of thiolate ligands thus completing the ligand spheres homology with the natural system (Scheme 30).<sup>203</sup>



**Scheme 30** Deprotection of model complex to yield acylmethylpyridinol ligand containing model by Hu. This model is then treated with AgBF<sub>4</sub> and acetonitrile to yield complex **66**. Complex **66** can be reacted with a variety of thiols.<sup>203</sup>

The models so far mentioned have demonstrated advances in structural similarity to the [Fe]-hydrogenase active site but with no ability to function like the natural system. Meyer and co-workers have recently developed a model that mimics the natural system functionally rather than structure (shown in Figure 41).<sup>204</sup>

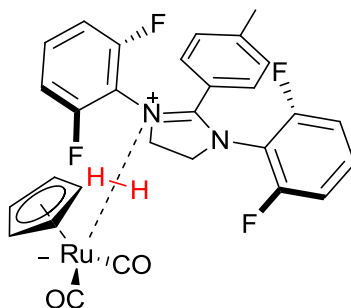
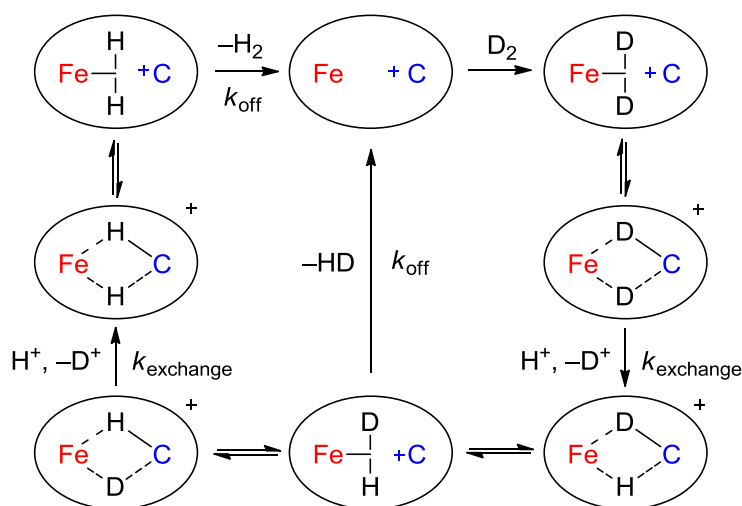


**Figure 41** Functional model for the [Fe]-hydrogenase by Meyer and co-workers.<sup>204</sup>

This model for [Fe]-hydrogenase uses a Lewis acidic imidazolinium ion as a biomimetic hydride acceptor in combination with an organometallic Lewis base to heterolytically cleave dihydrogen. Here the proton generated from the splitting of dihydrogen binds directly to the metal centre of the anion. This system may have some functional analogy to the natural system but it is hard to draw any firm conclusions as Meyer and co-worker's model is a ruthenium based complex with a different ligand arrangement.

### 3.1.3 Mechanistic aspects and potential intermediates in the catalytic cycle

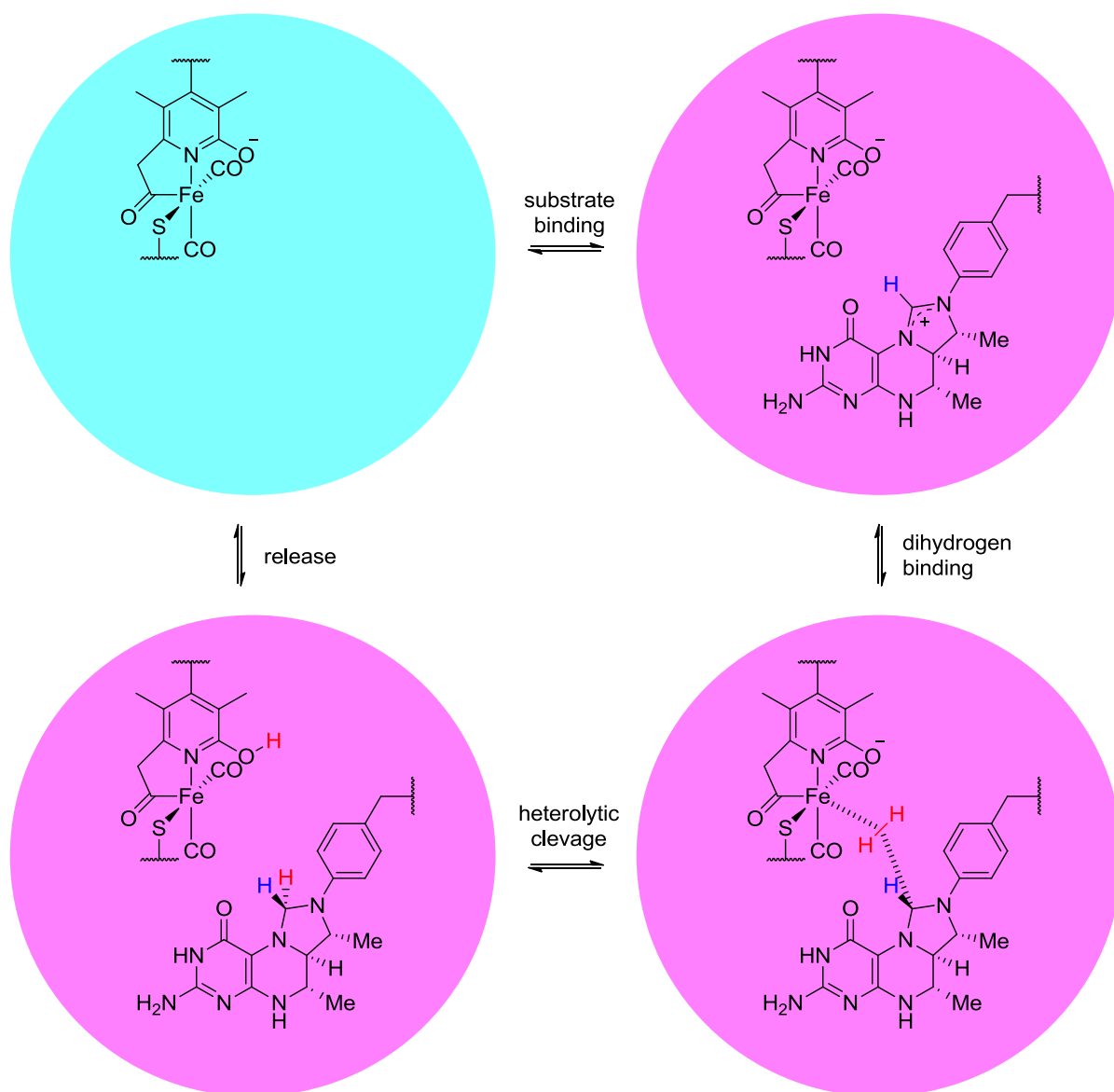
Although the active site of the enzyme has been fully characterised<sup>15</sup> the mechanism by which it works is not yet fully understood. The first studies into the mechanism of action of [Fe]-hydrogenase began shortly after it was first purified. Several early studies involving isotopic exchange reactions, kinetic isotope effects and two-dimensional NMR showed that a) the substrate must be present for the enzyme to carry out its function,<sup>136</sup> b) the mechanism involves hydride transfer to **1**<sup>231</sup> and c) this transfer is stereospecific to the *pro-R* side of the substrate.<sup>232, 233</sup> In a study using *para*-hydrogen<sup>234</sup> (molecules of hydrogen in which the spins of the nuclei are in the opposite direction) it was established that the H–H bond is not cleaved unless both the enzyme and the substrate are present.<sup>235</sup> At the same time isotopic studies have shown that both HD and H<sub>2</sub> are formed when the enzyme is reacted with substrate in the presence of D<sub>2</sub> in unlabelled water. This result is consistent with an interpretation in which the rate of dissociation of dihydrogen  $k_{\text{off}}$  is equal to the rate of exchange  $k_{\text{exchange}}$  (Scheme 31).



**Scheme 31** Mechanism to explain parallel formation of H<sub>2</sub> and HD from a reaction mixture containing D<sub>2</sub>, H<sub>2</sub>O, the [Fe]-hydrogenase and the cationic substrate **4**. The metal centre and substrate are represented by the red ‘Fe’ and blue ‘C’, respectively.<sup>235</sup>

The most plausible explanation for the available kinetic data is that the enzyme operates by a “push-pull” mechanism in which both of the  $\delta^+$  and  $\delta^-$  centres are required to polarise dihydrogen. This concept is reminiscent of the frustrated Lewis pair approach in which dihydrogen is most commonly activated by an electrophilic boron and nucleophilic phosphorus centre.<sup>236</sup>

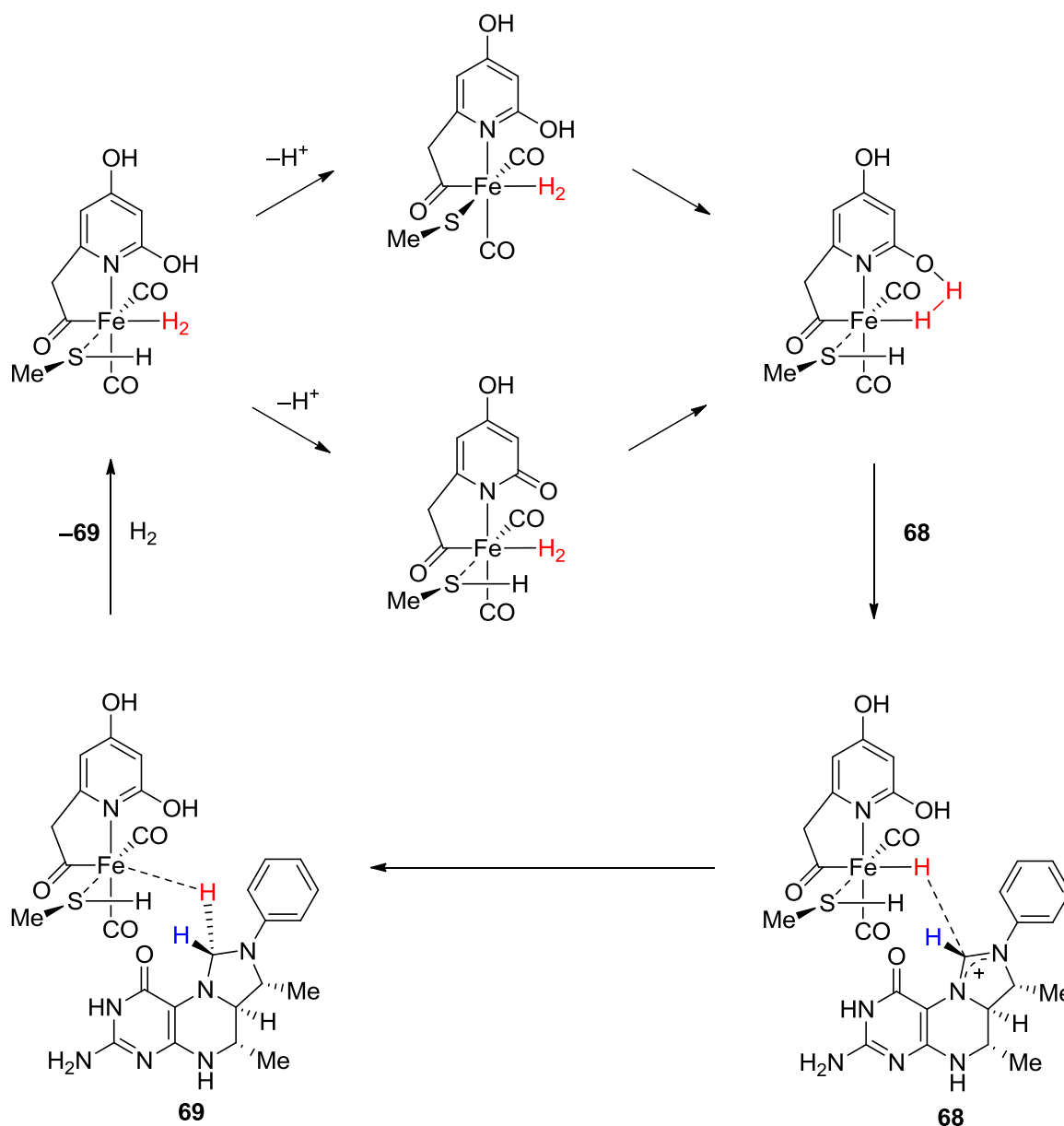
It is important when investigating the mechanism of the [Fe]-hydrogenase to consider both the chemistry taking place and the role the enzyme protein structure has to play on the reactivity. The [Fe]-hydrogenase enzyme is a homodimeric protein made up of two peripheral and one central globular unit and can exist in an open and closed state.<sup>137</sup> Shima and co-workers crystallised a mutant enzyme in the presence of DTT (dithiothreitol) and the substrate.<sup>237</sup> The structure showed the enzyme in the open state with an essentially planar substrate molecule. They postulate that when the enzyme is in the catalytically active state the closure of the cleft forces conformational change in the substrate leading to side on H<sub>2</sub> binding and catalytic turnover (Scheme 32).



**Scheme 32** Postulated reaction mechanism for the [Fe]-hydrogenase.<sup>41</sup> The circles represent the enzyme scaffold, with the “open” conformer in blue and the “closed” conformer in pink.<sup>237</sup>

This mechanism is in good agreement with previous mechanistic data for the [Fe]-hydrogenase and shows how the Fe centre and the pyridone cofactor may be involved in dihydrogen activation. The role of the pyridone cofactor was further probed by DFT studies by Yang and Hall who looked into the roles of model metal complexes and substrates in dihydrogen cleavage.<sup>238, 239</sup> There is a two-step mechanism in which dihydrogen binding

takes place in the absence of substrate and then the substrate must bind in order for hydrogen cleavage to occur. The role of the hydroxyl on the pyridone appears important as hydrogen bonding is implicated in the activation step.



**Scheme 33** Mechanism proposed by Yang and Hall involving two possible activation pathways.<sup>239</sup> In the DFT simulation, the substrate and product were approximated by the phenyl-containing molecules shown (**68** and **69**, respectively).

A DFT study by Dey found that, in agreement with Yang and Hall, dihydrogen coordination in the absence of the substrate is energetically unfavourable.<sup>240</sup> Dey studied the role of the ligand system around the Fe centre in [Fe]-hydrogenase in binding small molecules. He found that the pyridinol-acyl ligand allows the Fe centre to behave as a Lewis acid, by delocalizing charge from the metal centre on binding an anionic ligand such as  $H^-$ .

Reiher and co-workers recently conducted a quantum mechanics/molecular mechanics (QM/MM) study on the mechanism of [Fe]-hydrogenase.<sup>241</sup> They showed that the hydroxyl group of the pyridinol can be easily deprotonated to oxypyridine. This group is close to the Fe centre and functions as an ideal Lewis base whilst the carbocationic substrate, methenyl- $H_4MPT^+$  acts as an ideal Lewis acid. Both species are ionic and subject  $H_2$  bound to the metal centre to a Lewis pair electronic push-pull effect. The spatial arrangement of bound dihydrogen in the closed conformation of the enzyme is such that the  $H_2$  lies between the cationic centre of the substrate and the negatively charged pyridinol. This leads to exothermic heterolytic cleavage of dihydrogen without any redox chemistry at the metal centre. The intermediate where  $H_2$  is bound to the Fe centre is not thought to be long lived as the energy barrier for cleavage is small (only around  $1 \text{ kcal mol}^{-1}$ ). The mechanism of activation of dihydrogen described by Reiher and co-workers is reminiscent of activation by frustrated Lewis pairs, indeed a recent study discussed the synthesis of a functional [Fe]-hydrogenase model based on the frustrated Lewis pair concept.<sup>204</sup> The proton of pyridinol is thought to be taken up by the His14 residue of the enzyme in order to form the Lewis base oxypyridine. The implied crucial role of this residue is supported by the observation that the enzyme loses 99 % of its activity upon His14 mutation.<sup>241</sup>

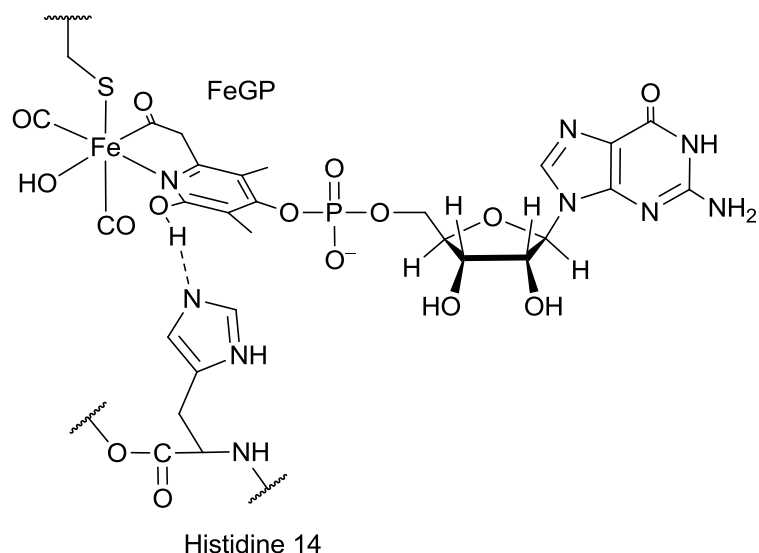
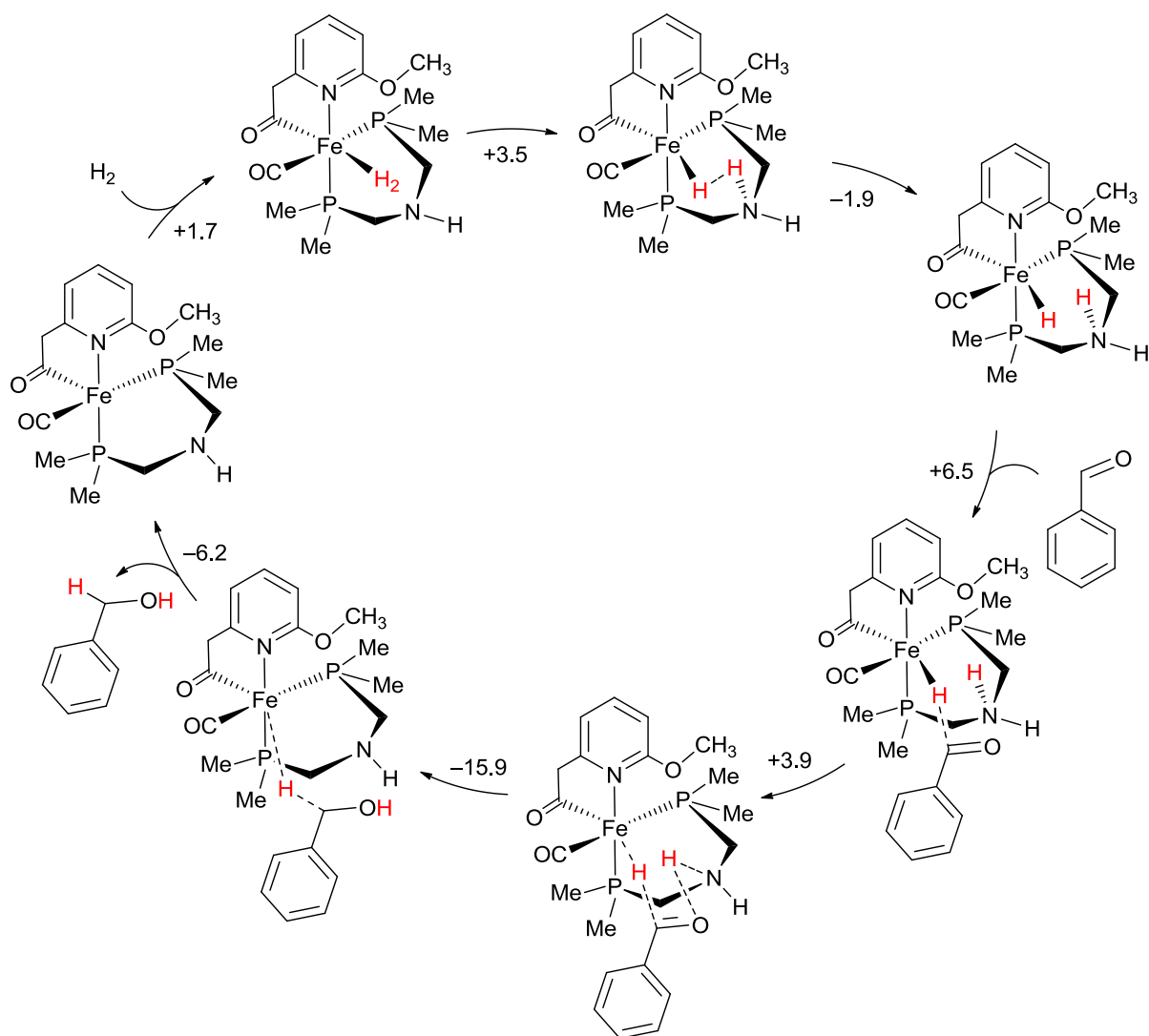


**Figure 42** Suggested role of His14: interaction with proton on pyridinol.<sup>241</sup>

Very recent work by Murray et al. reveals further computational insight. In this study they too modelled [Fe]-hydrogenase active site mimics using DFT focusing not on close structural models but rather the systematic study of the replacement of biological ligands with synthetic counterparts potentially producing models that can activate dihydrogen in the absence of the biological environment. In this way, it was hoped to predict attractive synthetic targets which may have catalytic activity comparable to [Fe]-hydrogenase. A mimic featuring a chelating diphosphine with an internal nitrogen base was discovered to have a particularly promising energetic profile with regards to hydrogen activation. This model was then studied in closer detail looking at the role of the proton/hydride acceptors in this complex in a catalytic cycle where hydrogen is split heterolytically. It was revealed computationally that an experimentally accessible energetic pathway involving a benzaldehyde proton/hydride acceptor was possible and that the complex studied could be a potential catalyst. Scheme 34 shows the catalytic cycle proposed by Murray et al.



**Scheme 34** Catalytic cycle of a biomimetic of [Fe]-hydrogenase proposed by a computational study with an aldehyde acceptor substrate. Free energies computed at the B3LYP-dDsC/TZ2P//M06/def2-SVP level in implicit THF solvent (COSMO-RS) and are given in kcal mol<sup>-1</sup>.

This study is an interesting approach to discovering potentially catalytically active [Fe]-hydrogenase mimics. The catalytic cycle in Scheme 34 shows that the splitting of hydrogen by this model complex may be energetically possible, but it requires redox chemistry to take place as the Fe centre of the complex changes oxidation state from Fe(II) to Fe(I) during the cycle. It also involves the Fe centre of the [Fe]-hydrogenase mimic acting as an acceptor for

hydride, this has previously been suggested. Electrochemical studies of a comparable complex **56a** a trimethylphosphine coordinated [Fe]-hydrogenase mimic showed that it carried out irreversible oxidation at +1.26 V. It remains to be experimentally determined that the simulated complex in Scheme 34 will be able to carry out the reversible redox chemistry required for the catalytic mechanism proposed. Significantly there is currently no evidence for the formation of a discrete dihydrogen complex in the natural system or in any structural mimic.

Evidence surrounding the mechanism of the inner workings of the [Fe]-hydrogenase is on its way to forming a full picture. It is clear that both the enzyme and the organic substrate have to be present for the heterolytic cleavage of dihydrogen to take place and that the role of the hydroxyl group in the second coordination sphere of the active site is important. However the role of the Fe centre in the catalytic cycle is not yet completely understood. There are several open questions, for example what intermediates are formed in the catalytic cycle? Does the iron function only to coordinate to dihydrogen or are there Fe–H intermediates in the catalytic cycle? There is great scope for future work and the next section discusses the objectives of the work in this thesis on active site models of the [Fe]-hydrogenase.

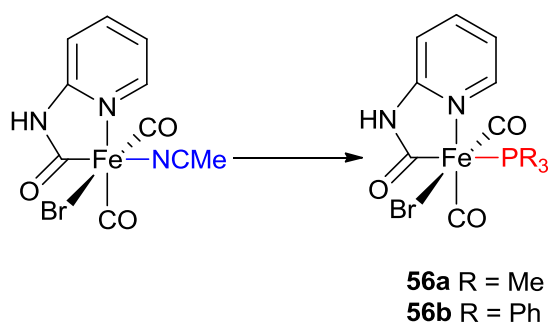
### **3.1.4 Objectives of this work**

Existing model complexes of the enzyme active site have provided some insight into both the fundamental coordination chemistry and the inner workings of the [Fe]-hydrogenase. Three key aspects of the chemistry of [Fe]-hydrogenases were addressed in this study, 1) stabilization of the coordination sphere by replacing the solvent molecule at a synthetic site by a tightly binding tertiary phosphine. 2) At the start of this work no pyridinol structures were known in which an OH group was juxtaposed to an Fe centre in the 2-position, strategies for introduction of this moiety at an Fe<sup>II</sup> core were investigated. However, during

the course of this work Hu et al. in a seminal study showed that a pyridinol functionality could be introduced by a protection/deprotection strategy<sup>203</sup> and further work in our laboratory was curtailed. 3) The catalysis by the natural system implicates a possible role for a mono hydride as a transient intermediate during turnover (Scheme 33).<sup>239</sup> The synthesis of ferracyclic systems possessing an Fe–H moiety were explored.

### 3.2 Modification of the Fe-coordination sphere with donor ligands

The parent ferricyclic carbamoyl **51**, which was the starting model for coordination sphere modifications, was synthesised following literature procedures.<sup>227</sup> In **51** the Fe centre is ligated by a pyridine carbamoyl, *cis* carbonyls, an abiological bromide and a potentially labile solvent (MeCN) ligand. The idea behind this work was to investigate if the labile solvent can be replaced by more tightly bonding ligands such as tertiary phosphines and to explore the effect on the structural and spectroscopic properties.



**Scheme 35** Substitution of solvent ligand of parent ferricyclic carbamoyl complex with tertiary phosphines.

Slow addition of a dilute solution of  $\text{PMe}_3$  to **51** in THF enabled the isolation of **56a** as red-orange crystals. X-ray crystallography established that the ligating solvent is replaced by the phosphine ligand as in Figure 43.

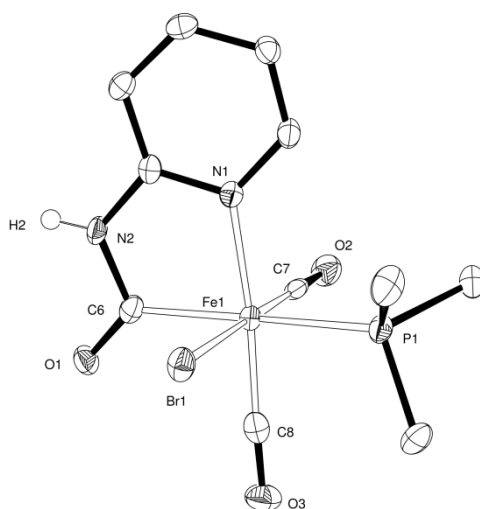


**Figure 43** ORTEP representation of the crystal structure of **56a** showing 50 % probability ellipsoids; hydrogen atoms except for H(2) have been omitted for clarity.

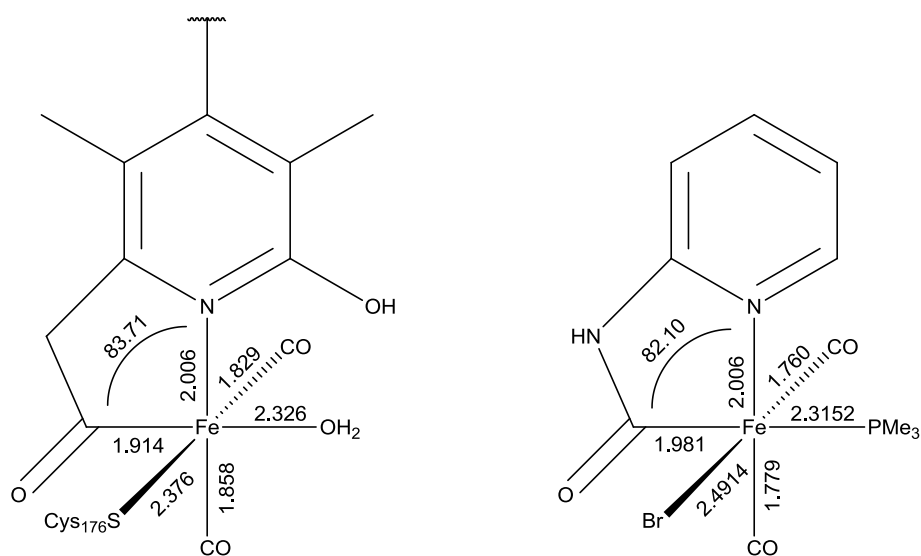


**Figure 44** Metrical data for the wild-type enzyme of *M. jannaschii* reconstituted with FeGP-cofactor (left)<sup>15</sup> and complex **56a** (right): distances in Å, angles in °, standard uncertainties have been omitted for clarity but are summarised in Table 2. Figure adapted from ref 16.

The structure of **56a** is compared to the active site of [Fe]-hydrogenase in Figure 44. The bond lengths of the Fe-ferracycle are similar with the Fe-CO bond lengths around 0.1 Å

shorter in the model compared to the natural system. However, the bond angles within the ferracycle are very similar in both the synthetic and natural case.

Compared to complex **51**, the crystallographic structure showed that carbamoyl ligand in **56a** is ‘twisted’ such that the pyridine ring does not lie directly above the Fe–P bond, reducing steric clash between the phosphine and pyridine groups. In **51** the torsion angle  $Y^\circ$  (as illustrated in Figure 45) is  $5.31^\circ$  in **56a** this angle is four times greater  $20.9^\circ$ .

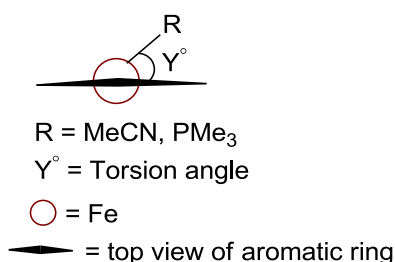


**Figure 45** A Newman-style projection looking through the top of the molecule illustrating the torsion angle between the pyridine ring and the bond Fe–X.

In THF solution, the IR spectrum of **56a** shows peaks at  $1967$  and  $2035\text{ cm}^{-1}$ , absorptions which are shifted to lower wavenumbers with respect to the parent complex and indicative of better electron-donating ability of the  $\text{PMe}_3$  ligand compared with MeCN at the Fe(II) centre see Table 1. The reaction of **51** in THF with one equivalent of  $\text{PPh}_3$  gave a mixture of mono- and di-substituted compounds. Carrying out and working up the reaction under an atmosphere of CO allowed isolation of **56b**, which exhibits solution IR stretches at  $2040\text{ cm}^{-1}$  and  $1990\text{ cm}^{-1}$  in the carbonyl region. Compound **56b** gave satisfactory elemental analysis to support formulation as the monophosphine  $\text{Fe}(\text{CO})_2(\text{PPh}_3)(\text{Br})(\text{C}_6\text{H}_5\text{N}_2\text{CO})$ . The di-substituted complex  $\text{Fe}(\text{CO})(\text{PPh}_3)_2(\text{Br})(\text{C}_6\text{H}_5\text{N}_2\text{CO})\cdot\text{THF}$  was isolated as a minor product which was characterised by crystallography.

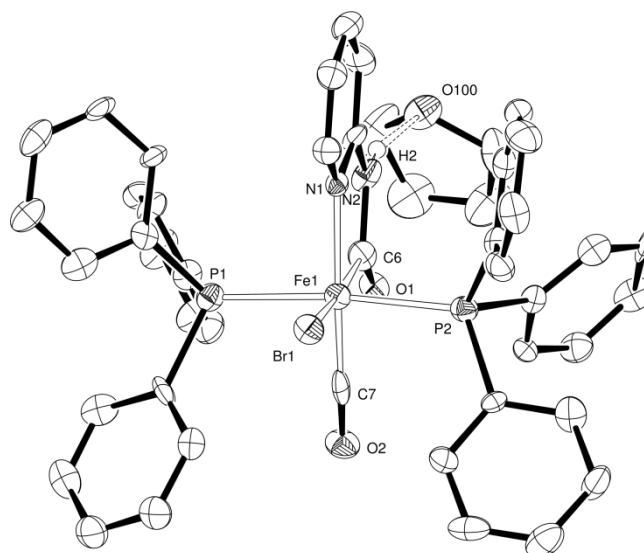
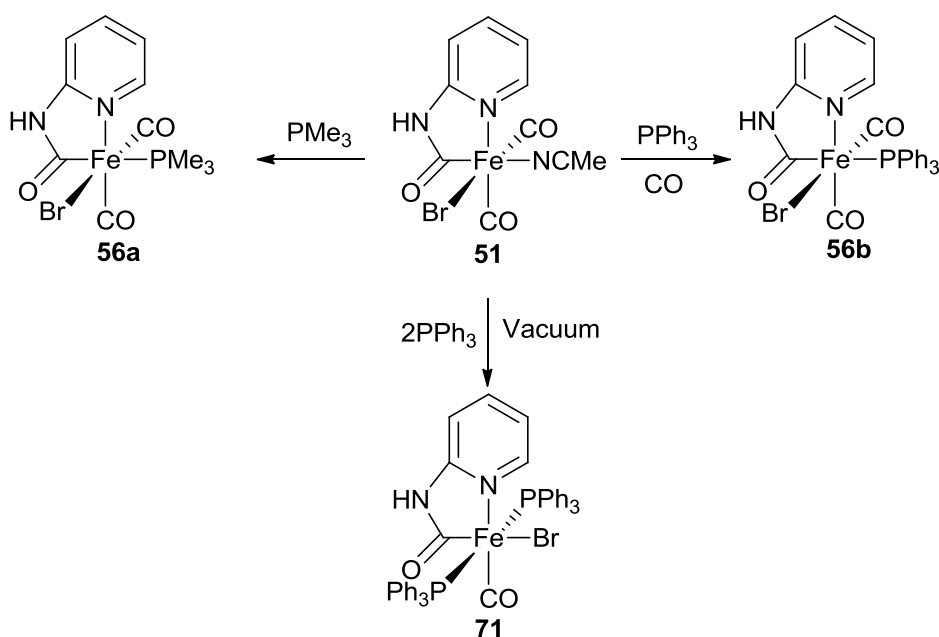


**Figure 46** ORTEP representation of the of the crystal structure of  $\text{FeBr}(\text{C}_6\text{H}_5\text{N}_2\text{O})(\text{CO})(\text{PPh}_3)_2 \cdot \text{THF}$  (**71**) showing 50 % probability ellipsoids; hydrogen atoms except for H(2) have been omitted for clarity.

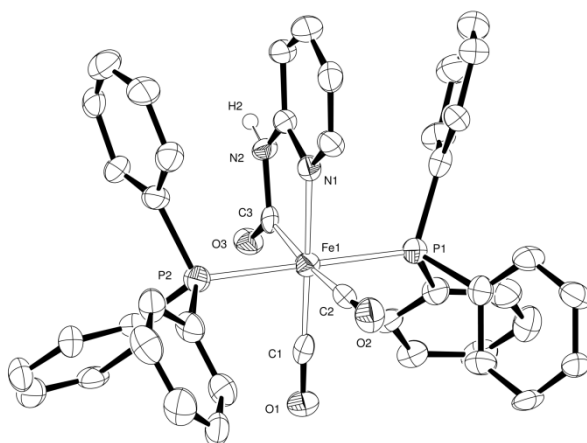
This bis-substituted phosphine has a CO stretch at  $1936 \text{ cm}^{-1}$ . A similar stretch ( $1934 \text{ cm}^{-1}$ ) can be seen in the solution IR spectrum of the reaction of complex **51** with  $\text{PMe}_3$  in THF: this band is absent in a spectrum of isolated crystals of **56a** in THF before recrystallisation. In a reaction of **51** with  $\text{PPh}_3$  the mono substituted product is favoured when the solution is concentrated by sparging with CO gas. The bis-phosphine product is favoured by putting the reaction under dynamic vacuum, thus encouraging substitution of CO for  $\text{PPh}_3$ .



**Scheme 36** Summary of synthetic routes to tertiary phosphine substituted [Fe]-hydrogenase models **56a** and **56b** and related bis-substituted compound **71**.

It has been shown that a CO in addition to a MeCN ligand in **51** can be replaced by PPh<sub>3</sub> to give **71** and that this complex gives rise to a single band at 1936 cm<sup>-1</sup>. The IR spectrum of crude **56a** possesses a comparable CO band at 1934 cm<sup>-1</sup> indicative of the formation of a di-substituted product.

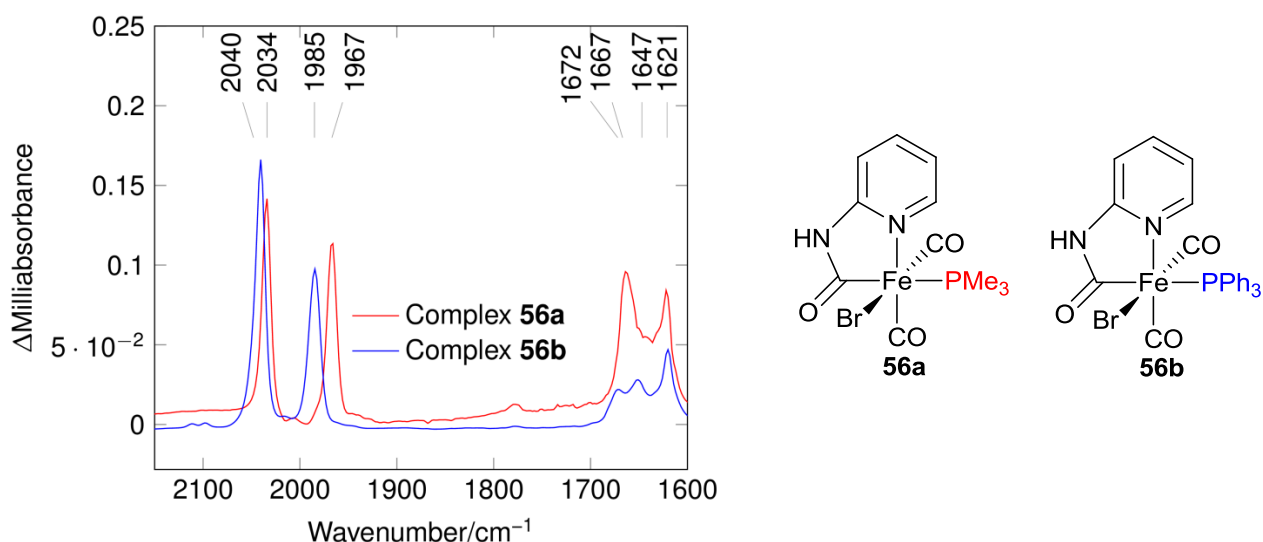
Attempts to crystallise the mono PPh<sub>3</sub> substituted complex **56b** were unsuccessful however, in one case in the work up of the reaction of **51** with PPh<sub>3</sub> in layered THF/CH<sub>2</sub>Cl<sub>2</sub>, a minor product was isolated. In this species Br<sup>-</sup> and MeCN had been displaced by PPh<sub>3</sub> and a cationic product with retained *cis* carbonyls was formed as shown in Figure 47.



**Figure 47** ORTEP representation of the cation of  $[\text{Fe}(\text{C}_6\text{H}_5\text{N}_2\text{O})(\text{PPh}_3)_2(\text{CO})_2]_2^{2+}$  **(70)** showing 50 % probability ellipsoids; hydrogen atoms except for H(2) have been omitted for clarity.

This species is evidently formed by decomposition during workup because the counter anion  $[(\text{Br}_3\text{Fe})_2\text{O}]^-$  must originate from extensive oxidative decomposition.

Figure 48 compares the IR spectrum of **56a** and **56b** in THF, it can be seen that the relative intensities of the carbonyl bands are similar, characteristic of these closely related compounds. The carbonyl bands of **56a** are shifted to lower wavenumber relative to **56b** consistent with  $\text{PMe}_3$  being a more electron donating ligand than  $\text{PPh}_3$ .



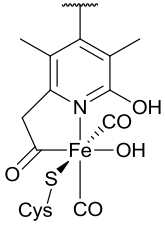
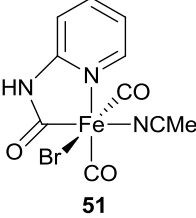
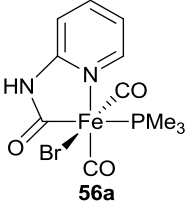
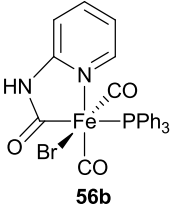
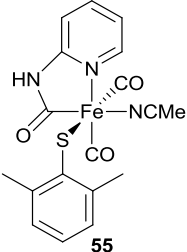
**Figure 48** Comparison of the IR spectra of complexes **56a** and **56b** in THF illustrating the effect of different tertiary phosphines on the carbonyl and carbamoyl amide stretching frequencies and intensities.

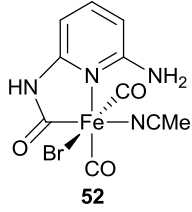
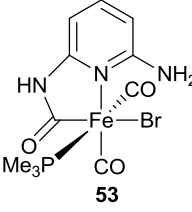
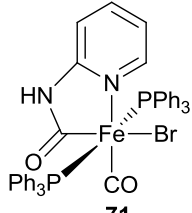
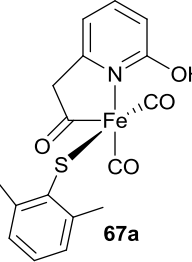
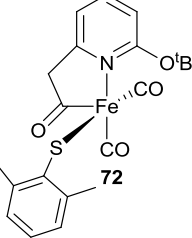
Table 1 summarises the IR data for the family of [Fe]-hydrogenase models synthesised in this work together with previously reported data. In the formation of **56a** and **56b** it can be seen that the carbonyl bands change in number and wavenumber whilst the wavenumber of the amide bands remain relatively unchanged at around 1670 and 1620  $\text{cm}^{-1}$  relative to the parent complex **51**. In both cases the CO bands shift to lower wavenumber relative to the parent complex **51** indicative of the association of a more electron donating ligand (MeCN vs phosphine). It is noteworthy that the larger number of carbonyl bands than expected seen in the solution IR of **51** are due to the exchange of the labile MeCN forming isomers in solution. From the IR spectroscopic data it could be argued that introduction of a tertiary phosphine (a less labile and more bulky ligand than MeCN) reduces this exchange. This is why we see fewer carbonyl bands for **56a** and **56b** than in **51**. In the bis- $\text{PPh}_3$  substituted model **71** only one carbonyl band is seen indicative of substitution of one of the two carbonyls in the parent complex for  $\text{PPh}_3$ .

When comparing IR data from the model compounds in Table 1 with reported IR data from the natural system it can be seen that the infrared stretching frequencies of the carbonyl bands of the  $\text{PMe}_3$  substituted complex **56a** highly concordant (2031 and 1972  $\text{cm}^{-1}$  vs 2034 and 1967  $\text{cm}^{-1}$ ). This indicates that in this model, though an abiological tertiary phosphine has been incorporated the electronic environment at the Fe(II) centre is likely to be similar to that in the natural system. The CO stretching frequencies of **56b** and the natural system are not in such close agreement. A previously synthesised model by the Pickett group such as the thiolate substituted complex **55** mimic the active site structurally as well as electronically. The incorporation of the thiolate ligand models the cysteine ligation of the natural system while the CO stretching frequencies (Natural system: 2031, 1972  $\text{cm}^{-1}$  vs **55**: 2052, 2032, 1971  $\text{cm}^{-1}$ ) are very close with exclusion of the band at 2052  $\text{cm}^{-1}$  which may be due to an isomer of **55**. Other models by the Pickett group such as the pendant amine containing complex **52** model the second coordination sphere of the natural system but this does not lead to IR spectroscopic data in closer agreement to the models discussed above. The Hu group have reported the models **67a** and **72** that model both the sulfur ligation and the pendant oxygen of the natural system. However, the IR spectroscopic data are for these complexes are not in good agreement with the natural system (see below).

**Table 1** Summary of IR stretching frequencies in of [Fe]-hydrogenase active site models.

Synthetic complexes measured in THF except **67a** and **72** (Hu group) which were measured in MeCN and the natural system, measured in water.

Complex	CO stretch/ $\text{cm}^{-1}$	Carbamoyl amide stretches I and II/ $\text{cm}^{-1}$	Amine bend/ $\text{cm}^{-1}$	Reference
 Natural system	2031, 1972	N/A	N/A	137
 <b>51</b>	2048, 1993, 1967	1667, 1621	N/A	227
 <b>56a</b>	2034, 1967	1667, 1621	N/A	16
 <b>56b</b>	2040, 1985	1672, 1647, 1620	N/A	16
 <b>55</b>	2052, 2032, 1971	1620	N/A	227

 <p><b>52</b></p>	2044, 1984, 1973	1670, 1621	1649	16
 <p><b>53</b></p>	2038, 1984	1670, 1624	1650	16
 <p><b>71</b></p>	1936	1670, 1619	N/A	16
 <p><b>67a</b></p>	2011, 1944	N/A	N/A	203
 <p><b>72</b></p>	2013, 1948	N/A	N/A	203

A discussion of the effect of changes in the coordination sphere on the infrared spectra of compounds in the family of ferracyclic carbamoyl model complexes by the Pickett group is pertinent to the complete analysis of this work. The IR spectra in THF of the previously reported<sup>16,227</sup> complexes by the Pickett group **51** and complex **52** are compared in Figure 49. Incorporation of a pendant amine functionality shifts the carbamoyl bands very slightly to lower wavenumber. The intensity of the carbamoyl bands in **52** is much greater than in **51**

this could possibly be due to a by-product in the reaction mixture where two ferracycles have been formed. Interestingly the IR spectrum of the comparable species **53** which features a pendant amine and a  $\text{PMe}_3$  moiety does not have such an intense carbamoyl amide band as seen in **52**.

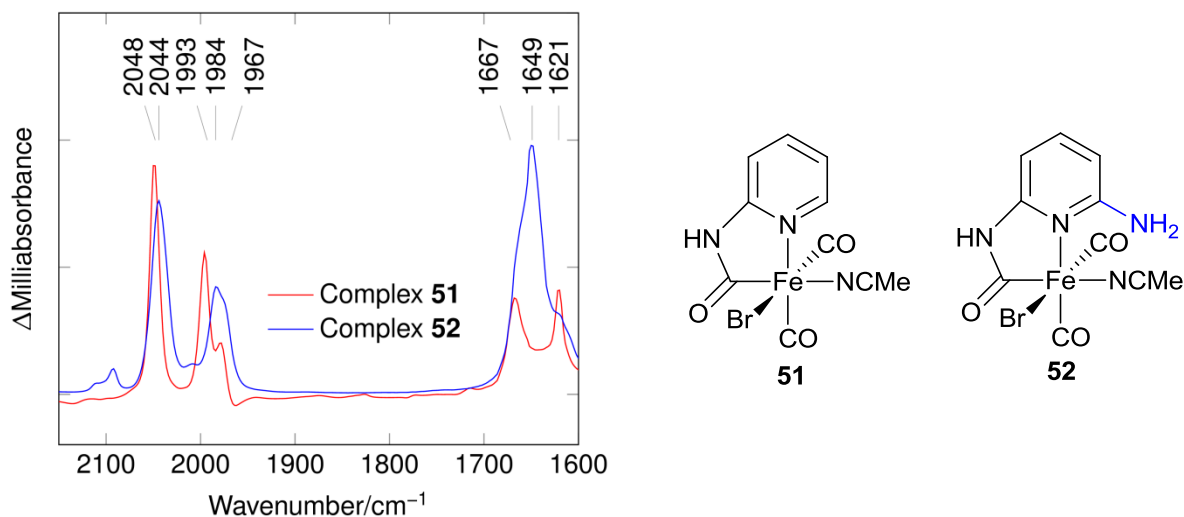


**Figure 49** Comparison of the IR spectra of complex **51** and **52** in THF illustrating the effect of incorporation of a pendant amine functionality on the carbonyl and carbamoyl amide stretching frequencies and intensities.

The IR spectra in THF of complex **53** and complex **56a** are compared in Figure 50. The carbonyl bands are similar in wavenumber and intensity (closely related compounds).

In the amide region there are two principle bands around 1667 ( $\text{CO}$  stretch) and  $1621\text{ cm}^{-1}$  ( $\text{NH}$  bend). In the spectra of **52** and **53** an additional band is seen at around  $1650\text{ cm}^{-1}$  corresponding to the  $\text{NH}$  bend of the pendant amine.

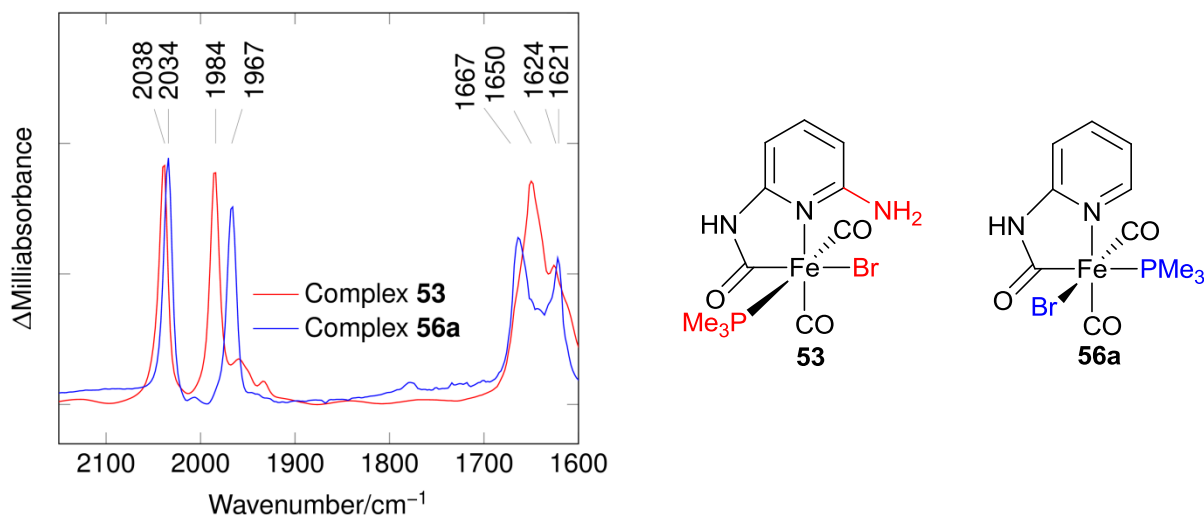


**Figure 50** Comparison of the IR spectra of complex **53** and **56a** in THF illustrating the effect of incorporation of a pendant amine functionality on the carbonyl and carbamoyl amide stretching frequencies and intensities of a  $\text{PMe}_3$  substituted  $[\text{Fe}]$ -hydrogenase model.

Table 2 summarises the bond lengths and angles for the family of  $[\text{Fe}]$ -hydrogenase models synthesised in this work and in earlier work by Pickett and Hu and compares them to the values for the natural system. Figure 51 illustrates the atom labelling scheme in support of Table 2.

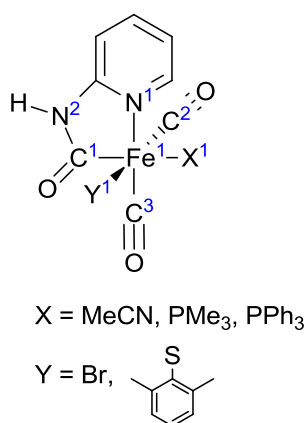


**Figure 51** Numbering scheme for  $[\text{Fe}]$ -hydrogenase crystallographic data in support of Table 2. Atom labels are highlighted in blue.

**Table 2** Summary of bond lengths and angles of a family of [Fe]-hydrogenase models compared to the natural system. Data for [Fe]-hydrogenase from EXAFS study.

Complex	Bond length/ Å				
	Fe(1)–N(1)	Fe(1)–C(1)	Fe(1)–C(2)	Fe(1)–C(3)	Fe(1)–Y
[Fe]-hydrogenase	2.006	1.914	1.829	1.858	2.376
<b>51</b>	1.992(2)	1.931(2)	1.811(3)	1.782(3)	2.4632(5)
<b>56a</b>	2.006(3)	1.981(3)	1.760(4)	1.779(4)	2.4914(6)
<b>55</b>	2.0000(17)	1.9390(19)	1.766(2)	1.776(2)	2.3845(6)
<b>53</b>	2.077(8)	1.917(11)	1.826(14)	1.789(13)	2.5488(18)
<b>71</b>	2.038(8)	1.927(10)	1.759(12)	N/A	2.5605(19)
<b>72</b>	1.953(9)	1.827(13)	1.761(15)	1.773(13)	2.219(4)

Complex	Bond angle/ °	
	N(1)–Fe(1)–C(1)	C(2)–Fe(1)–C(3)
[Fe]-hydrogenase	83.71	93
<b>51</b>	82.68(9)	92.35(11)
<b>56a</b>	82.10(13)	90.19(16)
<b>55</b>	82.54(8)	90.64(10)
<b>53</b>	82.5(4)	92.8(5)
<b>71</b>	82.2(6)	N/A
<b>72</b>	86.3(5)	90.8(6)

### 3.2.1 Electrochemistry

As discussed in the introduction section 1.1.2 [Fe]-hydrogenase has been shown to be redox inactive in the accessible physiological domain, which is circa  $-1$  to  $+1$  V at pH 7 vs a standard hydrogen electrode (redox window of water at pH 7).<sup>16</sup> It might be expected that these synthetic Fe(II) species might exhibit an Fe(III)/ Fe(II) redox couple. To examine this we have explored the redox chemistry of the  $\text{PMe}_3$  ferracyclic complex **56a** in which a labile solvent molecule has been replaced by a tertiary phosphine. Figure 52 shows a set of voltammograms for this complex recorded in MeCN 0.1 M  $[\text{NBu}_4][\text{BF}_4]$  at a vitreous carbon electrode.

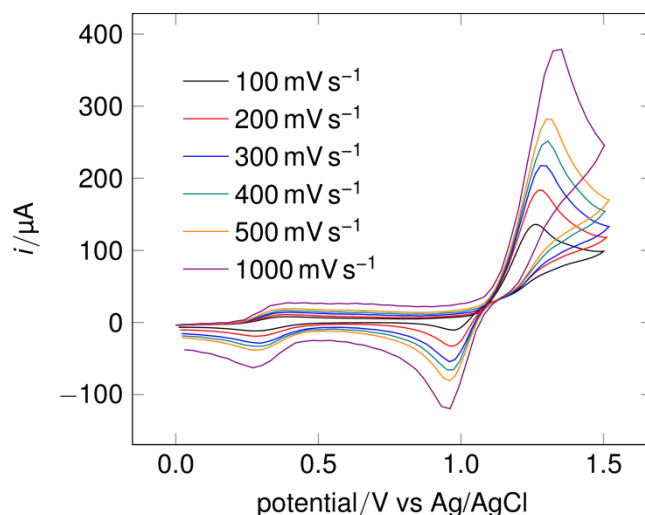


**Figure 52** A set of cyclic voltammograms illustrating the scan rate dependence of the oxidation processes of **56a**. Electrode: vitreous carbon; 0.1 M  $[\text{Bu}_4\text{N}][\text{BF}_4]$  – MeCN; RT;  $[\text{56a}] = 5$  mM.

A major oxidation process is observed with a peak potential at +1.27 V. A plot of the peak current vs the square root of the scan rate is linear indicative of a diffusion-controlled process.

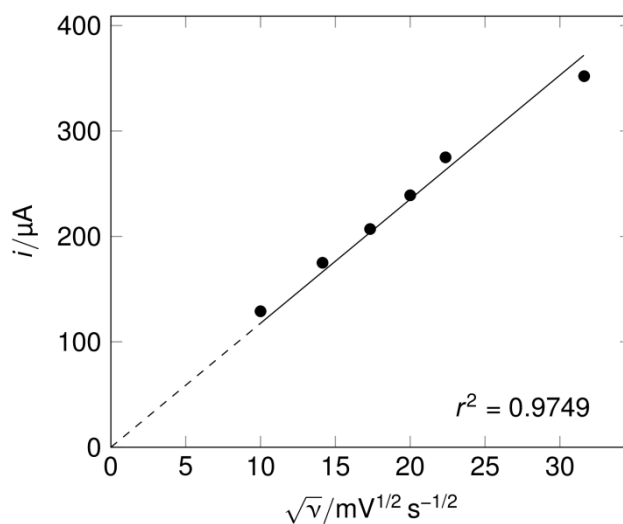
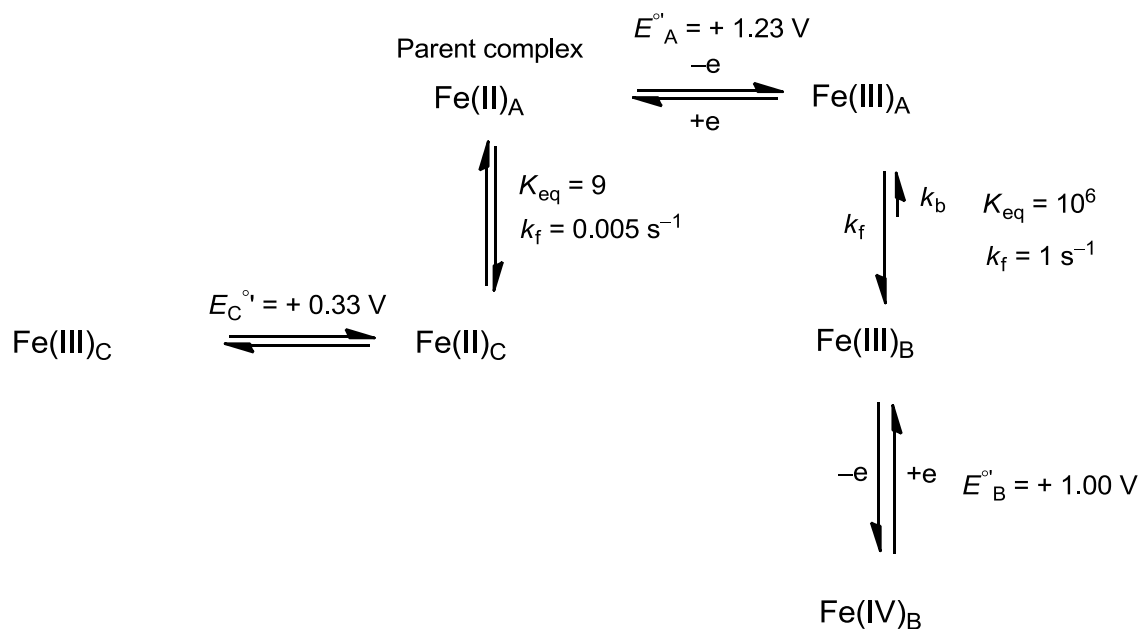


**Figure 53** Peak current of irreversible oxidation at +1.27 V of complex **56a** vs the square root of the scan rate. Electrode: vitreous carbon; 0.1 M  $[\text{Bu}_4\text{N}][\text{BF}_4]$  – MeCN; RT;  $[\text{Complex}] = 5$  mM.

However, the redox chemistry is evidently complex as at slow scan rates the voltammogram shows a cross-over process as can be seen in Figure 54 as marked with a \*. This can be modelled by the sequence of electron transfer steps shown in Scheme 37.



**Scheme 37** Sequence of electron transfer steps used to model the redox chemistry of **56a**.

$K_{\text{eq}}$  = equilibrium constant,  $k_f$  = forward rate constant.

The primary oxidation process is followed by a kinetically slow step which leads to the formation of a redox active product which oxidises at a potential negative of the primary step. The principle parameters used in the digital simulation of the experimental voltammogram based on this set of reactions are shown in Scheme 37 and Table 3. The experimental inputs together with the modelled rate constants and diffusion coefficients are given in Table 3.

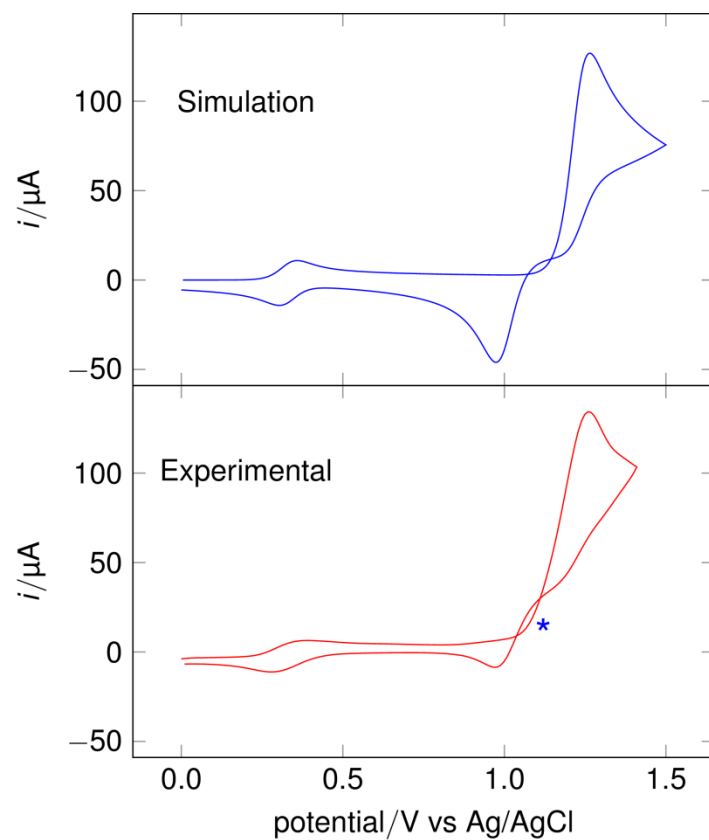


**Figure 54** Comparison of a computationally simulated cyclic voltammogram modelling the behaviour outlined in Scheme 37 with an experimentally derived cyclic voltammogram of **56a**. Electrode: vitreous carbon;  $100 \text{ mV s}^{-1}$ ;  $0.1 \text{ M } [\text{Bu}_4\text{N}][\text{BF}_4] - \text{MeCN}$ ; RT;  $[\text{56a}] = 5 \text{ mM}$ ,

**Table 3** Parameters used to simulate the cyclic voltammogram in Figure 54.  $E^0$  is the standard potential at which the charge transfer process occurs,  $\alpha$  is the electron transfer coefficient (a factor determining the effect of a change in potential on the activation energy of a reaction),  $k_s$  is the heterogenous rate constant (a measure of how fast electrons are crossing the electrode interface),  $D$  is the diffusion coefficient ( $1.30 \times 10^{-5}$  for each species),  $C_{\text{anal}}$  is the amount of analyte added to the system,  $C_{\text{init}}$  is the amount present once initial equilibrium is achieved.

Charge-Transfer Reaction	$E^0 / \text{V}$	$\alpha$	$k_s / \text{cm s}^{-1}$
$\text{Fe(IV)}_{\text{B}} + \text{e}^- = \text{Fe(III)}_{\text{B}}$	1.00	0.50	10000
$\text{Fe(III)}_{\text{A}} + \text{e}^- = \text{Fe(III)}_{\text{A}}$	1.23	0.50	10000
$\text{Fe(III)}_{\text{C}} + \text{e}^- = \text{Fe(II)}_{\text{C}}$	0.33	0.50	10000

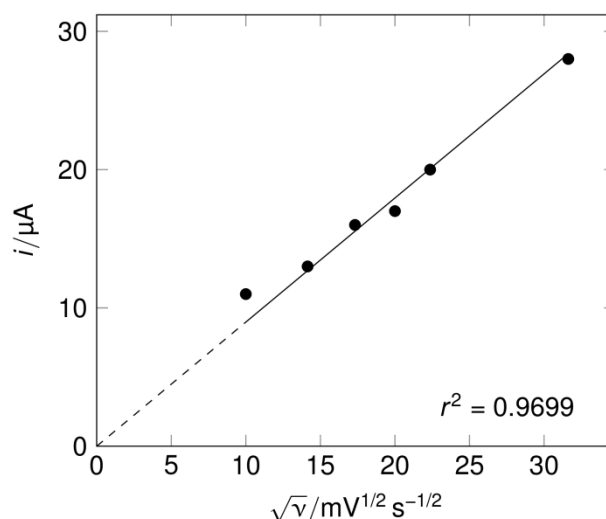
  

Chemical reaction	$K_{\text{eq}}$	$k_{\text{f}}$	$k_{\text{b}}$
$\text{Fe(III)}_{\text{A}} = \text{Fe(III)}_{\text{B}}$	$1.00 \times 10^6$	1.00	$1.00 \times 10^6$
$\text{Fe(II)}_{\text{C}} = \text{Fe(II)}_{\text{A}}$	9.00	$5.00 \times 10^{-3}$	$5.56 \times 10^{-4}$

Species	$C_{\text{anal}} / \text{mol L}^{-1}$	$C_{\text{init}} / \text{mol L}^{-1}$
$\text{Fe(III)}_{\text{A}}$	0	0
$\text{Fe(III)}_{\text{B}}$	0	0
$\text{Fe(IV)}_{\text{B}}$	0	0
$\text{Fe(II)}_{\text{A}}$	$5.00 \times 10^{-3}$	$4.56 \times 10^{-3}$
$\text{Fe(III)}_{\text{C}}$	0	0
$\text{Fe(II)}_{\text{C}}$	0	$5.00 \times 10^{-4}$

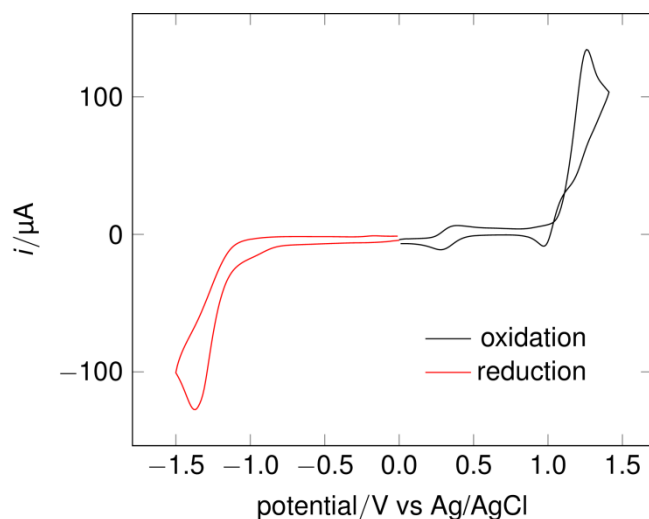
The small reversible process at +0.32 V in the cyclic voltammogram of **56a** as shown in Figure 52 has been modelled as a minor species in slow equilibrium with the major redox active component. A plot of the experimental peak current vs the square root of the scan rate is linear indicative of a diffusion-controlled process for this couple.



**Figure 55** Peak current of irreversible oxidation at +0.32 V of complex **56a** vs the square root of the scan rate. Electrode: vitreous carbon; 0.1 M  $[\text{Bu}_4\text{N}][\text{BF}_4]$  – MeCN; RT;  $[\text{Complex}] = 5 \text{ mM}$ .

It was suspected that the minor species might be associated with  $\text{Br}^-$  dissociating from the complex however the  $\text{Br}^-/\text{Br}^{3-}$  was not detected in the voltammogram and the potential for this couple was measured independently at +1.18 V.

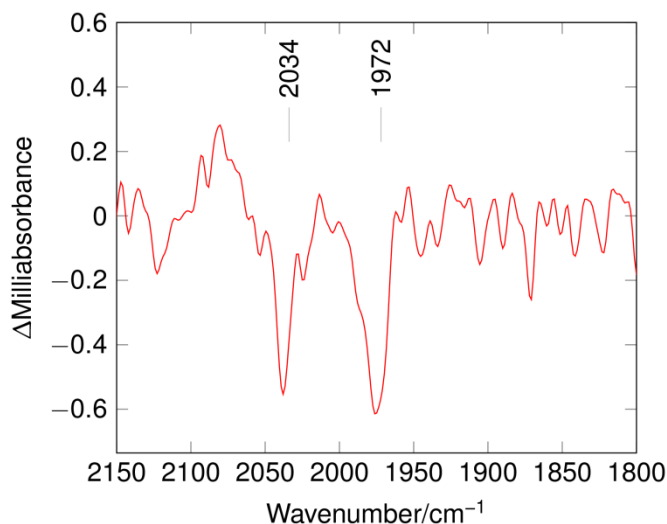
The reduction of **56a** was also briefly examined. It was found to undergo an irreversible reduction process close to  $-1.4 \text{ V}$ . An irreversible process is one in which the peak current of the forward wave is greater than that of the reverse wave. The magnitude of the peak current was similar to that of the oxidation when measured at the same scan rate as is consistent with an overall 1 electron reduction step. Using the same simulation parameters as for the oxidation, an irreversible 1 electron process would have a peak current of  $102 \mu\text{A}$ . The observed value of  $125 \mu\text{A}$  at  $100 \text{ mV s}^{-1}$  suggests a primary one-electron reduction followed by a slow chemical step and a second electron transfer, i.e. an ECE process.



**Figure 56** Cyclic voltammogram of the oxidation (black) and reduction (red) processes of **56a**. Electrode: vitreous carbon;  $100 \text{ mV s}^{-1}$ ;  $0.1 \text{ M } [\text{Bu}_4\text{N}][\text{BF}_4] - \text{MeCN}$ ; RT;  $[\text{Complex}] = 5 \text{ mM}$ .

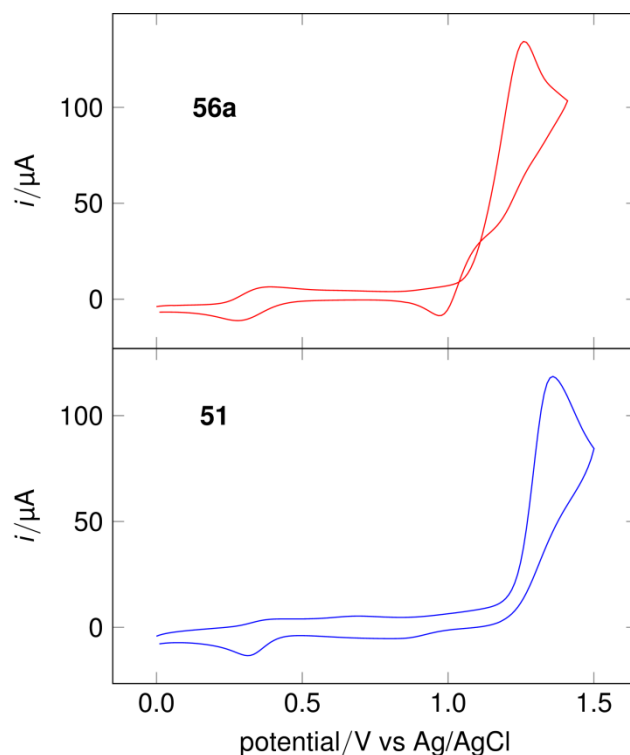
To further probe the **56a** system an FTIR spectroelectrochemical study was undertaken. Oxidation of the complex led to the rapid depletion of the carbonyl bands. The Spectral window used did not extend to the carbonyl region as a compromise had to be made between signal to noise ratio and the width of the window used to study **56a** spectroelectrochemically. The decision was made to focus on the carbonyl region to achieve clearer results. The spectral window used was determined by the inclusion of an optical filter in the path see experimental for details.

Figure 57 shows the depletion of the carbonyl bands associated with **56b** during the spectroelectrochemical experiment. No new carbonyl bands were observed, which is consistent with rapid loss of CO in the overall 2 electron oxidation of the complex on the 4 s time-scale of the experiment.



**Figure 57** Infrared spectroelectrochemistry of **56a** in the MeCN electrolyte, 0.1 M  $[\text{Bu}_4\text{N}][\text{BF}_4]$ ; RT;  $[\text{Complex}] = 5 \text{ mM}$ . Difference spectrum after 4 s.

These oxidation processes of **56a** at +1.26 and +0.32 V are comparable to those for the parent complex **51** (shown in Figure 58). Complex **51** exhibits similar oxidation behaviour seen giving an irreversible wave at +1.36 V and a reversible feature at + 0.33 V. The oxidation potentials for both oxidative features of the cyclic voltammogram of **51** are at more positive potential than **56a**. Indicating that **51** has a less electron rich iron centre. **51** exhibits irreversible reduction at  $-1.35 \text{ V}$  a more positive potential than the reduction process seen in **56a**.



**Figure 58** Cyclic voltammogram of the oxidation processes of **56a** (above) and **51** (below). Electrode: vitreous carbon;  $100 \text{ mV s}^{-1}$ ;  $0.1 \text{ M } [\text{Bu}_4\text{N}][\text{BF}_4] - \text{MeCN}$ ; RT;  $[\mathbf{56a}] = 5 \text{ mM}$ ,  $[\mathbf{51}] = 2.6 \text{ mM}$ .

A possible explanation for the observed feature in both the parent complex **51** and the  $\text{PMe}_3$  substituted analogue **56a** is as follows. The peak observed near  $+0.3 \text{ V}$  in the voltammograms of **51** and **56a** might be reasonably attributed to species resulting from CO loss and MeCN substitution as is suggested in Figure 59.

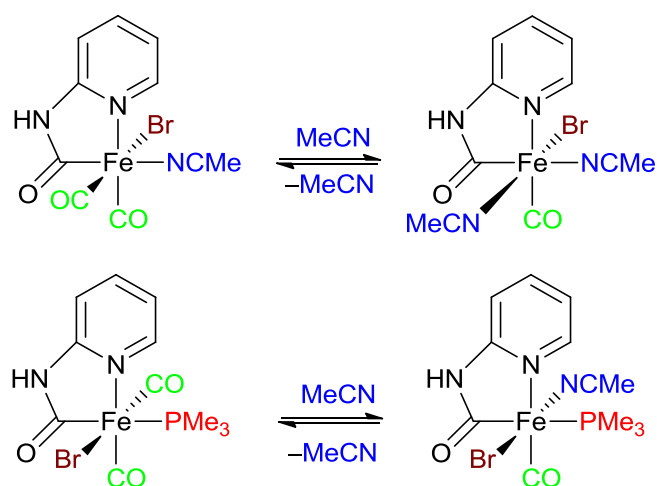


**Figure 59** Illustration of CO loss and MeCN substitution in **51** (above) and **56a** (below).

MeCN is a strong donor ligand and its replacement by CO would be expected to result in a substantial shift in oxidation potential to a more negative potential as is observed in the voltammograms. The forward peaks near +0.3 V are of smaller current magnitude than that of the back scan, particularly in **51**. This suggests that oxidation leads to CO loss and substitution of MeCN into the oxidation products of  $[\text{Fe}(\text{CO})(\text{MeCN})_2(\text{C}_5\text{H}_5\text{N}_2\text{CO})(\text{Br})]^{2+}$  and  $[\text{Fe}(\text{CO})(\text{MeCN})(\text{PMe}_3)(\text{C}_5\text{H}_5\text{N}_2\text{CO})(\text{Br})]^{2+}$  detected on the reverse scan.

In summary, the electrochemical oxidation studies show the *cis*-carbonyl ferracyclic species **56a** and **51** having very positive oxidation potentials as is consistent with the natural *cis*-carbonyl ferracyclic centre of [Fe]-hydrogenase being redox inactive in the physiological oxidation domain. That a minor reversible process is observed near 0.3 V versus Ag/AgCl for **56a**, together with a similar process for **51**, is in accord with the presence of a mono-carbonyl in which one CO has been replaced by solvent, MeCN.

### 3.3 Modification of the second coordination sphere

The role of the second coordination sphere pyridone group in the active site of [Fe]-hydrogenase has been discussed in section 3.1.3. Approaches to the introduction of an –OH functionality in the second coordination sphere of the synthetic ferracyclic carbamoyl [Fe]-hydrogenase models was therefore explored.

Based on the formation of **51** from  $\text{Fe}(\text{CO})_4\text{Br}_2$  and 2-aminopyridine attempts to introduce ligand **73a** were carried out in an analogous fashion. The ligand synthesis was adapted from Tisza and Joos<sup>242</sup> and afforded **73a** in good yield. It was determined by X-ray diffraction data that **73a** exists as the keto form **73a'** in the solid state as shown in Figure 60.

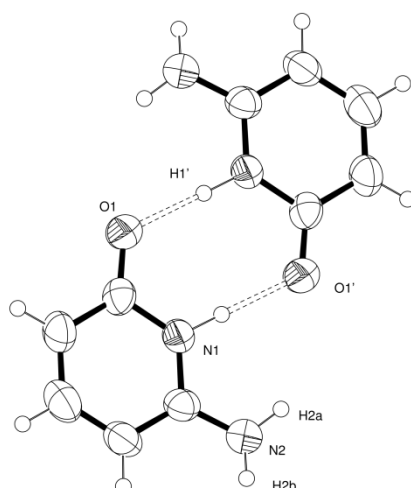


**Figure 60** ORTEP representation of the one of the two independent hydrogen-bonded dimers of the keto form of 2-hydroxy-6-aminopyridine (**73a'**) in the unit cell of  $2(\text{C}_5\text{H}_6\text{N}_2\text{O}) \cdot (\text{H}_2\text{O})$  showing 50 % probability ellipsoids. The two independent dimers of  $\text{C}_5\text{H}_6\text{N}_2\text{O}$  in the cell have similar metrical parameters.

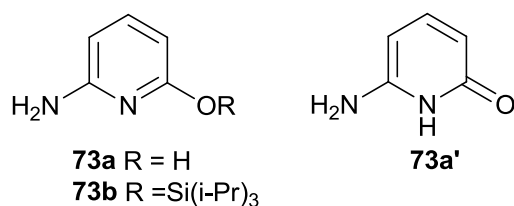


**Figure 61** Oxygen-functionalised aminopyridines

Reaction of **73a** with  $\text{Fe}(\text{CO})_4\text{Br}_2$  led to a very rapid reaction with significant effervescence; IR spectroscopy showed that all bound CO had been lost. Attempts were made to moderate the reaction by reducing temperature and concentration of the ligand. The reaction vessel was cooled to  $-20\text{ }^\circ\text{C}$  and dilute ligand was added drop-wise but this strategy was unsuccessful. The high reactivity of the ligand **73a** with  $\text{Fe}(\text{CO})_4\text{Br}_2$  and the rapid loss of carbonyl could be explained by the possible binding of the pendant oxygen to Fe displacing CO. It is possible that **73a** might form Fe complexes with multiple pyridine ligands and oxidised species such as  $[(\text{Br}_3\text{Fe})_2\text{O}]^-$  (previously demonstrated to be a by-product in the formation of the cationic species **70**, Figure 47), The bidentate tendency of 2-pyridones is a common feature of their chemistry with examples in the literature.<sup>243</sup> It is the likely cause of the loss of CO from the complex. Indeed in nature a probable role of the ferracyclic ring is to prevent coordination of the hydroxyl functionality to the iron i.e. preventing bidentate *N,O* coordination (Figure 62).

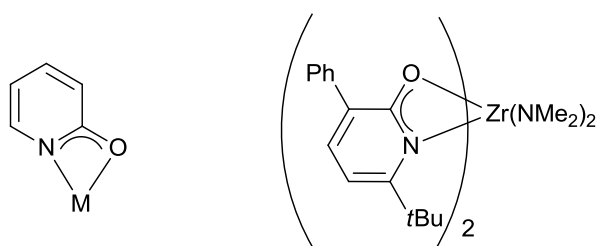
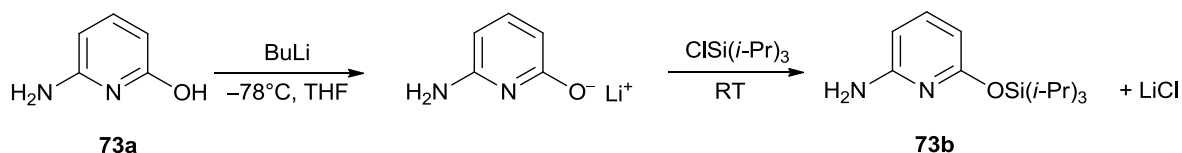


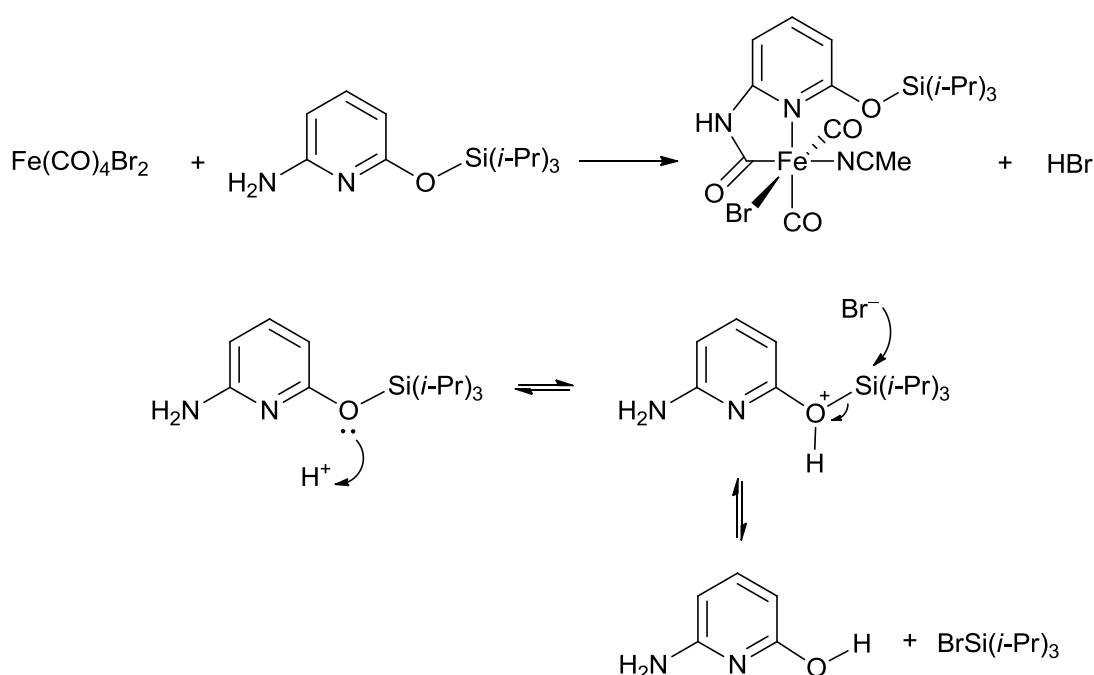
**Figure 62** Illustration of the common bidentate binding mode of 2-pyridones (left), example of this binding mode in an aminoalkene cyclohydroamination catalyst (right).<sup>243</sup>

In the light of this it was considered that protection of the –OH group prior to the introduction at the site might afford a route to the desired product. To this end, the silylated ligand **73b** was synthesised (Scheme 38).



**Scheme 38** Synthesis of silylated ligand **73b**.

The silylated ligand **73b** was then reacted with the  $\text{Fe}(\text{CO})_4\text{Br}_2$  precursor. Unfortunately this reaction gave similar results to that with **73a**: complete loss of carbonyl signals in the infrared. It is possible that HBr liberated in the formation of the carbamoyl is able to attack the silyl group, deprotecting in situ and thus leading to the same reactivity as seen in **73a**.



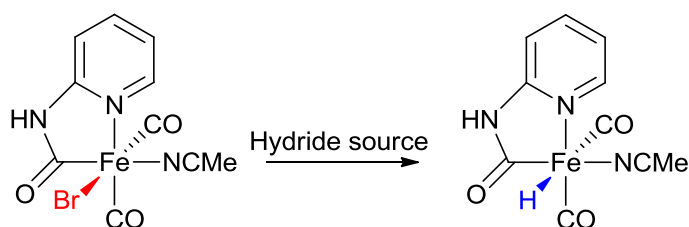
**Scheme 39** Possible deprotection mechanism in the reaction of  $\text{Fe}(\text{CO})_4\text{Br}_2$  with **73b**.

During the course of this work as noted in the introduction Hu and co-workers took a similar approach but protected the -OH function by forming a *t*-Bu ether. In their case formation of

acid is not a problem because they create an acyl ferracyclic ring rather than a carbamoyl, the formation of which releases HBr. Given the results obtained by Hu further work was not pursued.

### 3.4 Attempts to introduce a hydride ligand

As discussed previously and shown in Scheme 33 hydride species are plausible transient species in the natural system. Therefore effort was made to introduce hydride into the coordination sphere of **51** by replacing bromide represented in Scheme 40.



**Scheme 40** Proposed scheme for the introduction of hydride into a [Fe]-hydrogenase model.

Sources of hydride explored: NaBH<sub>3</sub>CN, NaBH<sub>4</sub>, LiAlH<sub>4</sub>, LiEt<sub>3</sub>BH.

The first attempt to do this was done by reacting **51** with a mild hydride donor NaBH<sub>3</sub>CN: this led to no observable reaction over the course of two days at 40 °C. The decision was made not to elevate the temperature further due to possible decomposition of the complex. A stronger hydride donor, NaBH<sub>4</sub> was then selected. The reaction of this hydride with **51** led to a colour change (gold-orange solution to red-brown) and IR spectral changes indicating the possible formation of multiple species, but ultimately depletion of the CO carbamoyl and the amide signal in the IR as shown in Figure 63. No isolable products were obtained.

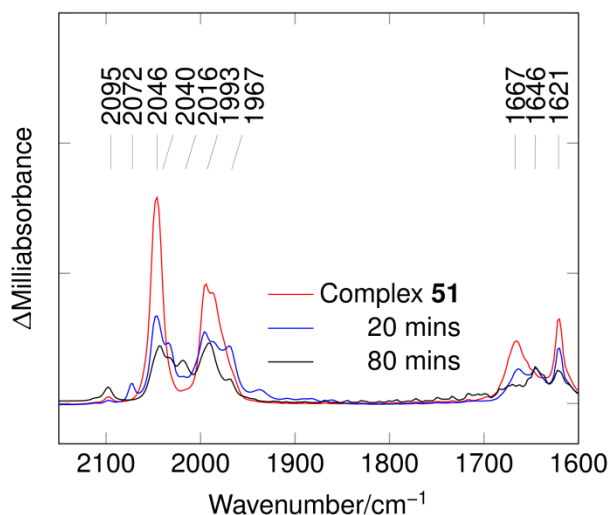


**Figure 63** Reaction of **51** with NaBH<sub>4</sub> in MeCN followed over time.

Following the lack of success with NaBH<sub>4</sub> a different source of hydride, LiAlH<sub>4</sub>, was then used. LiAlH<sub>4</sub> is a very powerful hydride transfer reagent. It was thought that if H<sup>-</sup> could be introduced rapidly then perhaps a stable product could be trapped. A somewhat cleaner spectrum was observed without significant loss of relative intensity of the CO and amide bands (shown in Figure 64). Attempts were made to crystallise this species however, it appeared to decompose (colour change from red-brown to green) over the course of a few hours before any products could be isolated by crystallisation.

It would be expected that replacing Br<sup>-</sup> by H<sup>-</sup> would lead to a shift to slightly (electronic effects on Fe likely to be similar) lower wavenumber but retention of the essential band pattern. The observed IR spectrum shows some unreacted parent material and a pattern of new bands similar to the parent but shifted to lower frequency.

The reaction of **51** with LiEt<sub>3</sub>BH (superhydride) was also examined. It led to shifts in the CO bands to lower wavenumber in the IR spectrum but ultimately no tractable products were obtained.

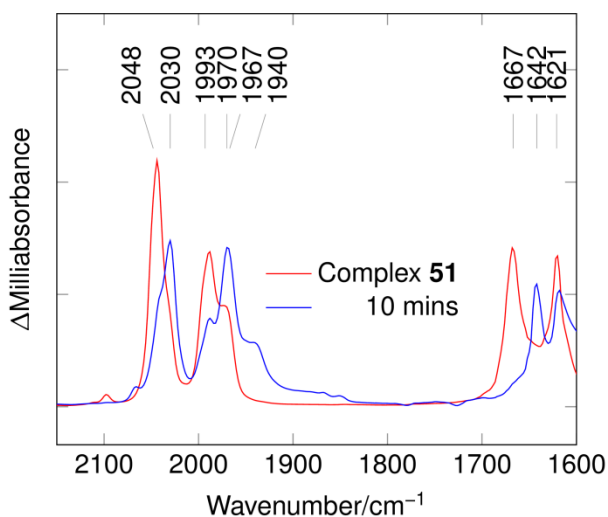


**Figure 64** Reaction of **51** with LiAlH<sub>4</sub>.

In summary the reaction of **51** with sources of hydride leads to the formation of new species. Changes in IR spectra appear to be transient over the minutes time-scale. This made it difficult to provide evidence that the IR shifts seen are due to direct interaction of hydride with the Fe centre. The changes in IR spectra could be due to interaction of the ligands with hydride rather than direct Fe binding. Loss of the CO and the carbamoyl bands was observed. Reactions involving the ferracyclic ligand could take place such as reduction of the amide or its deprotonation. Whatever the pathways involved no clean products were isolable.

### 3.4.1 Conclusion

The replacement of a labile solvent molecule in a ferracyclic carbamoyl complex **51**, which possesses the Fe(II) *cis*-carbonyl motif of [Fe]-hydrogenase by a tertiary phosphine ligand PMe<sub>3</sub> has been shown. Further substitution of **51** by bulky tertiary phosphines can occur in which a CO ligand is also displaced. X-ray crystallographic structures of both mono- and bis-phosphine complexes have been determined.

Attempts to extend the second coordination sphere of the model complexes with a pyridinol ligand have proven unsuccessful. This was due to the high reactivity of Fe(CO)<sub>4</sub>Br<sub>2</sub> with **73a**

and **73b**. In parallel with the work reported here, within the Pickett group a diaminopyridine ligand was incorporated into a model complex.<sup>16</sup> This provided an analogous structure to the pyridinol in the [Fe]-hydrogenase active site.

The mechanistic role of the iron centre in the natural system is not yet understood and biological studies cannot answer all the questions. In this study endeavour was made to answer the question “Does the iron centre have a role in accepting hydride from dihydrogen?”. Attempts to react synthetic complexes with various sources of hydride were undertaken in order to probe the possibility of producing stable Fe–H bonds. Reactions of various hydride sources with **51** gave substantial changes in infrared spectra but led to ultimately unstable (over the minutes time-scale) compounds that decomposed into species that did not contain carbonyls. No direct evidence was found for hydride binding in the synthetic systems. Metal hydrides tend to appear between –3 and –50 ppm and this no peak in this region was observed.

Electrochemical studies of the ferracyclic *cis*-carbonyl complexes **56b** and **51** shows that the Fe<sup>II/III</sup> couples are not redox active at potentials <1 V versus Ag/AgCl, broadly in keeping with the absence of an Fe<sup>II/III</sup> redox couple for [Fe]-hydrogenase in this domain.

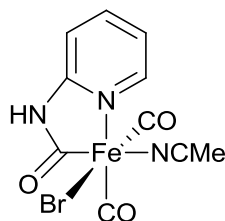
### 3.5 Experimental

General synthetic methodology is outlined in section 2.1.

#### [Fe(CO)<sub>4</sub>Br<sub>2</sub>]

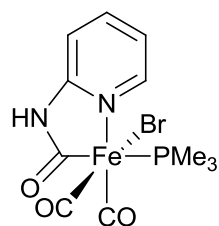
Fe(CO)<sub>5</sub> (2.3 mL, 17 mmol) was dissolved in CH<sub>2</sub>Cl<sub>2</sub> (100 mL) and cooled to -40 °C. Br<sub>2</sub> (1 mL, 19 mmol) in CH<sub>2</sub>Cl<sub>2</sub> (100 mL) was added drop-wise over the course of 15 minutes. The solution was kept for 1 h at -40 °C, it was then warmed slowly to room temperature over 1 h. The solvent was then removed under vacuum and the crude red-brown product was sublimed at 75 °C onto a cold finger yielding shiny red-brown needles (1.22 g, 22 %).  $\nu_{\text{max}}/\text{cm}^{-1}$  (CH<sub>2</sub>Cl<sub>2</sub>) 2156, 2112, 2086. Synthesis adapted from ref. 227.

#### [FeBr(C<sub>6</sub>H<sub>5</sub>N<sub>2</sub>O)(CO)<sub>2</sub>(MeCN)] (51)



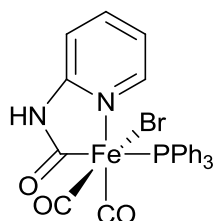
[Fe(CO)<sub>4</sub>Br<sub>2</sub>] (330 mg, 1.0 mmol) was dissolved in CH<sub>2</sub>Cl<sub>2</sub> (60 mL) and solid 2-aminopyridine (188 mg, 2.0 mmol) was added. The resulting solution was allowed to react at room temperature for 2 hours at which point precipitation was complete; the solution discoloured from brown to pale yellow over this time. The supernatant was removed and the remaining yellow powder was dried under vacuum and recrystallised in MeCN (4 mL) yielding orange-red crystals (160 mg, 44 %).  $\nu_{\text{max}}/\text{cm}^{-1}$  (THF) 2046, 1994, 1986, 1967, 1665, 1621. Adapted from ref. 227.

**[FeBr(C<sub>6</sub>H<sub>5</sub>N<sub>2</sub>O)(CO)<sub>2</sub>(PMe<sub>3</sub>)] (56a)**



PMe<sub>3</sub> (34 μL, 0.33 mmol) was dissolved in THF (20 mL), and was added drop-wise to solid **51** (131 mg, 0.33 mmol) over 15 minutes. A red-brown solution was formed. The solvent was then reduced to 6 mL under vacuum and cooled to -20 °C. A small amount of colourless solid precipitated and was discarded. The supernatant was removed and the remaining solvent was taken off under vacuum resulting in a sticky oil. This was then dissolved in a small amount of MeCN (ca 1 mL) and stored at -20 °C yielding red crystals of X-ray quality (55 mg, 38 %). Found C 34.04, H 3.55, N 7.12 %; C<sub>11</sub>H<sub>14</sub>BrFeN<sub>2</sub>O<sub>3</sub>P requires C 33.95, H 3.63, N 7.20 %.  $\nu_{\max}/\text{cm}^{-1}$  (MeCN) 2035, 1967.  $m/z$  (Cl<sup>-</sup>) 361.8, 359.9, (M - H - CO). <sup>31</sup>P NMR (121 MHz, CD<sub>2</sub>Cl<sub>2</sub>):  $\delta$  -12.51.

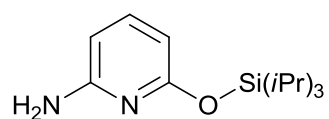
**[FeBr(C<sub>6</sub>H<sub>5</sub>N<sub>2</sub>O)(CO)<sub>2</sub>(PPh<sub>3</sub>)] (56b)**



Solid PPh<sub>3</sub> (211 mg, 0.805 mmol) was added to a solution of **51** (316 mg, 0.805 mmol) in THF (20 mL). The solvent was removed by sparging with CO gas, and a red-brown precipitate was formed. The resulting brown paste was washed with cold THF (-20 °C, 5 mL) to yield a red-brown powder (315 mg, 68 %). Found C 54.19, H 3.60, N 4.89 %; C<sub>26</sub>H<sub>20</sub>BrFeN<sub>2</sub>O<sub>3</sub>P requires C 54.19, H 3.50, N 4.87 %.  $\nu_{\max}/\text{cm}^{-1}$  (THF) 2040, 1990, 1666, 1620. <sup>31</sup>P NMR (121 MHz, CD<sub>2</sub>Cl<sub>2</sub>):  $\delta$  37.47.



### 6-{{Tris(propan-2-yl)silyl}oxy}pyridine-2-amine (73b)



6-Aminopyridin-2-ol **39a'** (618 mg, 5.62 mmol) was dissolved in THF (100 mL) and cooled to  $-78\text{ }^{\circ}\text{C}$ . Butyl lithium (1.6 M in THF, 3.51 mL) was added slowly, and the reaction stirred for 2 h before warming to room temperature. Tris(isopropyl)silyl chloride (1.20 mL, 5.62 mmol) was added and the reaction stirred for 48 h. The solvent was removed at reduced pressure and the product extracted from the residue with  $\text{CH}_2\text{Cl}_2$ . This was then filtered and the solvent removed at reduced pressure to leave a yellow-brown oil (910 mg, 61 %).  $^1\text{H}$  NMR (300 MHz,  $\text{CD}_2\text{Cl}_2$ ):  $\delta$  1.20 (m, 21H,  $J = 7.4$  Hz), 6.04 (d, 1H,  $J = 1.7$  Hz), 6.07 (d, 1H,  $J = 1.7$  Hz), 7.32 (t, 1H,  $J = 7.8$  Hz).  $m/z$  (orbitrap) calcd for  $\text{C}_{14}\text{H}_{25}\text{N}_2\text{OSi}$  267.1887, found 267.1892.

#### 3.5.1 Crystallography experimental

Crystals were suspended in oil, and one was mounted on a glass fibre and fixed in the cold nitrogen stream of the diffractometer. Data were collected on an Oxford Diffraction Xcalibur-3 CCD diffractometer equipped with Mo-K $\alpha$  ( $\lambda = 0.71073\text{ \AA}$ ) radiation and graphite monochromator [ $2(\text{C}_5\text{H}_6\text{N}_2\text{O})\cdot(\text{H}_2\text{O})$ ](**73a**) and [ $\text{Fe}(\text{C}_5\text{H}_6\text{N}_2\text{CO})(\text{PPh}_3)_2(\text{CO})_2$ ] $_2$ - $[(\text{Br}_3\text{Fe})_2\text{O}]\cdot 2(\text{CH}_2\text{Cl}_2)$  (**71**), or a Bruker–Nonius FR591 molybdenum rotating anode and confocal mirrors [ $\text{Fe}(\text{C}_5\text{H}_6\text{N}_2\text{CO})(\text{PMe}_3)(\text{CO})_2$  (**56a**) and  $\text{Fe}(\text{C}_5\text{H}_6\text{N}_2\text{CO})(\text{Br})(\text{PPh}_3)_2(\text{CO})\cdot\text{THF}$ ]. Data were processed using the programs CrysAlisPro<sup>244</sup> [ $2(\text{C}_5\text{H}_6\text{N}_2\text{O})\cdot(\text{H}_2\text{O})$  and [ $\text{Fe}(\text{C}_5\text{H}_6\text{N}_2\text{CO})(\text{PPh}_3)_2(\text{CO})_2$ ] $_2$ - $[(\text{Br}_3\text{Fe})_2\text{O}]\cdot 2(\text{CH}_2\text{Cl}_2)$ ] or DENZO and COLLECT<sup>245</sup> [ $\text{Fe}(\text{C}_5\text{H}_6\text{N}_2\text{CO})(\text{PMe}_3)(\text{CO})_2$  and  $\text{Fe}(\text{C}_5\text{H}_6\text{N}_2\text{CO})(\text{Br})(\text{PPh}_3)_2(\text{CO})\cdot\text{THF}$ ]. Structures were determined by the charge flipping routine in the program Superflip [ $\text{Fe}(\text{C}_5\text{H}_6\text{N}_2\text{CO})(\text{PMe}_3)(\text{CO})_2$ ]<sup>246</sup> or by direct methods

routines in the program SIR-92 [all others], and were refined by full-matrix least-squares methods on  $F^2$  in SHELXL-97.<sup>247</sup> Non-hydrogen atoms were refined with anisotropic thermal parameters. Hydrogen atoms bound to nitrogen were located in the Fourier difference map and freely refined where possible; in all other cases they were included in idealised positions and their  $U_{\text{iso}}$  values were set to ride on the  $U_{\text{eq}}$  values of the parent carbon atoms.<sup>248</sup>

**Table 4** Summary of crystallographically characterised data.

	<b>56a</b>	<b>70</b>	<b>71</b>	<b>73a'</b>
Formula	C <sub>11</sub> H <sub>14</sub> BrFeN <sub>2</sub> O <sub>3</sub> P	2(C <sub>44</sub> H <sub>33</sub> FeN <sub>2</sub> O <sub>3</sub> P <sub>2</sub> ), Br <sub>6</sub> Fe <sub>2</sub> O, 2(CH <sub>2</sub> Cl <sub>2</sub> )	C <sub>43</sub> H <sub>33</sub> BrFeN <sub>2</sub> O <sub>2</sub> P <sub>2</sub> , C <sub>4</sub> H <sub>8</sub> O	2(C <sub>5</sub> H <sub>6</sub> N <sub>2</sub> O), H <sub>2</sub> O
M	388.97	2292.07	881.53	238.25
Space group	P2 <sub>1</sub> /a	P2 <sub>1</sub> /c	P $\bar{1}$	P $\bar{1}$
a/Å	13.2378(3)	17.685(5)	11.061(5)	4.8603(6)
b/Å	7.5324(3)	11.969(5)	12.238(5)	9.3209(11)
c/Å	15.4174(5)	21.518(5)	15.979(5)	13.5944(19)
$\alpha$ /°	90	90	69.894(5)	97.673(10)
$\beta$ /°	110.218(2)	91.909(5)	86.657(5)	91.575(11)
$\gamma$ /°	90	90	77.321(5)	92.141(10)
V/Å <sup>3</sup>	1442.58(8)	4552(3)	1981.3(14)	609.59(13)
T/K	120(2)	140(2)	120(2)	140(2)
Z	4	2	2	2
R <sub>int</sub>	0.056	0.168	0.138	0.055
R <sub>1</sub> [I > 2 $\sigma$ ]	0.040	0.090	0.089	0.054
wR <sub>2</sub> (all data)	0.079	0.222	0.173	0.117

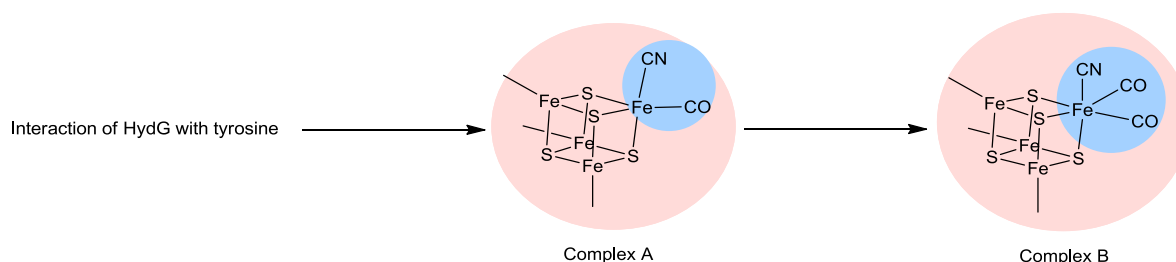
## 4 Reactions of $[\text{Fe}_4\text{S}_4(\text{SR})_4]^{2-}$ clusters with CO and $\text{CN}^-$

### 4.1 Context of interactions of clusters with CO and $\text{CN}^-$ and the biosynthesis of the H-cluster

The biosynthesis of the H-cluster, and current understanding of the action of its maturases is discussed in Section 1.2.5. HydG plays a key role in the bioassembly of the H-cluster as it is the source of all iron in the subsite and uses radical SAM chemistry to generate the CO and  $\text{CN}^-$  ligands.<sup>62</sup> A recent study by Kuchenreuther and co-workers<sup>62</sup> proposes that the CO and  $\text{CN}^-$  generated bind to the corner of a cube on the C-terminal cluster of HydG and form a “synthon” for the H-cluster. They report the spectroscopic *signature* for two distinct intermediates, an  $\text{Fe}(\text{CO})(\text{CN})$  (complex A) and an  $\text{Fe}(\text{CO})_2(\text{CN})$  (complex B) (see Scheme 41). The idea of CO and  $\text{CN}^-$  interacting with an  $\{4\text{Fe}4\text{S}\}^{2+}$  cluster in this way is unprecedented. Indeed additional supporting evidence is required in order to verify the identity of these intermediates. A very recent study by Roach and co-workers<sup>87</sup> suggests that the C-terminal cluster of HydG is a  $[5\text{Fe}5\text{S}]$  cluster containing a labile fifth iron (the suggested site of synthon generation). This study requires further supporting evidence in order to prove the existence of this fifth iron in the cluster.

The idea that CO and  $\text{CN}^-$  could bind to the corner of a  $[4\text{Fe}4\text{S}]^{2+}$  cluster is attractive to investigate. Not only is this novel substitution chemistry but it could also give insight into the biosynthetic pathway of the H-cluster. This chapter describes the interaction of synthetic undifferentiated (iron-sulfur clusters where all four iron sites are equivalent)  $[\text{Fe}_4\text{S}_4(\text{SR})_4]^{2-}$  clusters with CO and  $\text{CN}^-$ . Here we have looked for chemical precedence for the binding of CO and  $\text{CN}^-$  to simple  $[\text{Fe}_4\text{S}_4(\text{SR})_4]^{2-}$  clusters and the bearing this might have on the biosynthetic pathway to the H-cluster postulated by Kuchenreuther.<sup>62</sup> The next section

explores the substitution chemistry of synthetic  $\{4\text{Fe}4\text{S}\}^{2+}$  clusters and outlines what is currently known about their interaction with CO and  $\text{CN}^-$ .



**Scheme 41** Proposed intermediates on the biosynthetic pathway to the H-cluster.<sup>62</sup>

## 4.2 Earlier studies on general substitution reactions of $\{4\text{Fe}4\text{S}\}^{2+}$ clusters

Before examining the substitution mechanisms of iron-sulfur clusters we must first discuss the general electronic and structural features of associated with  $[\text{Fe}_4\text{S}_4(\text{SR})_4]^{2-}$  clusters. Simple studies of the oxidation states of these clusters indicate these clusters contain two Fe(II) and two Fe(III) sites.<sup>249-251</sup> However, it has been demonstrated using a variety of spectroscopic techniques that electronically there is only one kind of iron.<sup>252-254</sup> The high spin state of the clusters is paramagnetic resulting in a  $\mu_{\text{eff}} = 2.3$ , in other words the electrons are delocalised over the entire cluster and are best described as  $\text{Fe}^{2.5+}$ . The substitution chemistry of iron-sulfur clusters will clearly be influenced by the electronic structure of the metal centres. If the clusters contained both Fe(II) and Fe(III) centres then we might expect to see chemistry that reflects the difference in lability between the two different kinds of sites. In the case of all iron sites being equivalent initial substitution at each site would be identical. Figure 65 summarises the redox states and spin couplings within iron-sulfur clusters in three different oxidation states.

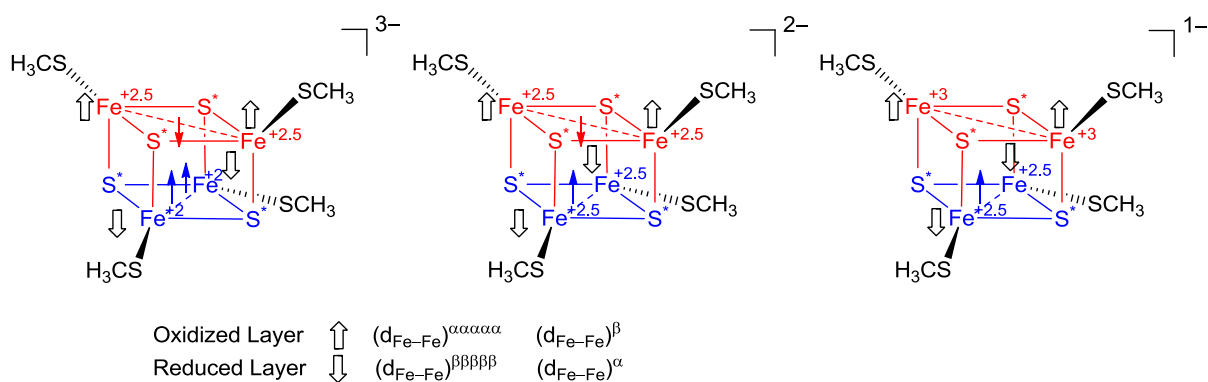


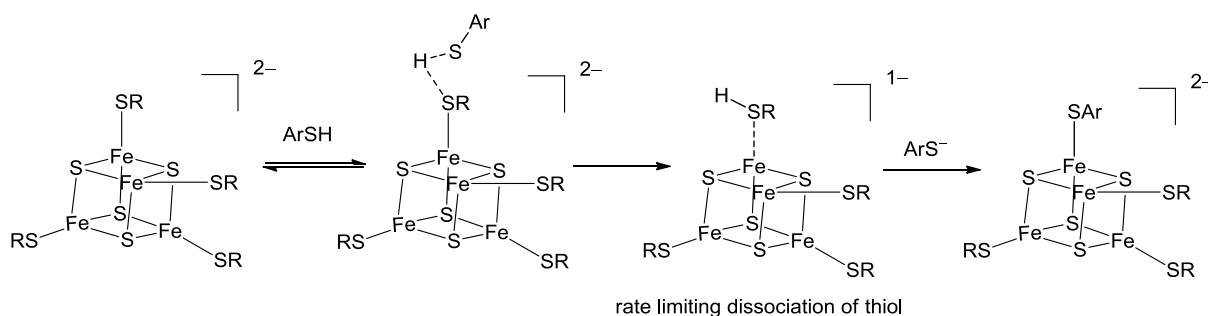
**Figure 65** Schematic models of the spin couplings between the two redox sublayers of  $\{4\text{Fe}4\text{S}\}$  cubane complexes at three different oxidation states, (a)  $3^-$ , (b)  $2^-$ , and (c)  $1^-$ . In each sublayer, the two high spin Fe centres couple ferromagnetically, while the two sublayers couple antiferromagnetically to give a low spin state. The 10 majority spins (represented by the large hollow arrows) are stabilised relative to the minority spin (represented by the small arrows), which is delocalised between the two Fe in each sub-layer. Adapted from ref. 255.

The substitution chemistry of transition metal complexes has been classified in terms of monometallic complexes.<sup>256</sup> Association, dissociation and ligand exchange mechanisms can be extended to polymetallic clusters. These basic categories are adequate to describe the behaviour of terminal ligands on clusters, though there is some mechanistic behaviour that is unique to clusters. The effect of adjacent metals on substitution chemistry needs to be considered. In a cluster a nucleophile may attack one metal centre and a leaving group may depart from another. In addition one Fe centre in a cluster can have an effect upon the chemistry of its neighbours, as can protonation at core sulfur and thiolate sulfur on iron.<sup>257</sup>

Substitution reactions of iron-sulfur clusters can be too fast for conventional spectroscopic methods and need to be studied by stopped-flow techniques. IR spectra of alkane thiolates are rather featureless, however if substitutions on the cluster are made by CO and  $\text{CN}^-$  distinct peaks form due to the formation of  $\text{CN}^-$ , CO bound cluster. In iron-sulfur cluster substitution

chemistry two main kinds of behaviour can be seen. The first kind of behaviour can be described by the reaction  $[\text{Fe}_4\text{S}_4\text{Cl}_4]^{2-}$  with  ${}^t\text{BuNC}$ : here a single exponential absorbance-time curve is observed. The behaviour associated with this is the substitution at only two of the iron sites. In this reaction the initial substitution is the slowest step and the partially substituted clusters react more rapidly to produce di-, tri- and tetra-substituted clusters. The second type of behaviour can be illustrated by the reaction of  $[\text{Fe}_4\text{S}_4\text{Cl}_4]^{2-}$  with  $\text{PhS}^-$ . The absorbance-time graph of this reaction fits two exponentials and the reaction results in a fully substituted cluster. This can be interpreted in two ways a) the first and second steps are similar in rate but slower than the third and fourth steps b) the rate of all four substitution steps differ in only small amounts.<sup>257</sup>

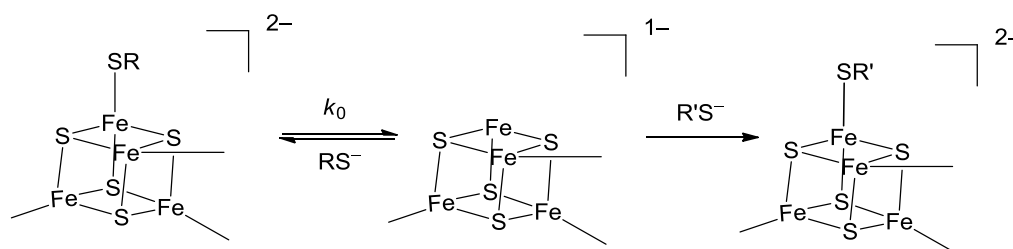
The mechanism of substitution of iron-sulfur clusters was first reported by Duker and Holm.<sup>258</sup> They studied the reactions of  $[\text{Fe}_4\text{S}_4(\text{SR})_4]^{2-}$  ( $\text{R} = \text{Et}$  or  ${}^t\text{Bu}$ ) with  $4\text{-R}'\text{C}_6\text{H}_4\text{SH}$  ( $\text{R}' = \text{NH}_2, \text{Me}$  or  $\text{NO}_2$ ). The report showed that the reactions undergo simple second order kinetics: first order with respect to the cluster and the thiol. The rate of these reactions were noted by the authors to be correlated to the acidity of the aryl thiol. These reactions are therefore acid catalysed. The mechanism is outlined in Scheme 42.



**Scheme 42** Mechanism of the reaction between  $[\text{Fe}_4\text{S}_4(\text{SR})_4]^{2-}$  ( $\text{R} = \text{Et}$  or  ${}^t\text{Bu}$ ) and  $4\text{-R}'\text{C}_6\text{H}_4\text{SH}$  ( $\text{R}' = \text{NH}_2, \text{Me}$  or  $\text{NO}_2$ ) proposed by Duke and Holm.<sup>258</sup>

The aryl thiol here plays three roles: it is the source of acid, the nucleophile and the conjugate base. This three-faceted role is a problem as it is difficult to focus on the mechanism of substitution alone.

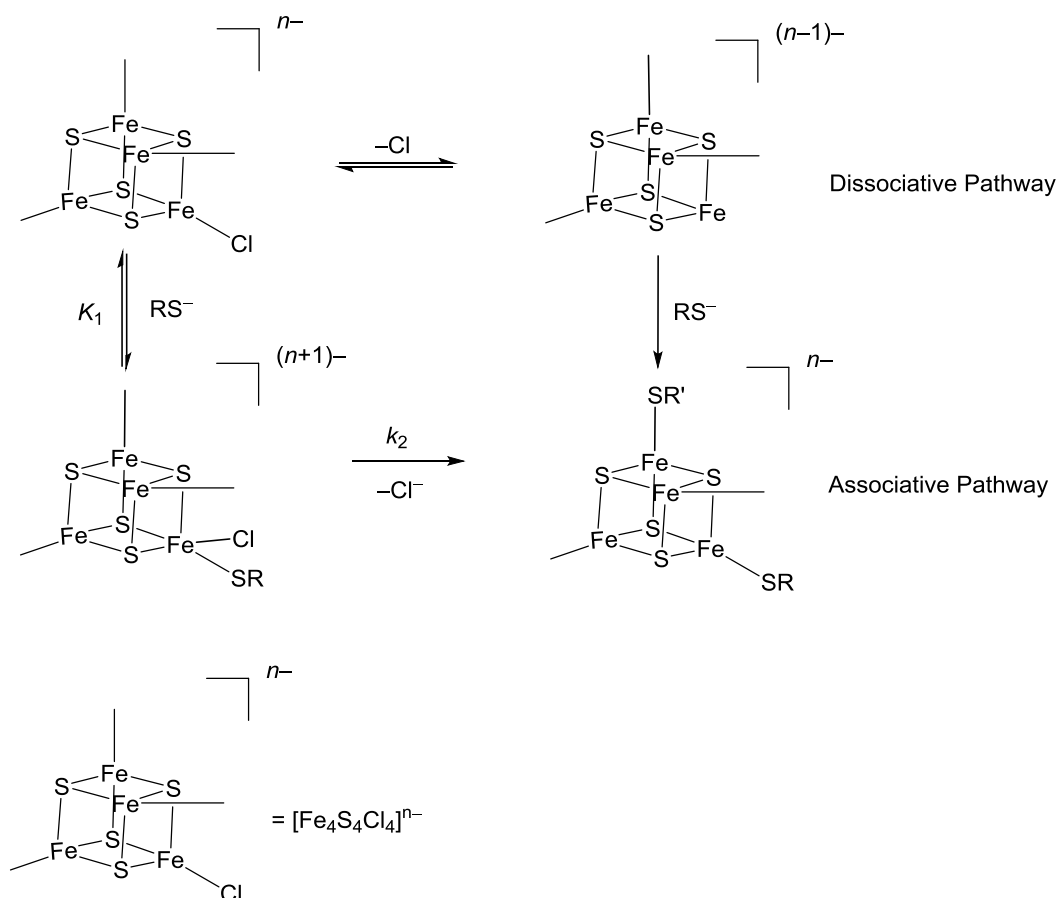
Studies on the substitution chemistry of  $[\text{Fe}_4\text{S}_4(\text{SR})_4]^{2-}$  (RS = alkyl or aryl thiolate)<sup>259</sup> with  $\text{R}'\text{S}^-$  show that the substitution reaction occurs at a rate in keeping with first order kinetics with respect to the cluster where dissociation of ligand from the cluster is the rate determining step. This dissociative behaviour is outlined in Scheme 43 and shows the formation of a coordinatively unsaturated cluster which is rapidly attacked by  $\text{R}'\text{S}^-$ . This is classified as a dissociative interchange mechanism since the low coordination number intermediate cannot be detected. The dissociation of  $\text{RS}^-$  is the rate limiting step.



**Scheme 43** The dissociative mechanism for substitution of terminal ligands in Fe-S-based clusters.<sup>257</sup>

More complex behaviour can be seen in studies on the reactions of  $[\text{Fe}_4\text{S}_4\text{X}_4]^{2-}$  (X = Cl or Br) with  $\text{PhS}^-$ .<sup>260</sup> It has been shown that, under all conditions, the rate has first order dependence on the concentration of the cluster but the dependence on the concentration of the nucleophile is more convoluted. At low concentration the rate appears to be dependent on the concentration of thiolate, whilst at high concentration the rate appears to be independent. As the concentration of  $\text{PhS}^-$  is increased the rate increases in a non-linear fashion as outlined in the work of Henderson and co-workers.<sup>257</sup> The kinetics described are in keeping with

substitution chemistry with a parallel associative and dissociative pathway as shown in Scheme 44.



**Scheme 44** The dissociative and associative mechanisms for substitution of terminal ligands in Fe–S based clusters.<sup>257</sup>

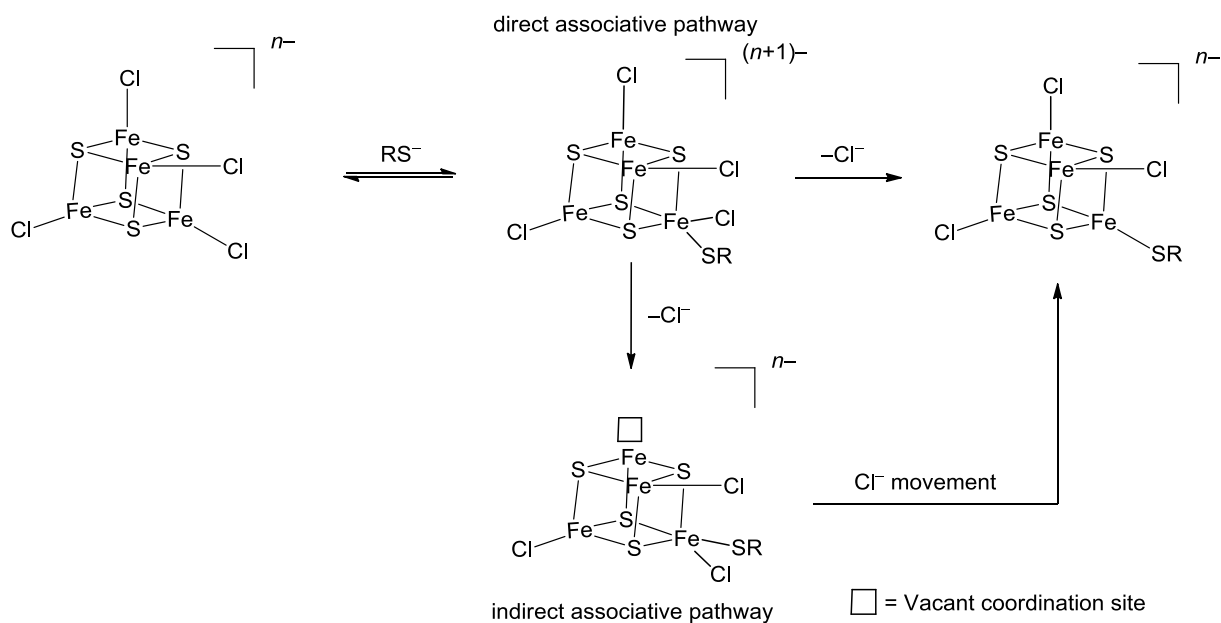
The dissociation of  $\text{Cl}^-$  from  $[\text{Fe}_4\text{S}_4(\text{SPh})\text{Cl}_4]^{3-}$  was followed on the UV-vis stopped-flow time-scale of milliseconds. This allowed the determination of equilibrium constants for the nucleophile binding to the cluster and the rate of dissociation of the chloro ligand. In this proposed associative mechanism there is practically no dissociation of the leaving group whilst the nucleophile is binding. The  $\text{Cl}^-$  stays bound to the cluster up until the  $\text{PhS}^-$  has formed a complete bond. The rate law associated with this reaction shows that at higher concentrations of thiolate there is accumulation of a higher coordination number

intermediate,  $[\text{Fe}_4\text{S}_4(\text{SPh})\text{Cl}_4]^{3-}$ . However, there is no definitive spectroscopic evidence for this type of species. Electronic spectra associated with iron-sulfur cubane clusters are dominated by transitions associated with the core, these are largely unperturbed by changes in the ligation.<sup>257</sup>

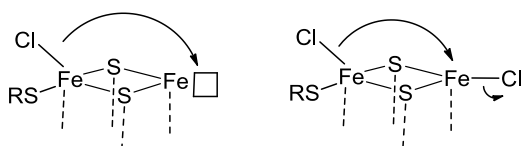
To summarise,  $[\text{Fe}_4\text{S}_4(\text{SR})_4]^{2-}$  undergoes substitution chemistry via a dissociative pathway, whilst  $[\text{Fe}_4\text{S}_4\text{Cl}_4]^{2-}$  undergoes substitution via an associative mechanism, the reasons why are not entirely clear.<sup>257</sup> Considerations of the lability of the two different kinds of ligands it can be seen that the Fe–Cl bond is more labile than the Fe–SR bond (derived from the dissociative rate constants). Therefore the preferred mechanistic pathway cannot be attributed to the lability of the respective bonds. It has been highlighted that the steric bulk of the two ligands may be a more important factor in determining the mechanistic pathway for substitution. In a study of a bulky PCy<sub>3</sub> (Cy = cyclohexyl) substituted  $[\text{Fe}_4\text{S}_4(\text{PR}_3)_4]$  cluster it was found that PCy<sub>3</sub> protected the Fe centres from nucleophiles and the clusters thus underwent dissociative substitution.<sup>261</sup> This indicated the importance of steric factors but it must be taken into account that  $[\text{Fe}_4\text{S}_4(\text{PR}_3)_4]$  and  $[\text{Fe}_4\text{S}_4(\text{SR})_4]^{2-}$  are in different oxidation states and therefore may not be directly comparable. The influence of oxidation state has not yet been studied directly. There have however, been early studies that indicate that  $\text{PhS}^-$  in  $[\text{Fe}_4\text{S}_4(\text{SPh})_4]^{3-}$  is similar in lability to that in  $[\text{Fe}_4\text{S}_4(\text{SPh})_4]^{2-}$ .

The effect of electronic factors on the associative substitution chemistry of iron-sulfur clusters has been investigated in a study of the reaction of  $[\text{Fe}_4\text{S}_4\text{Cl}_4]^{2-}$  with 4-RC<sub>6</sub>H<sub>4</sub>S<sup>-</sup> (R = MeO, Me, H, Cl, or NO<sub>2</sub>).<sup>262</sup> It was shown that with stronger electron withdrawing groups on the nucleophile the rate of substitution increases. This was explained by the electron withdrawing group stabilising the electron rich transition state. The overall binding of a thiolate to an iron centre increases the net charge on that centre by one unit thereby weakening the  $\sigma$  bond between Cl and Fe.

Clusters are of course multinuclear and other pathways for substitution can be considered. An associative reaction at one Fe may affect the lability of ligands at the three other Fe centres. This could lead to dissociation followed by migration as shown in Scheme 45 or concerted migration and dissociation via a bridged intermediate. These two pathways would be kinetically indistinguishable.



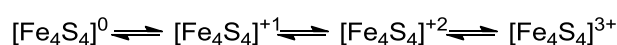
Possible Cl<sup>-</sup> migration pathways



**Scheme 45** Possible pathways for the associative substitution reaction of Fe-S-based clusters showing the direct pathway (top) in which the nucleophile and the leaving group are involved at the same Fe site, and the indirect pathway (bottom), in which nucleophilic attack is at one Fe and the leaving group dissociates from another Fe.<sup>257</sup>

#### 4.2.1 General electrochemical studies on $[\text{Fe}_4\text{S}_4(\text{SR})_4]^{n-}$ clusters

The electrochemical behaviour of  $\{4\text{Fe}4\text{S}\}$ -clusters has been reasonably well defined for some time. Soon after the first examples of synthetic iron-sulfur cluster models electrochemical studies revealed that  $\{4\text{Fe}4\text{S}\}^z$  clusters in terms of core oxidation states form a four member electron transfer series (outlined in Scheme 46) in which the cubane core is retained.<sup>263</sup> It has been shown that in a non-nucleophilic solvent all members of the series  $[\text{Fe}_4\text{S}_4(\text{SPh})_4]^{z-}$  ( $z = 1, 2, 3, 4$ ) can be detected electrochemically.<sup>264</sup>



**Scheme 46** Core oxidation states of  $\{4\text{Fe}4\text{S}\}$  clusters.<sup>265</sup>

The redox potential of  $\{4\text{Fe}4\text{S}\}$  clusters is dependent on the substituent R group in  $[\text{Fe}_4\text{S}_4(\text{SR})_4]^{z-}$  clusters and on the nature of the anion substituent in  $[\text{Fe}_4\text{S}_4\text{Nu}_4]^{z-}$  clusters (Nu = Cl, Br, MeO, AcO). Mixed complexes of the type  $[\text{Fe}_4\text{S}_4(\text{SR})_{4-n}\text{X}_n]^{2-}$  have been studied by cyclic voltammetry. It has been shown that the effect of the substitution of  $\text{RS}^-$  by  $\text{Nu}^-$  on the potential of the 2-/3- couple is additive. This is discussed in more detail below in the context of experimental results that have been obtained for the substitution of  $\text{RS}^-$  in cubane clusters by  $\text{CN}^-$ .<sup>266</sup>

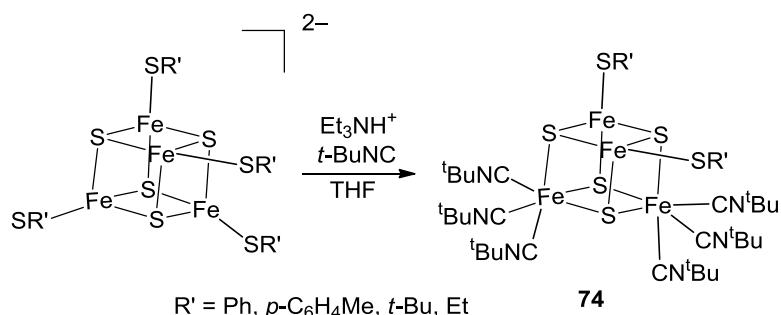
#### 4.2.2 Independent interactions of $[\text{Fe}_4\text{S}_4(\text{SR})_4]^{n-}$ clusters, $n = 2-4$ with CO and $\text{CN}^-$

Now some of the general substitution chemistry of iron-sulfur clusters has been considered it is useful to look at what is known about the interaction of iron-sulfur cluster with CO and  $\text{CN}^-$  independently. Hitherto, there have been no studies of iron-sulfur clusters with CO and  $\text{CN}^-$  as co-substrates, other than a study of FeMoco as is discussed below.<sup>267</sup>

Early studies investigated the multi-electron reduction of  $[\text{Fe}_4\text{S}_4(\text{SPh})_4]^{2-}$  clusters under one atmosphere of CO.<sup>268</sup> There was interaction at oxidation states that are not commonly observed in biology but no interaction of CO with  $[\text{Fe}_4\text{S}_4(\text{SPh})_4]^{2-}$ .

Isolation and characterization of salts of the tetra-cyanide substituted anions  $[\text{Fe}_4\text{S}_4(\text{CN})_4]^{3-}$  and  $[\text{Fe}_4\text{S}_4(\text{CN})_4]^{4-}$  clusters have been described.<sup>265, 269</sup> Although salts of the dianion  $[\text{Fe}_4\text{S}_4(\text{CN})_4]^{2-}$  have not been synthesised, the  $E_{1/2}$  of the 2-/3- couple of  $[\text{Fe}_4\text{S}_4(\text{CN})_4]^{3-}$  has been measured to be  $-0.44$  V vs a standard calomel electrode in an MeCN electrolyte.

Isocyanides RNC are isoelectronic with CO and  $\text{CN}^-$ , they are good sigma donors and strong  $\pi^*$  acceptors. Goh and co-workers<sup>270</sup> explored the reactivity of  $[\text{Fe}_4\text{S}_4\text{Cl}_4]^{2-}$  with isocyanides. It was reported that the reaction of  $[\text{Fe}_4\text{S}_4\text{Cl}_4]^{2-}$  with excess isocyanide gives  $[\text{Fe}_4\text{S}_4\text{Cl}_2(\text{RCN})_6]^{2-}$  (R = Me, *t*-Bu) in good yield. These experiments were the first to extensively study [2:2] site differentiated clusters where there are two pairs of equivalent iron atoms. The diagram below gives an example of a [2:2] site differentiated cluster.



**Scheme 47** Reaction of  $[\text{Fe}_4\text{S}_4(\text{SPh})_4]^{2-}$  with tertiary butyl isocyanide to yield a [2:2] site differentiated cluster.<sup>270</sup>

There are currently no examples of the chemistry of simple  $\{4\text{Fe}4\text{S}\}$ -clusters in which CO and  $\text{CN}^-$  are co-substrates nor characterised materials in which CO and  $\text{CN}^-$  are co-ligands to a cubane core. However, synergistic binding of CO and  $\text{CN}^-$  has been demonstrated in a study on the reactivity of the active site of nitrogenase, FeMoco, with these ligands.<sup>267</sup> Thus

electrochemical and infrared data on the binding of cyanide to the isolated iron–molybdenum cofactor of nitrogenase, FeMoco showed that cyanide stabilises a hitherto unrecognised, low-spin, EPR-active ( $S = 1, 2$ ), superoxidised form of FeMoco. Furthermore the first evidence for carbon monoxide and cyanide binding synergically to the oxidised and semireduced states of the isolated cofactor was presented, notably these states were unreactive to carbon monoxide alone. A discussion of this feature of the chemistry can be found in section 6.2.

### **4.3 Probing interactions of undifferentiated $[\text{Fe}_4\text{S}_4(\text{SR})_4]^{2-}$ ( $\text{R} = \text{Et}$ and $\text{Ph}$ ) clusters with CO and $\text{CN}^-$ as single substrates**

#### **4.3.1 Introduction to experimental techniques**

Cyclic voltammetry and stopped-flow FTIR techniques were principally used to explore the interactions of iron-sulfur clusters with CO and  $\text{CN}^-$ . The general aspects of cyclic voltammetry were introduced in section 2.2.6 and the detailed experimental protocol is described in the experimental section of this chapter. FTIR and stopped-flow FTIR has also been introduced in Chapter 2 and a detailed description of the experiments are provided in the experimental section. For clarity, how a stopped-flow FTIR time-course spectrum is presented in this work is shown in Figure 66. Early scans are depicted in blue with red indicating a scan at longer time. Thus in Figure 66 it can be deduced that we are seeing the growth of two bands. The time in between scans increases on a pseudo-logarithmic scale. Therefore at short time scans are very frequent, allowing the detection of short-lived intermediates, whilst at longer time scans are further apart.

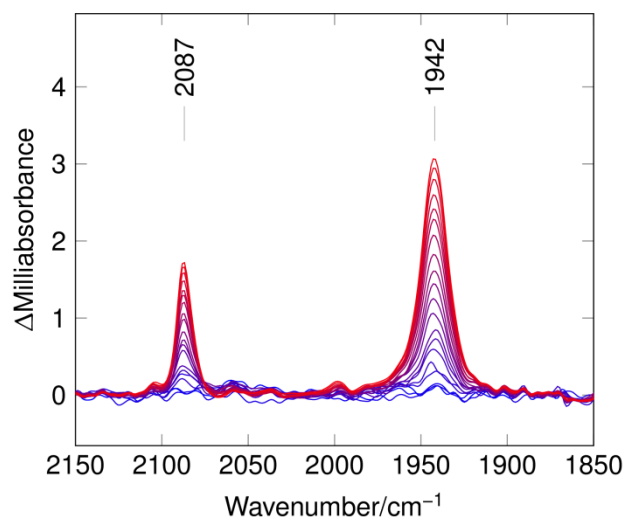


**Figure 66** An example of a stopped-flow FTIR time-course spectrum from this work showing the reaction of a site differentiated cluster with CO and  $\text{CN}^-$  (see Section 5.4.1). Recorded over 12 min with time between the data presented increasing on a pseudo-logarithmic time-scale. Blue: early scans, red: later scans.

#### 4.3.2 The effect of CO on the cyclic voltammetry and stopped-flow FTIR of $[\text{Fe}_4\text{S}_4(\text{SR})_4]^{2-}$ clusters (R = Et and Ph)

The interaction of  $[\text{Fe}_4\text{S}_4(\text{SPh})_4]^{2-}$  in MeCN solution with CO was first investigated using cyclic voltammetry. On changing from an atmosphere of dinitrogen to one of carbon monoxide the  $E_{1/2}$  of the observed couple of the parent compound was unchanged. The ratio of the  $i_p^{\text{ox}}/i_p^{\text{red}}$  remained unchanged and close to 1, and no new peaks were detected, Figure 67. The displacement of the voltammogram under CO is a consequence of increasing the concentration of the parent species with after prolonged purging.

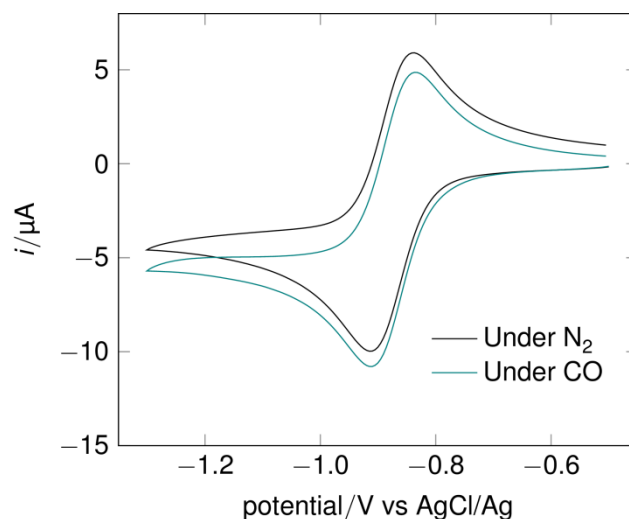


**Figure 67** Cyclic voltammogram of  $[\text{Fe}_4\text{S}_4(\text{SPh})_4]^{2-}$  Under  $\text{N}_2$  (black) and under CO (blue). Electrode: vitreous carbon;  $50 \text{ mV s}^{-1}$ ;  $0.1 \text{ M } [\text{Bu}_4\text{N}][\text{BF}_4] - \text{MeCN}$ ; RT;  $[\text{Cluster}] = 0.80 \text{ mM}$ .

That  $[\text{Fe}_4\text{S}_4(\text{SPh})_4]^{2-}$  does not react with CO alone to a measurable extent was supported by further analysis by stopped-flow FTIR. On the time-scale of the experiment (5 min) no new IR bands in the carbonyl IR region were seen.

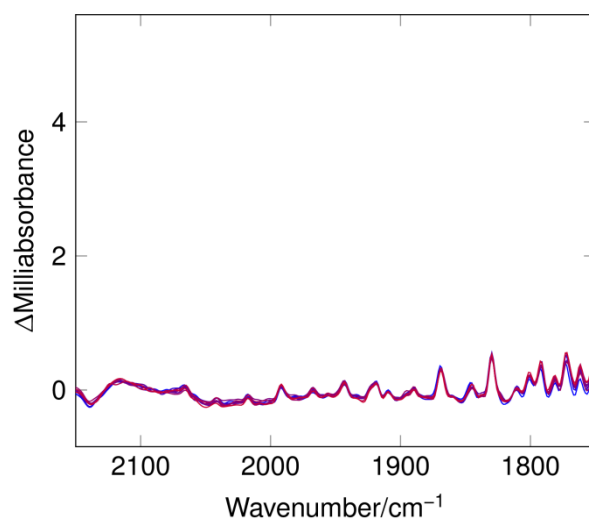


**Figure 68** Stopped-flow FTIR spectra of  $[\text{Fe}_4\text{S}_4(\text{SPh})_4]^{2-}$  in MeCN under CO. Blue: early scans (from 1 s), red: later scans over the course of 5 min.  $[\text{Cluster initial}] = 1 \text{ mM}$ .

The interaction of CO with  $[\text{Fe}_4\text{S}_4(\text{SEt})_4]^{2-}$  was also investigated. In cyclic voltammetry experiments, it was observed that on changing from an atmosphere of dinitrogen to carbon monoxide some loss of the wave corresponding to the parent species at  $E_{1/2} = -1.2$  V was seen accompanied by the growth of a new wave at more positive potential  $E_{1/2} = -1.07$  V as shown in Figure 69.

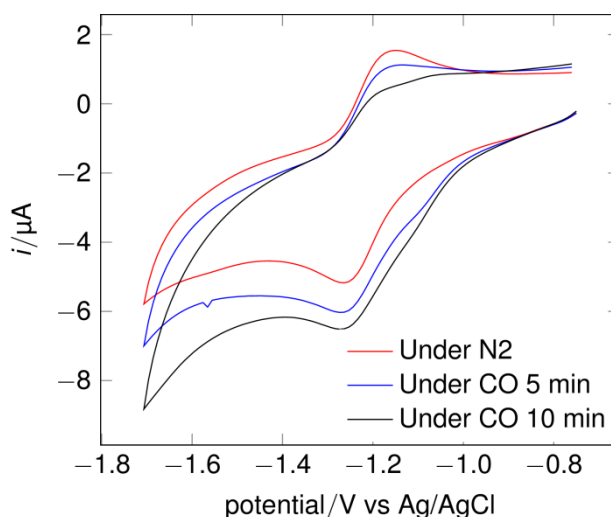


**Figure 69** Cyclic voltammogram of  $[\text{Fe}_4\text{S}_4(\text{SEt})_4]^{2-}$  Under  $\text{N}_2$  (black) and under CO 5 min (light blue), under CO 10 min (dark blue). Electrode: vitreous carbon;  $50 \text{ mV s}^{-1}$ ;  $0.1 \text{ M}$   $[\text{Bu}_4\text{N}][\text{BF}_4] - \text{MeCN}$ ; RT;  $[\text{Cluster}] = 0.93 \text{ mM}$ .

It seemed curious that an  $[\text{Fe}_4\text{S}_4(\text{SEt})_4]^{2-}$  cluster would interact with CO whereas an  $[\text{Fe}_4\text{S}_4(\text{SPh})_4]^{2-}$  cluster would not. However, the *same* effect on the voltammogram was observed upon prolonged purging of the complex with  $\text{N}_2$ , Figure 69. Notably adding EtSH restored the response of the parent complex before purging as shown in Figure 70.

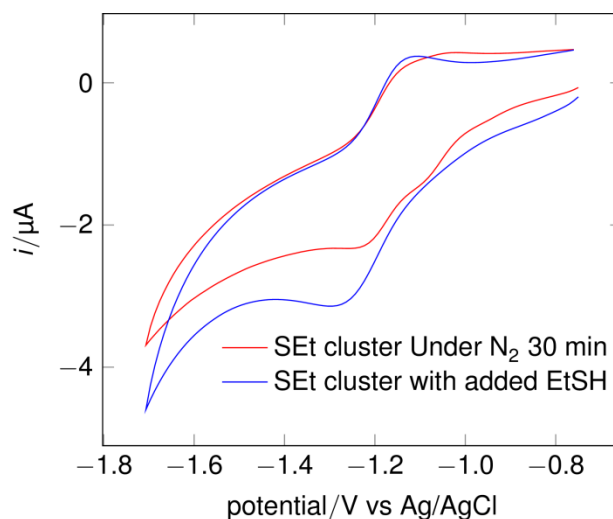
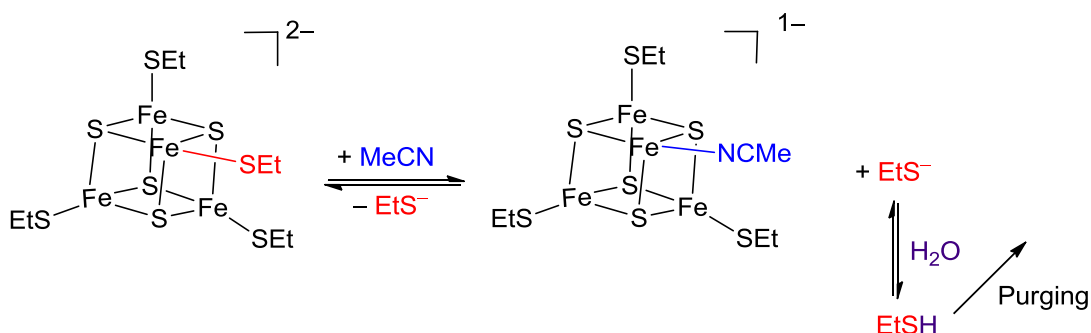


**Figure 70** Cyclic voltammogram of  $[\text{Fe}_4\text{S}_4(\text{SEt})_4]^{2-}$  Under  $\text{N}_2$  for 30 min (red) and after addition of ethane thiol (blue). Electrode: vitreous carbon;  $50 \text{ mV s}^{-1}$ ;  $0.1 \text{ M } [\text{Bu}_4\text{N}][\text{BF}_4] - \text{MeCN}$ ; RT;  $[\text{Cluster}] = 0.46 \text{ mM}$ .

This can be explained by loss of a thiolate and replacement by MeCN or a weakly coordinated  $\text{BF}_4^-$ . The ethanethiolate group is basic and protonation by adventitious water, together with gas-purging driving off the volatile EtSH (Scheme 48) might lead to a more easily reduced cluster species.



**Scheme 48** Postulated mechanism of the loss of  $\text{EtS}^-$  from  $[\text{Fe}_4\text{S}_4(\text{SEt})_4]^{2-}$  during purging with  $\text{N}_2$  or  $\text{CO}$ .

That the new wave in Figure 4 is *not* attributable to the binding of  $\text{CO}$  to the cluster was unambiguously confirmed by stopped-flow FTIR experiments as shown in Figure 71.

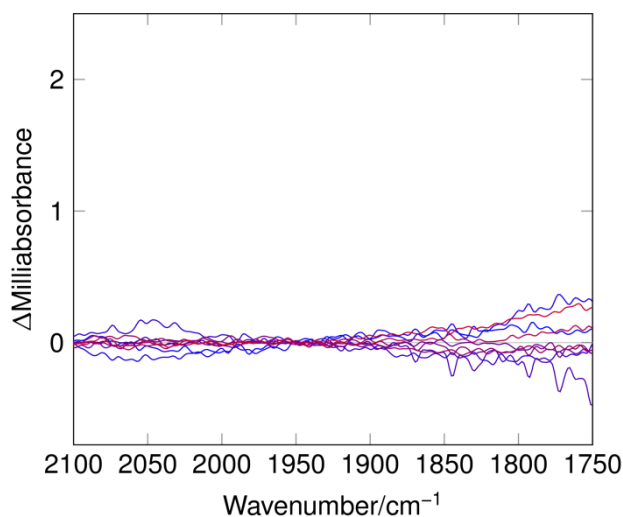


**Figure 71** Stopped-flow FTIR spectra of  $[\text{Fe}_4\text{S}_4(\text{SET})_4]^{2-}$  in MeCN under CO. Blue: early scans (from 1 s), red: later scans over the course of 10 min. Initial  $[\text{Cluster}] = 1 \text{ mM}$ .

#### 4.3.3 The effect of $\text{CN}^-$ on the cyclic voltammetry of $[\text{Fe}_4\text{S}_4(\text{SR})_4]^{2-}$ clusters (R = Et and Ph)

It has been shown above that CO alone does not interact with the dianionic iron-sulfur clusters (or on the cyclic voltammetry time-scale with the trianionic clusters). In this section the aim was to establish the landscape of  $\text{CN}^-$  substitution at synthetic iron-sulfur clusters. The only well-defined  $\text{CN}^-$  ligated clusters are the crystallographically characterised tetracyano-species  $[\text{Fe}_4\text{S}_4(\text{CN})_4]^{3-}$  and  $[\text{Fe}_4\text{S}_4(\text{CN})_4]^{4-}$  and evidence for  $[\text{Fe}_4\text{S}_4(\text{CN})_4]^{2-}$  species which has been detected in solution by cyclic voltammetry as a redox partner in the reversible  $[\text{Fe}_4\text{S}_4(\text{CN})_4]^{2-/3-}$  couple.<sup>269</sup> Partially substituted species have neither been synthetically isolated nor spectroscopically characterised. It is clear that there must be intermediates on the path to tetra-cyano species. The reaction of two  $[\text{Fe}_4\text{S}_4(\text{SR})_4]^{2-}$  clusters (R = Ph and Et) with  $\text{CN}^-$  alone was probed to help with the interpretation of subsequent co-substrate CO plus  $\text{CN}^-$  studies.

The cyclic voltammetry of  $[\text{Fe}_4\text{S}_4(\text{SPh})_4]^{2-}$  under dinitrogen in the presence of cyanide was investigated. On progressive addition of cyanide the wave corresponding to the reversible

reduction of the parent cluster decreased and new waves at more positive potentials appeared as is globally shown by Figure 72. For clarity, the voltammograms recorded at each incremental addition of cyanide concentration are shown separately in Figure 73, the growth and loss in peak height of the parent cluster and cyanide products is shown in Figure 74 and an overlay of the cyclic voltammograms before and after addition of 4 equivalents of cyanide by Figure 75.

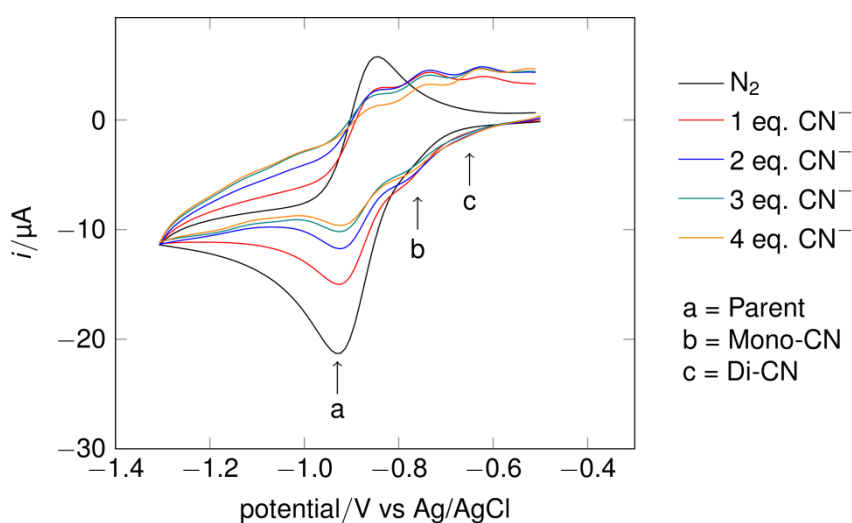


**Figure 72** Cyclic voltammogram of  $[\text{Fe}_4\text{S}_4(\text{SPh})_4]^{2-}$  under dinitrogen with increasing number of added equivalents of cyanide. Electrode: vitreous carbon;  $100 \text{ mV s}^{-1}$ ;  $0.1 \text{ M } [\text{Bu}_4\text{N}][\text{BF}_4] - \text{MeCN}$ ; RT;  $[\text{Cluster}] = 1.02 \text{ mM}$ .

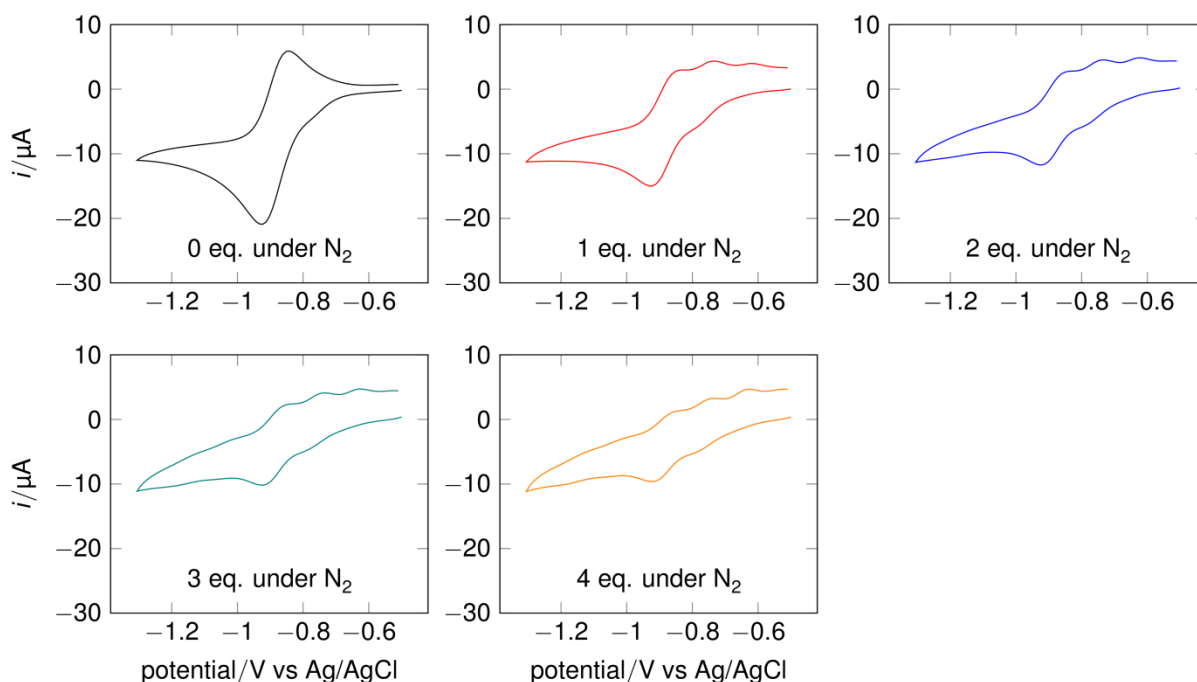


**Figure 73** Panel depiction of cyclic voltammograms of  $[\text{Fe}_4\text{S}_4(\text{SPh})_4]^{2-}$  under dinitrogen with increasing number of added equivalents of cyanide. Electrode: vitreous carbon;  $100 \text{ mV s}^{-1}$ ;  $0.1 \text{ M } [\text{Bu}_4\text{N}][\text{BF}_4] - \text{MeCN}$ ; RT;  $[\text{Cluster}] = 1.02 \text{ mM}$ .

Decay of the parent species is observed concerted with the growth and subsequent loss of the peak current associated with the couple at  $-0.76 \text{ V}$  and gradual growth of the couple at  $-0.64 \text{ V}$ . These processes observed at  $-0.76$  and  $-0.64 \text{ V}$  are assigned to mono- and di-cyanide substituted cluster species,  $[\text{Fe}_4\text{S}_4(\text{SPh})_3(\text{CN})]^{2-}$  and  $[\text{Fe}_4\text{S}_4(\text{SPh})_2(\text{CN})_2]^{2-}$  respectively. The evidence for this is that replacement of four  $\text{PhS}^-$  by the electron-withdrawing  $\text{CN}^-$  anion shifts the redox couple  $[\text{Fe}_4\text{S}_4(\text{SPh})_4]^{2-/3-}$  to a potential more than  $500 \text{ mV}$  positive.<sup>269</sup> Successive substitution of one thiolate by  $\text{CN}^-$  would be expected to shift the potentials incrementally by about  $0.12 \text{ V}$  (as observed in the voltammetry). Further evidence in support of a stepwise change in potential on substitution is provided in the discussion below (see Figure 80).

The loss in peak intensity for the parent complex is not matched by the increase in intensity for the product species observed as is clear from Figure 74. This may be attributable to the

formation of tri- or tetra-substituted species (or other products) which are not electroactive in the detection window of our experiments. The positive limit of the window was restricted by multi-electron oxidation of the cluster<sup>264</sup> and phenylthiolate oxidation which occurs as an irreversible process near 0.3 V. The negative range of the window was limited by the second reduction process of the parent dianion (near -1.5 V).

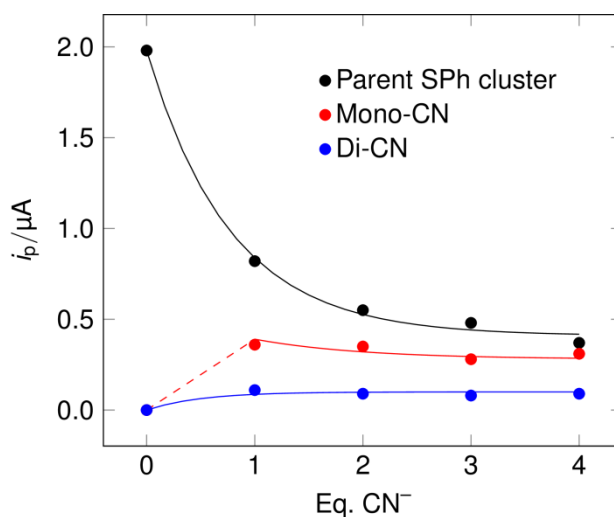


**Figure 74** Peak current  $i_p^{\text{red}}$  vs number of added cyanide equivalents under a N<sub>2</sub> atmosphere for the waves corresponding to the parent [Fe<sub>4</sub>S<sub>4</sub>(SPh)<sub>4</sub>]<sup>2-</sup> cluster and the putative mono- and di-cyanide substituted clusters at  $E_{1/2}$  potentials of -0.89, -0.76 and -0.64 V respectively. Electrode: vitreous carbon; 100 m Vs<sup>-1</sup>; 0.1 M [Bu<sub>4</sub>N][BF<sub>4</sub>] – MeCN; RT; [Cluster] = 1.02 mM.

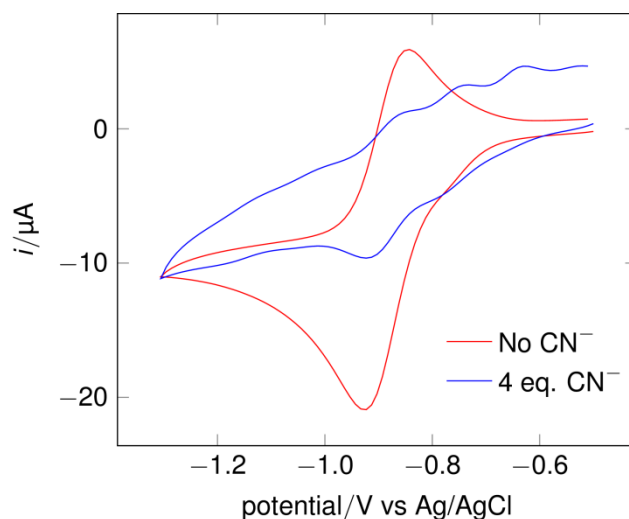


**Figure 75** Cyclic voltammogram of  $[\text{Fe}_4\text{S}_4(\text{SPh})_4]^{2-}$  under dinitrogen with 0 eq. and 4 eq. of tetraethylammonium cyanide. Electrode: vitreous carbon;  $100 \text{ mV s}^{-1}$ ;  $0.1 \text{ M } [\text{Bu}_4\text{N}][\text{BF}_4] - \text{MeCN}$ ; RT;  $[\text{Cluster}] = 1.02 \text{ mM}$ .

In the cyclic voltammetry of  $[\text{Fe}_4\text{S}_4(\text{SEt})_4]^{2-}$  under dinitrogen in the presence of cyanide, the peak current of the wave corresponding to the starting material decreased in size with increasing  $\text{CN}^-$  concentration and two new waves at more positive potentials are observed, Figure 76. This parallels the behaviour of the thiophenolate system except that the process is better defined.

The values of the two reversible couples at  $E_{1/2} = -0.97$  and  $-0.79 \text{ V}$  and these are correspondingly assigned to the mono- and di- cyanide substituted cluster couples  $[\text{Fe}_4\text{S}_4(\text{SEt})_3(\text{CN})]^{2-/3-}$  and  $[\text{Fe}_4\text{S}_4(\text{SEt})_2(\text{CN})_2]^{2-/3-}$ , respectively. As discussed this assignment is supported by the observation that substitution of  $\text{RS}^-$  for  $\text{CN}^-$  shifts the redox potentials to more positive values as is subsequently demonstrated for the series  $[\text{Fe}_4\text{S}_4(\text{SR})_{4-n}(\text{CN})_n]^{2-/3-}$  as discussed later in this chapter.

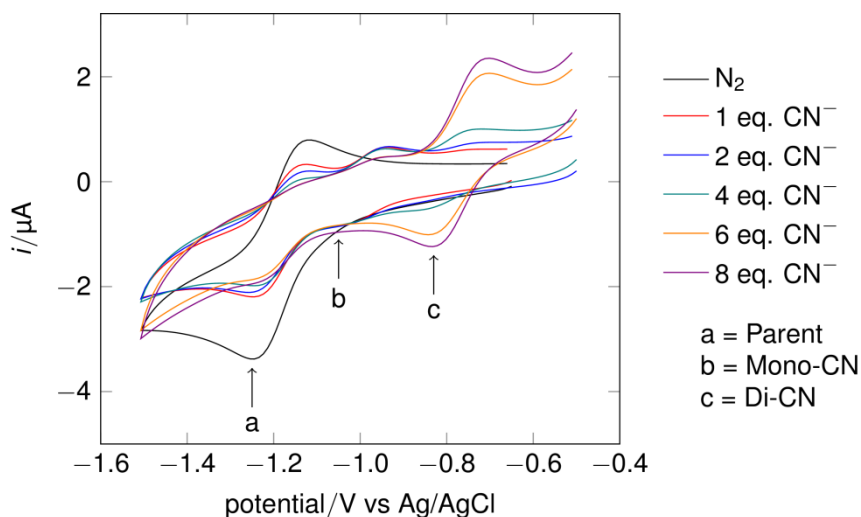


**Figure 76** Cyclic voltammogram of  $[\text{Fe}_4\text{S}_4(\text{SEt})_4]^{2-}$  under dinitrogen with increasing concentration of cyanide. a = parent  $[\text{Fe}_4\text{S}_4(\text{SEt})_4]^{2-3-}$ , b = mono-cyanide  $[\text{Fe}_4\text{S}_4(\text{SEt})_3(\text{CN})]^{2-3-}$ , c = di-cyanide  $[\text{Fe}_4\text{S}_4(\text{SEt})_2(\text{CN})_2]^{2-3-}$ . Electrode: vitreous carbon;  $50 \text{ mV s}^{-1}$ ;  $0.1 \text{ M } [\text{Bu}_4\text{N}][\text{BF}_4] - \text{MeCN}$ ; RT;  $[\text{Cluster}] = 0.55 \text{ mM}$ .

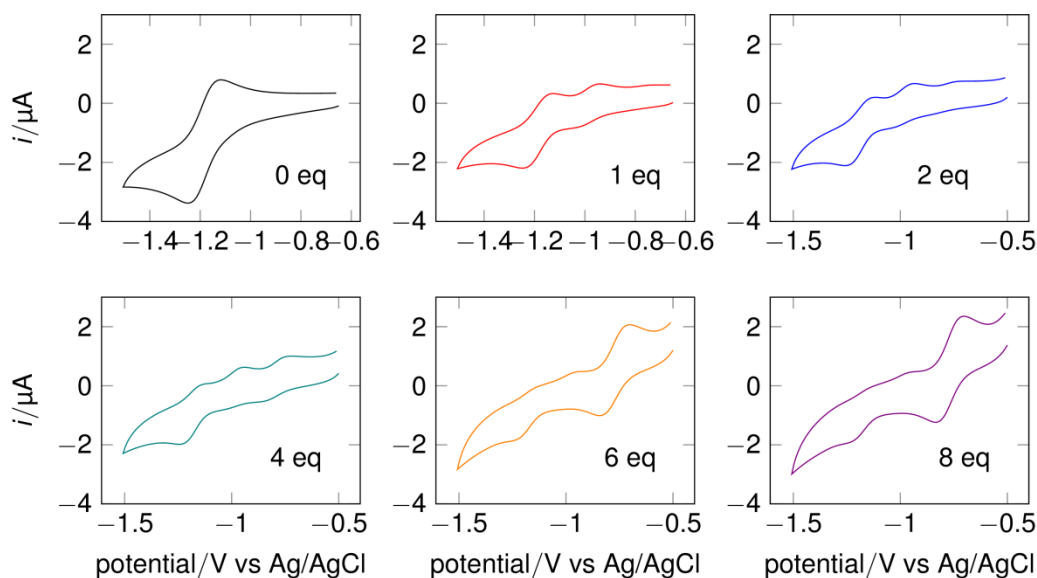


**Figure 77** Cyclic voltammogram of  $[\text{Fe}_4\text{S}_4(\text{SET})_4]^{2-}$  under dinitrogen with increasing concentration of cyanide. Electrode: vitreous carbon;  $50 \text{ mV s}^{-1}$ ;  $0.1 \text{ M } [\text{Bu}_4\text{N}][\text{BF}_4] - \text{MeCN}$ ; RT;  $[\text{Cluster}] = 0.55 \text{ mM}$ .

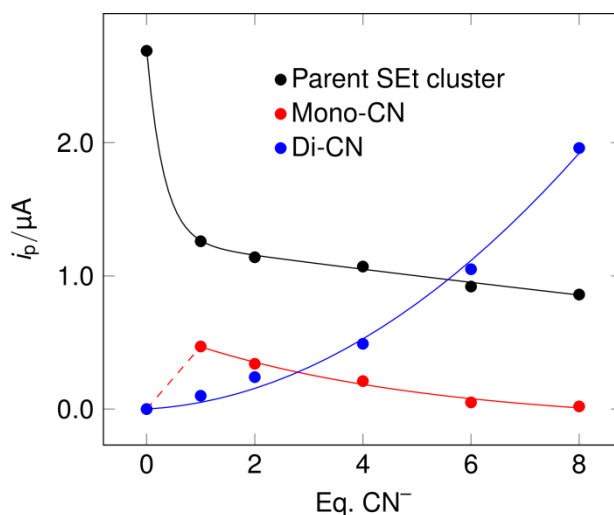


**Figure 78** Peak current of the parent cluster  $[\text{Fe}_4\text{S}_4(\text{SEt})_4]^{2-}$ , mono- and di-cyanide substituted species  $[\text{Fe}_4\text{S}_4(\text{SEt})_3(\text{CN})]^{2-}$  and  $[\text{Fe}_4\text{S}_4(\text{SEt})_2(\text{CN})_2]^{2-}$  respectively, versus number of  $\text{CN}^-$  equivalents added. Electrode: vitreous carbon;  $50 \text{ mV s}^{-1}$ ;  $0.1 \text{ M } [\text{Bu}_4\text{N}][\text{BF}_4] - \text{MeCN}$ ; RT;  $[\text{Cluster}] = 0.55 \text{ mM}$ .

Figure 78 shows the plot of the peak currents for the parent and product species versus  $[\text{CN}^-]$ . The peak assigned to the mono-cyanide species decreases with increasing cyanide whereas that for the di-cyanide product progressively increases and is the major species at 8 equivalents of cyanide. The parent peak initially rapidly decreases with addition of cyanide but then apparently plateaus at higher concentrations. Figure 79 shows that the redox system observed at  $-1.20 \text{ V}$  in the presence of 8 equivalents of  $\text{CN}^-$  is only partially reversible compared to that of the parent complex which is fully reversible but the  $E_{1/2}$  for the process is essentially unchanged. The partial reversibility suggests that a new species may have been formed via a redox process at a potential close to that of the parent  $[\text{Fe}_4\text{S}_4(\text{SEt})_4]^{2-/3-}$  couple. A possible redox couple that we have considered is  $[\text{Fe}_4\text{S}_4(\text{CN})_4]^{3-/4-}$  which is the secondary reduction step of the tetra cyano-dianion. However, Holm and co-workers have reported this to be at  $-1.29 \text{ V}$  as corrected for our potential scale.<sup>265</sup>

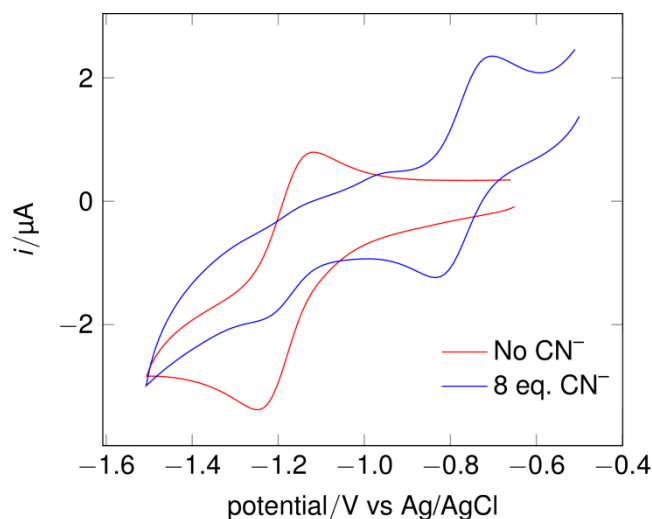


**Figure 79** Cyclic voltammogram of  $[\text{Fe}_4\text{S}_4(\text{SEt})_4]^{2-}$  under dinitrogen with 8 eq. of cyanide. Electrode: vitreous carbon;  $50 \text{ mV s}^{-1}$ ;  $0.1 \text{ M } [\text{Bu}_4\text{N}][\text{BF}_4] - \text{MeCN}$ ; RT;  $[\text{Cluster}] = 0.55 \text{ mM}$ .

The difference in substitution behaviour between the  $[\text{Fe}_4\text{S}_4(\text{SEt})_4]^{2-}$  cluster and the  $[\text{Fe}_4\text{S}_4(\text{SPh})_4]^{2-}$  as observed in these CV experiments in the presence of  $\text{CN}^-$  suggests that there is a greater tendency for the thiophenolate cluster to undergo extensive  $\text{CN}^-$  substitution whereas the tetra-ethyl thiolate appears to give predominantly the di-substituted product with excess  $\text{CN}^-$ . The  $\text{EtS}^-$  ligand is more electron donating than the thiophenolate and as electron-withdrawing  $\text{CN}^-$  is added to the core the remaining ethane thiolate-Fe bonding may be enhanced by the depletion of electron density from the cluster core. This may involve engagement of the lone pairs of the thiolate in bonding.

A summary of the proposed substitution pattern of the clusters with  $\text{CN}^-$  is shown later in this chapter in Figure 80. Integral to this scheme and the discussion above is that the redox processes observed at successively positive potentials are for the mono- and di- substituted species for both types of cluster. Further support for these assignments is now provided by the following observations which relate the redox potentials of homoleptic clusters to their

degree of substitution by a heteroligand. Here it is appropriate to consider comparable work illustrating this additive effect in other cluster systems.

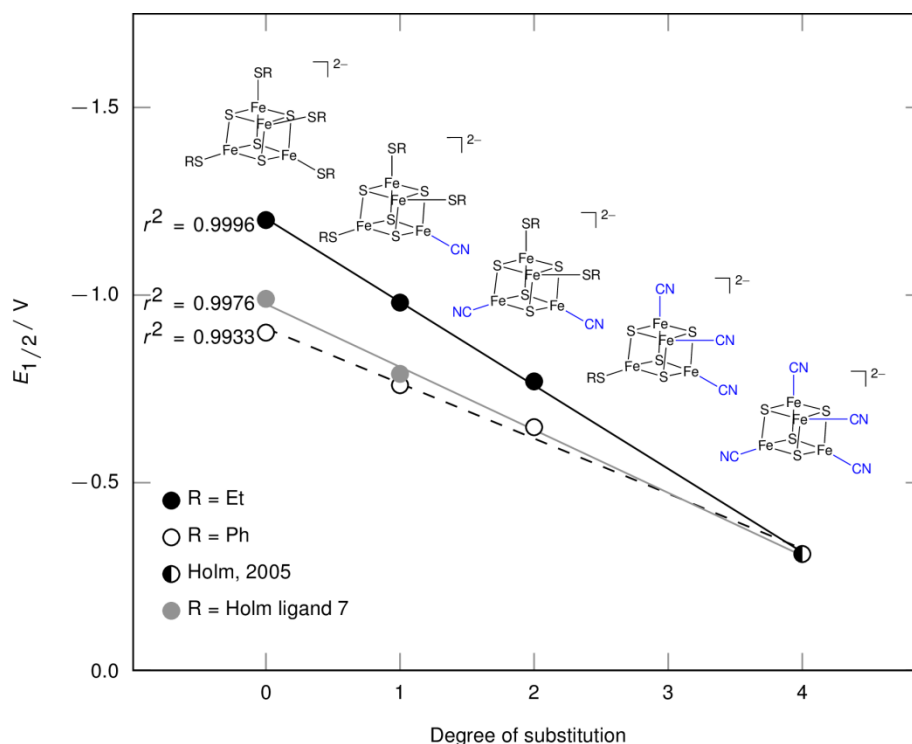
Work by the Wang group reports a photoelectron spectroscopy study (PES) probing the effect of terminal ligands on the electronic structure of  $\{4\text{Fe}4\text{S}\}^{2+}$  clusters in several series of substitutions involving different ligands.<sup>266</sup> Intrinsic oxidation energies can be represented by the electron binding energies of the respective gaseous complexes. In the substitution series  $[\text{Fe}_4\text{S}_4\text{Cl}_{4-n}(\text{CN})_n]^{2-}$  for  $n = 0, 1, 2, 3, 4$  (and for the other ligand series reported in the work) the resulting additivity pattern is linear and is consistent with patterns seen in redox potentials of mixed-ligand  $\{4\text{Fe}4\text{S}\}^{2+}$  complexes in solution but for the  $\{4\text{Fe}4\text{S}\}^{2+/1+}$  couples. Work by the Holm group demonstrates that in the two ligand substitution series  $[\text{Fe}_4\text{S}_4(\text{SCH}_2\text{Ph})_{4-n}\text{Cl}_n]^{2-}$  and  $[\text{Fe}_4\text{S}_4(\text{SCH}_2\text{Ph})_{4-n}(\text{OAc})_n]^{2-}$ , with  $n = 1, 2, 3, 4$  a positive shift in potential is observed with each successive substitution of around 100 mV illustrating a linear relationship between the number of substitutions  $n$  and the reduction potential.<sup>271</sup> This is a similar observation to the results reported by Wang and co-workers of the gas phase electron binding energies for mixed ligand  $\{4\text{Fe}4\text{S}\}^{2+}$  complexes.

Table 5 lists the redox potentials of the  $[\text{Fe}_4\text{S}_4(\text{SR})_{4-n}(\text{CN})_n]^{2-/3-}$  couples measured in this work for the  $n = 0, 1, 2$  the value for the  $[\text{Fe}_4\text{S}_4(\text{CN})_4]^{2-/3-}$  as reported by Holm,<sup>265</sup> together with data for the site-differentiated cluster (see Chapter 5). The relationship between number of cyanide substitutions and potential is shown to be linear, Figure 80.

**Table 5** Redox potentials of the  $[\text{Fe}_4\text{S}_4(\text{SR})_{4-n}(\text{CN})_n]^{2-/3-}$  couples measured in this work for  $n = 0, 1, 2$  and the value for the  $[\text{Fe}_4\text{S}_4(\text{CN})_4]^{2-/3-}$  as reported by Holm,<sup>265</sup> together with data for the site-differentiated cluster  $[\text{Fe}_4\text{S}_4(\text{LS}_3)(\text{SEt})_{1-n}(\text{CN})_n]^{2-/3-}$ . No data is available (n/a) for the tri-cyano substituted clusters or for the partially ligated Holm cluster **8**; where a dash (-) is given in the tabulation the redox series  $[\text{Fe}_4\text{S}_4(\text{SR})_{4-n}(\text{CN})_n]^{2-/3-}$  does not apply.

Degree of substitution	Redox potential of $[\text{Fe}_4\text{S}_4(\text{SR})_{4-n}(\text{CN})_n]^{2-/3-}$ / V				Reference
	$n$	R = Ph	R = Et	R = LS <sub>3</sub> (7)	
0	-0.90	-1.20	-0.99	-	This work
1	-0.76	-0.98	-0.79	-	This work
2	-0.65	-0.79	n/a	-	This work
3	n/a	n/a	n/a	-	
4	-0.31	-0.31	-0.31	-0.31	Ref. 265

Figure 80 shows a plot of the potentials for the various  $[\text{Fe}_4\text{S}_4(\text{SR})_{4-n}(\text{CN})_n]^{2-/3-}$  couples as listed in Table 5 versus the degree of substitution  $n$ . The least mean squares fits to the three sets of data all show high correlation coefficients ( $>0.99$ ) and *most importantly* converge for  $n = 4$  at the “common” value for the tetracyano-cluster. Thus this analysis strongly supports the assignments of the observed redox processes to the mono- and di-cyanide substituted clusters.



**Figure 80** Plot of the potentials of  $[\text{Fe}_4\text{S}_4(\text{SR})_{4-n}(\text{CN})_n]^{2-/3-}$  couples. The  $r^2$  values are the correlation coefficients for the least mean squares fit to the data. Error in potentials are estimated to be  $\pm 5$  mV.

#### 4.3.4 Stopped-flow FTIR studies of the reaction of cyanide and $[\text{Fe}_4\text{S}_4(\text{SR})_4]^{2-}$ clusters (R = Et and Ph) under $\text{N}_2$

In the previous section cyclic voltammetry experiments on the  $[\text{Fe}_4\text{S}_4(\text{SR})_4]^{2-}$  (R = Ph or Et) clusters in the presence of  $\text{CN}^-$  provided evidence for the formation of substituted clusters. It was therefore thought that stopped-flow FTIR experiments on the  $[\text{Fe}_4\text{S}_4(\text{SR})_4]^{2-}$  might allow spectroscopic characterization of the stable species formed and possible intermediates on the pathway(s) to these. Here it is appropriate to consider some general aspects of the infrared spectra of cyanide coordination to metal centres.

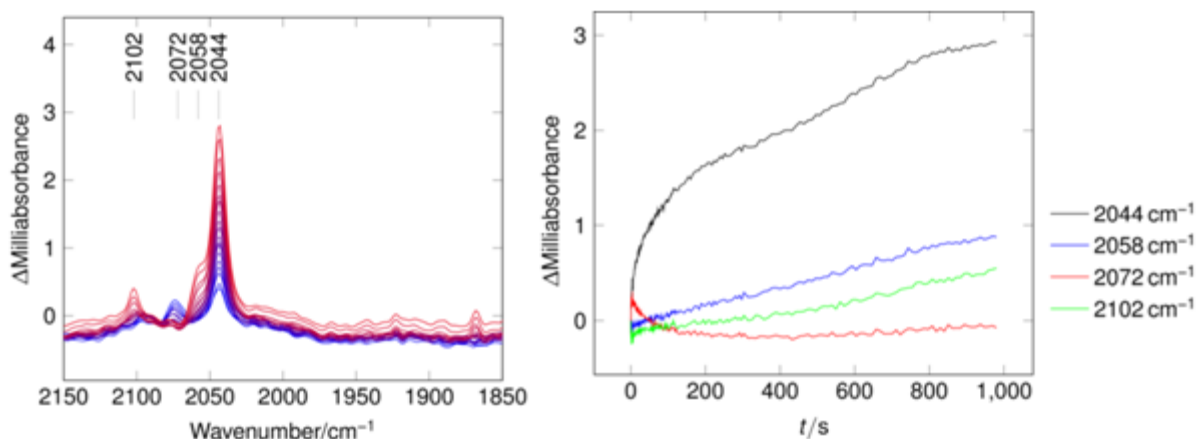
In the octahedral ferric and ferrous compounds  $\text{K}_3[\text{Fe}(\text{CN})_6]$  and  $\text{K}_4[\text{Fe}(\text{CN})_6]$ , the  $\text{CN}^-$  stretching frequencies are reported as 2116 and 2041  $\text{cm}^{-1}$ , respectively.<sup>265</sup> Thus the frequency of the major vibrational stretching mode of cyanide is shifted to lower

wavenumber as the electron complement of the metal centre is formally increased. This can be explained by increased back bonding from metal  $d\pi$  into cyanide  $\pi^*$  orbitals which weakens the CN bond in the same fashion as is observed for CO stretching frequencies. Another perhaps more relevant example is the comparison between  $[\text{Fe}_4\text{S}_4(\text{CN})_4]^{4-}$  and  $[\text{Fe}_4\text{S}_4(\text{CN})_4]^{3-}$ . Holm reports  $\nu(\text{CN})$  of the former species as  $2050\text{ cm}^{-1}$  and that of the latter, more oxidised cluster, as  $2103\text{ cm}^{-1}$ . This is again emphasizing how the electron density of the cluster influences the stretching frequencies.<sup>265</sup> There is no reported value for the  $[\text{Fe}_4\text{S}_4(\text{CN})_4]^{2-}$ . A crude extrapolation suggests that  $\nu(\text{CN})$  would be in the region of  $2150\text{ cm}^{-1}$ . Whereas the tetracyano  $3-$  and  $4-$  clusters clearly illustrate the effect of core oxidation state on  $\nu(\text{CN})$ , comparative data for successive mono, di and tri-substituted cyano-clusters is unavailable. Dr Maurizio Bruschi (Milan-Biccoca) has kindly undertaken advanced DFT calculations on the mono- and di-substituted clusters  $[\text{Fe}_4\text{S}_4(\text{SPh})_3(\text{CN})]^{2-}$  and  $[\text{Fe}_4\text{S}_4(\text{SPh})_2(\text{CN})_2]^{2-}$  the calculated  $\nu(\text{CN})$  values for these species are shown in

Table 6 Table 6. Here it is notable that the mono-cyanide cluster has  $\nu(\text{CN})$  at a higher frequency ( $2114 \text{ cm}^{-1}$ ) than the dicyano-species ( $2093 \text{ cm}^{-1}$ ). Which is perhaps surprising considering the change observed upon reduction of the cluster. What must be taken into account is that removing electron density from the cluster core by replacing a thiolate ligand with overlap contributions from the sulfur lone pairs and replacing it by  $\text{CN}^-$  would deplete electron density on the core and enhance donation from  $\text{CN}^-$  N–C–Fe sigma framework, thereby weakening the CN bond and lowering the stretching frequency. Thus there are two mechanisms for moderating the frequency of  $\nu(\text{CN})$ : enhancing the back-donation in  $\pi^*$  or depleting electron density through the sigma system. These effects are discussed as synergistic but their relative contribution can clearly be influenced by co-ligands.

The cluster  $[\text{Fe}_4\text{S}_4(\text{SPh})_4]^{2-}$  was reacted with  $\text{CN}^-$  in MeCN under  $\text{N}_2$  and was monitored by stopped-flow FTIR. Figure 81 shows the pattern of bands which emerge over the course of 16 minutes upon reaction of the cluster with five equivalents of  $\text{CN}^-$ , together with the time-course of the growth of the four observed bands. The band at  $2072 \text{ cm}^{-1}$  decays with time and is likely to be an intermediate on the pathway to the other products. The frequency  $2072 \text{ cm}^{-1}$ , is close to that predicted in the DFT experiments for the  $[\text{Fe}_4\text{S}_4(\text{SPh})_4(\text{CN})]^{3-}$  species where cyanide and thiolate share a corner of the cube. A species with two cyanides displacing a single thiolate is predicted to give two bands at  $2071$  and  $2066 \text{ cm}^{-1}$ , which would probably not be distinguishable as two bands. It is possible that the major band observed at  $2044 \text{ cm}^{-1}$  which occurs in this spectrum and subsequent spectra involving other clusters is attributable to  $[\text{Fe}(\text{CN})_6]^{4-}$ . The solid state spectra of  $\text{K}_4[\text{Fe}(\text{CN})_6]$  has been reported as  $2041 \text{ cm}^{-1}$ .<sup>265</sup> Dissolution of this species in MeCN using 18-crown-6-ether shifts this band to  $2045 \text{ cm}^{-1}$ . The ferrocyanide band may arise removal of an  $\text{Fe}^{\text{II}}$  from the cluster core. The (reversible) removal of a single iron atom from a cubane core in biological systems has been demonstrated.<sup>272</sup>

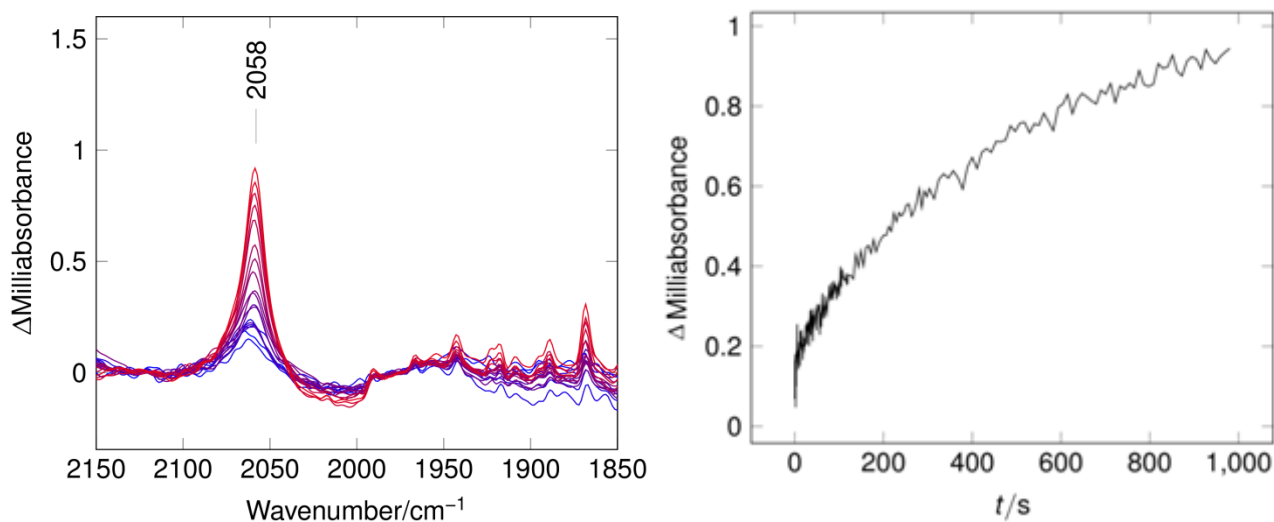
The band which grows in at  $2102\text{ cm}^{-1}$  has a frequency between that predicted for the mono- and the di-cyanide substituted clusters. It is likely to be the mono-cyanide species as a similar band is observed in studies of the site differentiated cluster at  $2098\text{ cm}^{-1}$  (see Chapter 5).



**Figure 81** Stopped-flow FTIR spectra of the reaction of  $[\text{Fe}_4\text{S}_4(\text{SPh})_4]^{2-}$  with five equivalents of  $\text{CN}^-$  in MeCN under  $\text{N}_2$ . Blue: early scans, red: later scans. Initial  $[\text{Cluster}] = 1 \text{ mM}$ .

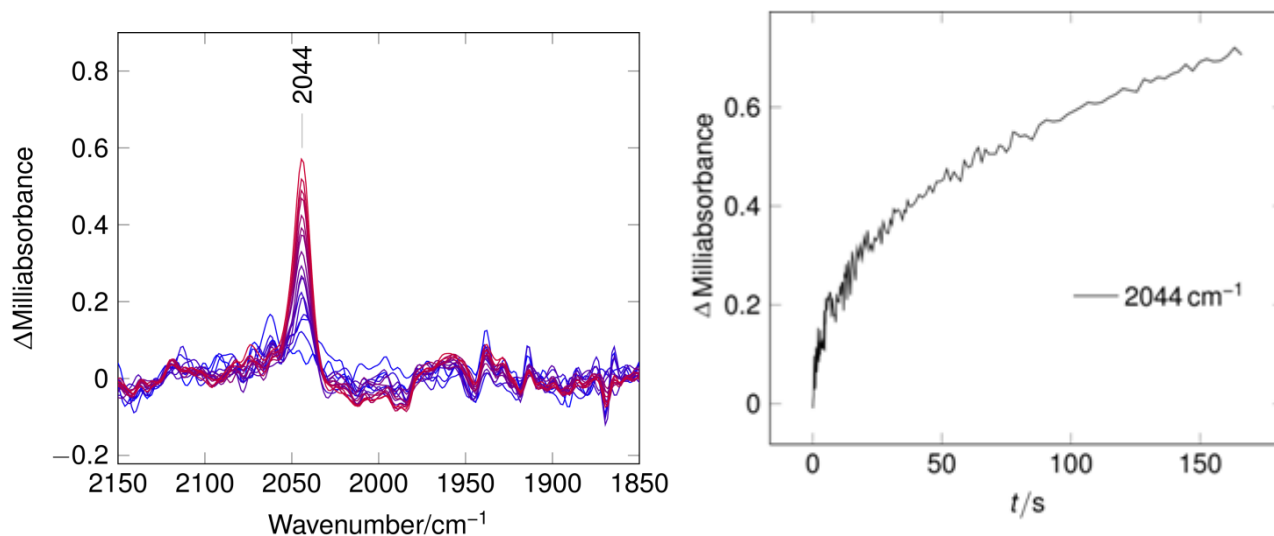
Growth of bands at 2102, 2072, 2058 and 2044  $\text{cm}^{-1}$  over 16 min.

We have also examined the effect of one equivalent of cyanide on the stopped-flow FTIR of  $[\text{Fe}_4\text{S}_4(\text{SPh})_4]^{2-}$ , Figure 82. The spectrum shows the growth of a dominant species at 2058  $\text{cm}^{-1}$ . This band is not readily assignable. As it grows in before the formation of the 2044  $\text{cm}^{-1}$  band, at high  $\text{CN}^-$ , we suggest that it may be a precursor to ferrocyanide. This might be a species in which three cyanides are coordinated to a single Fe atom or a released mono-nuclear iron complex. A possible candidate would be an  $[\text{Fe}(\text{SPh})(\text{CN})_3]^{2-}$  species extruded from the cubane core. Whereas  $[\text{Fe}(\text{SPh})_4]^{2-}$  is a well-established species, partial substitution of thiolate ligands by  $\text{CN}^-$  has not been reported as far as we are aware.



**Figure 82** Left: Stopped-flow FTIR spectra of the reaction of  $[\text{Fe}_4\text{S}_4(\text{SPh})_4]^{2-}$  with one equivalent of  $\text{CN}^-$  in MeCN under  $\text{N}_2$ . Blue: early scans, red: later scans. [Cluster initial] = 1 mM. Right: growth of band at 2058  $\text{cm}^{-1}$  over 16 min.

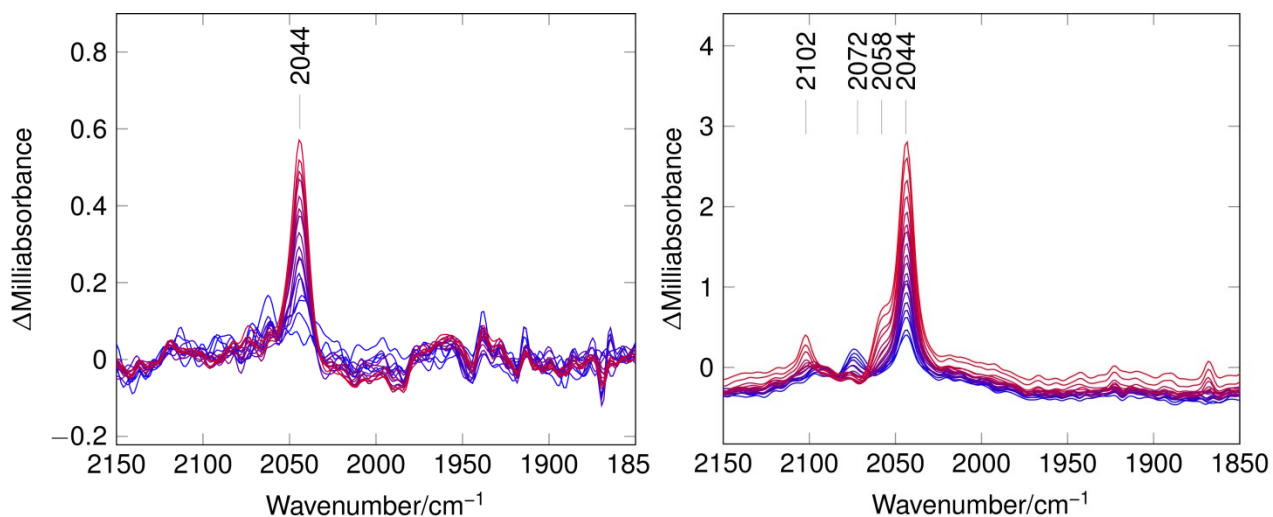
Stopped-flow experiments with the  $[\text{Fe}_4\text{S}_4(\text{SEt})_4]^{2-}$  showed that with 8 eq. of cyanide the a single species was detected at 2044  $\text{cm}^{-1}$  (Figure 83), i.e. at a frequency identical to that observed for the phenylthiolate cluster under similar conditions. At lower concentration of cyanide bands at 2056 and 2044  $\text{cm}^{-1}$  were observed.



**Figure 83** Left: Stopped-flow FTIR spectra of the reaction of  $[\text{Fe}_4\text{S}_4(\text{SEt})_4]^{2-}$  with eight equivalents of  $\text{CN}^-$  in MeCN under  $\text{N}_2$ . Blue: early scans, red: later scans.  $[\text{Cluster initial}] = 1 \text{ mM}$ . Right: growth of band at  $2044 \text{ cm}^{-1}$  over 3 min.

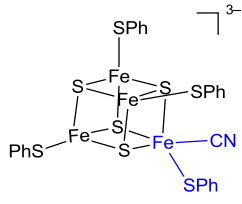
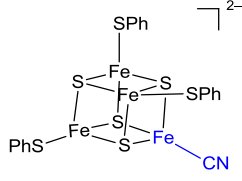
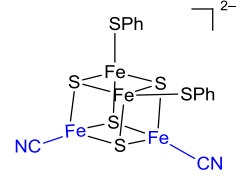
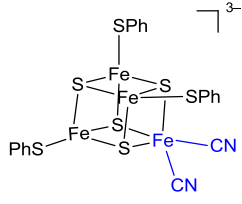
If we accept that the common  $2044 \text{ cm}^{-1}$  band is ferrocyanide then we are clearly not observing the same chemistry as is observed in the cyclic voltammetry. The tetraethanethiolate cluster is more oxygen sensitive than is its tetraphenylthiolate counterpart. Low levels of oxygen in the glovebox where the samples were manipulated may lead to cluster degradation and ferrocyanide formation, a problem not evident in the cyclic voltammetry experiments. What is clear is that experiments in which CO and  $\text{CN}^-$  are present as co-substrates, lead to well-defined spectra in which the bands at  $2044$  and  $2058 \text{ cm}^{-1}$  are suppressed and do not appear except at long times with high concentrations of cyanide as minor products. If the  $2045 \text{ cm}^{-1}$  band of ferrocyanide is not that which is observed as the major absorption in our experiments then  $2044 \text{ cm}^{-1}$  can be correlated with the cyclic voltammetry as arising from a di-cyanide species and that at  $2058 \text{ cm}^{-1}$  with the mono-cyanide. The frequencies differ considerably from those that have been calculated by DFT however, that the di-cyanide has a lower frequency than the mono-cyanide is consistent with the calculations. Further insight into the interpretation of the reactions of the clusters with cyanide alone comes from a study of the site differentiated cluster as discussed in Chapter 5.

What has been established is the bands and frequencies that can be associated with cyanide as a single substrate for comparison with its reaction as a co-substrate with CO. Unequivocally CO, which has intense absorption when bound as a terminal ligand does not bind to the parent clusters alone.



**Figure 84** Comparison of stopped-flow FTIR spectra of reaction of  $[\text{Fe}_4\text{S}_4(\text{SR})_4]^{2-}$  clusters at “high cyanide” concentration in MeCN. Left:  $[\text{Fe}_4\text{S}_4(\text{SEt})_4]^{2-}$  with 8 eq.  $\text{CN}^-$  over 3 min, Right:  $[\text{Fe}_4\text{S}_4(\text{SPh})_4]^{2-}$  with 5 eq.  $\text{CN}^-$  over 16 min.

**Table 6** DFT calculated IR stretching frequencies for possible CN<sup>-</sup> substituted clusters.

Proposed structure	DFT calculated CN <sup>-</sup> band(s) / cm <sup>-1</sup>
	2070
	2114
	2093
	2071, 2066

## 4.4 Synergic interactions of CO and CN<sup>-</sup> with [Fe<sub>4</sub>S<sub>4</sub>(SR)<sub>4</sub>]<sup>2-</sup> clusters

### 4.4.1 Cyclic voltammetry experiments

The interaction of the co-substrates CO and CN<sup>-</sup> with [Fe<sub>4</sub>S<sub>4</sub>(SPh)<sub>4</sub>]<sup>2-</sup> was first investigated. A solution of [Fe<sub>4</sub>S<sub>4</sub>(SPh)<sub>4</sub>]<sup>2-</sup> (circa 1 mM) was dissolved in 0.1 M [Bu<sub>4</sub>][BF<sub>4</sub>] – MeCN saturated with carbon monoxide at 1 atm (circa 13 mM at 22 °C).<sup>273</sup> Tetraethylammonium cyanide was added in aliquots up to a total of five equivalents. The effect on the cyclic voltammetry was dramatically different from that observed in the presence of either substrate alone. The reversible 2<sup>-</sup>/3<sup>-</sup> redox couple of the parent starting cluster diminished with

increasing cyanide concentration and this was concerted with the appearance of two new overlapping reversible processes at more negative potentials. These grew in near  $-1.1$  V versus the Ag/AgCl reference electrode. With increasing cyanide concentration the more negative of these closely spaced couples was suppressed and at five equivalents a single species dominated. These results are illustrated by Figure 85 and a panel of the voltammograms shown in Figure 86.

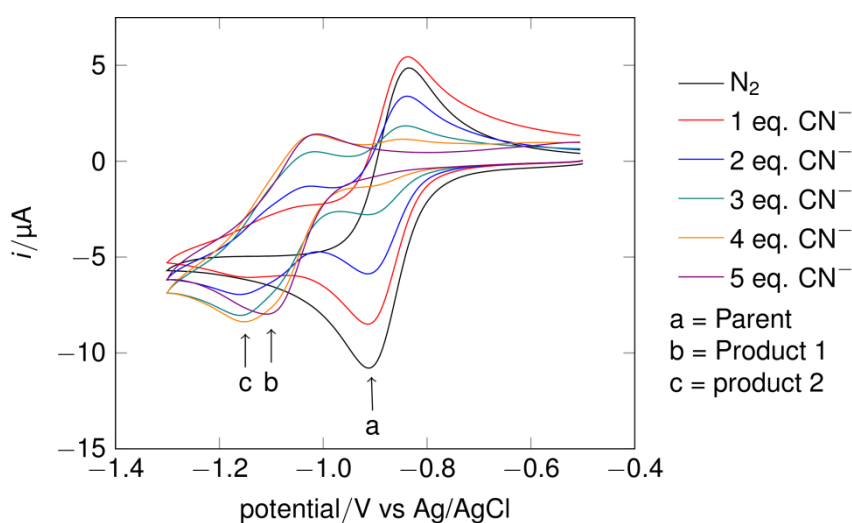


**Figure 85** Cyclic voltammogram of  $[\text{Fe}_4\text{S}_4(\text{SPh})_4]^{2-}$  under carbon monoxide with increasing concentration of cyanide. Electrode: vitreous carbon;  $50 \text{ mV s}^{-1}$ ;  $0.1 \text{ M } [\text{Bu}_4\text{N}][\text{BF}_4] - \text{MeCN}$ ; RT;  $[\text{Cluster}] = 0.9 \text{ mM}$ .

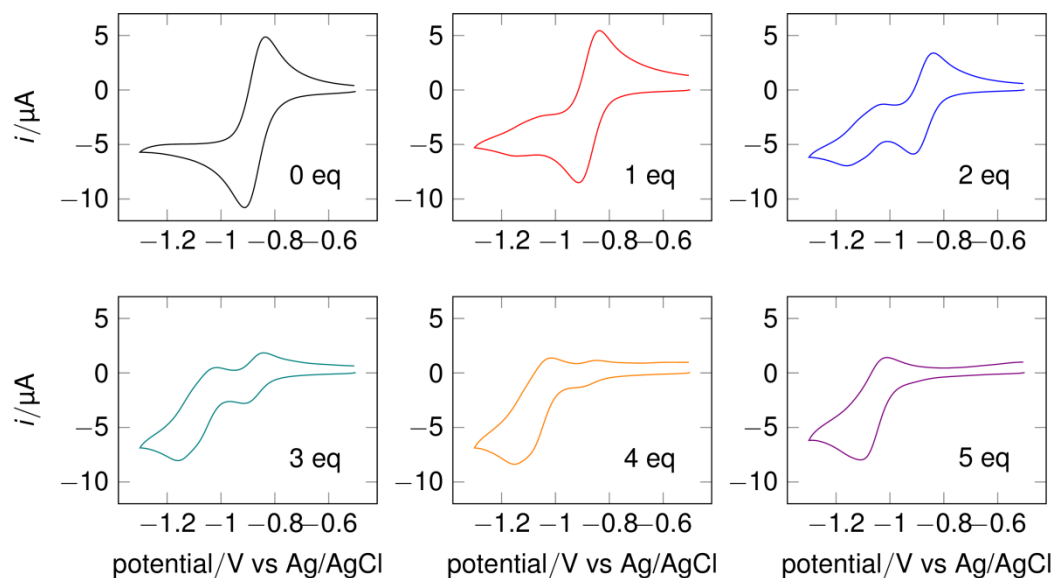


**Figure 86** Panel depiction of cyclic voltammograms of  $[\text{Fe}_4\text{S}_4(\text{SPh})_4]^{2-}$  under carbon monoxide with increasing concentration of cyanide. Electrode: vitreous carbon;  $50 \text{ mV s}^{-1}$ ;  $0.1 \text{ M } [\text{Bu}_4\text{N}][\text{BF}_4] - \text{MeCN}$ ; RT;  $[\text{Cluster}] = 0.9 \text{ mM}$ .

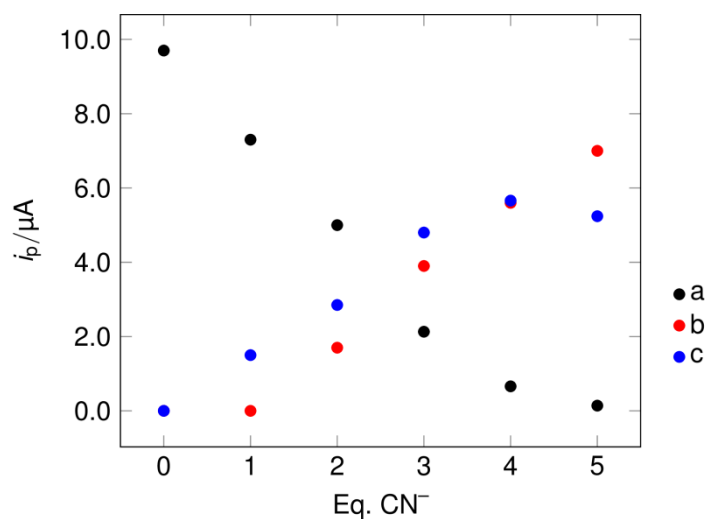


**Figure 87** The peak current  $i_p^{\text{red}}$  at the potentials  $-0.90$ ,  $-1.11$  and  $-1.16 \text{ V}$  (a, b and c, respectively, as shown in Figure 85) versus cyanide concentration in CO saturated MeCN. Electrode: vitreous carbon;  $50 \text{ mV s}^{-1}$ ;  $0.1 \text{ M } [\text{Bu}_4\text{N}][\text{BF}_4] - \text{MeCN}$ ; RT;  $[\text{Cluster}] = 0.9 \text{ mM}$ .

How the two new redox processes evolve with addition of cyanide is illustrated by Figure 87 which shows the observed peak currents for the parent material and those measured at  $-1.11$  and  $-1.16$  V, respectively. The peak currents are indicative but are not absolute measurements of species concentration because of the overlap of the two redox processes.

The order of addition of CO and  $\text{CN}^-$  does not influence the formation of the observed products. Figure 86 shows the cyclic voltammogram of the parent cluster after addition of four equivalents of cyanide under dinitrogen and the voltammetry of the same solution after purging with carbon monoxide. The two overlapping redox processes near  $-1.1$  V are generated, the peaks attributable to the mono- and the di-cyanide clusters are lost whilst the peak associated with the parent cluster is enhanced. These results suggest there is an equilibration between CO and  $\text{CN}^-$  containing species and the parent compound. This is further supported by the observation that flushing the CO saturated solution with  $\text{N}_2$  regenerates starting material and cyanide containing clusters although the process is slow.

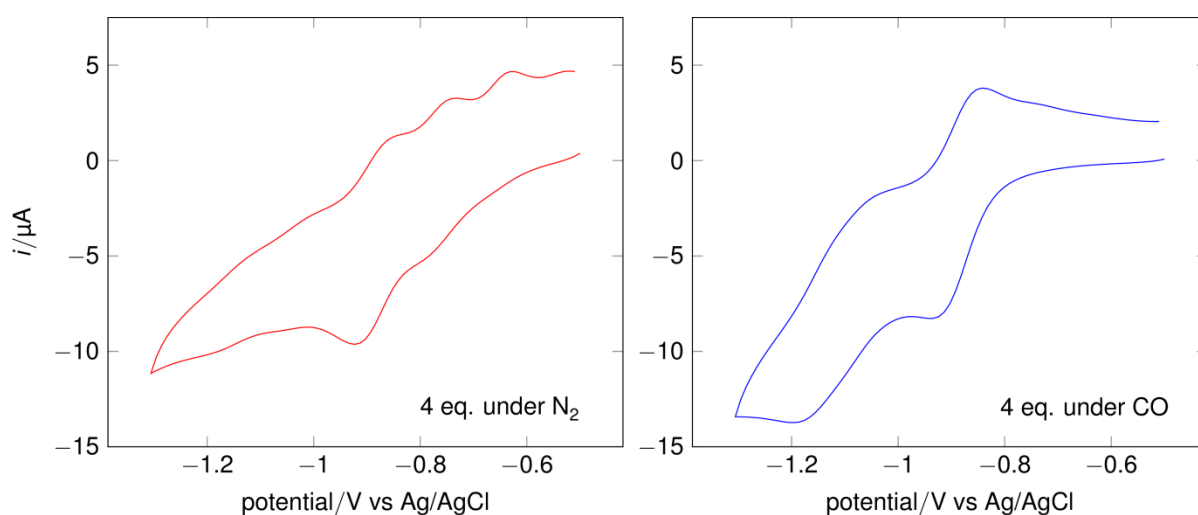


**Figure 88** Cyclic voltammogram of  $[\text{Fe}_4\text{S}_4(\text{SPh})_4]^{2-}$  with 4 eq.  $\text{CN}^-$  under  $\text{N}_2$  (red) and with 4 eq.  $\text{CN}^-$  under CO (blue). Electrode: vitreous carbon;  $100 \text{ mV s}^{-1}$ ;  $0.1 \text{ M } [\text{Bu}_4\text{N}][\text{BF}_4] - \text{MeCN}$ ; RT;  $[\text{Cluster}] = 1.02 \text{ mM}$ .

The interaction of CO and  $\text{CN}^-$  as co-substrates with  $[\text{Fe}_4\text{S}_4(\text{SEt})_4]^{2-}$  has also been examined by cyclic voltammetry. Figure 89 shows that addition of cyanide under CO results in a broadly similar pattern, a major new reversible couple is similarly observed negative of the parent couple. These voltammograms are shown separately in Figure 90.

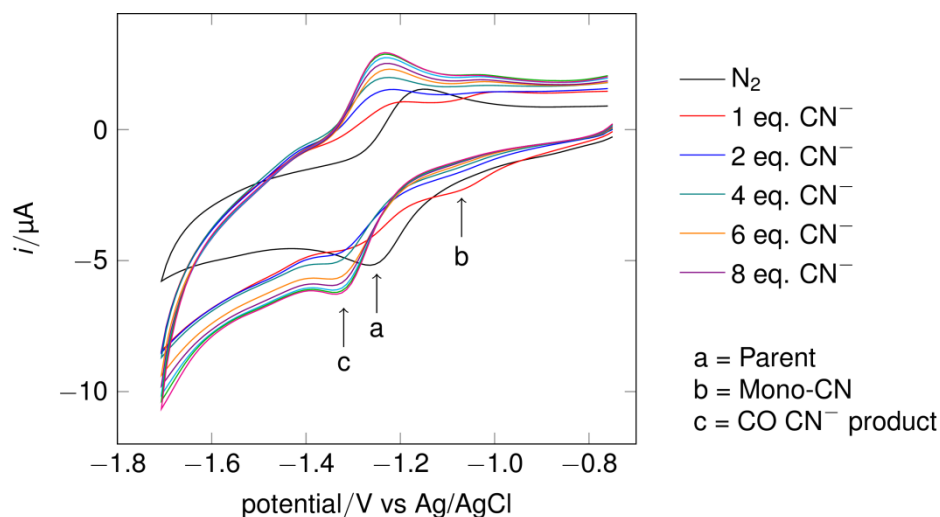


**Figure 89** Cyclic voltammogram of  $[\text{Fe}_4\text{S}_4(\text{SEt})_4]^{2-}$  under carbon monoxide with increasing concentration of cyanide. Electrode: vitreous carbon;  $50 \text{ mV s}^{-1}$ ;  $0.1 \text{ M } [\text{Bu}_4\text{N}][\text{BF}_4] - \text{MeCN}$ ; RT;  $[\text{Cluster}] = 0.54 \text{ mM}$ .

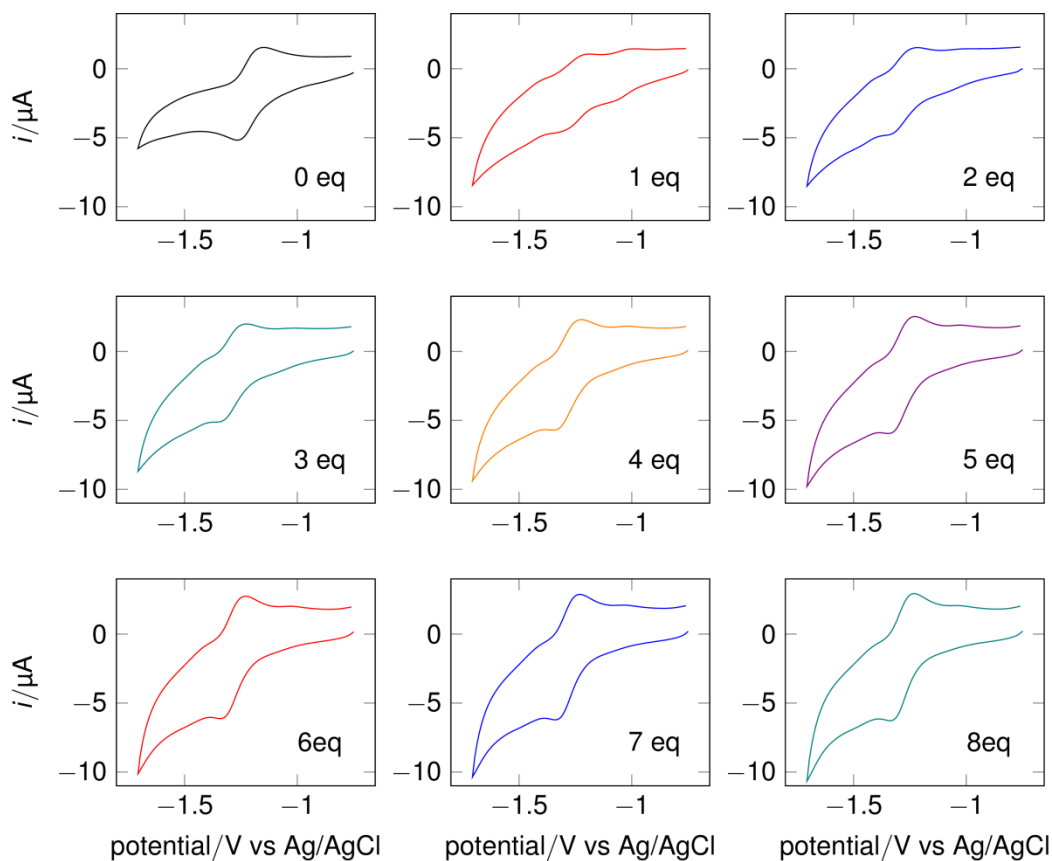


**Figure 90** Panel depiction of cyclic voltammograms of  $[\text{Fe}_4\text{S}_4(\text{SEt})_4]^{2-}$  under carbon monoxide with increasing concentration of cyanide. Electrode: vitreous carbon;  $100 \text{ mV s}^{-1}$ ;  $0.1 \text{ M } [\text{Bu}_4\text{N}][\text{BF}_4] - \text{MeCN}$ ; RT;  $[\text{Cluster}] = 0.54 \text{ mM}$ .

There are instructive differences between the two undifferentiated clusters studied. First, the observed potential of the major product differs from those observed with the thiophenolate cluster thus  $\text{EtS}^-$  (and  $\text{PhS}^-$ ) must be retained as a ligand(s) to the cluster core. Secondly, whereas the phenylthiolate system clearly shows two CO-dependent species formed at four equivalents of  $\text{CN}^-$ , the ethanethiolate system is dominated by a single reversible process. In the ethanethiolate system the more negative CO-dependent couple near  $-1.3 \text{ V}$  remains a minor process even at low  $\text{CN}^-$  concentration. Figure 91 shows the dependence of the peak currents on  $\text{CN}^-$  concentration for the parent, mono-cyanide and the CO dependent species. With the tetraethanethiolate cluster the peak current of the product at high cyanide is very close to that for the parent species before reaction. In contrast peak current of the

tetraphenylthiolate cluster CO dependent product is only about 75 % of the peak current parent cluster, Figure 87. This has correlation with the reactions of these two clusters with  $\text{CN}^-$  alone, where the tetraethanethiolate cluster shows a high conversion to the di-cyanide cluster product.

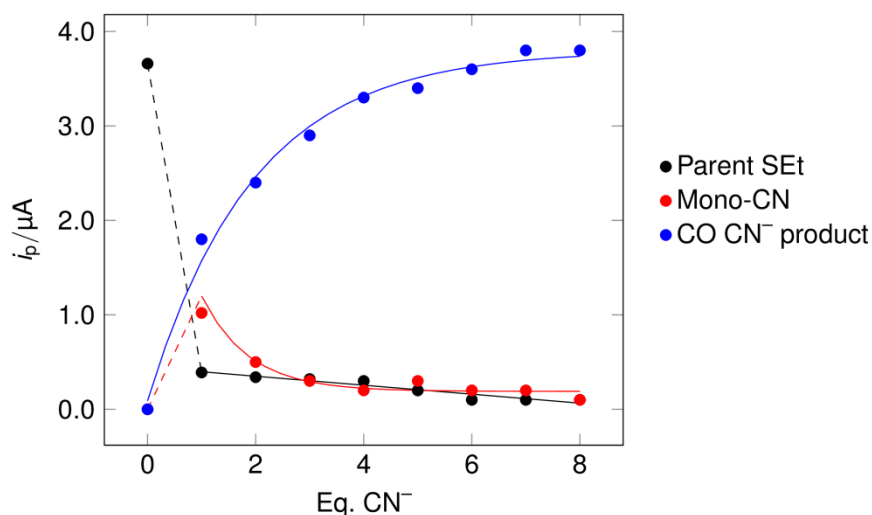


**Figure 91** Peak current  $i_p^{\text{red}}$  vs cyanide concentration under a CO atmosphere for the waves corresponding to the parent  $[\text{Fe}_4\text{S}_4(\text{SEt})_4]^{2-}$  cluster, the putative mono-cyanide and the CO, CN substituted clusters found at the potentials  $-1.21$ ,  $-1.04$  and  $-1.28$  V, respectively. Electrode: vitreous carbon;  $50 \text{ mV s}^{-1}$ ;  $0.1 \text{ M } [\text{Bu}_4\text{N}][\text{BF}_4] - \text{MeCN}$ ; RT;  $[\text{Cluster}] = 0.54 \text{ mM}$ .

As with the phenylthiolate cluster, generation of the CO-dependent product from the ethanethiolate cluster followed by sparging with  $\text{N}_2$  substantially alters the cyclic voltammetry, again indicative of an equilibrium reaction and the lability of CO. A peak which can be assigned to the di-cyanide cluster is observed at  $-0.79$  V and the CO-dependent peak at  $-1.28$  V is diminished, Figure 92. Unlike the phenylthiolate system there is limited regeneration of the parent cluster but a wave assigned to the MeCN solvato-species as discussed in Section 4.3.2 is observed. Notably a couple clearly attributable to a monocyanide species is not observed.

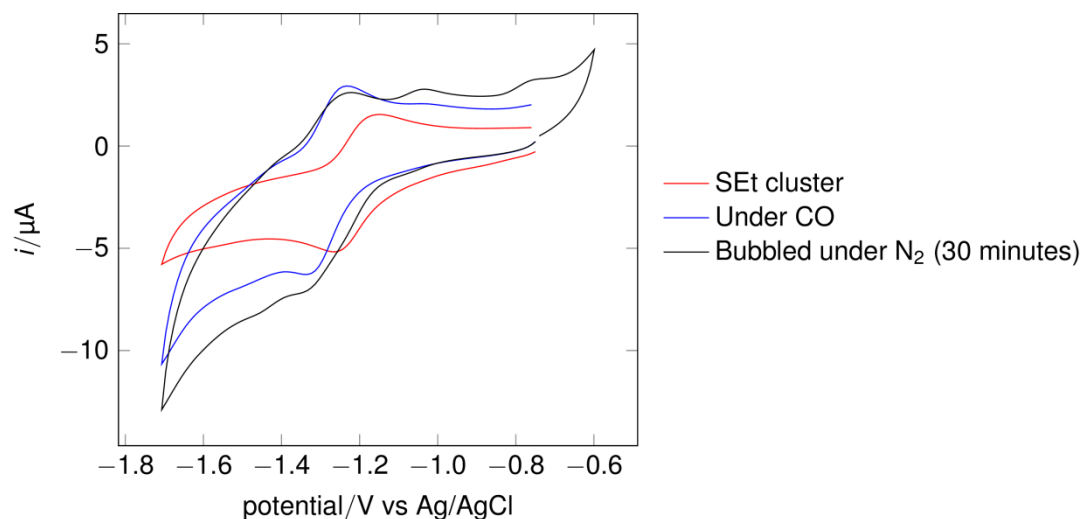


**Figure 92** Cyclic voltammogram of  $[\text{Fe}_4\text{S}_4(\text{SEt})_4]^{2-}$  under  $\text{N}_2$  with no cyanide (red), with 8 eq. of cyanide under carbon monoxide (blue) then following this treatment under  $\text{N}_2$  for 30 min (black). Electrode: vitreous carbon;  $50 \text{ mV s}^{-1}$ ;  $0.1 \text{ M } [\text{Bu}_4\text{N}][\text{BF}_4] - \text{MeCN}$ ; RT;  $[\text{Cluster}] = 0.54 \text{ mM}$ .

#### 4.5 Probing interactions of CO and $\text{CN}^-$ with $[\text{Fe}_4\text{S}_4(\text{SR})_4]^{2-}$ clusters, R = Ph or Et, by stopped-flow FTIR

The interactions of  $[\text{Fe}_4\text{S}_4(\text{SR})_4]^{2-}$  R = Ph or Et with CO and  $\text{CN}^-$  as co-substrates were investigated by stopped-flow FTIR. A solution of CO saturated cyanide solution and a CO saturated solution of the parent cluster in separate syringes were rapidly mixed in the stopped-flow mixing chamber and FTIR measurements on the resulting solution were recorded. The concentration of the clusters was generally circa  $0.5 \text{ mM}$  after mixing, cyanide concentration was varied between  $0.5$  and  $4 \text{ mM}$ . Details are given in the experimental section. Figure 93 shows the evolution of  $\text{CN}^-$  and CO bands in the IR over a period of twelve minutes after rapid mixing of a CO saturated solution of  $[\text{Fe}_4\text{S}_4(\text{SPh})_4]^{2-}$  in MeCN with a CO saturated solution of  $[\text{Et}_4\text{N}]\text{CN}$  in MeCN.

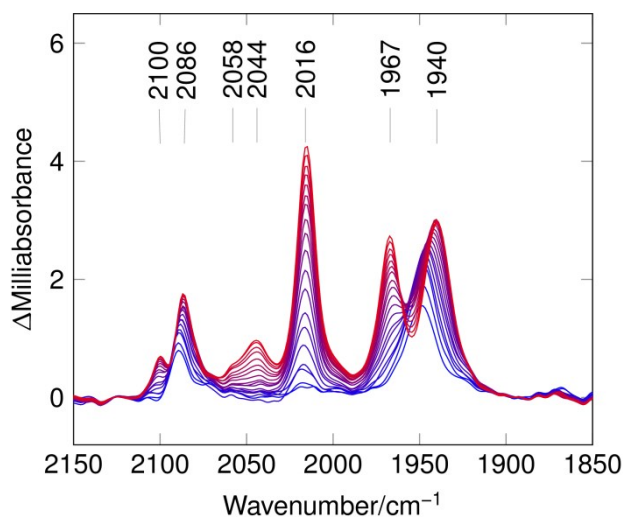


**Figure 93** Stopped-flow FTIR spectra of the reaction of  $[\text{Fe}_4\text{S}_4(\text{SPh})_4]^{2-}$  with four equivalents of  $\text{CN}^-$  in MeCN under CO over a time-course of 12 min with the time between scans increasing on a pseudo-logarithmic scale. Blue: early scans, red: later scans. Initial [Cluster] = 1 mM.

In the first two seconds after mixing, the spectrum is dominated by two bands at 2089 and 1948  $\text{cm}^{-1}$ . These frequencies are indicative of CN and CO stretching vibrations respectively, as was confirmed by the isotopic labelling experiments described below. At intermediate (70 s) and longer times a more complex spectrum evolves with three major CO stretches at 2016, 1967 and 1940  $\text{cm}^{-1}$  together with two cyanide stretches at 2100 and 2086  $\text{cm}^{-1}$ . These short, mid, and long time species are shown in Figure 94 and Figure 95. At the longer time, two cyanide bands at frequencies close to those observed for the cluster in the absence of CO at 2044 and 2058  $\text{cm}^{-1}$  also appear, Figure 95.

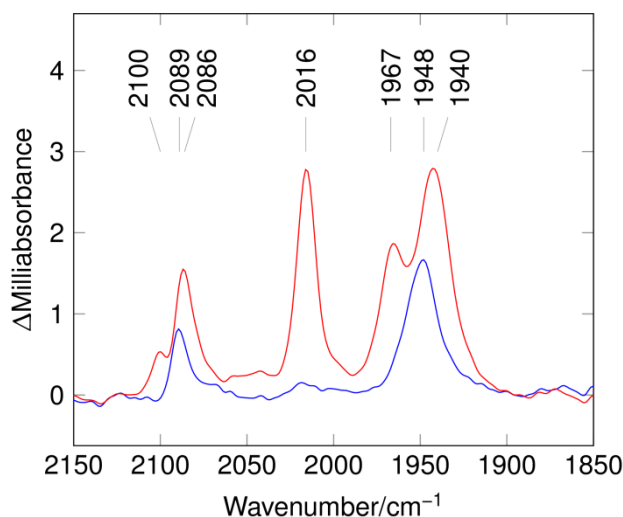


**Figure 94** Stopped-flow FTIR of the reaction of  $[\text{Fe}_4\text{S}_4(\text{SPh})_4]^{2-}$  with four equivalents of  $\text{CN}^-$  in MeCN under CO. Blue = short time (2 s), red = long time scan 70 s. Initial [cluster] = 1.1 mM.

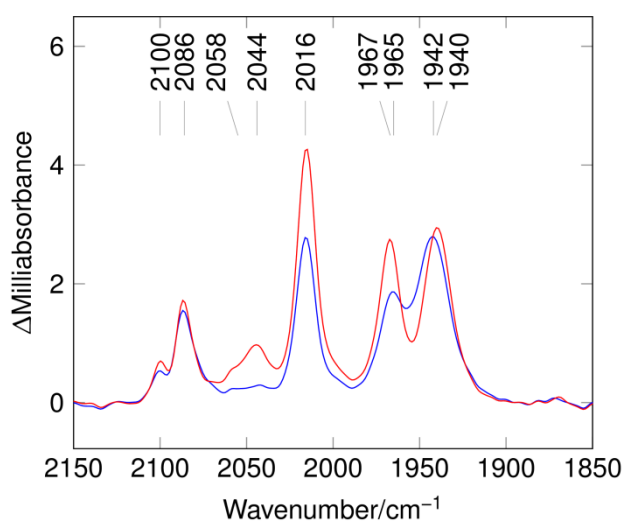


**Figure 95** Stopped-flow FTIR of the reaction of  $[\text{Fe}_4\text{S}_4(\text{SPh})_4]^{2-}$  with four equivalents of  $\text{CN}^-$  in MeCN under CO. Blue = mid time 70 s, red = long time scan 684 s. Initial [cluster] = 1.1 mM.

The bands at 2044 and 2058  $\text{cm}^{-1}$  in Figure 95 have been observed in previous stopped-flow FTIR experiments on the  $[\text{Fe}_4\text{S}_4(\text{SPh})_4]^{2-}$  with  $\text{CN}^-$  under  $\text{N}_2$ . It is clear that it is only at long time after mixing that these bands appear and are evidently suppressed by CO. This suggests

that CO must intercept an intermediate(s) on the pathway to their formation. Thus the CO dependent products are kinetically favoured species but at longer time cyanide can replace CO. Plausible intermediates which could be intercepted by CO are the mono-cyanide substituted cluster, the  $[\text{Fe}_4\text{S}_4(\text{SR})_4(\text{CN})]^{3-}$  cluster where cyanide and thiolate share an Fe atom or the di-cyanide substituted clusters,  $[\text{Fe}_4\text{S}_4(\text{SR})_2(\text{CN})_2]^{2-}$  and  $[\text{Fe}_4\text{S}_4(\text{SR})_3(\text{CN})_2]^{3-}$ .

Figure 96 details the growth of the bands at 2089 and 1940  $\text{cm}^{-1}$  and Figure 97 shows a plot of the absorbance of the band at 2089  $\text{cm}^{-1}$  versus that at 1940  $\text{cm}^{-1}$  at identical times. The linear plot is fully consistent with the initial formation of a single species possessing one CO ligand and one  $\text{CN}^-$  ligand. That the frequency of the  $\text{CN}^-$  ligand is over 40  $\text{cm}^{-1}$  higher than that assigned to the (CO-free) mono-cyanide species suggests these two ligands are bound to the same Fe atom and competing for back-donation from the metal centre. This species is designated **ISPh**.

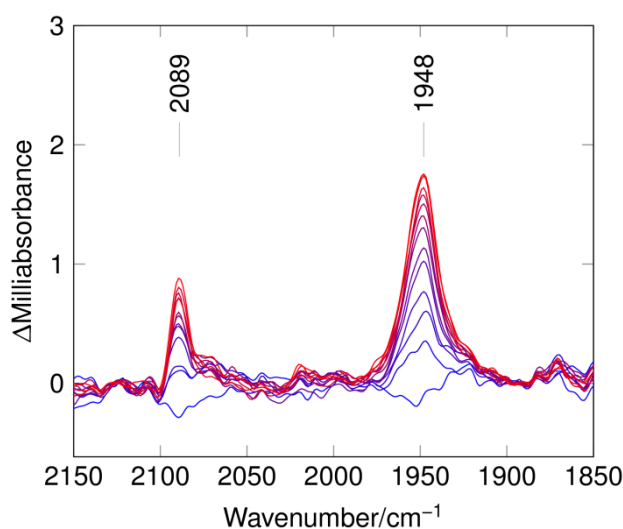


**Figure 96** Stopped-flow FTIR of the reaction of  $[\text{Fe}_4\text{S}_4(\text{SPh})_4]^{2-}$  with four equivalents of  $\text{CN}^-$  in MeCN under CO at short time (2.3 s). Blue: early scans, red: later scans. Initial [cluster] = 1 mM.

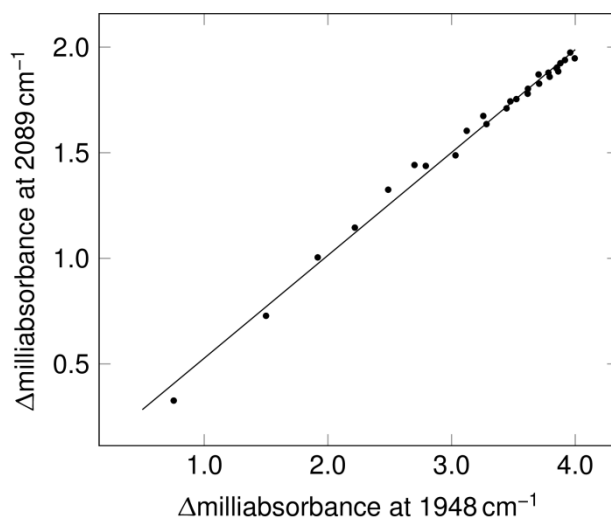


**Figure 97** Growth of the IR band at 2089 cm<sup>-1</sup> against growth of the IR band at 1948 cm<sup>-1</sup> in **ISPh**.

The interaction of [Fe<sub>4</sub>S<sub>4</sub>(SEt)<sub>4</sub>]<sup>2-</sup> with 4 eq. CN<sup>-</sup> in CO saturated solution was also investigated by stopped-flow FTIR. Similar behaviour to the [Fe<sub>4</sub>S<sub>4</sub>(SPh)<sub>4</sub>]<sup>2-</sup> system was observed. At short time (4 s) the growth of two bands at 2083 and 1940 cm<sup>-1</sup> was seen, Figure 98. The plot of the absorbance at 2083 cm<sup>-1</sup> versus that at 1940 cm<sup>-1</sup> at corresponding times was linear, Figure 100, which is again indicative of the initial formation of a species closely analogous to **ISPh** and which is designated as **ISet**.

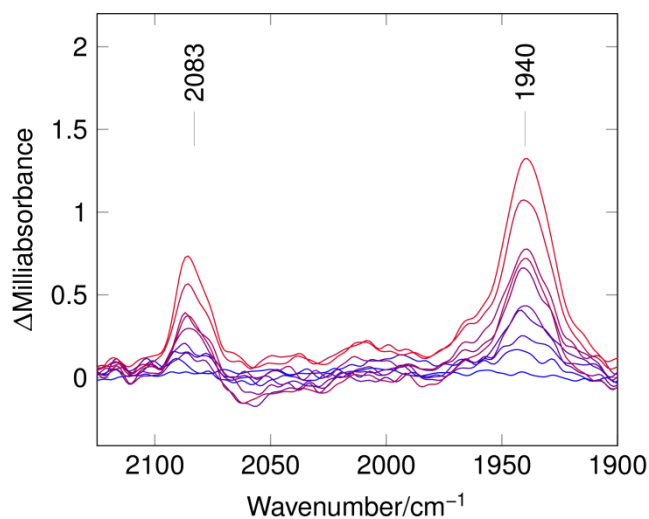


**Figure 98** Stopped-flow FTIR of the reaction of  $[\text{Fe}_4\text{S}_4(\text{SEt})_4]^{2-}$  with four equivalents of  $\text{CN}^-$  in MeCN under CO at short time 3.6 s. Blue: early scans, red: later scans. Initial [cluster] = 0.9 mM.

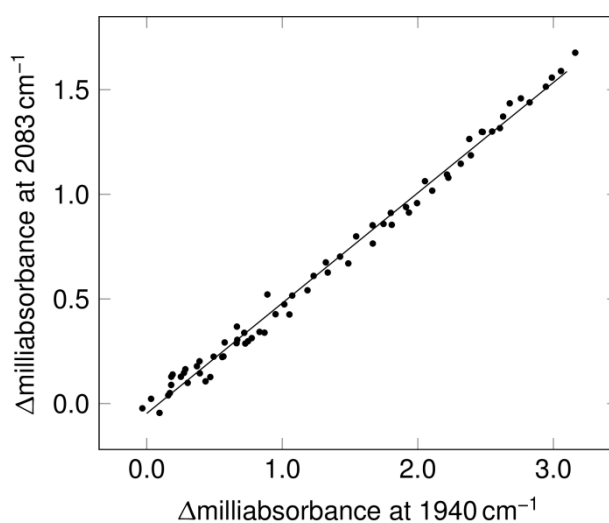


**Figure 99** Growth of the IR band at  $2083\text{ cm}^{-1}$  against growth of the IR band at  $1940\text{ cm}^{-1}$  in **ISet**.

That the frequencies of the IR bands corresponding to **ISPh** and **ISet** are similar, 2089 and  $1948\text{ cm}^{-1}$  vs 2083 and  $1940\text{ cm}^{-1}$  respectively but not identical clearly shows that  $\text{PhS}^-$  and  $\text{EtS}^-$  ligands are retained. The lower frequencies for **ISet** relative to **ISPh** are in keeping with  $\text{EtS}^-$  being the more electron-donating ligand allowing greater back-bonding to the CO and

CN ligands on the cluster. A comparison of the behaviour at short (3.5 s) and long (136 s) time for the reaction of  $[\text{Fe}_4\text{S}_4(\text{SEt})_4]^{2-}$  with four equivalents of  $\text{CN}^-$  in MeCN under CO is shown in Figure 100.

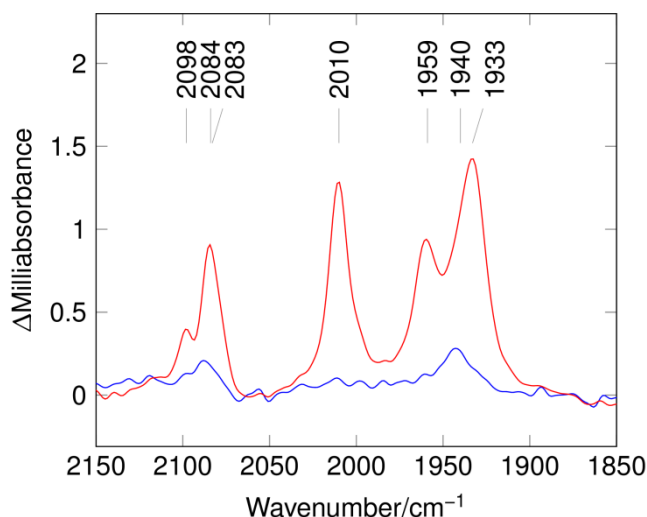


**Figure 100** Stopped-flow FTIR of the reaction of  $[\text{Fe}_4\text{S}_4(\text{SEt})_4]^{2-}$  with four equivalents of  $\text{CN}^-$  in MeCN under CO after blue: 3.5 s, red: 136 s. Initial  $[\text{cluster}] = 0.9 \text{ mM}$ .

The behaviour at “long time” (136 s) for  $[\text{Fe}_4\text{S}_4(\text{SEt})_4]^{2-}$  with 4 eq.  $\text{CN}^-$  in CO saturated solution closely parallels that seen for the reaction with the phenylthiolate cluster under similar conditions with the formation of five major bands, Figure 101. When referring to this spectrum and the specie(s) it corresponds to in subsequent sections it will be called “SEt cluster species II” (**IISEt**).

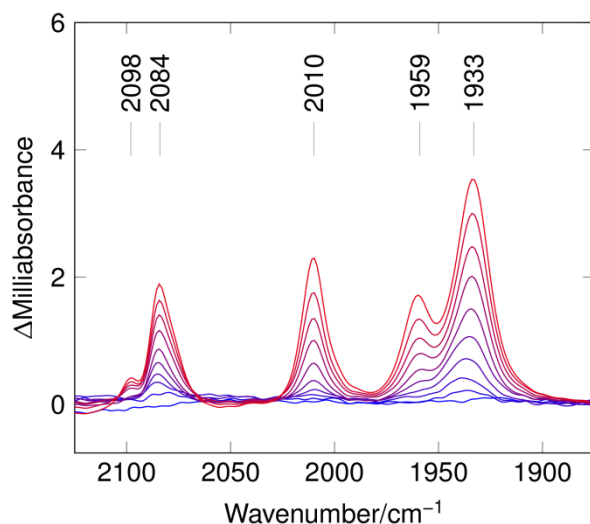


**Figure 101** Stopped-flow FTIR of the reaction of  $[\text{Fe}_4\text{S}_4(\text{SET})_4]^{2-}$  with four equivalents of  $\text{CN}^-$  in MeCN under CO at long time 169 s (**IISET**). Blue: early scans, red: later scans. Initial  $[\text{cluster}] = 1 \text{ mM}$ .

The intensities of the bands at wavenumbers characteristic of cyanide bands (at 2098 and  $2084 \text{ cm}^{-1}$ ) were plotted at identical times giving a linear correlation as shown in Figure 102. This data supports the inference that the spectrum of **IISET** corresponds to a species with two cyanide ligands on one cluster.

The growth of the bands in the spectrum of **IISET** all correlate in a linear fashion, thus they are likely to arise from a single species. A nine second period where the growth is not linear, an apparent “lag” period in the growth of one of the bands is a consequence of an underlying absorption of species **IISET** which builds up and decays in this time frame. This behaviour can be seen in the growth comparison plots in Figure 102, Figure 103, Figure 104 and Figure 105. This is consistent with **IISET** being an intermediate on the pathway to **IISET**.

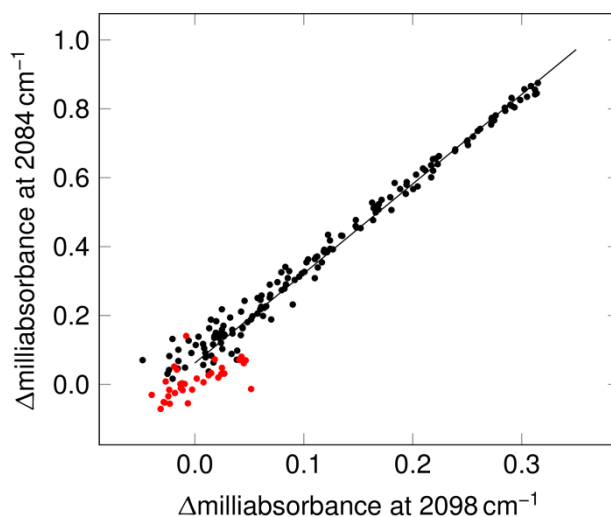


**Figure 102** Growth of the IR band at  $2098\text{ cm}^{-1}$  against growth of the IR band at  $2084\text{ cm}^{-1}$ . Complete data set shown. Data points in the non-linear “lag” period of 9.0 s coloured red.

Investigation of the growth correlations of the bands at 2084, 2010, 1959 and  $1933\text{ cm}^{-1}$  as shown in Figure 103, Figure 104 and Figure 105 show linear relationships between CO/CN<sup>-</sup> bands and CO/CO bands at longer time.

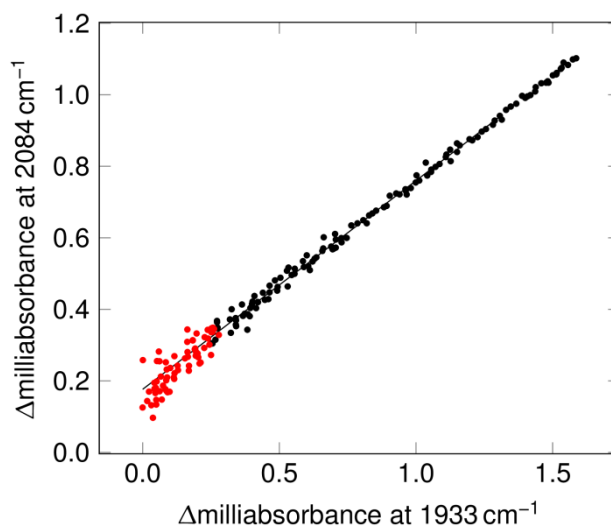


**Figure 103** Growth of the IR band at  $2084\text{ cm}^{-1}$  against growth of the IR band at  $1932\text{ cm}^{-1}$ . Complete data set shown. Data points in the non-linear “lag” period of 9.0 s coloured red.

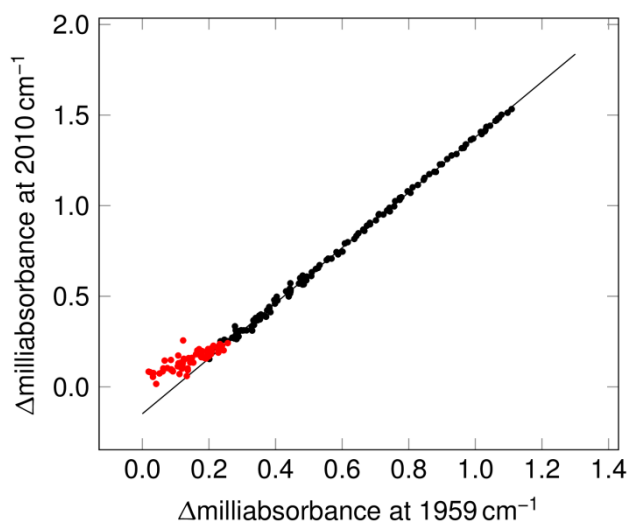


**Figure 104** Growth of the IR band at 2010 cm<sup>-1</sup> against growth of the IR band at 1959 cm<sup>-1</sup>. Complete data set shown. Data points in the non-linear “lag” period of 9.0 s coloured red.

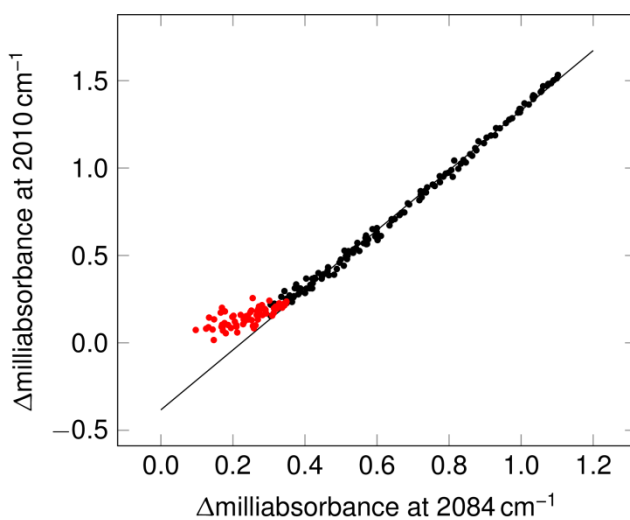


**Figure 105** Growth of the IR band at 2010 cm<sup>-1</sup> against growth of the IR band at 2084 cm<sup>-1</sup>. Complete data set shown. Data points in the non-linear “lag” period of 9.0 s coloured red.

#### 4.5.1 Comparison of products from the reactions of $[\text{Fe}_4\text{S}_4(\text{SEt})_4]^{2-}$ and $[\text{Fe}_4\text{S}_4(\text{SPh})_4]^{2-}$ with $\text{CN}^-$ in CO saturated MeCN

The species detected at short time (less than 10 s) in the stopped-flow FTIR spectra of  $[\text{Fe}_4\text{S}_4(\text{SEt})_4]^{2-}$  and  $[\text{Fe}_4\text{S}_4(\text{SPh})_4]^{2-}$  with  $\text{CN}^-$  in CO saturated MeCN, **ISET** and **ISPh** are compared in Figure 106. That the bands of the two respective species are close in wavenumber and relative intensities is indicative of the formation of similar species in solution. Importantly the bands the bands are not at identical frequencies. Those corresponding to **ISET** are shifted to lower wavenumber relative to those of **ISPh** indicating that thiolate is still attached to these species.

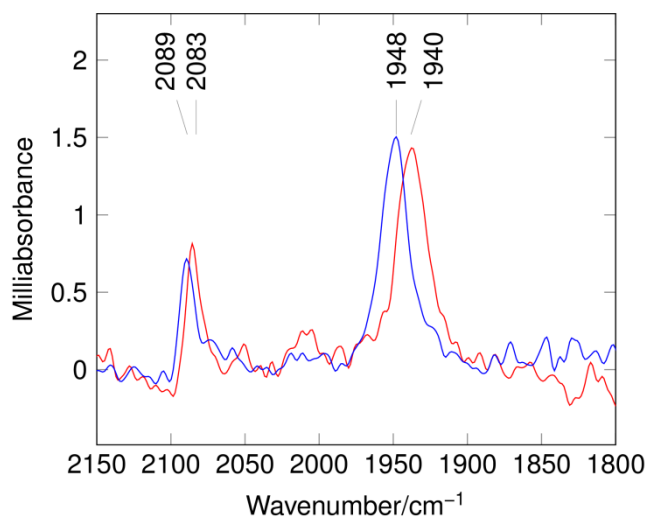


**Figure 106** Stopped-flow FTIR spectra of the reaction of  $[\text{Fe}_4\text{S}_4(\text{SR})_4]^{2-}$  with four equivalents of  $\text{CN}^-$  in MeCN under CO at “short time”. Blue: R = Ph scan 3.0 s, red: R = Et scan 6.1 s.

Table 7 and Figure 107 compare the IR bands of **IISPh** and **ISET**. As observed for **ISPh** and **ISET** there is great similarity between the two sets of IR data, providing evidence that both clusters form analogous species at long time. The observed frequencies for the two sets of data are close but not identical. This is consistent with the retention of  $\text{RS}^-$  ligand(s) in the

product. As expected frequencies for **IISet** are all lower in wavenumber than those of **IISPh** in keeping with  $\text{EtS}^-$  being a more electron donating ligand than  $\text{PhS}^-$ .

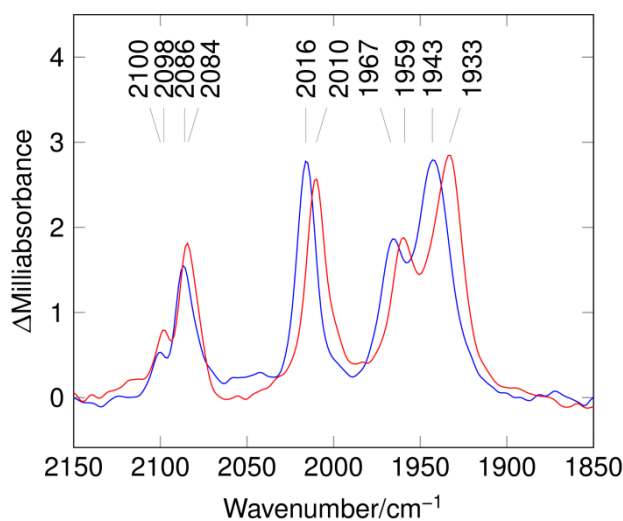


**Figure 107** Stopped-flow FTIR spectra of the reaction of  $[\text{Fe}_4\text{S}_4(\text{SR})_4]^{2-}$  with four equivalents of  $\text{CN}^-$  in MeCN under CO at “long time”. Blue: R = Ph scan 150s, red: R = Et scan 136 s.

**Table 7** Comparison of FTIR bands of the product(s) formed from the reaction of two different undifferentiated  $[\text{Fe}_4\text{S}_4(\text{SR})_4]^{2-}$  clusters with 4 eq.  $\text{CN}^-$  in CO saturated solution around 150 s.  $[\text{Fe}_4\text{S}_4(\text{SEt})_x(\text{CO})_y(\text{CN})_z]^{2-} = \mathbf{IISet}$ ,  $[\text{Fe}_4\text{S}_4(\text{SPh})_x(\text{CO})_y(\text{CN})_z]^{2-} = \mathbf{IISPh}$ . IR bands 1-5 in order of highest wavenumber band to lowest. The letters s, m, and w correspond to strong, medium and weak intensity bands, respectively.

IR band	<b>IISet</b>	<b>IISPh</b>
CN w	2098	2100
CN s	2084	2086
CO s	2010	2015
CO m	1959	1967
CO s	1933	1943

Further support for **IISpEt** and **IISPh** being similar species is provided by Figure 108 which shows the correlation between the wavenumber values of the bands of each species in ascending order.

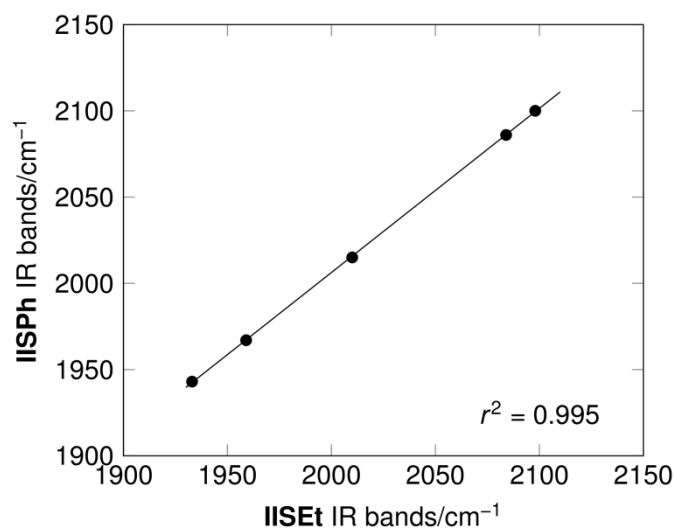


**Figure 108** IR bands of the species **IISPh** against those corresponding to **IISpEt**. The correlation coefficient  $r^2$  is shown on the figure.

#### 4.5.2 Addition of $^{13}\text{CN}^-$ to CO saturated solution of cluster

To provide evidence for the assignment of the bands in the spectra above as CO and  $\text{CN}^-$  stretches, isotopic labelling experiments were carried out.

The reaction of  $[\text{Fe}_4\text{S}_4(\text{SPh})_4]^{2-}$  with  $^{13}\text{CN}^-$  at short time (3.5 s) shows the band  $2089\text{ cm}^{-1}$  had shifted to  $2045\text{ cm}^{-1}$ . The predicted value for this shift using the equation below is  $2045\text{ cm}^{-1}$ .

$$\tilde{\nu} = \frac{1}{2\pi c} \sqrt{\frac{k_f}{\mu}}$$

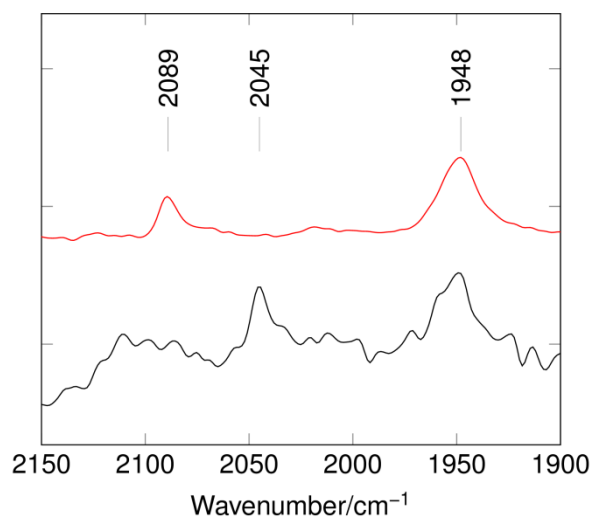


**Figure 109** Difference FTIR spectrum of the reaction of  $[\text{Fe}_4\text{S}_4(\text{SPh})_4]^{2-}$  with two equivalents of  $\text{CN}^-$  (red) and  $^{13}\text{CN}^-$  (black) in MeCN under CO after 2.0 s. Normalised for initial  $[\text{Cluster}] = 1 \text{ mM}$ .

At 150 s the peaks in the spectrum of **IISPh**, 2100 and 2089  $\text{cm}^{-1}$ , are shifted to lower wavelength with one new frequency to 2056 and 2044  $\text{cm}^{-1}$ . The observed isotopic shifts are consistent with assignment of these bands as  $\text{CN}^-$  stretches (calculated values 2056.05 and 2045.28  $\text{cm}^{-1}$ ). The labelling of cyanide also has a direct effect on the carbonyl bands. The peak at 2015  $\text{cm}^{-1}$  shifts to slightly lower wavenumber and there is a new peak at 2001  $\text{cm}^{-1}$ . The bands at around 1974 and 1940  $\text{cm}^{-1}$  are broader and weaker. The shift in frequency of the carbonyl bands are indicative of strong coupling between CO and  $\text{CN}^-$  as the energy of the vibrations become more closely matched.

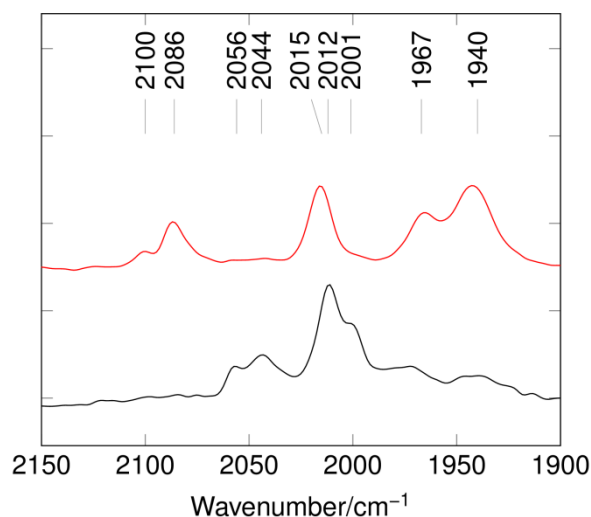


**Figure 110** Difference FTIR spectrum of the reaction of  $[\text{Fe}_4\text{S}_4(\text{SPh})_4]^{2-}$  with two equivalents of  $\text{CN}^-$  (red) and  $^{13}\text{CN}^-$  (black) in MeCN under CO at long time (150 s). Normalised for initial  $[\text{cluster}] = 1 \text{ mM}$ .

#### 4.5.3 Addition of cyanide to $^{13}\text{CO}$ saturated solution of cluster

The reaction of  $\text{CN}^-$  and  $[\text{Fe}_4\text{S}_4(\text{SPh})_4]^{2-}$  in  $^{13}\text{CO}$  saturated solution at short time shows that the band at  $1948 \text{ cm}^{-1}$  in the spectrum of **ISPh** shifts to  $1903 \text{ cm}^{-1}$ . The predicted value for this stretch is  $1905 \text{ cm}^{-1}$  in good agreement with the experimental value.

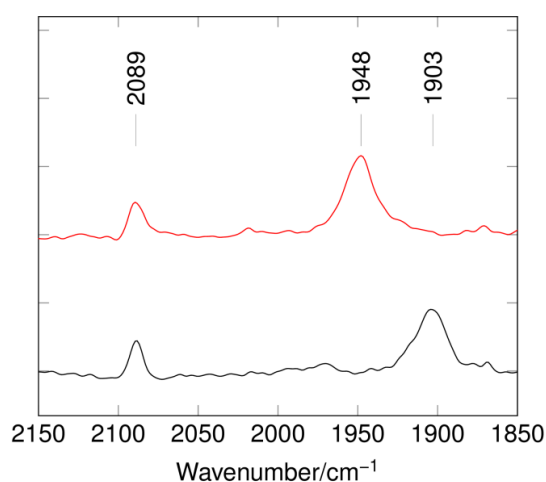


**Figure 111** Difference spectrum of the reaction of  $[\text{Fe}_4\text{S}_4(\text{SPh})_4]^{2-}$  with four equivalents of  $\text{CN}^-$  in MeCN under CO (red) and  $^{13}\text{CO}$  (black) at short time (2.0 s). Normalised for initial  $[\text{cluster}] = 1 \text{ mM}$ .

In the species formed at long time the peaks at 2015, 1967 and 1942  $\text{cm}^{-1}$  shift to 1970, 1920 and 1898  $\text{cm}^{-1}$  respectively. The calculated shifts for these bands are 1970, 1923 and 1899  $\text{cm}^{-1}$ .

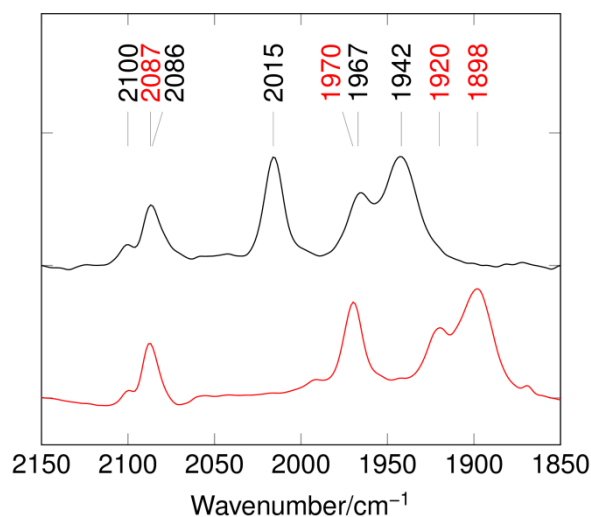


**Figure 112** Stopped-flow FTIR spectra of the reaction of  $[\text{Fe}_4\text{S}_4(\text{SPh})_4]^{2-}$  with four equivalents of  $\text{CN}^-$  in MeCN under CO (red) and  $^{13}\text{CO}$  (black) at 150 s.

#### 4.5.4 Mass spectrometry studies

A solution of  $[\text{Fe}_4\text{S}_4(\text{SPh})_4][\text{Bu}_4\text{N}]_2$  with four eq. of  $[\text{Et}_4\text{N}][\text{CN}]$  in CO saturated MeCN was analyzed by negative ion electrospray ionization mass spectrometry in an orbitrap mass spectrometer. No CO containing species were detected by mass spectroscopy; summary spectrum is shown in Figure 113.

10a01 #644-745 RT: 2.86-3.81 AV: 85 NL: 5.97E5  
F: FTMS - p ESI Full ms [400.00-1200.00]

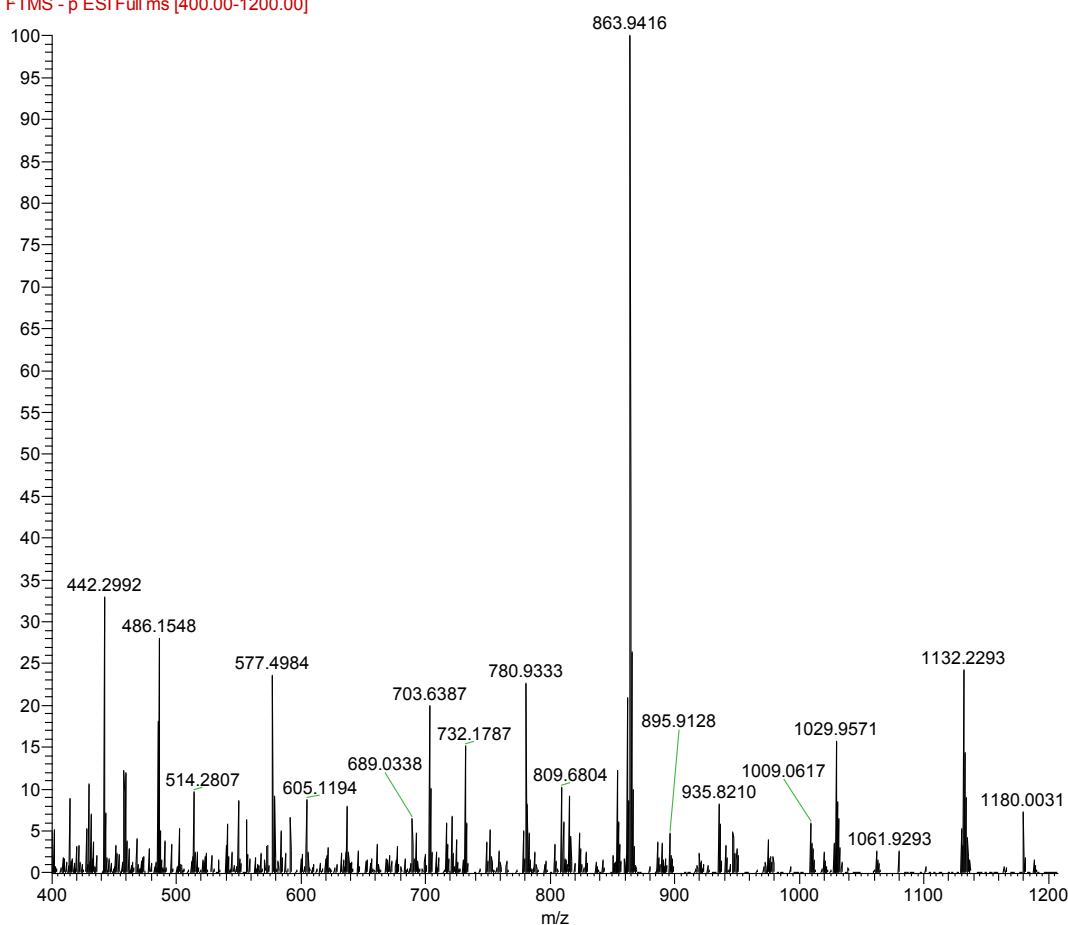


**Figure 113** Mass spectrum of a solution of  $[\text{Fe}_4\text{S}_4(\text{SPh})_4]^{2-}$  under CO with four equivalents of cyanide focused on the mass range 400–1200 Da.

There is strong evidence however, for the presence of a  $[\text{Fe}_4\text{S}_4(\text{SPh})_2(\text{CN})_2]^{2-}$  species. The mass spectrum in Figure 113 shows a major peak with a  $m/z$  value of 863.9410 which is in excellent agreement with the accurate mass calculated for a mono-anionic di-cyanide substituted cluster with one tetrabutylammonium counterion  $\{[\text{Fe}_4\text{S}_4(\text{SPh})_2(\text{CN})_2][\text{Bu}_4\text{N}]\}^-$ , ( $m/z$  863.9410  $\text{g mol}^{-1}$ ). Further evidence for this assignment is given by the match between the isotopic mass spectrum of the fragment at  $m/z$  863.9410 and the calculated isotopic pattern predicted for a  $[\text{Fe}_4\text{S}_4(\text{SPh})_2(\text{CN})_2]^{2-}[\text{Bu}_4\text{N}]^+$  fragment as shown in Figure 114 and Figure 115.

10a01 #650-738 RT: 2.86-3.76 AV: 81 NL: 5.97E5  
T: FTMS - p ESIFull.ms [400.00-1200.00]

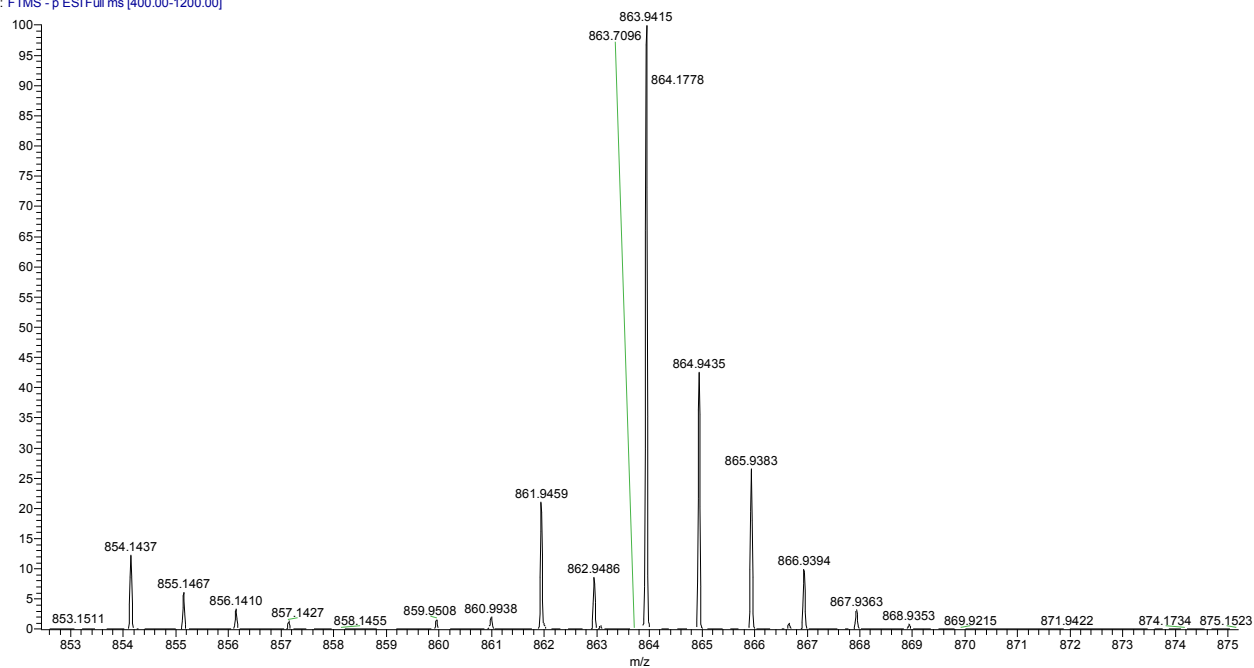


Figure 114 Isotopic mass spectrum of the fragment at  $m/z$  863.9415.

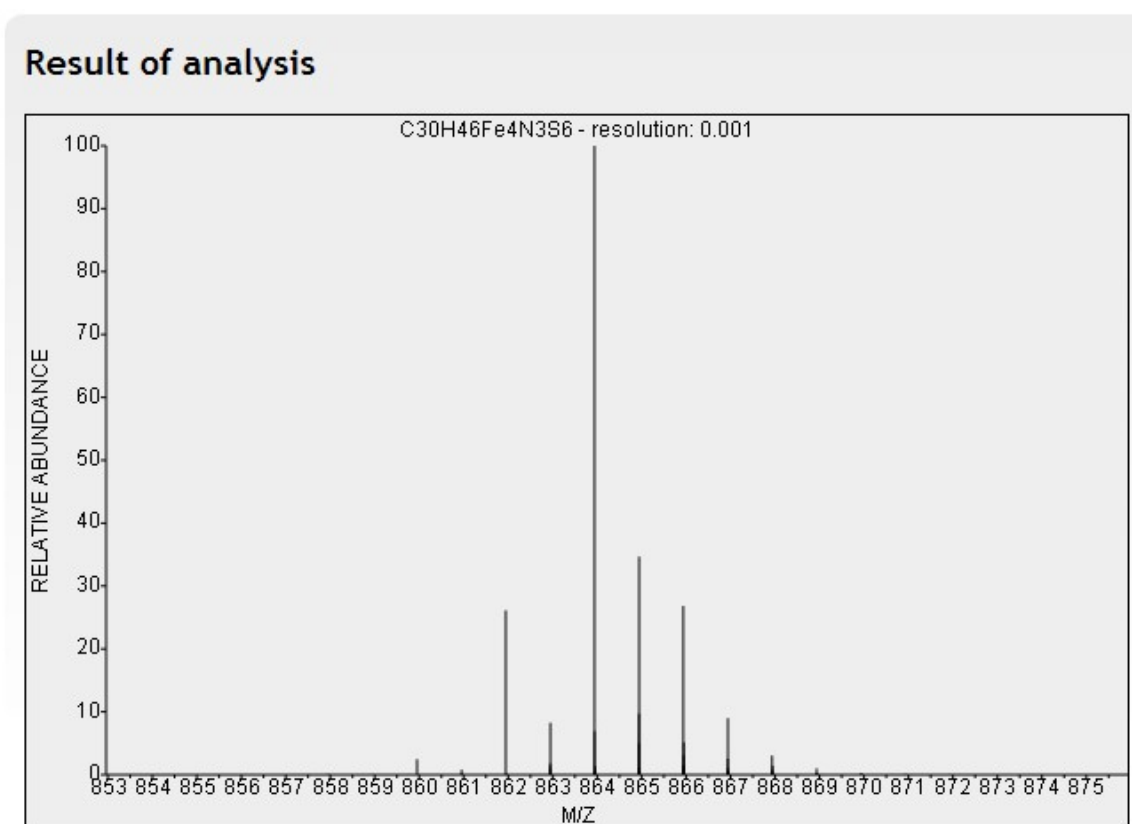
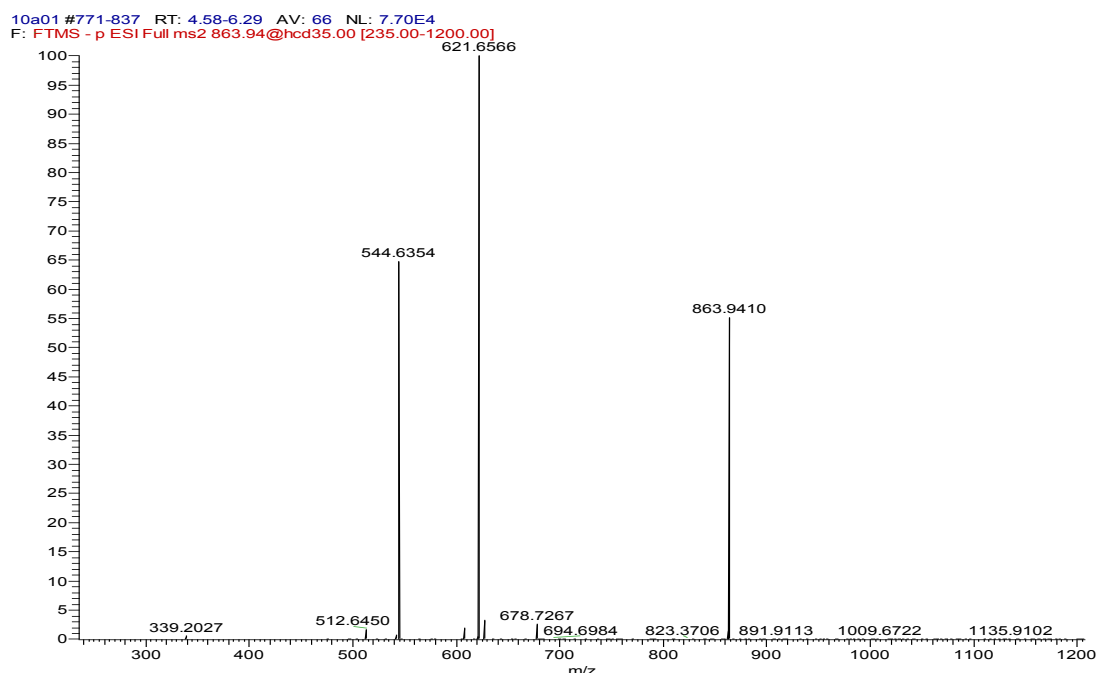


Figure 115 Calculated isotopic spectrum of  $[Fe_4S_4(SPh)_2(CN)_2][Bu_4N]$ .

The trapped parent ion  $m/z = 863.9410$ , was subsequently fragmented to give a derivative mass spectrum as shown in Figure 116. The iron-containing fragment has an  $m/z$  ratio of 621.6566 in complete agreement with that of the oxidised di-cyanide  $[\text{Fe}_4\text{S}_4(\text{SPh})_2(\text{CN})_2]^-$  cluster, which “flies” without the tetrabutylammonium counterion. The fragment at  $m/z = 544.6354$  is a non-iron-containing species (no major isotope masses).



**Figure 116** Second mass spectrum of the parent ion with  $m/z$  863.94. Peak at  $m/z = 621.6566$  is the parent ion minus the tetrabutylammonium counterion. Peak at  $m/z = 544.6354$  is non-iron-containing.

That a CO containing species can be observed in FTIR experiments but not in mass spectrometric studies is explained as follows. Carbon monoxide has been shown to bind reversibly to  $[\text{Fe}_4\text{S}_4(\text{SPh})_4]^{2-}$  clusters in the presence of cyanide in the cyclic voltammetry experiments (Section 4.4.), it is removed by purging the solution with  $\text{N}_2$ . Thus under high vacuum, high energy conditions (as in the orbitrap of the mass spectrometer) CO will undoubtedly be lost from the cluster.

A few minor bands have also been assigned:  $m/z = 1029.9571$  is in good agreement with the parent dianion associated with a  $\text{Bu}_4\text{N}^+$  counterion  $\{[\text{Fe}_4\text{S}_4(\text{SPh})_4][\text{NBu}_4]\}$ . The peak at  $m/z = 1132.2293$  matches  $\{[\text{Fe}_4\text{S}_4(\text{SPh})_2(\text{CN})_2][\text{Bu}_4]_2(\text{CN})\}$ , i.e. an overall one minus charge agglomerate or a species with an extra CN bound to an Fe on the cluster.

In the first mass spectrum shown in Figure 113 a peak at  $m/z$  854.1420 can be seen which is in concordance with a di-iron tetra thiolate species with a tetrabutylammonium counterion  $[\text{Fe}_2\text{S}_2(\text{SPh})_4][\text{Bu}_4\text{N}]$ . This peak is not present in subsequent spectra, thus it may be an artefact of oxidation during sample transfer from storage vessel to injection into the mass spectrometer. A crystal structure of the dianion with mixed counterions,  $[\text{Fe}_2\text{S}_2(\text{SPh})_4][\text{NBu}_4][\text{NEt}_4]$  as shown in Figure 124 was isolated from the reaction of  $[\text{Fe}_4\text{S}_4(\text{SPh})_4]^{2-}$  with two equivalents of  $\text{CN}^-$  under CO after 18 hours at  $-20^\circ\text{C}$ . The redox couple for  $[\text{Fe}_2\text{S}_2(\text{SPh})_4]^{2-/3-}$  should appear at  $-0.95\text{ V}$  (as corrected for Ag/AgCl).<sup>274</sup> However, no redox couple at this potential was observed during the time-course of the cyclic voltammetry experiments (circa 1 h).

#### 4.5.5 DFT modelling of interactions of cluster with CO and $\text{CN}^-$

In collaboration with Maurizio Brushchi, a series of CO and  $\text{CN}^-$  containing iron-sulfur clusters were modelled in order to provide some computational evidence for the postulated identity of the clusters mentioned so far in this chapter. Firstly, structures pertinent to the biochemistry of the H-cluster were investigated. A simple structure analogous to complex A<sup>62</sup> (a cluster with mono- CO and  $\text{CN}^-$  ligation at one Fe of the cube shown in Scheme 41) was modelled by DFT  $[\text{Fe}_4\text{S}_4(\text{SPh})_3(\text{CO})(\text{CN})]^{2-}$  the simulated spectrum is shown in Figure 117. The simulated IR bands are in very good agreement with those seen in the spectra of **ISPh** and **ISet** shown in Figure 96 and Figure 98. These IR bands for the experimental, calculated and those for the natural system are compared in Table 10 in section 4.6.2.

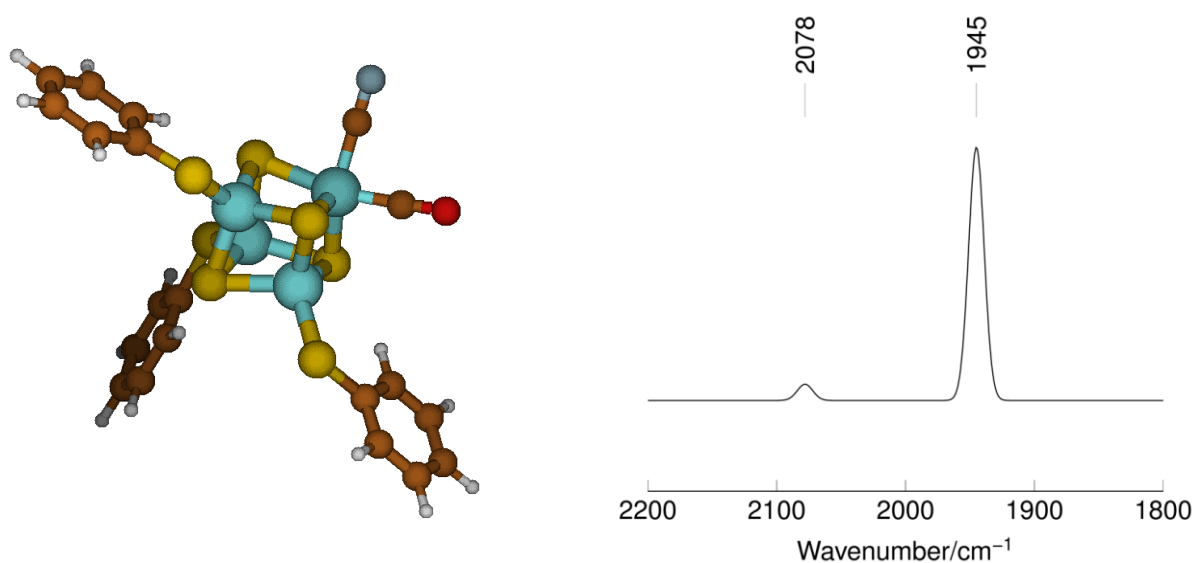


**Figure 117** Proposed structural identity  $[(\text{Fe}_4\text{S}_4)(\text{SPh})_3(\text{CO})(\text{CN})]^{2-}$  (left), DFT calculated IR.

The experimental IR spectra of **ISPh** and **ISEt** each show a cyanide band that is greater in intensity than that predicted by DFT for a  $[(\text{Fe}_4\text{S}_4)(\text{SPh})_3(\text{CO})(\text{CN})]^{2-}$  species. Therefore the possibility that the **ISPh** and **ISEt** could contain two closely overlapping  $\text{CN}^-$  bands (i.e. be  $[(\text{Fe}_4\text{S}_4)(\text{SR})_3(\text{CO})(\text{CN})_2]^{3-}$  species) was explored. In the calculated IR of this species the two cyanide bands are close together (and thus might appear as one more intense band experimentally). These bands are similar in wavenumber to those seen in the spectra of **ISPh** and **ISEt**. However, the carbonyl band in the calculated spectrum at  $1922\text{ cm}^{-1}$  is not in good agreement with the experimental values ( $1940$  and  $1948\text{ cm}^{-1}$  for **ISEt** and **ISPh**, respectively). In addition it has been demonstrated that in DFT studies on  $[\text{FeFe}]$ -hydrogenase active site models with CO and  $\text{CN}^-$  ligands, the calculated  $\text{CN}^-$  bands predict a much lower intensity than that experimentally observed.<sup>275</sup>

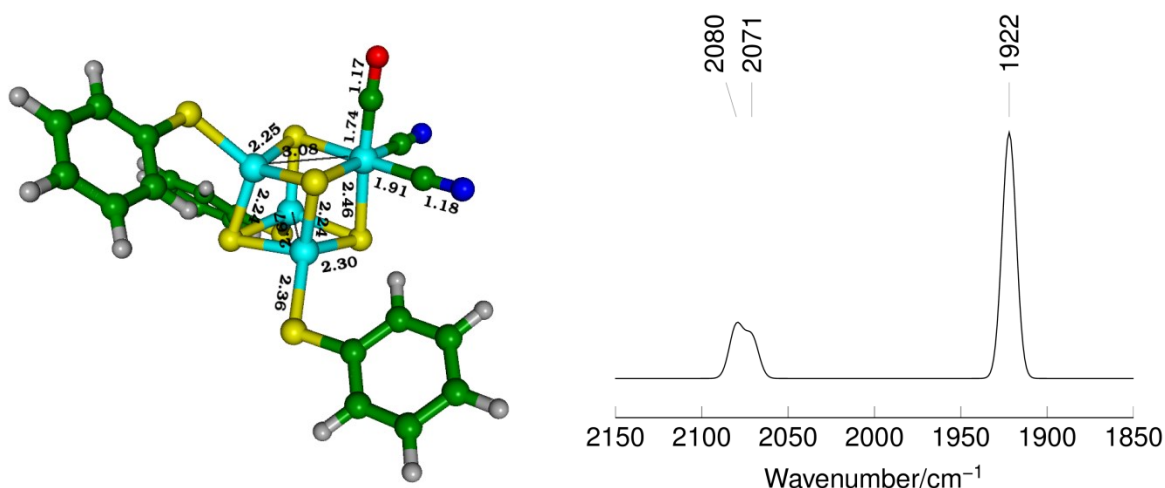


**Figure 118** Di-cyanide mono CO cluster  $[(\text{Fe}_4\text{S}_4)(\text{SPh})_3(\text{CO})(\text{CN})_2]^{3-}$  (left), DFT calculated IR.

Looking at the longer time behaviour in the synthetic clusters and in the natural system, it was first postulated that a structure analogous to the proposed biological intermediate “complex B” (Scheme 41)<sup>62</sup> (in which two CO and one  $\text{CN}^-$  are bound to one Fe) could be similar to those complexes formed for **IISPh** and **IISet** (spectra shown in Figure 93 and Figure 101, respectively). However, the simulated spectrum for this complex, as shown in Figure 119, gives bands that are neither in good agreement with the natural system “complex B” nor with the experimental species **IISPh** and **IISet** see Table 11 in section 4.6.2 for a comparison of the stretching frequencies.

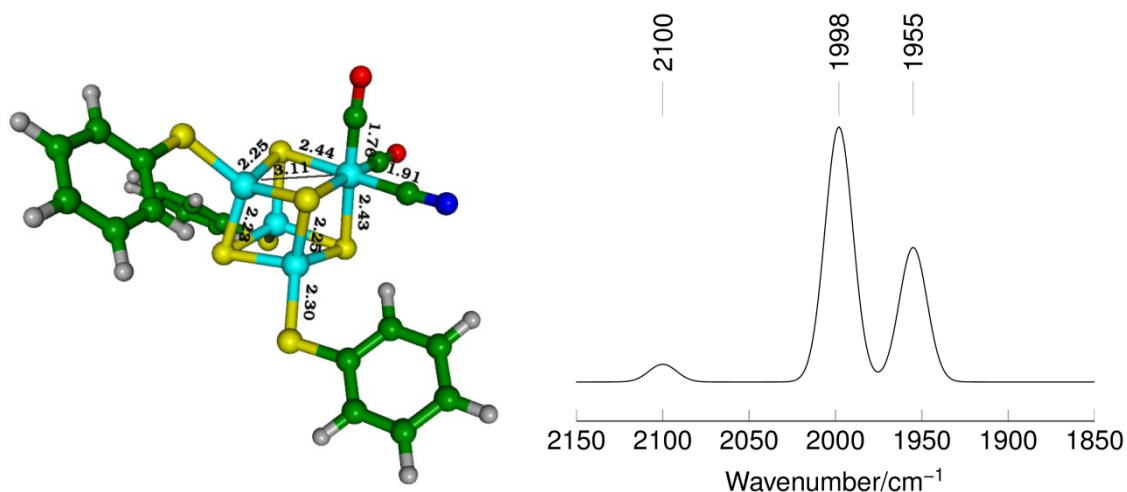


**Figure 119** Proposed structural identity  $[(\text{Fe}_4\text{S}_4)(\text{SPh})_3(\text{CO})_2(\text{CN})]^{2-}$  (left), DFT calculated IR spectrum (right).

The species **IISet** and **IISPh** give rise to spectra more complex than those seen at short time. There are many possible structures containing multiple CO and  $\text{CN}^-$  ligands (at perhaps more than one Fe centre) that could give rise to the pattern seen. As shown in the mass spectrometry studies above a di-cyanide species  $[\text{Fe}_4\text{S}_4(\text{SPh})_2(\text{CN})_2]^- [\text{Bu}_4\text{N}^+]$  was observed (where CO had likely been lost). This formed the basis for investigating structures with CO and  $\text{CN}^-$  ligation at two Fe centres. One proposed structure was  $[\text{Fe}_4\text{S}_4(\text{SR})_2(\text{CO})_3(\text{CN})_2]^{2-}$ . The simulated IR spectrum of  $[\text{Fe}_4\text{S}_4(\text{SPh})_2(\text{CO})_3(\text{CN})_2]^{2-}$  gave rise to a similar number of bands with similar positions and intensities to the synthetic species **IISPh** and **IISet** as shown in Figure 121.

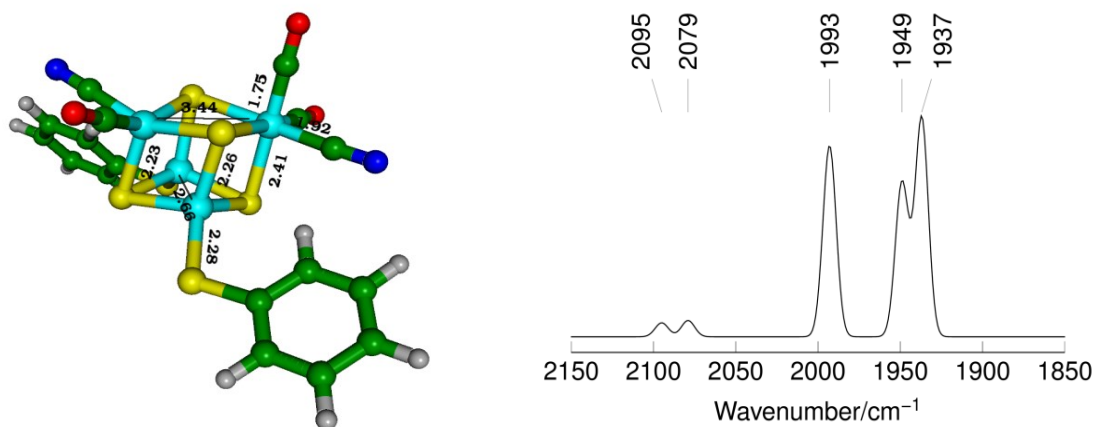


**Figure 120** Proposed structural identity  $[(\text{Fe}_4\text{S}_4)(\text{SPh})_2(\text{CN})_2(\text{CO})_3]^{2-}$  (left), DFT calculated IR spectrum (right).

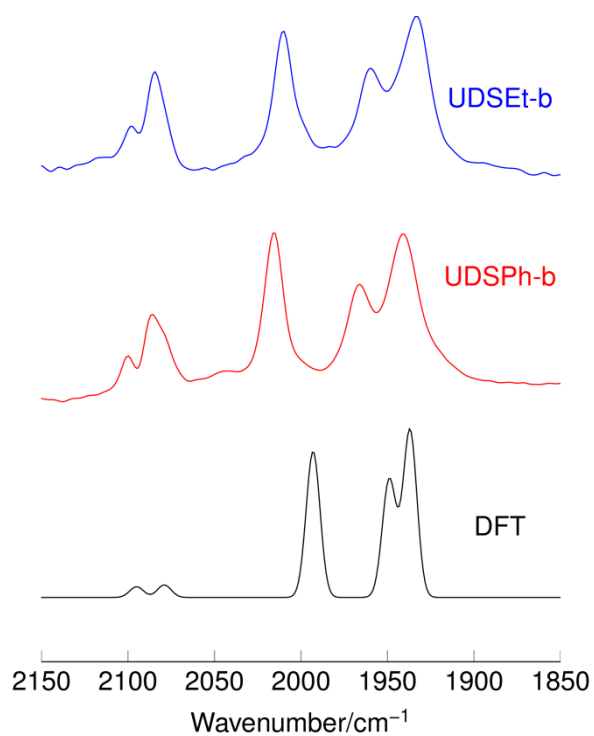


**Figure 121** Comparison of experimental IR spectra of **IISPh** and **ISEt** with the DFT calculated IR spectrum of  $[(\text{Fe}_4\text{S}_4)(\text{SPh})_2(\text{CN})_2(\text{CO})_3]^{2-}$  (see Figure 120).

The assignment of **IISPh** and **IISPh** as a  $[(\text{Fe}_4\text{S}_4)(\text{SR})_2(\text{CN})_2(\text{CO})_3]^{2-}$  like species is further supported by the linear correlation between the experimental and calculated IR bands as shown in Figure 123 and Figure 122.

**Table 8** Comparison of experimental IR bands for the species **IISPh** and **IISPh** and calculated IR data for a  $[\text{Fe}_4\text{S}_4(\text{SPh})_2(\text{CO})_3(\text{CN})_2]^{2-}$  species (illustrated in Figure 120).

IR band	<b>IISPh</b>	<b>IISPh</b>	Calculated
1	2098	2100	2095
2	2084	2086	2079
3	2010	2015	1993
4	1959	1967	1949
5	1933	1943	1937

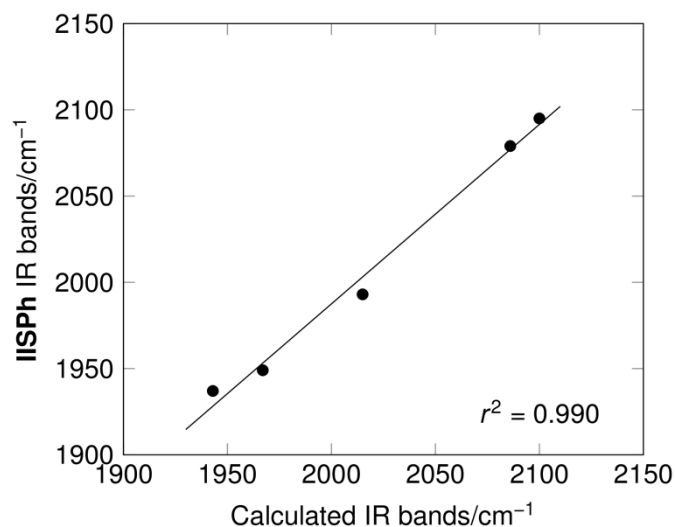


**Figure 122** IR bands of the species **IISPh** against those corresponding to the DFT calculated IR data for a  $[\text{Fe}_4\text{S}_4(\text{SPh})_2(\text{CO})_3(\text{CN})_2]^{2-}$  species (illustrated in Figure 120). The correlation coefficient  $r^2$  is shown on the figure.

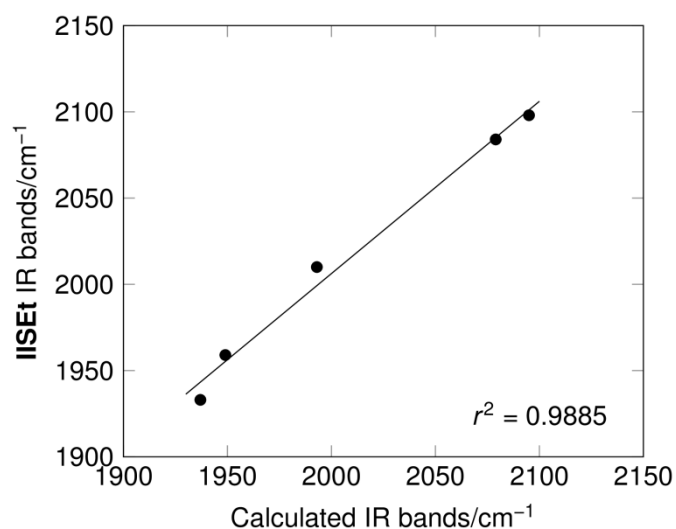


**Figure 123** IR bands of the species **IISet** against those corresponding to the DFT calculated IR data for a  $[\text{Fe}_4\text{S}_4(\text{SPh})_2(\text{CO})_3(\text{CN})_2]^{2-}$  species (illustrated in Figure 120). The correlation coefficient  $r^2$  is shown on the figure.

Other possible structures that were investigated by DFT are summarised in Table 9 but all of these were in poor agreement with the experimental data. In particular they are surpassed by the models already discussed above which are in much better agreement with the experimental data observed.



#### 4.5.6 Attempts to isolate products

A reaction mixture of two equivalents of  $\text{CN}^-$  with the phenylthiolate cluster under CO was stored at  $-20\text{ }^\circ\text{C}$  for 18 hours. Black crystals were isolated and found to be a mixed cation salt of the known di-iron tetraphenylthiolate dianion,  $[\text{NBu}_4][\text{NEt}_4][\text{Fe}_2\text{S}_2(\text{SPh})_4]$ , Figure 124.

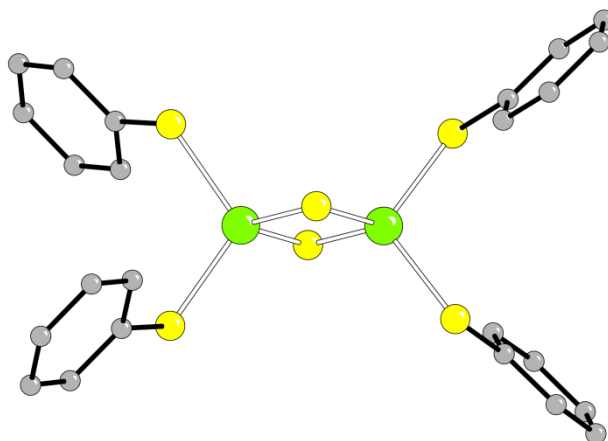
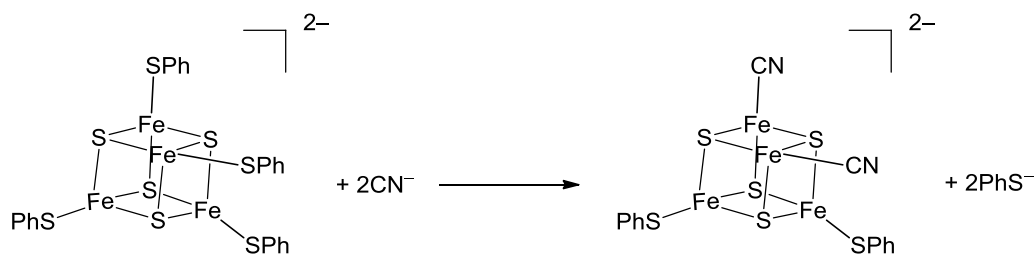


**Figure 124** Crystal structure of  $[\text{NBu}_4][\text{NEt}_4][\text{Fe}_2\text{S}_2(\text{SPh})_4]$  isolated from the reaction of  $[(\text{Fe}_4\text{S}_4)(\text{SPh})_4]^{2-}$  with two equivalents of  $\text{CN}^-$  under CO. Green = Fe, yellow = S, grey = carbon, hydrogens have been omitted for clarity.

This  $\text{Fe(III)Fe(III)}$  species might conceivably arise from attack by  $\text{PhS}^-$  on the “ $\text{PhSFeS}_2\text{FeSPh}$ ” layer of an  $[\text{Fe}_4\text{S}_4(\text{SPh})_2(\text{CN})_2(\text{CO})_3]^{2-}$  species cleaving this layer into two  $\{2\text{Fe}_2\text{S}\}$ -fragments. Two equivalents of  $\text{PhS}^-$  are nominally available from the initial  $\text{CN}^-$  substitution, Scheme 49.



**Scheme 49** Substitution of  $\text{PhS}^-$  for  $\text{CN}^-$  in  $[\text{Fe}_4\text{S}_4(\text{SPh})_4]^{2-}$ .

Stopped-flow FTIR data definitively shows that  $\text{CN}^-$  and CO do bind to  $[(\text{Fe}_4\text{S}_4)(\text{SPh})_4]^{2-}$ . However, no iron-bound CO,  $\text{CN}^-$  species from this reaction has been isolated. Looking at the tetraphenylthiolate diiron structure above, it is clear that the parent  $[(\text{Fe}_4\text{S}_4)(\text{SPh})_4]^{2-}$  cluster has been cleaved, potentially leading to two di-iron subunits. Formation of a  $[\text{NBu}_4][\text{NEt}_4][\text{Fe}_2\text{S}_2(\text{SPh})_4]$  species could mean that a corresponding CO and  $\text{CN}^-$  containing subunit has been formed such as that shown in Figure 125.

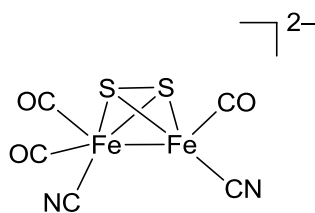
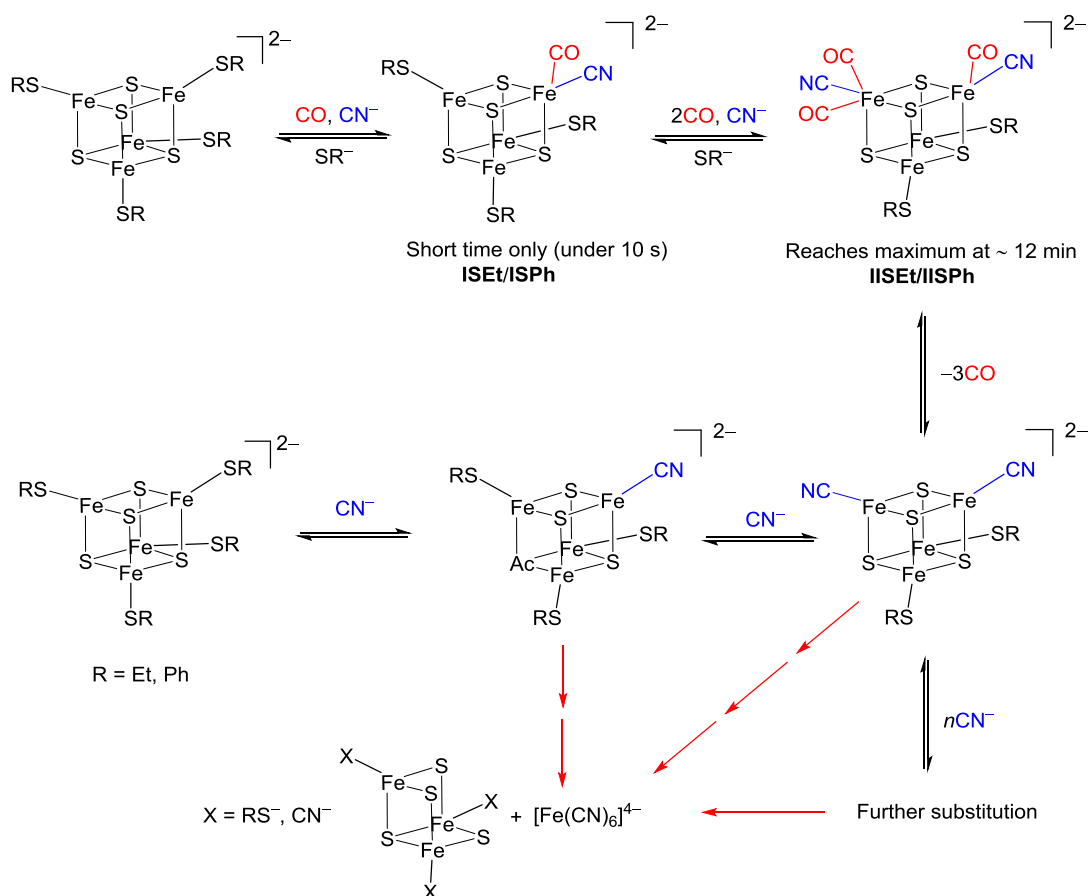


**Figure 125** Speculative product from the reaction of  $[(\text{Fe}_4\text{S}_4)(\text{SPh})_4]^{2-}$  with two equivalents of  $\text{CN}^-$  in CO-saturated solution.

## 4.6 Conclusions

### 4.6.1 Summary of the proposed interactions of undifferentiated clusters with CO and $\text{CN}^-$

The interactions of  $[\text{Fe}_4\text{S}_4(\text{SEt})_4]^{2-}$  and  $[\text{Fe}_4\text{S}_4(\text{SPh})_4]^{2-}$  with CO and  $\text{CN}^-$  individually and as co-ligands has been explored using cyclic voltammetry and stopped-flow FTIR. Scheme 50 summarises the key products from these reactions as supported by our results and our current understanding.



**Scheme 50** Summary of the proposed interactions of undifferentiated clusters with CO and  $\text{CN}^-$ .

In the presence of CO and  $\text{CN}^-$  together the tetrathiolate clusters studied both reacted in a similar way. Stopped-flow FTIR revealed the short time (less than 10 s) the spectroscopic signature of a cluster where a thiolate ligand had been replaced by one CO and one  $\text{CN}^-$ , **ISEt** and **ISPh**. This assignment was supported by  $^{13}\text{C}$  labelling experiments and a closely matching DFT calculated IR spectrum.

At longer time a more complex IR spectrum is seen. This was shown by  $^{13}\text{C}$  labelling experiments to contain two  $\text{CN}^-$  and three CO bands. Thus a DFT calculated spectrum for  $[\text{Fe}_4\text{S}_4(\text{SPh})_2(\text{CN})_2(\text{CO})_3]^{2-}$  where two CO ligands and one  $\text{CN}^-$  ligand share one corner of a cube and one CO and one  $\text{CN}^-$  share another corner was investigated. The calculated IR for

this species is in good agreement with the experimentally observed spectra for both clusters. Thus the “long time” species have been assigned as **IISet** and **IISPh** as shown in Scheme 50.

With cyanide alone, cyclic voltammetry experiments have offered great insight. Taking advantage of the additive effect that ligand substitution has on potential we were able to assign the new redox couples observed as mono- and di-cyanide substituted clusters. Stopped-flow FTIR experiments revealed a more complex scenario. Under the experimental conditions of the stopped-flow experiments a common IR band at  $2044\text{ cm}^{-1}$  was observed in both the thiolate clusters studied. This band is at a frequency that is uncannily close to that observed for ferrocyanide in MeCN solution ( $2045\text{ cm}^{-1}$ ). Our current understanding leads to a picture where an Fe atom is abstracted from our clusters. The 2-/3- couples of the mono-cyanide clusters,  $[\text{Fe}_4\text{S}_4(\text{SEt})_3(\text{CN})]^{2-}$  and  $[\text{Fe}_4\text{S}_4(\text{SPh})_3(\text{CN})]^{2-}$  are  $-0.76$  and  $-0.98\text{ V}$ , respectively, whilst those for the di-cyanide  $[\text{Fe}_4\text{S}_4(\text{SEt})_2(\text{CN})_2]^{2-}$  and  $[\text{Fe}_4\text{S}_4(\text{SPh})_2(\text{CN})_2]^{2-}$  clusters appear at  $-0.65$  and  $-0.79\text{ V}$ , respectively. Thus the electron density on the clusters at given level of substitution depends heavily on the nature of the R group on the thiolate. If the common feature at  $2044\text{ cm}^{-1}$  were to correspond to a mono- or di-cyanide substituted cluster we would not expect this frequency to be the same in both the phenyl- and the ethanethiolate clusters. The band at  $2044\text{ cm}^{-1}$  was assigned to ferrocyanide, a plausible breakdown product of the clusters in the presence of  $\text{CN}^-$ .

That CO does not react with the dianionic tetrathiolate clusters to a measurable extent was proven unequivocally in both stopped-flow FTIR and cyclic voltammetry experiments. It is clear that changes in the donicity between thiolate and cyanide must bring about a necessary alteration in the distribution of electrons at the metal centre. One may presume that in the thiolate case donation from CO to the metal is not energetically feasible.

#### 4.6.2 Similarity to spectral data of HydG

The aim of these experiments looking at the interaction of CO and  $\text{CN}^-$  with undifferentiated iron-sulfur clusters was to look for chemical precedence for the HydG intermediates proposed by Kuchenreuther and co-workers<sup>62</sup> (Scheme 41). Studying the reaction of  $[\text{Fe}_4\text{S}_4(\text{SPh})_4]^{2-}$  with  $\text{CN}^-$  under an atmosphere of CO a short lived intermediate at short time (less than 10 s) can be seen followed by the growth of a second species which reaches a maximum at around 12 min. The species at short time gives IR data in close agreement with the IR data for the natural system “complex A” (Table 10). Both are in concordance with the DFT calculated data for a  $[(\text{Fe}_4\text{S}_4)(\text{SPh})_3(\text{CO})(\text{CN})]^{2-}$  cluster (an analogous species to that proposed in the biochemistry).

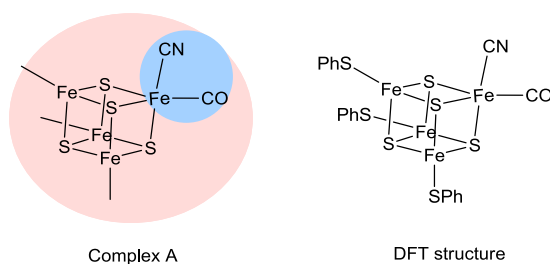


**Figure 126** “Complex A” proposed by Kuchenreuther and co-workers and an analogous DFT calculated structure.

**Table 10** Comparison of IR data from “Complex A” proposed by Kuchenreuther and co-workers,<sup>62</sup> the SPh cluster at short time and the DFT calculated IR values for  $[(\text{Fe}_4\text{S}_4)(\text{SPh})_3(\text{CO})(\text{CN})]^{2-}$ , all values given in  $\text{cm}^{-1}$ .

	“Complex A” Natural system <sup>62</sup>	<b>ISPh</b>	<b>ISet</b>	DFT
CN	2093	2089	2083	2078
CO	1949	1948	1940	1945
<sup>13</sup> CN	2048	2045		
<sup>13</sup> CO	1906	1903		

The data give strong support for the assignment of “Complex A” as a  $\text{Fe}(\text{CO})(\text{CN})$ , containing cluster. It suggests that an analogous  $\text{Fe}(\text{CO})(\text{CN})$  containing cluster is formed at short time in **ISPh** and **ISet** setting chemical precedence for this kind of chemistry in the biosynthesis of the H-cluster and for the synergistic binding of CO and  $\text{CN}^-$  to  $[\text{Fe}_4\text{S}_4(\text{SR})_4]^{2-}$  (where R = Et, Ph) clusters.

The second intermediate proposed by Kuchenreuther and co-workers,<sup>62</sup> “Complex B”, features two CO and one  $\text{CN}^-$  at Fe on the corner of an iron-sulfur on the C-terminus cluster in HydG. Comparison of the IR data for complex B with DFT calculated IR data for an analogous  $[(\text{Fe}_4\text{S}_4)(\text{SPh})_3(\text{CO})_2(\text{CN})]^{2-}$  species is not in good agreement. The DFT data therefore does not support the identity of “complex B” being an  $\text{Fe}(\text{CO})_2\text{CN}$  species.

**Table 11** Comparison of IR data for “complex B” proposed by Kuchenreuther and co-workers,<sup>62</sup> DFT calculated values for analogous structure  $[(\text{Fe}_4\text{S}_4)(\text{SPh})_3(\text{CO})_2(\text{CN})]^{2-}$  and tabulated values of the stretching frequencies of **IISet** and **IISPh**, all values given in  $\text{cm}^{-1}$ .

	“Complex B” Natural system	DFT
CN	2106	2100
CO	2057	1998
CO	2005	1955

IR band	<b>IISet</b>	<b>IISPh</b>
1	2098	2100
2	2084	2086
3	2010	2015
4	1959	1967
5	1933	1940

DFT, stopped-flow FTIR and mass spectroscopic studies support the assignment of **IISPh** and **IISet** as  $[(\text{Fe}_4\text{S}_4)(\text{SR})_2(\text{CN})_2(\text{CO})_3]^{2-}$  species.

Roach and co-workers have recently proposed that the formation of “complex A” may involve binding of an *exo*  $\text{Fe}^{\text{II}}$  centre linked to the C-terminal cluster in HydG. However, Britt et al. have also noted that cyanide binds to the cluster within HydG.<sup>87</sup>

#### 4.6.3 Simplification of reactions – site differentiated clusters

The stopped-flow FTIR spectra seen at long time for undifferentiated clusters is complex and indicative of clusters where more than one of the iron sites have been attacked by CO and  $\text{CN}^-$ . These reactions could be simplified using a site-differentiated cluster in which three of the iron sites are made less reactive by “wrapping up” with a large tridentate trithiolate ligand. This would leave one iron site more available for chemistry and should give rise to simpler spectra. It is worth noting that in the accessory protein HydG the C-terminal iron-sulfur cluster (where CO and  $\text{CN}^-$  coordinated Fe precursors to HydA are formed) is also site

differentiated: three iron sites are bound to cysteine residues. Thus a synthetic site-differentiated cluster could be said to be more structurally analogous to the natural system than an undifferentiated cluster and therefore may perform more similar chemistry.

## **4.7 Experimental techniques**

### **4.7.1 Stopped-flow measurements**

Stock solutions for stopped-flow were either prepared using standard Schlenk techniques or in a Belle Technology glove box (oxygen concentration <10 ppm), and were adjusted to the required concentration by dilution with acetonitrile. When preparing a CO saturated stock solutions, a Schlenk tube was sealed with a Subaseal and the solution was purged with CO for 5 min. The Subaseal was then wrapped in Parafilm and the Schlenk was inverted. Schlenks containing CO saturated solutions were kept sealed and inverted for the entire duration of the experiment.

IR measurements were carried out using a Tgk stopped-flow drive interfaced to a Bruker Vertex 80 spectrometer equipped with a custom-built flow cell (path length = 50  $\mu\text{m}$ ) fitted with  $\text{CaF}_2$  windows (Tgk Scientific). The drive unit was located inside the glove box, with the reagents carried to the cell prior to mixing via a flexible conduit. The cell itself was mounted in a miniature anaerobic chamber fixed inside the sample compartment of the IR instrument. The conduit and cell were set to  $21.0 \pm 0.2$  °C using a Thermo Scientific recirculating bath. Mixing of the two solutions occurred in a chamber within the cell body. The initial concentration of substrate was typically 0.50 mM after mixing. A Northumbria Optical Coatings filter (pass band 4.76 to 5.60  $\mu\text{m}$ ) was fitted in front of the cell, within the sample chamber. The stopped-flow system was controlled using the Tgk KinetaDrive and Bruker Opus 3D packages. IR data was processed and analysed using the Fit\_3D application

and curve fitting was carried out using SciDAVis. Data were normally collected at  $4 \text{ cm}^{-1}$  resolution. Typically between 60 and 225 time points were recorded for each experiment.

#### **4.7.2 Electrochemical measurements**

Cyclic voltammetry measurements were carried out in 0.1 M  $[\text{Bu}_4\text{N}][\text{BF}_4] - \text{MeCN}$  using a three compartment cell fitted with a glassy carbon working electrode (diameter 3 mm), a platinum counter electrode and a Ag/AgCl reference electrode interfaced with an Autolab PGSTAT302N potentiostat using the GPES software package.

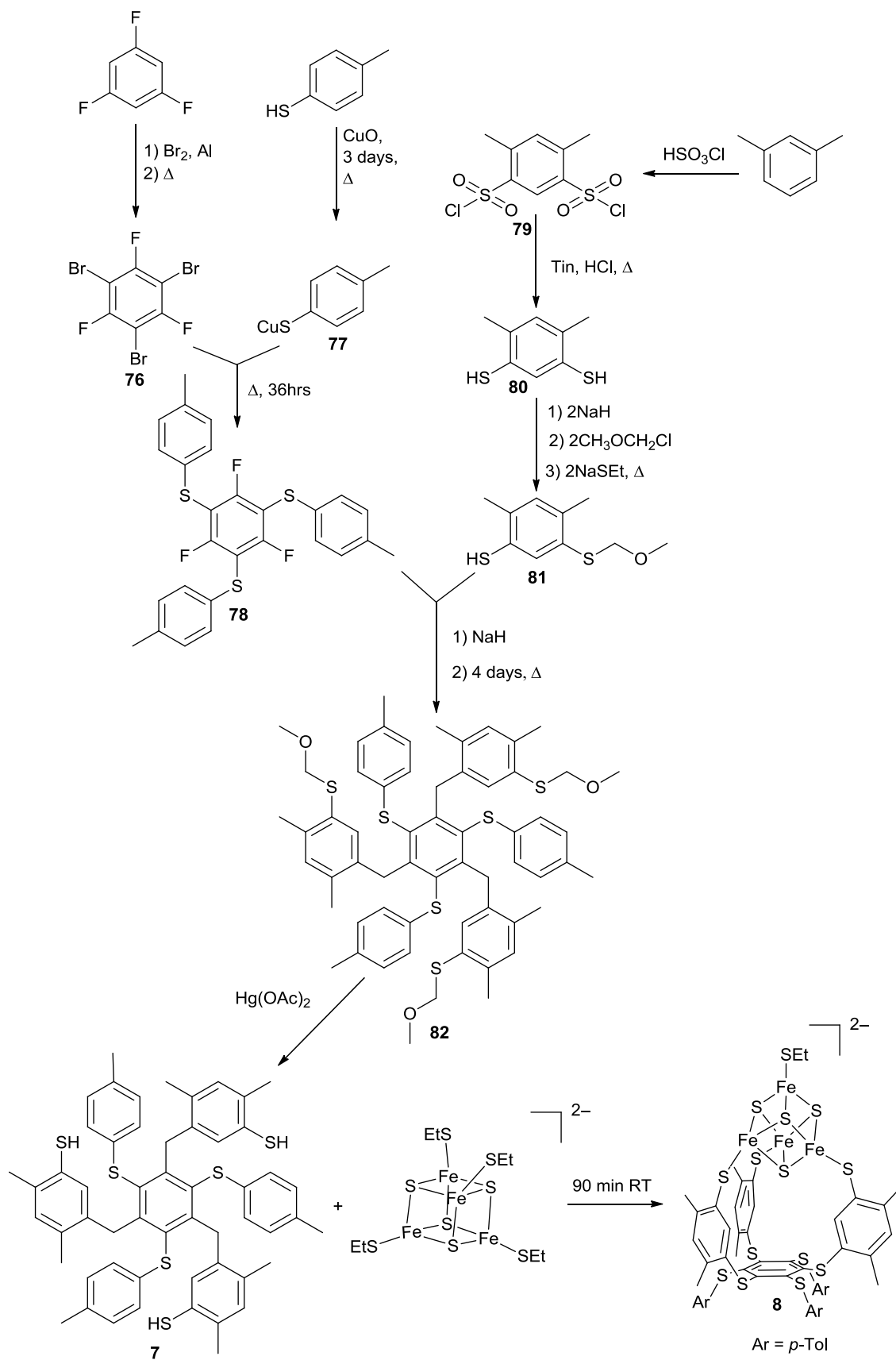
Cyanide equivalents were added by introducing small quantities (typically  $<10 \text{ }\mu\text{L}$ ) of concentrated cyanide in MeCN solution using a micro syringe. In experiments involving CO the solution was bubbled with a gentle flow of CO gas between measurements.

## 5 Reactions of a site-differentiated cluster with CO and CN<sup>-</sup>

### 5.1 Site-differentiated clusters

The chemical syntheses of site differentiated clusters, aspects of their chemistry, and relevance as models to biological systems are covered in Section 4.1. Synthetic site differentiated iron-sulfur clusters can be used to model many clusters found in biology. In catalytically active iron-sulfur clusters the cluster is invariably coordinated to the protein by cysteine at three of the four iron atoms. A trithiolate ligated synthetic cluster mimics this environment. The chemistry at the unique Fe site can be studied and thus yield information about how a natural site differentiated cluster might be expected to behave.

It has been demonstrated previously that [4Fe4S]<sup>2+</sup> clusters do not interact with CO alone.<sup>270</sup> In contrast CN<sup>-</sup> does coordinate to synthetic clusters (Scheme 9).<sup>159</sup> It has also been shown that in the biological site differentiated {4Fe4S} cluster of *Pyrococcus furiosus* ferredoxin (where three Fe sites are bound by cysteine residues) that a single CN<sup>-</sup> can bind reversibly to the unique Fe site<sup>271</sup> and more recently that CN<sup>-</sup> binding is likely involved in turnover of HydG.<sup>87</sup> The work in this section describes the interaction between the site differentiated cluster **8** and CO and CN<sup>-</sup>. The synthesis of the Holm cluster **8** is outlined in the experimental section of this chapter. A schematic overview is shown below in Scheme 51.



**Scheme 51** Overview of the synthesis of the Holm cluster **8**.

## 5.2 Probing interactions of CO and CN<sup>-</sup> by cyclic voltammetry

### 5.2.1 The effect of CO on the cyclic voltammetry of a site differentiated cluster

The interaction of the “Holm cluster” **8** (Figure 16) with CO was investigated using cyclic voltammetry. On changing from an atmosphere of N<sub>2</sub> to one of carbon monoxide no change in position of the parent redox couple at  $E_{1/2} = -0.99$  V. This parallels the behaviour observed for undifferentiated clusters as described in section 4.3.2.

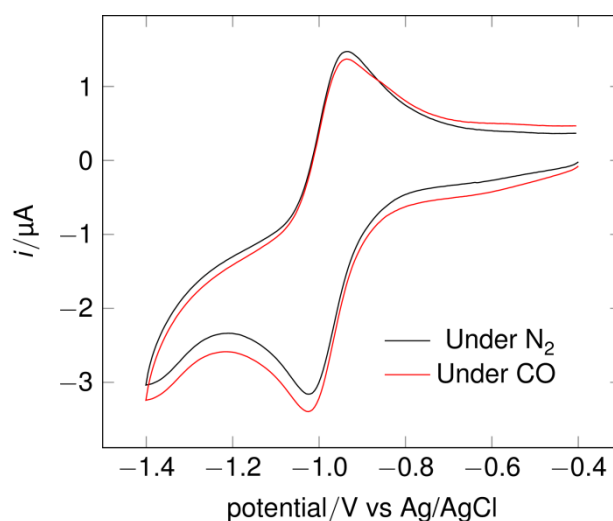


**Figure 127** Cyclic voltammogram of the “Holm cluster” under N<sub>2</sub> (black) and under CO (red). Electrode: vitreous carbon; 50 mV s<sup>-1</sup>; 0.1 M [Bu<sub>4</sub>N][BF<sub>4</sub>] – MeCN; RT; [Cluster] = 0.27 mM.

That there is no measurable interaction between **8** and CO alone was further supported by stopped-flow FTIR experiments (section 5.2.2).

### 5.2.2 Spectra following mixing of CO and clusters

On mixing of the “Holm cluster” with CO no IR bands are seen in the difference spectrum after 5 min. This indicates that there is no measurable interaction between **8** (Holm cluster) and CO alone. This is in keeping with what has been seen in the cyclic voltammetry for this cluster and also what is seen for the undifferentiated clusters [Fe<sub>4</sub>S<sub>4</sub>(SR)<sub>4</sub>]<sup>2-</sup> (R = Et, Ph).

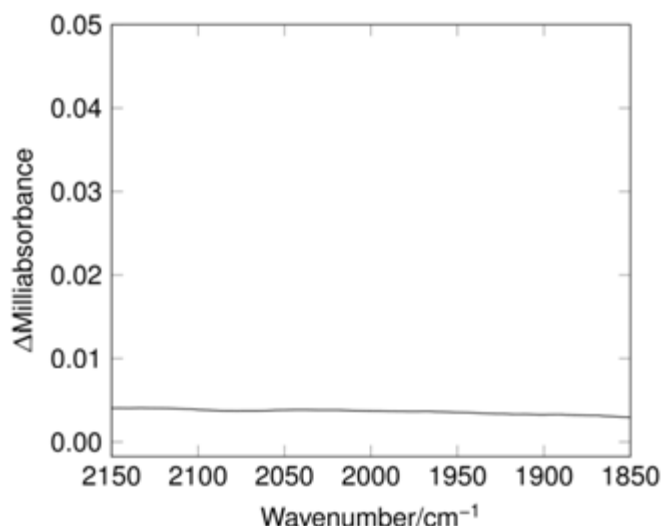


**Figure 128** FTIR spectrum of “Holm cluster” in MeCN under CO after 5 min.

### 5.2.3 The effect of $\text{CN}^-$ on the cyclic voltammetry of a site differentiated cluster

The cyclic voltammetry of the “Holm cluster” under dinitrogen in the presence of cyanide was investigated. On addition of increasing cyanide equivalents the wave corresponding to the starting material lessened in size and a new wave at more positive potential appeared ( $E_{1/2} = -0.79$  V) as shown in Figure 129 and shown separately in Figure 130. This shift of circa 190 mV is in keeping with substitution of  $\text{EtS}^-$  for  $\text{CN}^-$  as reported for this cluster in work by Zhou and co-workers.<sup>276</sup> In cyclic voltammetry experiments in the previous chapter it was demonstrated that the undifferentiated clusters  $[\text{Fe}_4\text{S}_4(\text{SR})_4]^{2-}$  (R = Et and Ph) react with  $\text{CN}^-$  to give mono- and di-cyanide substituted species. In the site differentiated case there is only one new wave observed corresponding to a mono cyanide containing species, as is consistent with the reactivity at the unique site.

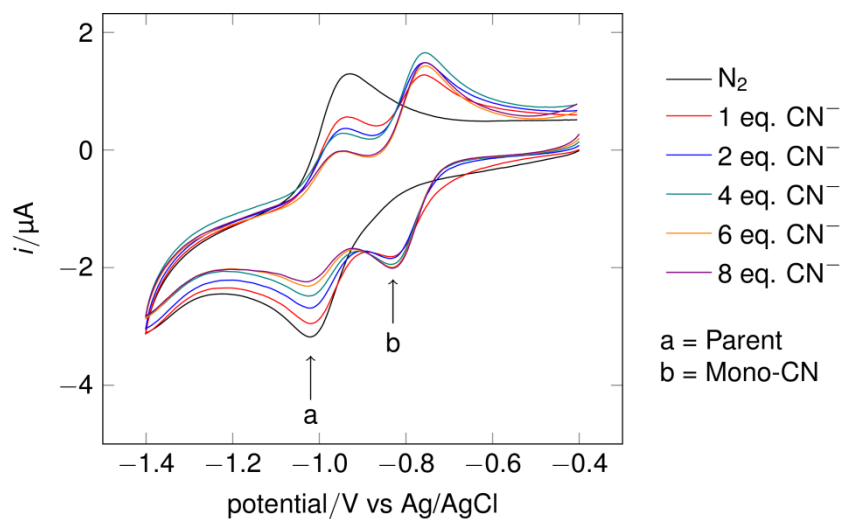


**Figure 129** Cyclic voltammogram of “Holm cluster” (**8**) under dinitrogen with increasing addition of cyanide in MeCN. Electrode: vitreous carbon;  $50 \text{ mV s}^{-1}$ ;  $0.1 \text{ M } [\text{Bu}_4\text{N}][\text{BF}_4] - \text{MeCN}$ ; RT;  $[\text{Cluster}] = 0.21 \text{ mM}$ .

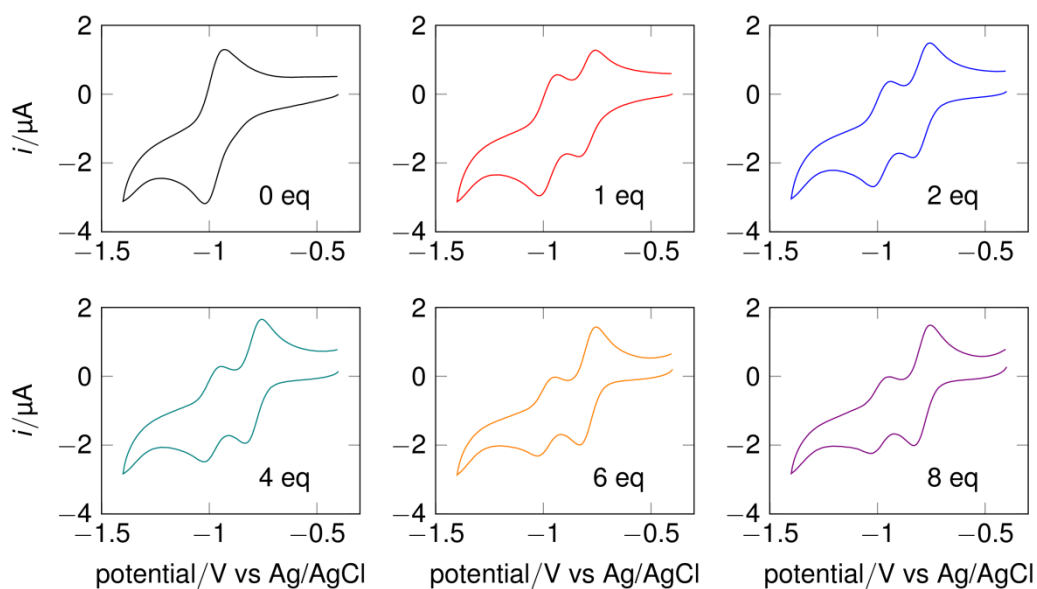


**Figure 130** Panel depiction of cyclic voltammogram of “Holm cluster” under dinitrogen with increasing concentration of cyanide. Electrode: vitreous carbon;  $50 \text{ mV s}^{-1}$ ;  $0.1 \text{ M } [\text{Bu}_4\text{N}][\text{BF}_4] - \text{MeCN}$ ; RT;  $[\text{Cluster}] = 0.21 \text{ mM}$

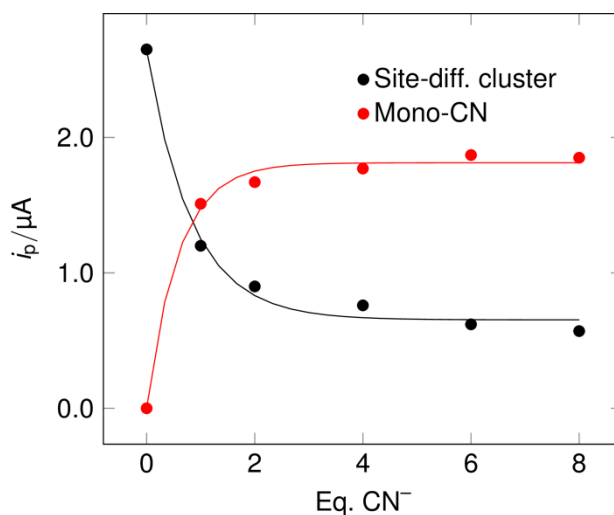
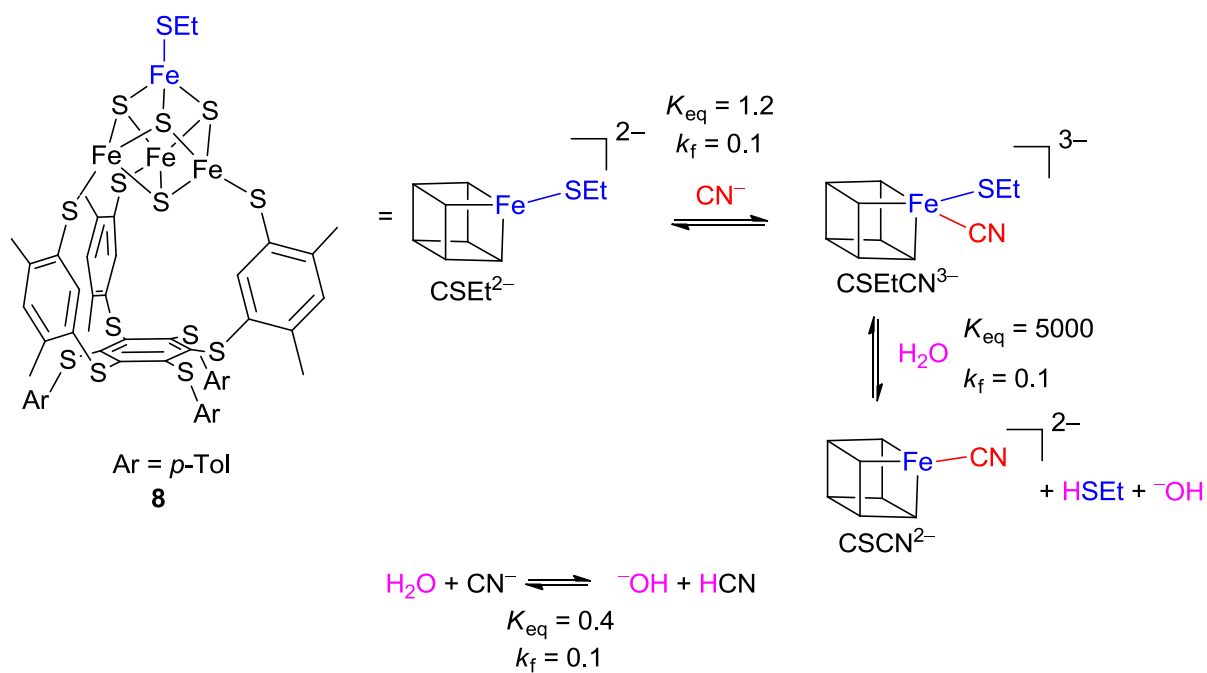


**Figure 131** Depletion of site differentiated parent compound “Holm cluster” vs growth of suspected mono cyanide species.

The equilibrium of the reaction between the Holm cluster **8** and CN<sup>-</sup> does not shift completely over to products, even at high CN<sup>-</sup> addition. The conversion of cluster to mono CN<sup>-</sup> appears to plateau at approximately 70 % product. This suggests that the substitution reaction is inhibited high cyanide concentration. The reaction mechanism behind this response in the cyclic voltammetry was probed using electrochemical simulation software (DigiElch). A satisfactory simulation of the experimental data was achieved using the mechanistic model outlined in Scheme 52 which depicts the associative addition of CN<sup>-</sup> followed by dissociation of EtSH (with adventitious water as a proton source).



**Scheme 52** Proposed reaction mechanism for electrochemical simulation of the behaviour of the “Holm cluster” **8** with  $\text{CN}^-$ . Electrochemical parameters outlined in Table 12.

In this model  $\text{CN}^-$  reacts with water to a small extent giving  $\text{HCN}$  and  $\text{}^-\text{OH}$ . The electrochemical parameters used in the simulation including equilibrium constants and diffusion coefficients are shown in Table 12.

**Table 12** Parameters used to simulate the cyclic voltammograms in Figure 134 and Figure 135, where  $E^0$  is the standard potential at which the charge transfer process occurs,  $\alpha$  is the electron transfer coefficient (a factor determining the effect of a change in potential on the activation energy of a reaction),  $k_s$  is the heterogenous rate constant (a measure of how fast electrons are crossing the electrode interface),  $D$  is the simulated diffusion coefficient for each species,  $C_{\text{anal}}$  is the amount of analyte added to the system,  $C_{\text{init}}$  is the amount present once initial equilibrium is achieved. The species annotated in the table as  $\text{CSEt}^{2-}$ , etc. correspond to the clusters and substrates identified in Scheme 52.

Charge-Transfer Reaction	$E^0 / \text{V}$	$\alpha$	$k_s / \text{cm s}^{-1}$
$\text{CSEt}^{2-} + \text{e}^- = \text{CSEt}^{3-}$	-0.98	0.5	10000
$\text{CCN}^{2-} + \text{e}^- = \text{CCN}^{3-}$	-0.8	0.5	10000

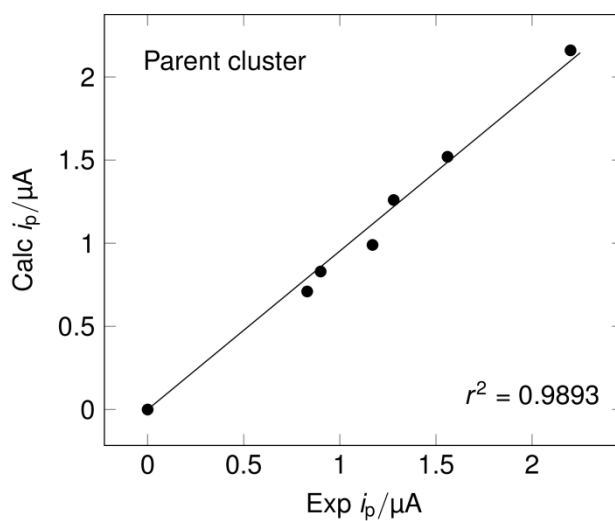
Chemical reaction	$K_{\text{eq}}$	$k_f$	$k_b$
$\text{CSEt}^{2-} + \text{CN}^- = \text{CSEtCN}^{3-}$	1.2	0.1	0.083333
$\text{H}_2\text{O} + \text{CSEtCN}^{3-} = \text{}^-\text{OH} + \text{CCN}^-$	5000	0.1	0.00002
$\text{H}_2\text{O} + \text{CN}^- = \text{HCN} + \text{}^-\text{OH}$	0.4	0.1	0.25

Species	$D$ $/\text{cm}^2 \text{s}^{-1}$ $\times 10^{-6}$	$C_{\text{anal}} /$ $\text{mol L}^{-1}$
$\text{CSEt}^{2-}$	7.5	0.00021
$\text{CSEt}^{3-}$	7.5	0
$\text{CCN}^{2-}$	7.5	0
$\text{CCN}^{3-}$	7.5	0
$\text{CN}^-$	10	$n$ eq.
$\text{CSEtCN}^{3-}$	7.5	0
$\text{H}_2\text{O}$	10	0.0004
$\text{HCN}$	10	0
$\text{}^-\text{OH}$	10	0

Support for this proposed mechanism as outlined in Scheme 52 is given by the linear relationship between the experimental and simulated peak currents of the respective mono-cyanide and parent species, Figure 132 and Figure 133. The peak currents of the parent and

mono-cyanide species at for each addition of  $\text{CN}^-$  were measured in the fashion depicted in Figure 136.



**Figure 132** Experimental vs calculated peak currents for the parent site differentiated cluster 8.

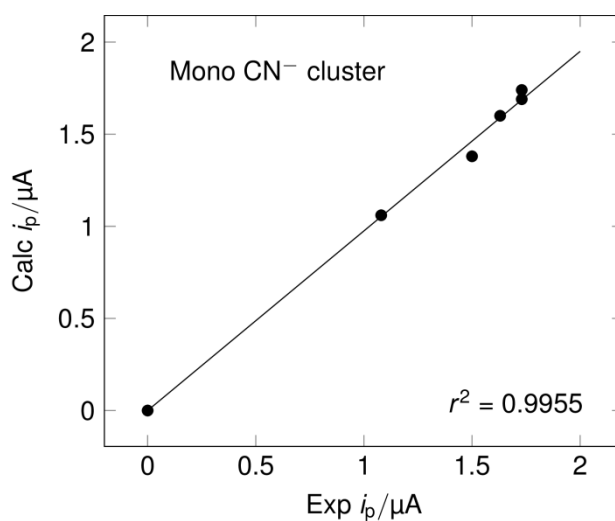


**Figure 133** Experimental vs calculated peak currents for the putative mono-cyanide derivative of the site differentiated cluster 8.

Comparative cyclic voltammograms of the simulated and experimental data from the reaction of the Holm cluster 8 with 1 equivalent and 8 equivalents of cyanide are shown in Figure 134 and Figure 135.

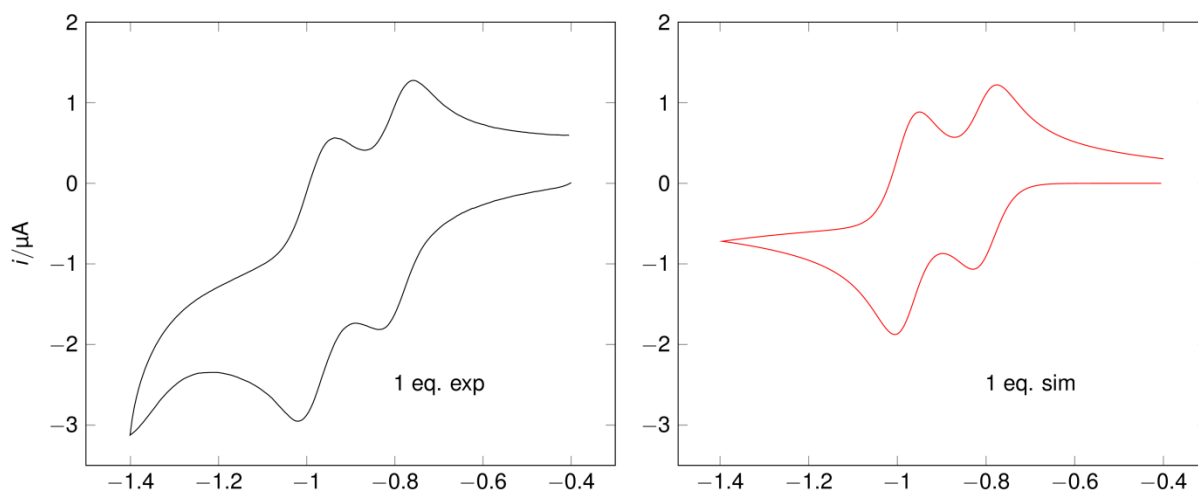


**Figure 134** Comparison of simulated (red) and experimental (black) data for the cyclic voltammetry of the “Holm cluster” under CO with 1 eq.  $\text{CN}^-$ . Experimental conditions: electrode: vitreous carbon;  $50 \text{ mV s}^{-1}$ ;  $0.1 \text{ M } [\text{Bu}_4\text{N}][\text{BF}_4] - \text{MeCN}$ ; RT;  $[\text{Cluster}] = 0.21 \text{ mM}$ . Simulation parameters in Table 12.

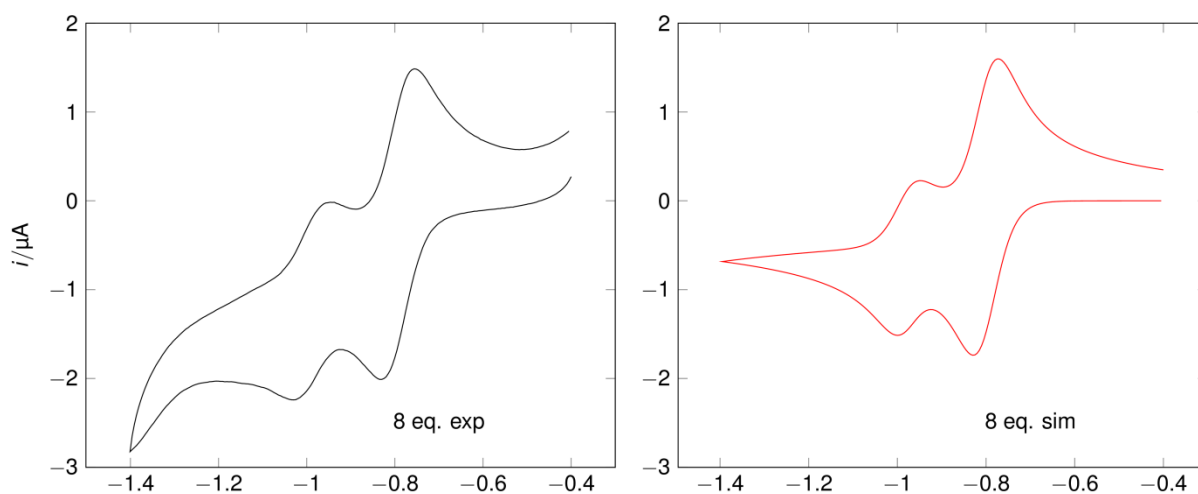


**Figure 135** Comparison of simulated (red) and experimental (black) data for the cyclic voltammetry of the “Holm cluster” under CO with 8 eq.  $\text{CN}^-$ . Experimental conditions: electrode: vitreous carbon;  $50 \text{ mV s}^{-1}$ ;  $0.1 \text{ M } [\text{Bu}_4\text{N}][\text{BF}_4] - \text{MeCN}$ ; RT;  $[\text{Cluster}] = 0.21 \text{ mM}$ . Simulation parameters in Table 12.

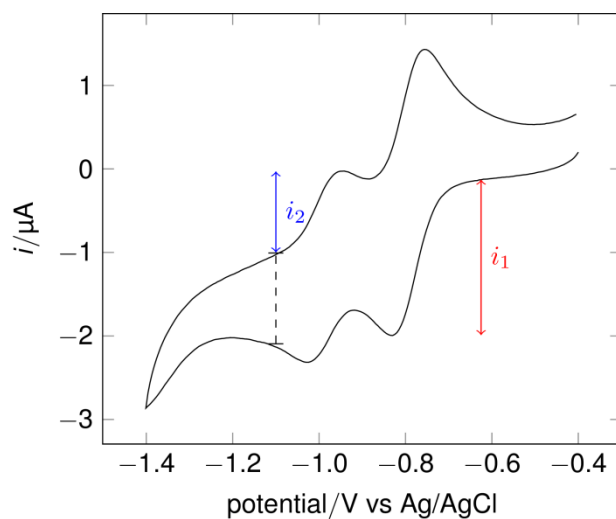


**Figure 136** Cyclic voltammogram illustrating the method by which peak currents of the parent and the mono cyanide species, at  $-0.99$  and  $-0.79$  V, respectively, were measured.  $i_1$  = peak current of mono-cyanide substituted species,  $i_2$  = parent **8**. Dashed line shows the potential at which the reverse peak current was measured ( $-1.1$  V).

The key mechanistic aspect of the modelling of the system as shown in Scheme 52 is that as the concentration of cyanide increases the extent of the conversion to product falls off. This is suggested to be a consequence of decreasing the availability of proton in the media as the concentration of basic cyanide increases.

#### 5.2.4 Probing the interaction of site differentiated cluster (8) with $\text{CN}^-$ under $\text{N}_2$ by stopped-flow FTIR

The time-course for the reaction of the site differentiated cluster with cyanide (four equivalents) is shown in Figure 137. As observed with the undifferentiated clusters a peak associated with extrusion of ferrocyanide is observed to grow-in at  $2044\text{ cm}^{-1}$  but the major peak is at  $2098\text{ cm}^{-1}$  which is assigned to the mono-cyanide product. As discussed for the reactions of the undifferentiated clusters the relative intensities of the  $2044$  and  $2098\text{ cm}^{-1}$  bands must be considered in the context of one and six IR active chromophores in the molecules. The weak band at  $2058\text{ cm}^{-1}$  is also observed in the reactions of the undifferentiated clusters and may be indicative of an intermediate leading to ferrocyanide formation.

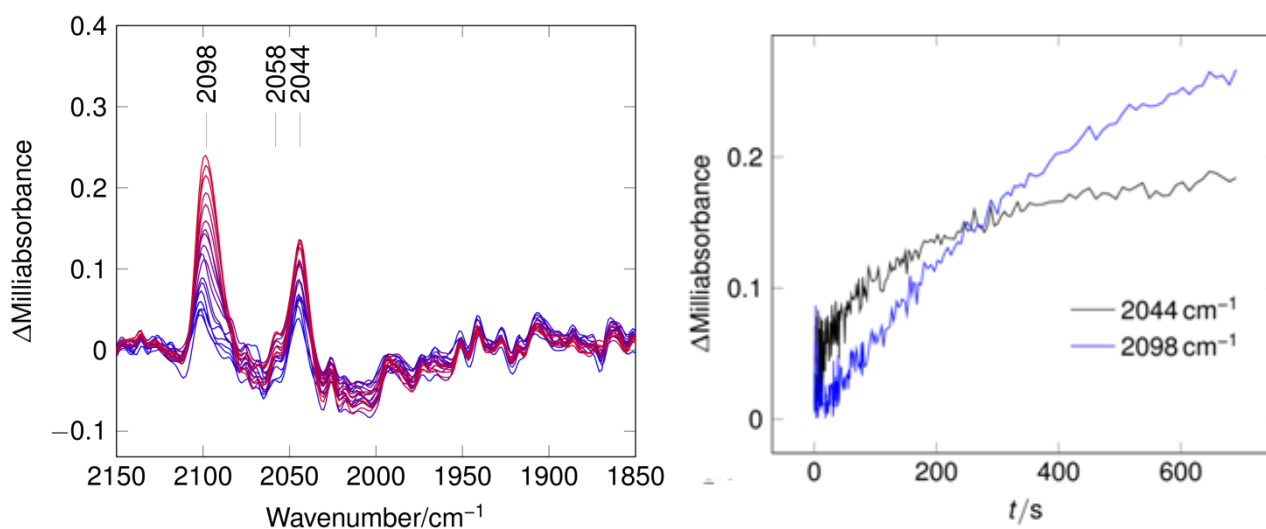


**Figure 137** Solution of the site differentiated “Holm cluster” with 4 eq. of tetraethylammonium cyanide in MeCN under  $\text{N}_2$ . Growth of bands at  $2044$  and  $2098\text{ cm}^{-1}$  over the course of 11 min. Initial [cluster] = 1 mM.

### 5.3 Reaction of CO and CN<sup>-</sup> with the site differentiated cluster.

The reaction of the site differentiated cluster **8** (Holm cluster) with both CN<sup>-</sup> and CO was investigated. Under CO with one eq. of cyanide there is an equilibrium between the previously observed “mono cyanide” species at  $E_{1/2} = -0.79$  V, the starting material at  $E_{1/2} = -0.99$  V and a *new* CO dependent species at more negative potential at  $E_{1/2} = -1.17$  V. When a second equivalent of cyanide is added the peak current of the redox couple corresponding to the “mono cyanide” species diminishes and there is a great increase in the peak current response of the CO dependent species. As the amount of cyanide is increased further the equilibrium between the starting material and the new species is pushed over to favor the new product as shown in Figure 138 and depicted in a panel fashion in Figure 139. At 8 equivalents of cyanide this equilibrium is pushed completely over to the CO dependent species as shown in Figure 140.

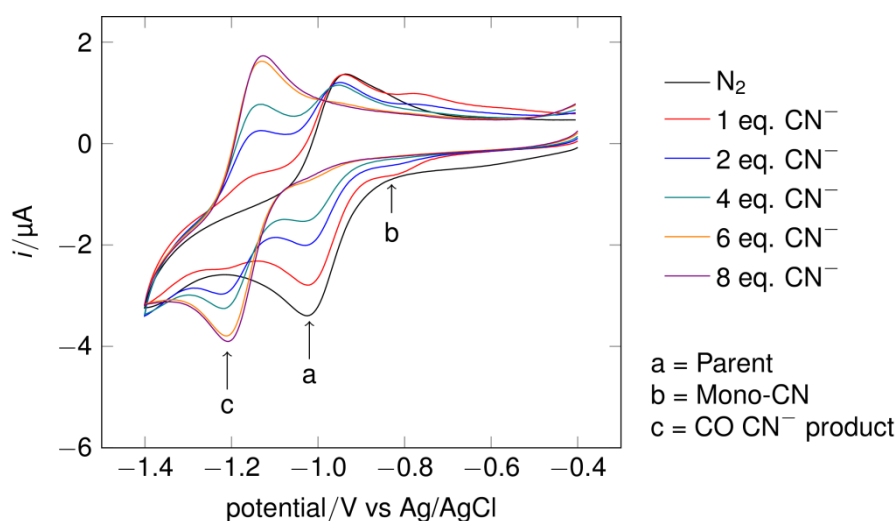


**Figure 138** Cyclic voltammogram of a solution of **8** (Holm cluster) under carbon monoxide with increasing addition of cyanide. Species a = parent site differentiated cluster **8**, b = mono-cyanide product, c = CO and CN<sup>-</sup> containing product. Electrode: vitreous carbon; 50 mV s<sup>-1</sup>; 0.1 M [Bu<sub>4</sub>N][BF<sub>4</sub>] – MeCN; RT; [Cluster] = 0.27 mM.

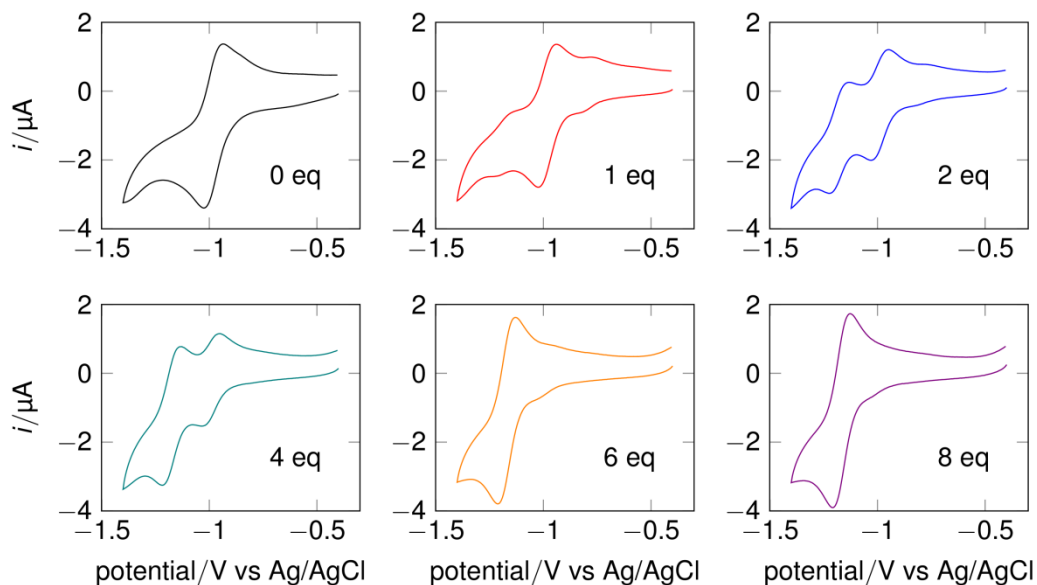


**Figure 139** Panel view of cyclic voltammogram of a solution of the “Holm cluster” under carbon monoxide with increasing concentration of cyanide. Electrode: vitreous carbon;  $50 \text{ mV s}^{-1}$ ;  $0.1 \text{ M } [\text{Bu}_4\text{N}][\text{BF}_4] - \text{MeCN}$ ; RT;  $[\text{Cluster}] = 0.27 \text{ mM}$ .

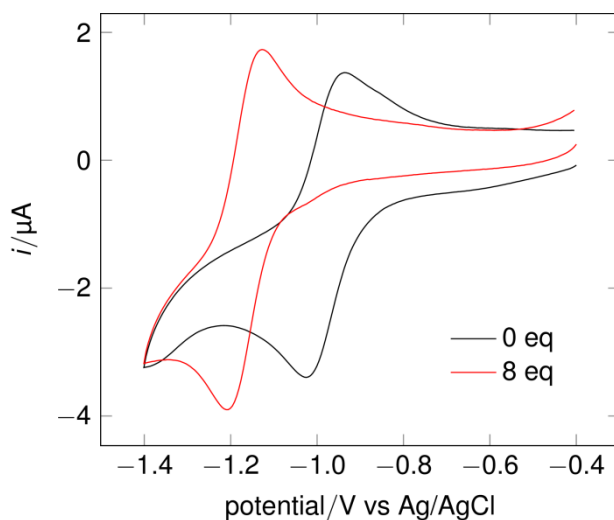


**Figure 140** Cyclic voltammogram of “Holm cluster” under carbon monoxide with no  $\text{CN}^-$  (blue) and 8 eq. of cyanide (red). Electrode: vitreous carbon;  $50 \text{ mV s}^{-1}$ ;  $0.1 \text{ M } [\text{Bu}_4\text{N}][\text{BF}_4] - \text{MeCN}$ ; RT;  $[\text{Cluster}] = 0.27 \text{ mM}$ .

The species at  $E_{1/2} = -1.17$  V can also be formed by first adding 8 eq. of  $\text{CN}^-$  to a solution of **8** (Holm cluster) under  $\text{N}_2$  followed by bubbling with CO as shown in Figure 141.

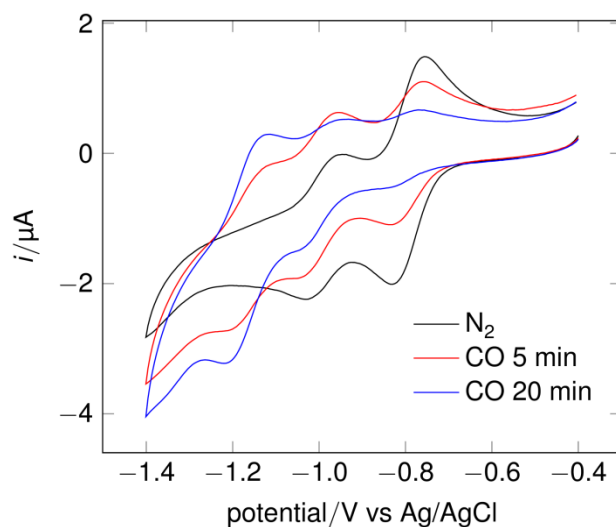


**Figure 141** Cyclic voltammogram of “Holm cluster” with 8 eq of  $\text{CN}^-$  under dinitrogen followed by bubbling the solution with CO for 20 min. Electrode: vitreous carbon;  $50 \text{ mV s}^{-1}$ ;  $0.1 \text{ M } [\text{Bu}_4\text{N}][\text{BF}_4] - \text{MeCN}$ ; RT;  $[\text{Cluster}] = 0.21 \text{ mM}$ .

Although the mono-cyanide species is removed by CO and the carbonyl species is evidently formed the equilibration is apparently slow compared with addition of  $\text{CN}^-$  to a CO saturated solution of the cluster. Moreover, the parent complex appears to not react with CO under these conditions. This can be explained by the model we have for cyanide substitution as discussed in section 5.2.3 whereby high  $\text{CN}^-$  concentration decreases available protons and thence associative displacement of EtSH. The implication is that the overall CO reaction must proceed via a cyanide coordinated cluster intermediate. Unless this intermediate is first formed no reaction can occur. This is consistent with previous experiments where CO alone does not react with the cluster. This observation excludes the possibility of an intermediate or transition state in which an  $\text{Fe}(\text{SEt})(\text{CO})$  species is attacked by  $\text{CN}^-$  concerted with  $\text{EtS}^-$  displacement. Here it is useful to compare the CO/ $\text{CN}^-$  species detected by cyclic voltammetry in this site differentiated system with the data for the undifferentiated clusters.

At low cyanide concentrations the tetrathiophenolate cluster reacts to give a species with  $E_{1/2} = -1.16$  V this is similar to that observed with the site differentiated cluster under similar conditions, which is at  $E_{1/2} = -1.17$  V. The small difference is readily accountable by the alkyl substituents on the aryl thiolates of the site differentiated cluster conferring more electron density on the cluster core. Notably the difference in potential of the site differentiated cluster and the thiophenylate cluster with a single  $\text{CN}^-$  substituent is only 30 mV. The final species formed at higher cyanide concentrations for the undifferentiated  $[\text{Fe}_4\text{S}_4(\text{SPh})_4]^{2-}$  and  $[\text{Fe}_4\text{S}_4(\text{SEt})_4]^{2-}$  have potentials of  $E_{1/2} = -1.11$  and  $-1.30$  V, respectively. These values are also fully consistent with the formation of closely analogous species. The difference in potentials of the di-cyanide clusters  $[\text{Fe}_4\text{S}_4(\text{SPh})_2(\text{CN})_2]^{2-}$  and  $[\text{Fe}_4\text{S}_4(\text{SEt})_2(\text{CN})_2]^{2-}$  is 140 mV. The same difference in potential is observed for the  $[\text{Fe}_4\text{S}_4(\text{SPh})_2(\text{CN})_2(\text{CO})_n]^{2-}$  and  $[\text{Fe}_4\text{S}_4(\text{SEt})_2(\text{CN})_2(\text{CO})_n]^{2-}$  species. This reinforces the interpretation of these closely related structures in the stopped-flow FTIR experiments with CO and  $\text{CN}^-$  with the undifferentiated clusters.

## 5.4 Probing interactions of CO and CN<sup>-</sup> by Stopped-flow FTIR

### 5.4.1 Addition of cyanide to CO saturated solution of “Holm cluster”

On addition of CN<sup>-</sup> to CO saturated solution of “Holm cluster” the growth of two bands can be seen reaching a maximum at around 12 min. The spectrum below in Figure 142 shows the growth of these bands over the first 90 s for clarity. At longer time (12 min) more background artefacts can be seen but these do not appear to be time dependent.

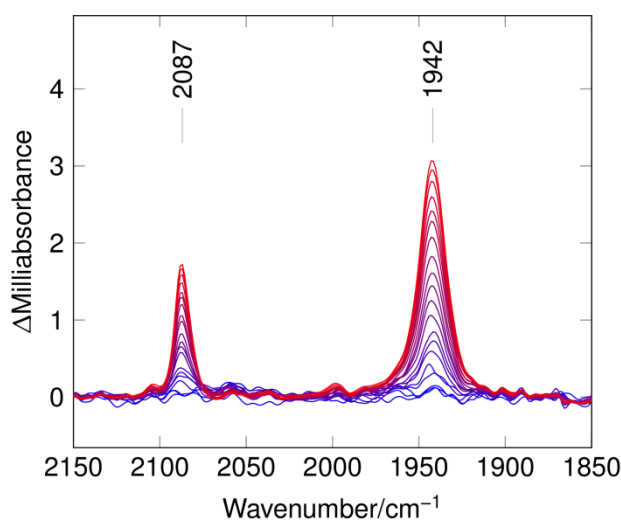


**Figure 142** Stopped-flow FTIR spectra of “Holm cluster” with four equivalents of CN<sup>-</sup> in MeCN under CO over the course of 83 s. Blue: early scans, red: later scans. Initial [cluster] = 1.0 mM

When the growth of one band is plotted against the other a straight line is seen. The linearity of the growth of the two bands is good evidence for them both being derived from a single species. When referring to this species in subsequent sections it will be referred to as **IS<sub>3</sub>**.

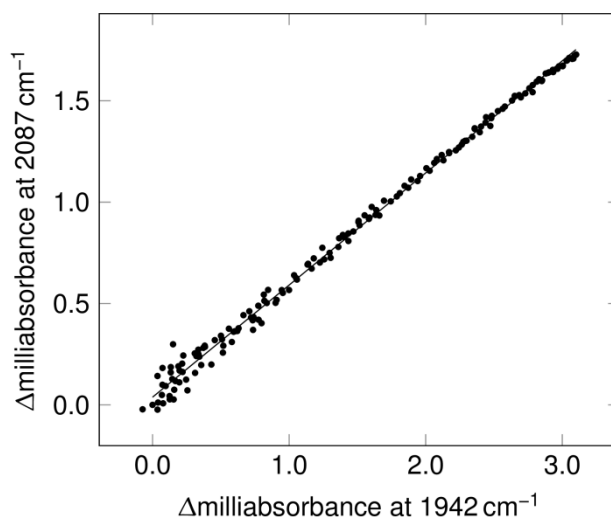


**Figure 143** Growth of the IR band at  $2087\text{ cm}^{-1}$  against growth of the IR band at  $1942\text{ cm}^{-1}$  from Figure 96.

The behaviour of the site differentiated cluster parallels that of the undifferentiated cluster at short time, however, in the presence of excess CO and  $\text{CN}^-$  **ISPh** and **ISet** are detected over a short time frame of ca 10 s as they are converted to the major product species **IISPh** and **IISet**. In contrast under the same conditions solutions of **IS<sub>3</sub>** appear to be stable over a greatly extended period under CO (up to 30 min). The longer lifetime of **IS<sub>3</sub>** must be attributable to the tripodal trithiolate protecting the other three irons from subsequent attack by cyanide and carbon monoxide. Thus the chelate effect will retain dissociated thiolate in high proximal concentration to an Fe centre following a dissociation or associative step, thus favouring recombination. Additionally the “umbrella” of the tripodal ligand superstructure is likely to sterically inhibit associative attack.

On a longer time-scale, there is some evidence of further chemistry which may be a consequence of unravelling of the tri-dentate coordination. After 30 min minor peaks at  $2104$  and  $1999\text{ cm}^{-1}$  begin to appear.

#### 5.4.2 Addition of cyanide to $^{13}\text{CO}$ saturated solution of “Holm cluster”

As for the undifferentiated clusters,  $^{13}\text{CO}$  isotopic labelling was used to confirm the identity of the carbonyl band(s) in the spectrum of  $\text{IS}_3$  (Figure 142). When four equivalents of cyanide are added to a  $^{13}\text{CO}$  saturated solution of “Holm cluster” the growth of two bands is seen, Figure 144. The band at  $1942\text{ cm}^{-1}$  observed in the reaction of the unlabelled complex is shifted to  $1898\text{ cm}^{-1}$ , Figure 144, in excellent agreement with the calculated isotopic shift of  $1898\text{ cm}^{-1}$  for a carbonyl band. The band at  $2087\text{ cm}^{-1}$  is not shifted, fully consistent with its assignment as a CN stretch and concordant with this analysis for the undifferentiated clusters. The labelled system, as expected, shows an excellent linear correlation in the growth of the two bands in the  $^{13}\text{CO}$  as shown in Figure 145.

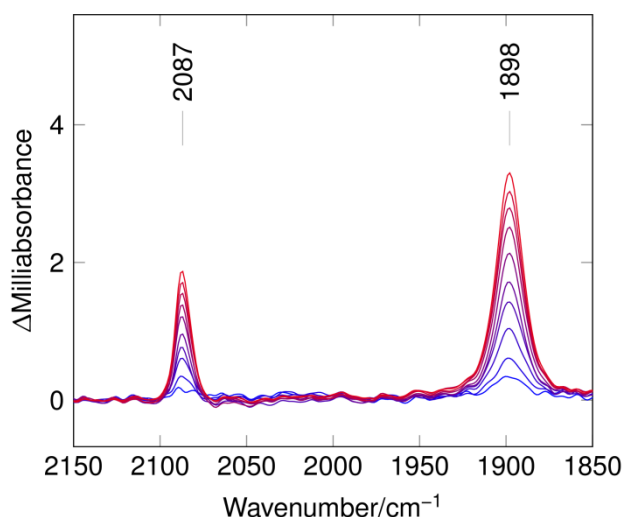


**Figure 144** Stopped-flow FTIR spectra of a reaction of “Holm cluster” with four equivalents of  $\text{CN}^-$  in MeCN under  $^{13}\text{CO}$ . Blue: early scans, red: later scans over the course of 90 s. Initial [cluster] = 1.1 mM.

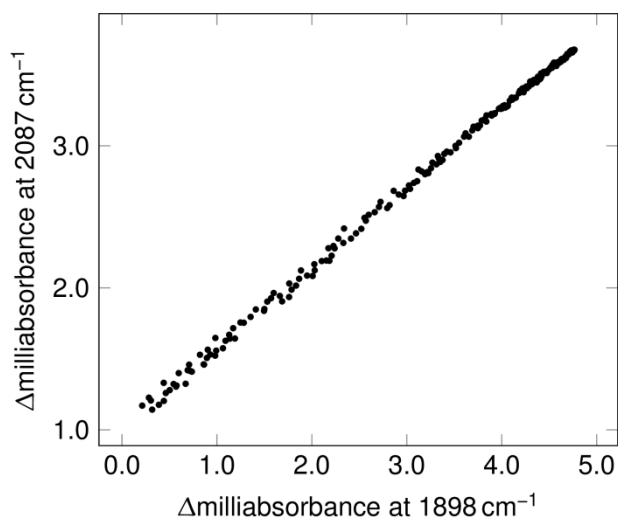


**Figure 145** Growth of the IR band at  $2087\text{ cm}^{-1}$  against growth of the IR band at  $1898\text{ cm}^{-1}$  from Figure 144.

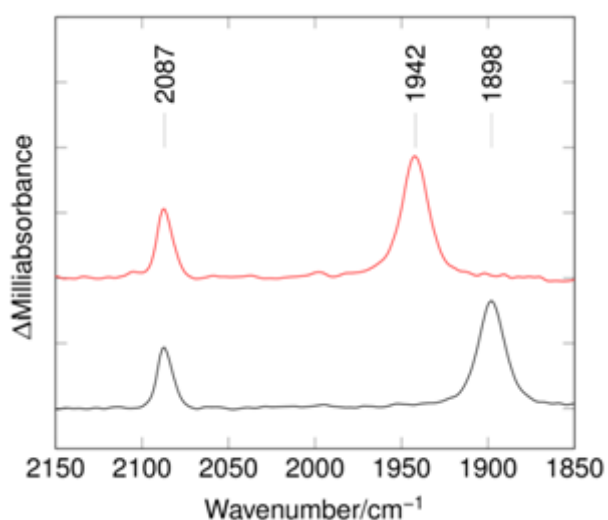


**Figure 146** FTIR of a reaction of “Holm cluster” with four equivalents of  $\text{CN}^-$  in MeCN red: under CO, black: under  $^{13}\text{CO}$ , over the course of 85 s. Normalised to 1 mM initial [cluster].

As discussed in chapter 4, for the undifferentiated clusters the experimental infrared spectra for **ISEt** and **ISPh** are in good agreement with the DFT calculated spectrum  $[\text{Fe}_4\text{S}_4(\text{SPh})_3(\text{CN})(\text{CO})]^{2-}$  species where CO and  $\text{CN}^-$  share an Fe centre. These experimentally and computationally observed spectra are in concordance with that observed for **IS<sub>3</sub>**. However, it was noted that a species where two  $\text{CN}^-$  and one CO share an Fe centre

could give a similar spectrum (although with poor agreement for the CO frequency) if the cyanide bands were unresolved. Here it is useful to compare the experimentally observed cyanide band with those other systems.

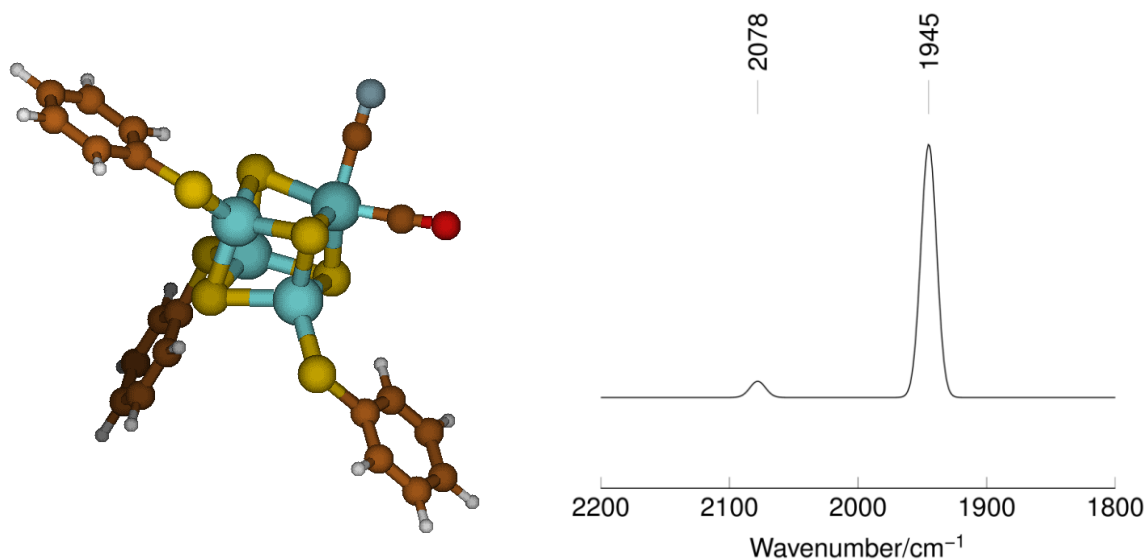


**Figure 147** Model cluster  $[(\text{Fe}_4\text{S}_4)(\text{SPh})_3(\text{CO})(\text{CN})]^{2-}$  (left), DFT calculated IR (right).

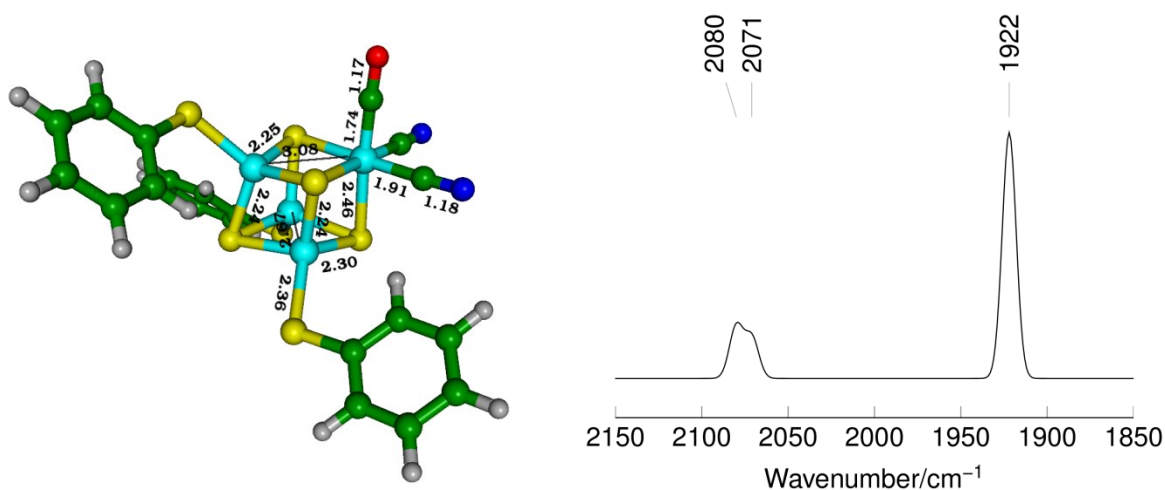


**Figure 148** Di-cyanide mono CO cluster  $[(\text{Fe}_4\text{S}_4)(\text{SPh})_3(\text{CO})(\text{CN})_2]^{3-}$  (left), DFT calculated IR.

If *two* cyanides were bound to a *single* Fe in a *cis* arrangement the vibrations would be coupled and two peaks would be expected. Examples of this arrangement include the Fe

centres of the Ni-C and the Ni-L states of the [NiFe]-hydrogenase which show bands at 2074 and 2085  $\text{cm}^{-1}$  and 2048 and 2061  $\text{cm}^{-1}$ , respectively.<sup>277</sup> In these examples the two cyanide bands are clearly distinguishable and separated by at least ten wavenumbers. In our system only a single band in the cyanide is observed. It could be arguable that two overlapping cyanide bands might not be resolved. However, some broadening of the single band would be expected. In the spectra for our  $^{12}\text{CO}$  and the  $^{13}\text{CO}$  experiments the peak width at half height for the cyanide bands are  $10.5 \pm 0.2 \text{ cm}^{-1}$ . In the complex  $[(\mu\text{-SCH}_2\text{CH}_2\text{CH}_2\text{S})\text{Fe}_2(\text{CO})_4(\text{CN})_2]$  in which unambiguously a single cyanide is bound to each Fe, the peak width at half height in the same solvent, (MeCN) is  $10.9 \pm 0.2 \text{ cm}^{-1}$ . Thus it is not evident that we have broadening due to overlapping bands, supporting the assignment of **IS<sub>3</sub>** as a  $[\text{Fe}_4\text{S}_4(\text{LS}_3)(\text{CO})(\text{CN})]^{2-}$  species where CO and  $\text{CN}^-$  are co-ligands at the unique Fe.

In further support of this assignment, in systems where two  $\text{CN}^-$  and one CO ligands are unambiguously bound to a single Fe centre in a mutually *cis* arrangement, two cyanide peaks are resolved. For example in the complex  $[\text{CpFe}(\text{CN})_2(\text{CO})]^-$  two cyanide peaks are observed at 2088 and 2094  $\text{cm}^{-1}$  as shown in Figure 149.<sup>278</sup> The nominal peak width at half maximum height is 12.6  $\text{cm}^{-1}$ .

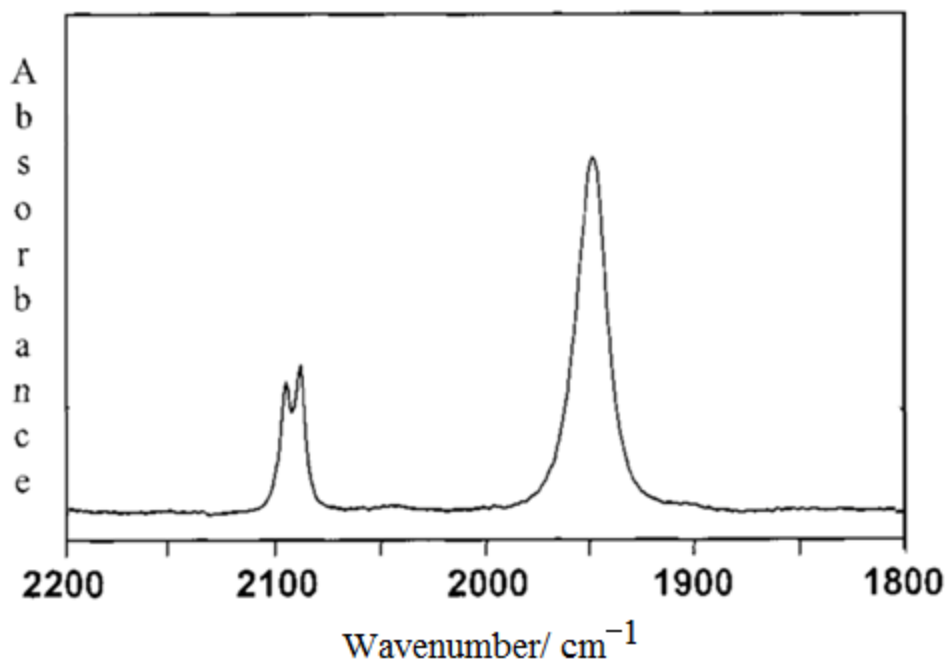


**Figure 149** Solution infrared of  $[\text{CpFe}(\text{CN})_2(\text{CO})]^-$  in MeCN adapted from ref 278.

The Ni-B state of NiFe hydrogenase contains an  $\text{Fe}^{\text{II}}$  atom coordinated by two  $\text{CN}^-$  and one CO ligand in a pseudo-octahedral environment. The IR spectrum corresponding to this centre in the protein has well-resolved cyanide bands at 2090 and 2079  $\text{cm}^{-1}$ .

### 5.4.3 Mass spectrometry studies

A solution of “Holm cluster” with four equivalents of tetraethylammonium cyanide under CO in MeCN was run on an LTQ Orbitrap mass spectrometer. A molecular ion for a “Complex A” like species (where CO and  $\text{CN}^-$  are at the unique iron site on the cluster) might be expected near 1622  $\text{g mol}^{-1}$ . This is not seen on this spectrum nor can any fragments be identified. It may be that this material does not form gaseous ions under the conditions used.

Negative ions for  $\{[\text{Fe}_4\text{S}_4(\text{LS}_3)(\text{CO})(\text{CN})][\text{NBu}_4]\}^-$  and  $\{[\text{Fe}_4\text{S}_4(\text{LS}_3)(\text{CO})(\text{CN})_2][\text{NBu}_4]\}^-$  at 1591.00 and 1621.01  $\text{g mol}^{-1}$ , respectively or their decarbonylated ions at 1567.01 and 1593.01  $\text{g mol}^{-1}$  are not observed. Analogous negative ion clusters “flying” with  $\text{Et}_4\text{N}^+$  such as  $\{[\text{Fe}_4\text{S}_4(\text{LS}_3)(\text{CN})][\text{NEt}_4]\}^-$  at 1454.88  $\text{g mol}^{-1}$  were also absent.

The higher mass peaks near 945.0980, 977.0883 and 1009.0614 g mol<sup>-1</sup> are attributable to the free ligand and two successive additions of O<sub>2</sub>/S respectively. The major peak at 458.2212 g mol<sup>-1</sup> has an accurate mass close to that of a [Fe(CN)<sub>4</sub>(CO)<sub>2</sub>][NBu<sub>4</sub>] (calc 458.2218 g mol<sup>-1</sup>). This behaviour is indicative of demetalation of the cluster with excess CO and CN<sup>-</sup> with liberation of the tridentate ligand. This may be a consequence of oxygen damage.

Importantly, *trans*-[Fe(CN)<sub>4</sub>(CO)<sub>2</sub>]<sup>2-</sup> is *not* the species **IS**<sub>3</sub> as observed in our experiments. Firstly, it oxidises near 1.38 V vs calomel and is not reducible, secondly the infrared spectrum of this species shows two bands at 1992 and 2104 cm<sup>-1</sup> in DMF, thirdly we have crystallographically characterised an intact site-differentiated cluster with an infrared signature identical to that observed in solution.<sup>279</sup>

10a02 #1-95 RT: 0.00-0.81 AV: 85 NL: 6.96E6

F: FTMS - p ESI Full ms [120.00-1200.00]

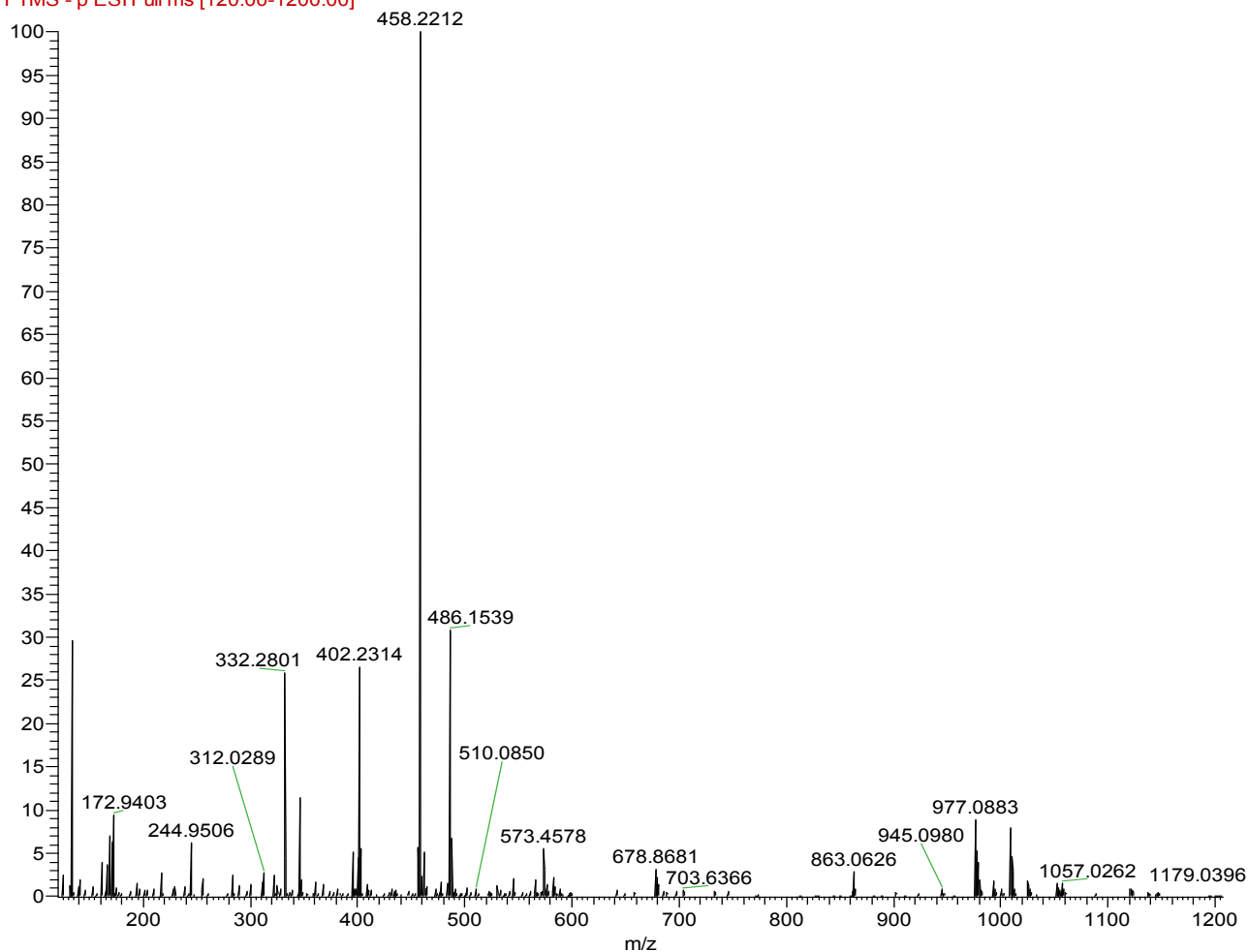


**Figure 150** Mass spectrum of a solution of “Holm cluster” under CO with four eq. of cyanide.

#### 5.4.4 Isolation of products by crystallisation

X-ray quality crystals were obtained from a solution of “Holm cluster” with 4 eq. of  $\text{CN}^-$  in CO saturated MeCN. A diffraction experiment gave data of moderate quality. The product crystallises in the rhombohedral space group  $R\bar{3}2$ . A crystallographic  $C_3$  axis passes through the central aromatic ring of the ligand, the apical sulfur of the cluster and the basal iron. As a result of this crystallographic symmetry the CO and  $\text{CN}^-$  positions are disordered. It is unclear whether the unique iron site is occupied by a (CO, CN) or a (CO,  $(\text{CN})_2$ ) arrangement. What is clear is that the tripodal ligand is wrapped around the cluster and the

cluster has at least two diatomic ligands at the unique iron site. An ATR of these crystals gives an IR spectrum as shown in Figure 152 in good agreement with what is seen in solution suggesting that these crystals are representative of the bulk solution.

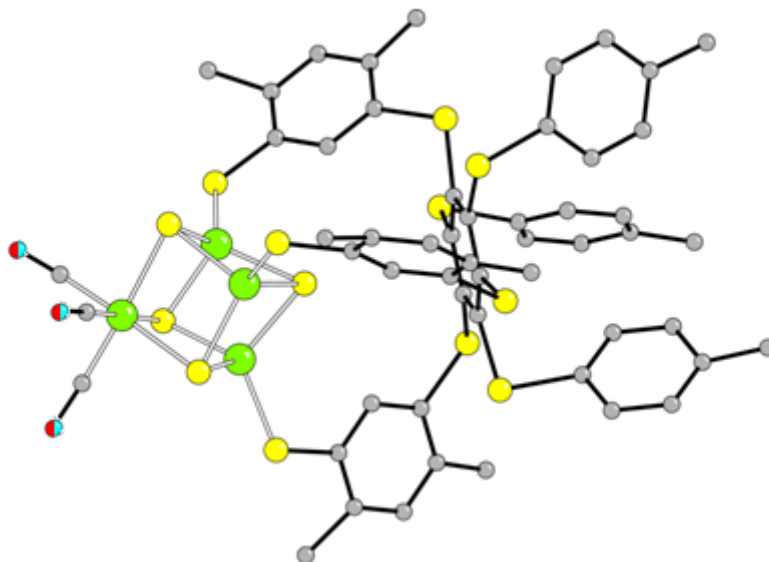


**Figure 151** Crystal structure 1 of isolated crystals from a reaction of “Holm cluster” with four eq.  $\text{CN}^-$  in CO saturated solution.

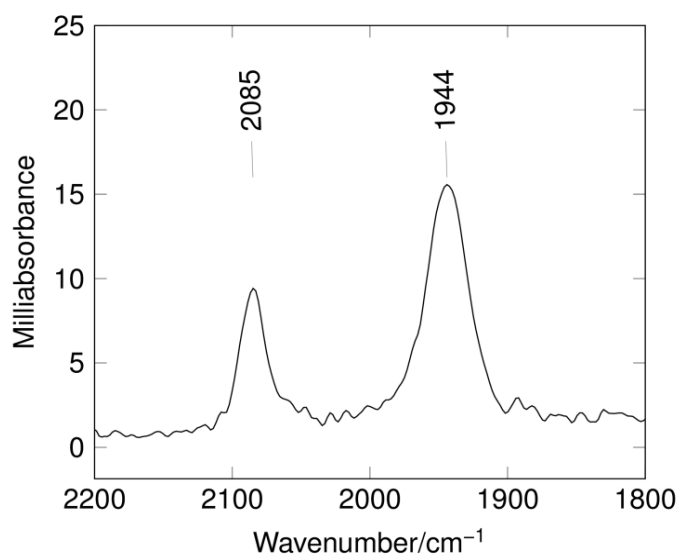


**Figure 152** ATR of crystals from a reaction of “Holm cluster” with four eq.  $\text{CN}^-$  in CO saturated solution.

Figure 153 and Table 13 summarise selected bond length data for **IS<sub>3</sub>**, a cubane complex and a [2:2] site differentiated complex which has  $\pi$ -accepting <sup>t</sup>BuNC ligands. In these species those bonds *trans* to the  $\pi$ -accepting CO/CN<sup>-</sup> ligands at the octahedral or square pyramidal site (Fe1–S1 bonds) are considerably elongated (>0.1 Å) compared to the FeS bonds at the tetrahedral sites Fe2–S1 and Fe3–S3. Those bonds at the tetrahedral sites are comparable (within 0.02 Å) to those in the simple iron-sulfur cluster **85**. Notably in complex **74** the FeS bonds *trans* to the iron atoms bearing a  $\pi$ -acceptor ligand are also similarly elongated with respect to the FeS bond lengths at the tetrahedral irons. This does not distinguish whether or not there are two or three ligands at the unique iron site but is fully with those ligands being  $\pi$ -acceptors.

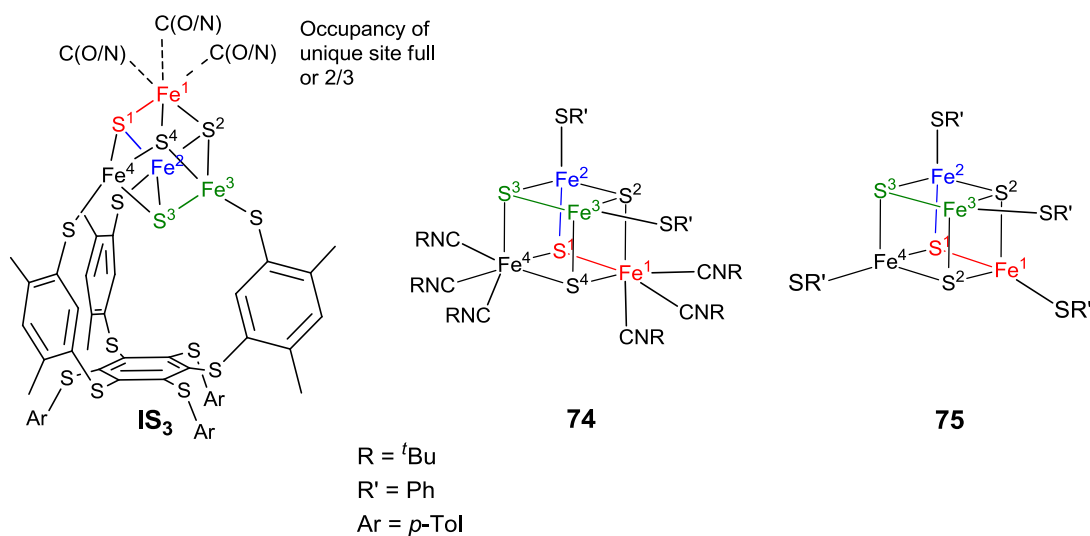


**Figure 153** Atom labelling for the structures **IS<sub>3</sub>**, **74** and **75** supporting Table 13. Ligations at Fe site could be two or three diatomic ligands.

**Table 13** Summary of the lengths of the unique bonds in the structures **8**, **74** and **75** as shown in Figure 153.<sup>270, 280</sup>

Bond	Iron-sulfur cluster bond length/ Å		
	[3:1] Site differentiated	[2:2] Site differentiated	Tetra thiolate cluster
	<b>IS<sub>3</sub></b>	<b>74</b>	<b>75</b>
<b>Fe1-S1</b>	2.377(4)	2.368(5)	2.272(5)
<b>Fe2-S1</b>	2.255(3)	2.388(4)	2.268(5)
<b>Fe3-S3</b>	2.262(5)	2.231(5)	2.277(5)

#### 5.4.5 Elemental Analysis

Elemental analysis of crystals from the reaction of the “Holm cluster” with four equivalents of cyanide under CO is shown in Table 14. Comparison of this data to theoretical results for an array of possible compounds with different ligands at the unique iron site is also shown. In Table 14 the % N closely matches a species where there are a CO and a CN<sup>-</sup> ligand at the unique iron site. The % N is most sensitive to the number of bound cyanides as moving from one to two cyanides at the unique iron site changes this by half as much again.

Although the elemental analysis results strongly support a CO, CN species they cannot conclusively distinguish between this species and a (CO)<sub>2</sub>CN species.

**Table 14** Theoretical elemental analysis of the “Holm cluster” with different ligands at the unique iron site vs experimentally derived data. Top: calculated values assuming all counterions are NEt<sub>4</sub>, bottom: calculated values assuming ¼ occupancy by NBu<sub>4</sub> and ¾ by NEt<sub>4</sub>.

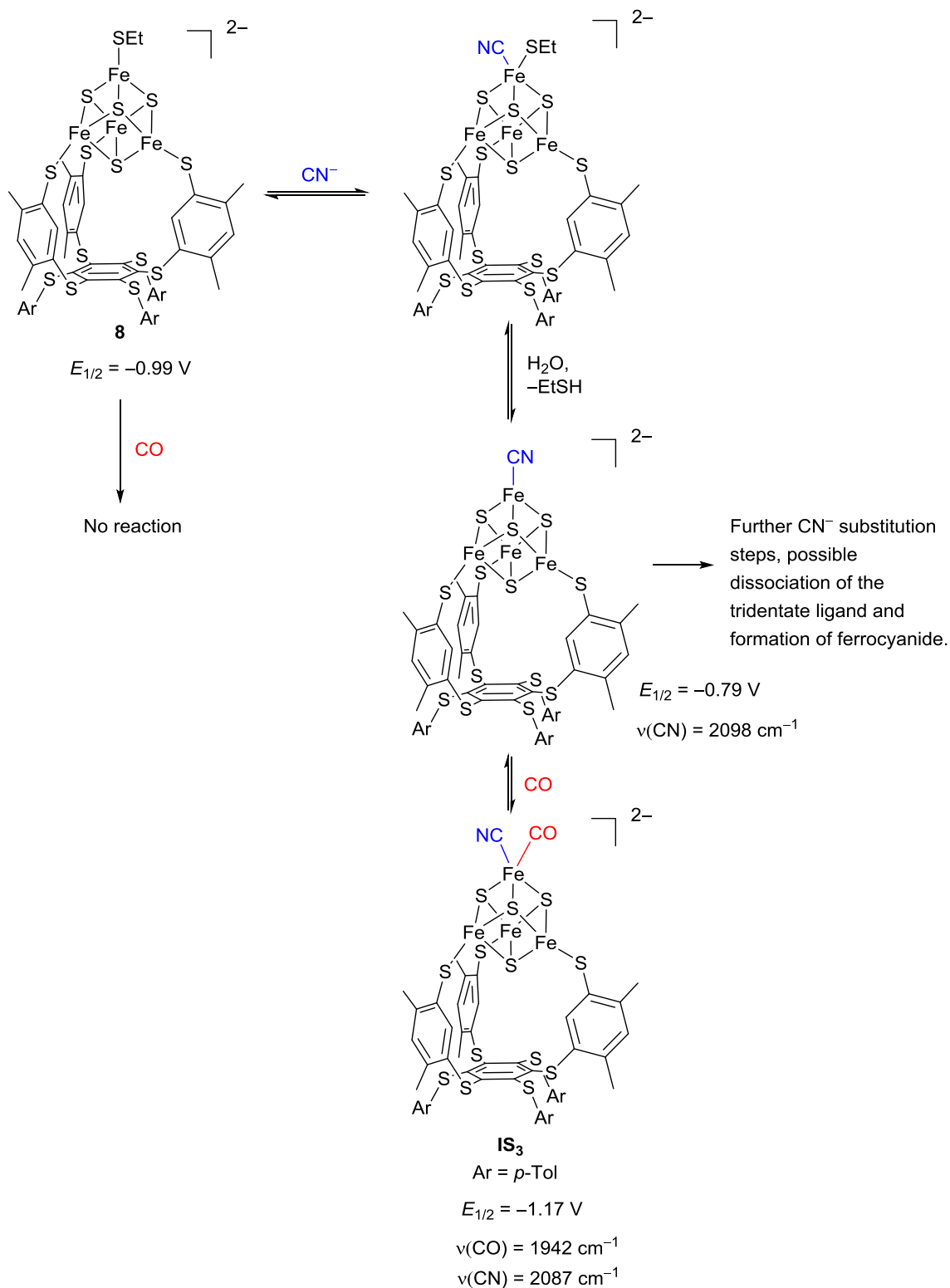
	Ligand(s) at unique iron site (All counterions NEt <sub>4</sub> )				Experimental
	SEt	CO, CN	CO, CO, CN	CO, CN, CN	
% N	1.6	2.6	2.5	3.8	2.43
% C	50.2	50.0	50.3	52.0	51.93
% H	5.5	5.2	5.1	5.8	5.43

	Ligand(s) at unique iron site (¾ counterions N(Et) <sub>4</sub> , ¼ NBu <sub>4</sub> )				Experimental
	SEt	CO, CN	CO, CO, CN	CO, CN, CN	
% N	1.6	2.52	2.48	3.78	2.43
% C	50.2	52.54	52.38	54.44	51.93
% H	5.5	5.62	5.52	6.36	5.43

## 5.5 Conclusions

### 5.5.1 General summary of reactions

Scheme 53 below summarises our interpretation of the reactions of the site differentiated cluster **8** with CO and CN<sup>-</sup>. In contrast with the undifferentiated clusters, the CO/CN<sup>-</sup> reactions are restricted to the formation of a mono-carbonyl mono-cyanide species at the unique site of the site differentiated cluster (see Scheme 50 and Scheme 53). Analytical and computational studies are consistent with this carbonyl species possessing a single cyanide co-ligand at the unique Fe. The X-ray crystallographic data definitively shows that the cluster retains the tripodal ligand and that two or three diatomic ligands are attached to the differentiated Fe. Partial occupancy of this site and the correspondingly the cationic counterions leaves some ambiguity. From the crystallographic structure, a five coordinate unique Fe site would have a geometry close to square pyramidal.



**Scheme 53** Reactions of **8** with CO and  $\text{CN}^-$  based on our current understanding of the data provided by our experiments. Potentials are relative to Ag/AgCl in the MeCN electrolyte.

From these reactions it is clear that substitution of thiolate by  $\text{CN}^-$  must occur to allow observable CO binding at these iron-sulfur clusters. One may speculate that this activation is due to the increased electron density of the iron centre. It is also notable that the  $\text{CN}^-$  ligand is a much stronger  $\pi$ -acceptor than the thiolate ligand it has replaced, which must result in a change in electron density distribution at the metal. The detail of how this synergic process functions is one that requires further theoretical investigation.

### 5.5.2 Relevance or otherwise to H-cluster intermediates in HydG

Table 15 compares the FTIR  $\nu\text{CO}$  and  $\nu\text{CN}$  stretching frequencies for the synthetic site differentiated CO/CN species **IS<sub>3</sub>** with the computational IR data for the analogous cluster  $[\text{Fe}_4\text{S}_4(\text{SPh})_3(\text{CO})(\text{CN})]^{2-}$  and that of the natural intermediate “complex A” of HydG.

**Table 15** Comparison of simulated and experimental IR data for the natural system “complex A” in HydG (Scheme 41),<sup>62</sup> a DFT calculated IR spectrum for a  $[(\text{Fe}_4\text{S}_4)(\text{SPh})_3(\text{CO})(\text{CN})]^{2-}$  species and a solution of **IS<sub>3</sub>**. The values in the table are given in  $\text{cm}^{-1}$ .

	HydG “Complex A”	<b>IS<sub>3</sub></b>	DFT
CN	2093	2087	2078
CO	1949	1942	1945
<sup>13</sup> CN	2048		
<sup>13</sup> CO	1906	1898	

As discussed above and in Chapter 4 the primary reactions of all the clusters with CO and  $\text{CN}^-$  give infrared stretching frequencies remarkably close to those reported by Kuchenreuther et al.<sup>62</sup> These bands were initially attributed to the formation of an  $\{\text{Fe}(\text{CO})(\text{CN})\}$  “synthon” at a unique Fe site of the C-terminus cluster of HydG. Subsequently, Roach and co-workers provided the first crystal structure of HydG which

revealed two types of C-terminal cluster one with an fifth Fe *exo* linked by a sulfide bridge to the cluster, the other where this fifth iron is absent, Figure 154.<sup>87</sup>

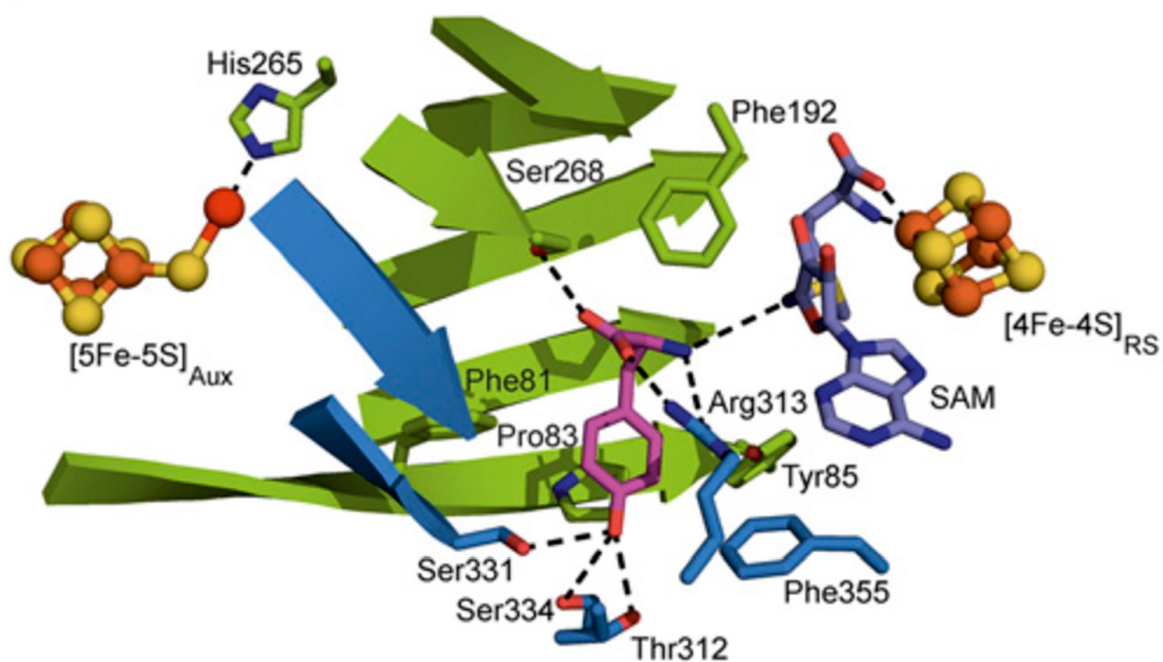


**Figure 154** A composite model illustrating the {4Fe4S} and {5Fe5S} clusters of HydG, reproduced from ref. 87 with permission from the National Academy of Sciences of the USA.

Subsequent studies have revised the 5Fe4S cluster as involving a cysteine or homocysteine bridge to the *exo* iron, Figure 155 A.<sup>281</sup>

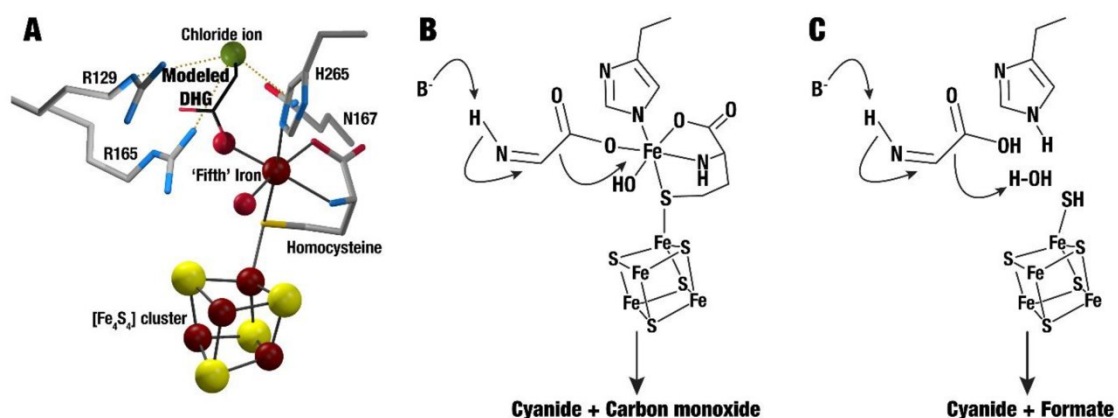


**Figure 155** Synthesis of CN<sup>-</sup>, ⁻:CO<sub>2</sub>(H) and formate from dehydroglycine (DHG). *A*) Docking of DHG based on the Cl<sup>-</sup> site (green ball) and one of the water ligands of the second FeS cluster fifth iron (red small ball). *B*) Elimination reaction that produces CN<sup>-</sup> and iron-bound ⁻:CO<sub>2</sub>(H). The latter generates CO and H<sub>2</sub>O. *C*) In the absence of the fifth iron CN<sup>-</sup> and CO<sub>2</sub>(H) are the final products. Reproduced from ref. 281 with permission from the National Academy of Sciences of the USA.

When HydG is exposed to CN<sup>-</sup> alone, a mono-cyanide species at the unique Fe site within the {4Fe4S} cluster is formed, Figure 156.<sup>87</sup>

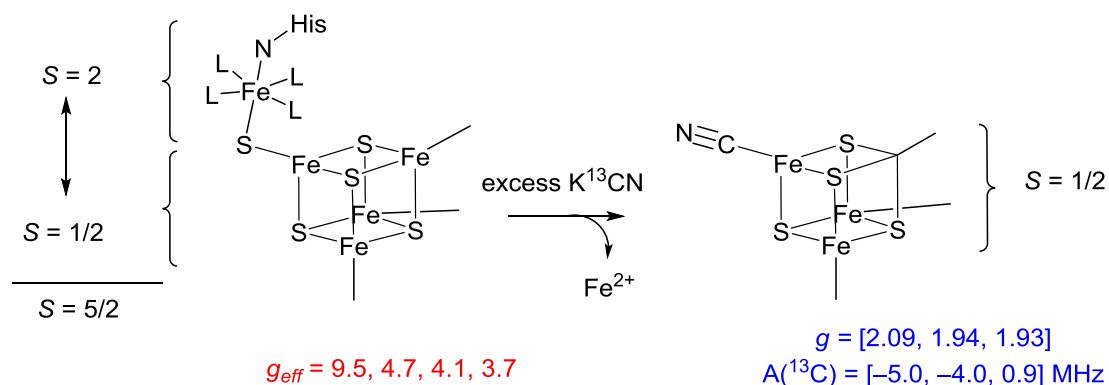


**Figure 156** Addition of CN<sup>-</sup> alone to HydG resulting in mono-cyanide ligation at the unique Fe within the {4Fe4S} cluster, reproduced from ref. 87 with permission from the National Academy of Sciences of the USA.

Surprisingly, exposure of HydG to CO and CN in any of its forms has so far not been reported. Recent work presented by Nicolet and Fontecilla-Camps suggests that CO and CN are generated from dehydroglycine by sequential pathways which in the absence of the *exo* Fe and C-terminus cluster produces formate and cyanide, Figure 155 B and C.<sup>282</sup> What is apparent in the reported data is that even under the most favourable conditions only a sub-stoichiometric amount of CO is formed, the dominant reaction pathways lead to generation of formate and CN<sup>-</sup>.<sup>281</sup>

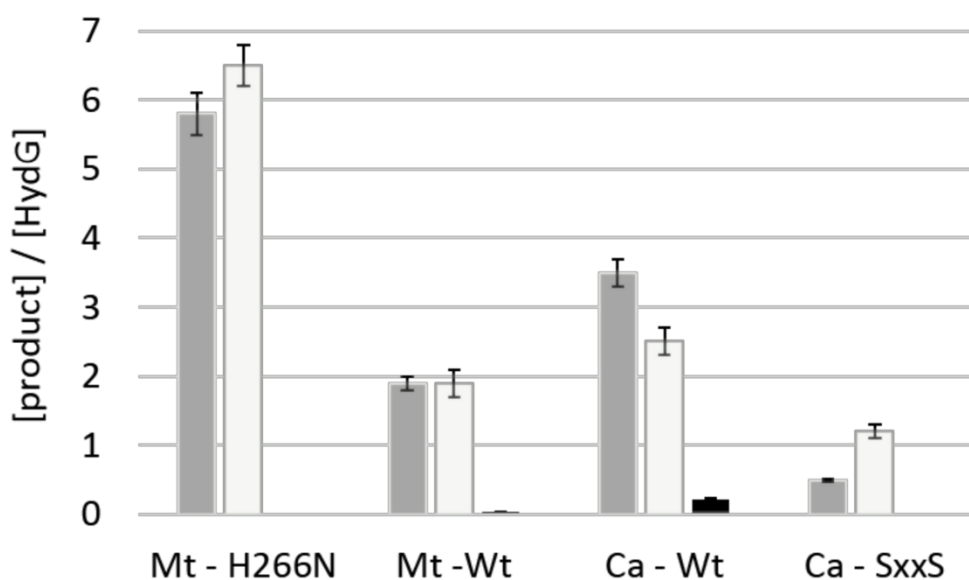


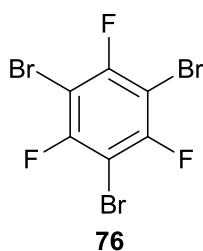
**Figure 157** Synthesis of cyanide (grey), formate (white) and carbon monoxide (black) by HydG. Mt-H266N: *M. thermoacetica* His266Asn variant; Mt-WT: *M. thermoacetica* wild-type enzyme; Ca-WT: *C. acetobutylicum* wild-type enzyme; Ca-SxxS: *C. acetobutylicum* variant lacking a functional second cluster. Assays contained 30  $\mu$ M of either Mt-H266N, Mt-Wt, Ca-Wt or Ca-SxxS ( $6.0 \pm 0.2$ ;  $4.0 \pm 0.1$ ;  $6.0 \pm 0.2$  and  $2.4 \pm 0.1$  Fe/protein, respectively), 1 mM tyrosine, 1 mM SAM, 1 mM dithionite, at 37  $^{\circ}$ C (except Ca-SxxS at 30  $^{\circ}$ C) in 50 mM Hepes, pH 7.4 for CaHydG or 50 mM Tris pH 8 for MtHydG, 150 mM NaCl, 5 mM DTT.

Each value corresponds to the average of three independent experiments. Reproduced from ref. 281 with permission from the National Academy of Sciences of the USA.

What is clear from these studies is that His266 is essential for CO production as is the presence of the C-terminus cluster.<sup>281</sup> It is not currently known whether the fifth Fe is essential or an artefact. Addition of Fe and homocysteine to HydG preparations enhances CO production, but these preparations contain only six Fe per mole of protein rather than eight or nine.<sup>281</sup> Unambiguously showing CO and CN<sup>-</sup> bound to this *exo* Fe site by spectroscopic means would provide firm evidence for the role of the fifth Fe as the site of catalysis and/or synthon generation.

## 5.6 Experimental

### 1,3,5-Tribromo-2,4,6-trifluorobenzene (76)

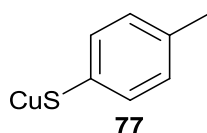


Aluminium powder (0.79 g, 29 mmol) was added to bromine (40 mL, 780 mmol) and the mixture cooled to 0 °C. Keeping the reaction cool, 1,3,5-trifluorobenzene (11.75 mL, 110 mmol) was added drop-wise, sparks were seen along with the evolution of HBr. After the addition was complete the mixture was stirred at 60 °C for one hour and then poured into water. The product was then extracted with diethyl ether (3 × 150 mL), dried with MgSO<sub>4</sub> and the solvent removed. The crude product was washed with cold ethanol (0 °C) yielding an off white crystalline solid (21.13 g, 52.5 %). <sup>19</sup>F (282 MHz, CDCl<sub>3</sub>) δ<sub>F</sub> 95.33.

## Copper oxide

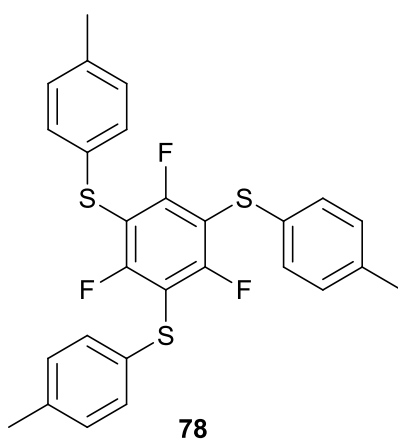
$\text{Cu}_2\text{SO}_4$  was dissolved in water (1000 mL) and 10 drops of  $\text{H}_2\text{SO}_4$  were added. Separately sodium tartrate (350 g, 1.5 mol) was dissolved in water (1000 mL) and NaOH (100 g, 2.5 mol) was added. The two solutions were then combined and D-glucose (54 g, 300 mmol) was added. The solution was then boiled until it became red-brown and a red precipitate had formed. The product was filtered, washed with hot water and cold ethanol and then dried in an oven overnight yielding a red powder (28.6 g, 94 %).

## *p*-Tolythiocuprate (77)



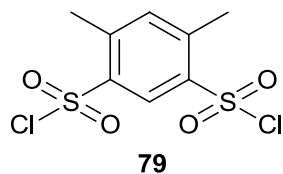
This method was carried out on a smaller scale than that reported in the literature<sup>283</sup> due to handling problems with larger quantities of air-sensitive material. To a solution of *p*-thiocresol (16.67 g, 134 mmol) in ethanol (170 mL),  $\text{Cu}_2\text{O}$  (11.75 g, 82 mmol) was added. The mixture was stirred mechanically under reflux for 3 days. The resulting product was filtered, washed with ethanol and dried under vacuum yielding an off-white solid (12.95 g, 84 %).

## 1,3,5-Tris(*p*-tolylthio)-2,4,5-trifluorobenzene (78)



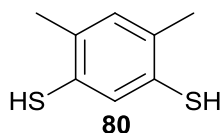
The tris-bromo and fluoro substituted benzene derivative **76** (9.7 g, 26 mmol) and the copper substituted thiol **77** (18.6 g 99.7 mmol) were dissolved in DMF (200 mL). The mixture was stirred mechanically at 140 °C for 36 h and then poured into ice (1.5 L) and conc. HCl (250 mL). The product was the extracted with diethyl ether (3 × 100 mL), washed with aq. K<sub>2</sub>CO<sub>3</sub> (10 %, 3 × 100 mL) and saturated NaCl solution (3 × 100 mL and dried with MgSO<sub>4</sub>. Removal of the solvent under vacuum yielded a white powder (1.28 g, 11 %). <sup>1</sup>H NMR (300 MHz, CDCl<sub>3</sub>): δ 2.29 (s, 9H), 7.05 (d, 6H, *J* = 8.1 Hz), 7.18 (d, 6H, *J* = 8.1 Hz), <sup>19</sup>F (282 MHz, CDCl<sub>3</sub>) δ<sub>F</sub> 91.15.

#### 4,6-Dimethylbenzene-1,3-disulfonyl dichloride (**79**)



To chlorosulfonic acid (100 mL, 1.5 mol), *m*-xylene (15 mL, 122 mmol) was added dropwise. The mixture was then stirred under reflux for 90 min. The red solution was then pipette slowly into ice (1.5 L) and stirred overnight to complete the precipitation of a white solid. The mixture was then filtered, the solid washed with water and dried under vacuum yielding a white solid (25 g, 68 %). <sup>1</sup>H NMR (300 MHz, CDCl<sub>3</sub>): δ 2.85 (s, 6H), 7.50 (s, 1H), 8.69 (s, 1H).

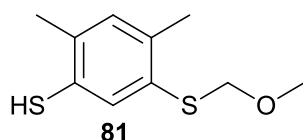
#### (CH<sub>3</sub>)<sub>2</sub>C<sub>6</sub>H<sub>2</sub>(SH)<sub>2</sub> 4,6-Dimethylbenzene-1,3-dithiol (**80**)



Tin granules (300 g, 2.5 mol) were dissolved in conc. HCl (800 mL). The disulfonyl dichloride **79** (25 g, 82 mmol) was added slowly in portions. The mixture was stirred

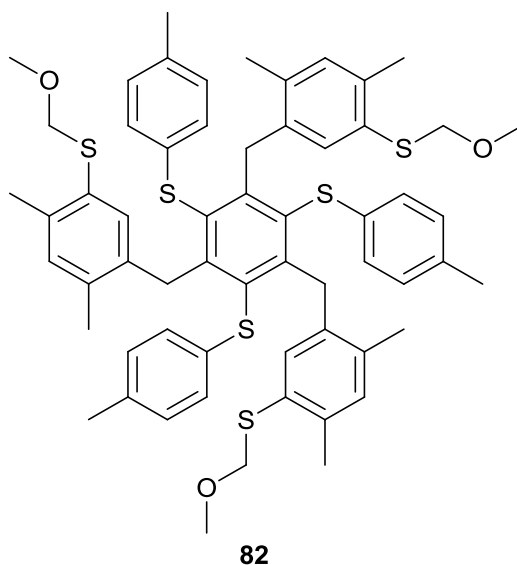
mechanically under reflux for 2 h. The product was purified by steam distillation and washed with water yielding a shiny white solid (8 g, 56 %).  $^1\text{H}$  NMR (300 MHz,  $\text{CDCl}_3$ ):  $\delta$  2.27 (s, 6H), 3.27 (s, 2H) 6.98 (s, 1H), 7.23 (s, 1H).

**$(\text{CH}_3)_2\text{C}_6\text{H}_2(\text{SH})(\text{SCH}_2\text{OCH}_3)$ , 4,6-dimethyl-3-[(methoxymethyl)thio]benzenethiol (**81**)**



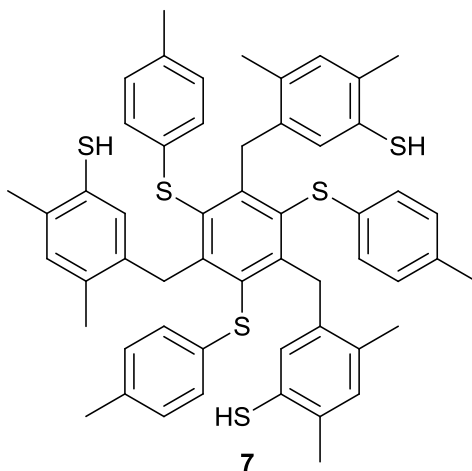
$\text{NaH}$  (2.0 g, 50 mmol, mineral oil dispersion 60 %) was dissolved in DMF (150 mL). The dithiol species **80** (4 g, 23 mmol) was added slowly in portions keeping the temperature below 50 °C and stirred at room temperature for 3 h. Chloromethyl methyl ether (3.8 mL, 51 mmol) was added the solution was stirred at room temperature overnight.  $\text{NaSEt}$  (1.94 g, 23 mmol) was added, the mixture heated to 120 °C for 3 h and the by-product (ethyl(2-methoxymethyl)sulfide) distilled off. The solvent was then removed at 60 °C under reduced pressure giving an orange-red oil. This was then dissolved in diethyl ether, extracted with aq.  $\text{NaOH}$  (5 %, 3  $\times$  30 mL), acidified with 2M  $\text{AcOH}$  (100 mL) and extracted with diethyl ether (3  $\times$  30 mL). The extracts were combined, dried with  $\text{MgSO}_4$  and the solvent removed to give the crude product (an orange-red oil). The product was then purified by flash chromatography (hexane, then hexane/ether 19:1) to give a colourless oil (1.6 g, 33 %).  $^1\text{H}$  NMR (300 MHz,  $\text{CDCl}_3$ ):  $\delta$  2.25 (s, 3H), 2.30 (s, 3H), 3.25 (s, 1H), 3.41 (s, 3H) 4.89 (s, 2H), 6.96 (s, 1H) 7.44 (s, 1H).

**1,3,5-Tris(4,6-dimethyl-3-(methoxymethylthio)phenylthio)-2,4,6-tris(*p*-tolylthio)benzene (82)**



NaH (0.37 g, 7.5 mmol) was washed with dry hexane and dissolved in THF (30 mL). The mono-protected dithiol **81** (1.6 g, 7.4 mmol) was added and the solution stirred for 1 h. The solvent was then removed under vacuum and the sticky residue dissolved in DMEU (1,3-dimethyl-2-imidazolidinone) (30 mL). The tris(*p*-tolylthio) substituted fluorobenzene **78** was added and the mixture was stirred at 85 °C for 4 days. The solution was then dissolved in diethyl ether (150 mL), washed with aq. K<sub>2</sub>CO<sub>3</sub> (10 %, 3 × 100 mL) and dried with MgSO<sub>4</sub>. The solvent was then removed resulting in a bright yellow solid containing a small amount of bright yellow oily material. This was proven to be of satisfactory purity by spectroscopic methods. <sup>1</sup>H NMR (300 MHz, CDCl<sub>3</sub>): δ 2.10 (s, 3H), 2.20 (s, 3H), 2.24 (s, 3H), 3.30 (s, 3H) 4.70 (s, 2H), 6.80 (s, 1H) 6.85 (d, 2H) 6.88 (s, 1H), 6.89 (d, 2H).

**1,3,5-Tris(4,6-dimethyl-3-(mercaptophenylthio)phenylthio)-2,4,6-tris(*p*-tolylthio)benzene (7)**



The protected trithiol **82** (0.57 g, 0.53 mmol) was dissolved in a mixture of degassed chloroform (30 mL) and ethanol (2 mL). Hg(OAc)<sub>2</sub> (0.68 g, 2.12 mmol) added and the solution was stirred at room temperature overnight. The solution was then bubbled with H<sub>2</sub>S for 20 min to consume the excess mercury compound and the colour of the solution changed from yellow to black. The solution was then sparged with N<sub>2</sub> for 45 min to remove the remaining H<sub>2</sub>S and filtered through a chloroform-moistened Celite column. The product was eluted from the column using warm chloroform until no yellow colour remained. The solvent was then removed under vacuum and the crude product was washed with warm acetonitrile (5 × 20 mL) yielding a bright yellow solid (460 mg, 91 %). <sup>1</sup>H NMR (300 MHz, CDCl<sub>3</sub>): δ 2.15(s, 3H), 2.16 (s, 3H), 2.17 (s, 3H), 3.04 (s, 1H) 6.42 (s, 1H), 6.80 (s, 1H) 6.81 (s, 1H) 6.84 (d, 2H, *J* = 12.1Hz), 6.96 (d, 2H, *J* = 11.7 Hz).



## 6 Summation of the work, conclusions and future work

The work in this thesis has focused on two main areas: 1) exploring the substitution chemistry of chemical models of the [Fe]-hydrogenase active site (chapter 3) and 2) investigating the interaction of  $[\text{Fe}_4\text{S}_4(\text{SR})_4]^{2-}$  clusters with CO and  $\text{CN}^-$  with relevance to the intermediates formed at HydG in the biosynthetic pathway of the H-cluster of [FeFe]-hydrogenase (chapters 4 and 5).

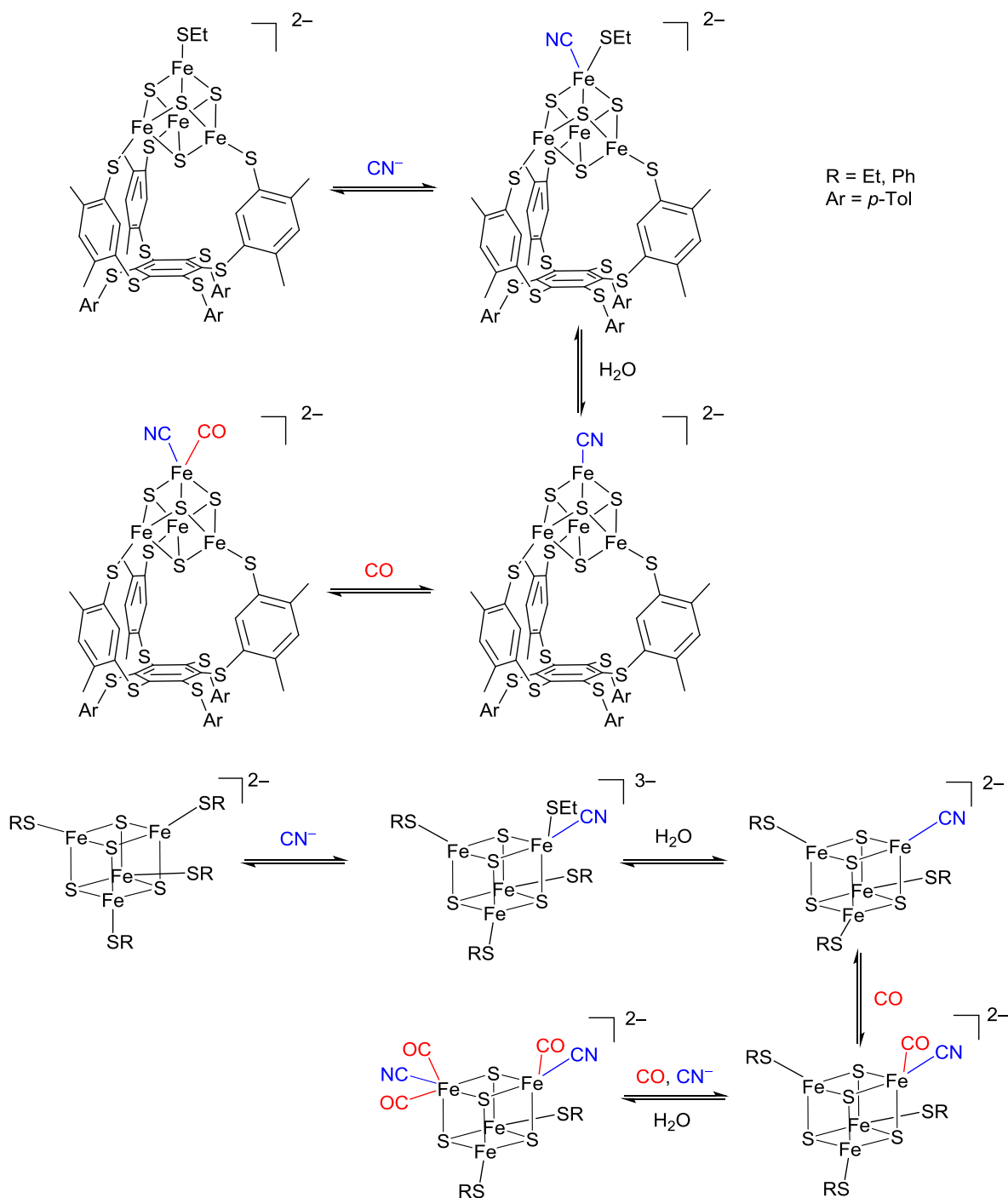
### 6.1 Summary of chapter 3

The work in chapter 3 builds on previous research<sup>227</sup> on the substitution chemistry of a parent ferracyclic [Fe]-hydrogenase model **51** and demonstrates that a solvent molecule coordinated to Fe can be substituted for a tertiary phosphine ( $\text{PMe}_3$ ,  $\text{PPh}_3$ ). Another focus of this chapter was to extend the second coordination sphere of the parent **51** by incorporation of a pendant OH group on the pyridine ring. This work had partial success but further research effort was curbed due to publication of similar but successful work by another group that used a different approach.<sup>203</sup> Investigations of the interaction of the parent model **51** with sources of hydride yielded no isolable products.

A close structural mimic of [Fe]-hydrogenase that can also model the enzyme's activity has yet to be reported. Much remains to be understood about how the enzyme performs the extraordinary heterolytic cleavage of dihydrogen, and modelling reactivity will undoubtedly be the focus of future research.

## 6.2 Summary of chapters 4 and 5

The work in chapters 4 and 5 looked at the interaction of undifferentiated and site differentiated  $[\text{Fe}_4\text{S}_4(\text{SR})_4]^{2-}$  clusters with CO and  $\text{CN}^-$ . Whereas no interaction was seen with CO alone in any of the clusters studied, in the presence of cyanide synergic binding of CO and  $\text{CN}^-$  has been unequivocally demonstrated. The current understanding of our cluster studies in the presence of both CO and  $\text{CN}^-$  are summarised in Scheme 54.



**Scheme 54** Summary of reactions of CO and  $\text{CN}^-$  with the clusters  $[\text{Fe}_4\text{S}_4(\text{SEt})_4]^{2-}$ ,  $[\text{Fe}_4\text{S}_4(\text{SPh})_4]^{2-}$  and the  $[\text{Fe}_4\text{S}_4(\text{LS}_3)(\text{SEt})]^{2-}$  based on evidence presented in this thesis.

Whilst the work in this thesis has contributed to aspects of the biosynthetic pathway to the H-cluster subsite, it has also extended knowledge of the substitution chemistry of iron-sulfur clusters with  $\pi$  acid ligands.

With respect to the biosynthesis of the H-cluster, via reactions involving the maturase HydG, we have shown that CO and CN<sup>-</sup> intermediates bound to an [Fe<sub>4</sub>S<sub>4</sub>]<sup>2-</sup> cluster have chemical precedence. Moreover the infrared spectroscopic data is remarkably similar to that observed for the natural system.<sup>62</sup> Future work should focus on obtaining better crystallographic data to firmly establish whether one or two cyanides are bound to the site differentiated cluster. Mössbauer studies will reveal whether the π acid ligands localise the oxidation state of the unique Fe. Spectroelectrochemistry on the CO/CN<sup>-</sup> cluster intermediates is likely to be informative, particularly the effect of reduction or oxidation on FTIR ν(CO) and ν(CN) frequencies. EPR studies of one-electron oxidised or reduced paramagnetic species in the reaction pathway is also likely give information on the electronic condition of the cluster. The more complex reactions of undifferentiated clusters with CO and CN<sup>-</sup> which appear to lead to CO/CN functionalisation of two irons at a cubane core requires further investigation, not least because two sulfur bridged Fe atoms provide the framework for the di-iron H-cluster subsite.

The recent work by Britt, Roach, Fontecilla-Camps and others strongly point to a role for an *exo* Fe.<sup>87</sup> Again it would be particularly attractive to explore the synthesis of models of this type of structure and their interaction with CO and CN<sup>-</sup>. Whereas <sup>57</sup>Fe labelling studies have shown that all the iron in the subsite originates from the HydG C-terminus {4Fe4S} cluster it remains to be demonstrated that the *exo* Fe is incorporated.<sup>87</sup> Furthermore it is not known whether iron is transferred as {Fe(CO)(CN)} intermediates for assembly at the subsite on HydF or whether a diiron unit is transferred. In the latter case an *exo* Fe and a cubane-derived unique Fe might provide the “synthon”, or indeed as discussed above two Fe atoms from an {4Fe4S} cube. In either case, turnover requires the import of iron atoms to replace the fifth iron and/or reconstitute the {3Fe4S} core as a {4Fe4S} cubane. In some ways the model chemistry of these systems is a can of worms but rather an intriguing and exciting can of worms.

## 7 References

- 1 F. Tian, O. B. Toon, A. A. Pavlov and H. De Sterck, *Science*, 2005, **308**, 1014.
- 2 P. M. Vignais and B. Billoud, *Chem. Rev.*, 2007, **107**, 4206.
- 3 K. Takai, T. Gamo, U. Tsunogai, N. Nakayama, H. Hirayama, K. H. Nealson and K. Horikoshi, *Extremophiles*, 2004, **8**, 269.
- 4 K. Takai, T. Gamo, U. Tsunogai, N. Nakayama, H. Hirayama, K. H. Nealson and K. Horikoshi, *Extremophiles*, 2004, **8**, 269.
- 5 K. H. Nealson, F. Inagaki and K. Takai, *Trends Microbiol.*, 2005, **13**, 405.
- 6 B. P. Weiss, Y. L. Yung and K. H. Nealson, *Proc. Natl. Acad. Sci. USA*, 2000, **97**, 1395.
- 7 J. D. Fox, R. L. Kerby, G. P. Roberts and P. W. Ludden, *J. Bacteriol.*, 1996, **178**, 1515.
- 8 P. C. Maness, S. Smolinski, A. C. Dillon, M. J. Heben and P. F. Weaver, *Appl. Env. Microbiol.*, 2002, **68**, 2633.
- 9 T. G. Sokolova, C. Jeanthon, N. A. Kostrikina, N. A. Chernyh, A. V. Lebedinsky, E. Stackebrandt and E. A. Bonch-Osmolovskaya, *Extremophiles*, 2004, **8**, 317.
- 10 R. Conrad, *Microbiol. Rev.*, 1996, **60**, 609.
- 11 R. K. Cammack, M. Frey, R. Robson, Hydrogen as a fuel: learning from nature, Taylor & Francis, London, New York 2001.
- 12 D. R. Lovley, D. E. Holmes and K. P. Nevin, in *Advances in Microbial Physiology*, Academic Press, 2004, pp. 219-286.
- 13 R. K. Thauer, A. K. Kaster, M. Goenrich, M. Schick, T. Hiromoto and S. Shima, *Ann. Rev. Biochem.*, 2010, **79**, 507.
- 14 C. Afting, E. Kremmer, C. Brucker, A. Hochheimer and R. K. Thauer, *Arch. Microbiol.*, 2000, **174**, 225.

- 15 T. Hiromoto, K. Ataka, O. Pilak, S. Vogt, M. S. Stagni, W. Meyer-Klaucke, E. Warkentin, R. K. Thauer, S. Shima and U. Ermler, *FEBS Lett.*, 2009, **583**, 585.
- 16 P. J. Turrell, A. D. Hill, S. K. Ibrahim, J. A. Wright and C. J. Pickett, *Dalton Trans.*, 2013, **42**, 8140.
- 17 R. K. Thauer, A R. Klein and G. C. Hartmann, *Chem. Rev.*, 1996, **96**, 3031.
- 18 K. A. Vincent, A. Parkin and F. A. Armstrong, *Chem. Rev.*, 2007, **107**, 4366.
- 19 M. Frey, *ChemBioChem*, 2002, **3**, 153.
- 20 T. Krämer, M. Kampa, W. Lubitz, M. van Gastel and F. Neese, *ChemBioChem*, 2013, **14**, 1898.
- 21 A. Volbeda, L. Martin, E. Barbier, O. Gutiérrez-Sanz, A. L. Lacey, P. P. Liebgott, S. Dementin, M. Rousset and J. C. Fontecilla-Camps, *J. Biol. Inorg. Chem.*, 2014, **20**, 11.
- 22 J. W. Peters, W. N. Lanzilotta, B. J. Lemon and L. C. Seefeldt, *Science*, 1998, **282**, 1853.
- 23 T. Spatzal, *Z. Anorg. Allg. Chem.*, 2015, **641**, 10.
- 24 B. M. Hoffman, D. Lukoyanov, D. R. Dean and L. C. Seefeldt, *Acc. Chem. Res.*, 2013, **46**, 587.
- 25 L. C. Seefeldt, B. M. Hoffman and D. R. Dean, *Ann. Rev. Biochem.*, 2009, **78**, 701.
- 26 D. C. Rees, F. A. Tezcan, C. A. Haynes, M. Y. Walton, S. Andrade, O. Einsle and J. B. Howard, *Phil. Trans. R. Soc. A*, 2005, **363**, 971.
- 27 J. B. Howard and D. C. Rees, *Chem. Rev.*, 1996, **96**, 2965.
- 28 J. B. Howard and D. C. Rees, *Annu. Rev. Biochem.*, 1994, **63**, 235.
- 29 P. C. Dos Santos, R. Y. Igarashi, H.-I. Lee, B. M. Hoffman, L. C. Seefeldt and D. R. Dean, *Acc. Chem. Res.*, 2005, **38**, 208.
- 30 L. C. Seefeldt, I. G. Dance and D. R. Dean, *Biochemistry*, 2004, **43**, 1401.

- 31 J. Kim and D. C. Rees, *Nature*, 1992, **360**, 553.
- 32 J. Kim and D. C. Rees, *Science*, 1992, **257**, 1677.
- 33 K. M. Lancaster, M. Roemelt, P. Ethenhuber, Y. Hu, M. W. Ribbe, F. Neese, U. Bergmann and S. DeBeer, *Science*, 2011, **334**, 974.
- 34 Y. Zhang and R. H. Holm, *J. Am. Chem. Soc.*, 2003, **125**, 3910.
- 35 P. C. Dos Santos and D. R. Dean, *Proc. Natl. Acad. Sci. USA*, 2008, **105**, 11589.
- 36 H. Beinert, *J. Biol. Inorg. Chem.*, 2000, **5**, 409.
- 37 C. Huber and G. Wächtershäuser, *Science*, 1997, **276**, 245.
- 38 L. Noodleman and D. A. Case, *Adv. Inorg. Chem.*, 1992, **38**, 423.
- 39 T. Glaser, B. Hedman, K. O. Hodgson, E. I. Solomon, *Acc. Chem. Res.*, 2000, **33**, 859.
- 40 D. C. Johnson, D. R. Dean, A. D. Smith and M. K. Johnson, *Ann. Rev. Biochem.*, 2005, **74**, 247.
- 41 J. Fritsch, P. Scheerer, S. Frielingsdorf, S. Kroschinsky, B. Friedrich, O. Lenz and C. M. T. Spahn, *Nature*, 2011, **479**, 249.
- 42 K. Brzóska, S. Męczyńska and M. Kruszewski, *Acta. Biochim. Pol.*, 2006, **4**, 685.
- 43 S. Bian and J. A. Cowan, *Coord. Chem. Rev.*, 1999, **190–192**, 1049.
- 44 D. H. Flint and R. M. Allen, *Chem. Rev.*, 1996, **96**, 2315.
- 45 Y. Nicolet, C. Piras, P. Legrand, C. E. Hatchikian and J. C. Fontecilla-Camps, *Structure*, 1999, **7**, 13.
- 46 A. Jablonskytė, Ph.D. Thesis, University of East Anglia, Norwich, 2014.
- 47 J. C. Fontecilla-Camps, A. Volbeda, C. Cavazza and Y. Nicolet, *Chem. Rev.*, 2007, **107**, 4273.
- 48 B. Bennett, B. J. Lemon and J. W. Peters, *Biochemistry*, 2000, **39**, 7455.

- 49 S. T. Stripp, G. Goldet, C. Brandmayr, O. Sanganas, K. A. Vincent, M. Haumann, F. A. Armstrong and T. Happe, *Proc. Natl. Acad. Sci. USA*, 2009, **106**, 17331.
- 50 D. Sehnal, R. Svobodova Varekova, K. Berka, L. Pravda, V. Navratilova, P. Banas, C.-M. Ionescu, M. Otyepka and J. Koca, *J. Cheminform.*, 2013, **5**, 39.
- 51 A. Adamska, A. Silakov, C. Lambertz, O. Rüdiger, T. Happe, E. Reijerse and W. Lubitz, *Angew. Chem. Int. Ed.*, 2012, **51**, 11458.
- 52 J. Wang, R. P. Woldring, G. D. Román-Meléndez, A. M. McClain, B. R. Alzua and E. N. G. Marsh, *ACS Chem. Biol.*, 2014, **9**, 1929.
- 53 C. Krebs, W. E. Broderick, T. F. Henshaw, J. B. Broderick and B. H. Huynh, *J. Am. Chem. Soc.*, 2002, **124**, 912.
- 54 M. Fontecave, E. Mulliez and S. Ollagnier-de-Choudens, *Curr. Opin. Struct. Biol.*, 2001, **5**, 506.
- 55 M. R. Challand, R. C. Driesener and P. L. Roach, *Nat. Prod. Rep.*, 2011, **28**, 1696.
- 56 G. N. L. Jameson, M. M. Cospér, H. L. Hernández, M. K. Johnson and B. H. Huynh, *Biochemistry*, 2004, **43**, 2022.
- 57 G. Layer, J. Moser, D. W. Heinz, D. Jahn and W. D. Schubert, *EMBO J.*, 2003, **22**, 6214.
- 58 F. Berkovitch, Y. Nicolet, J. T. Wan, J. T. Jarrett and C. L. Drennan, *Science*, 2004, **303**, 76.
- 59 D. W. Mulder, E. S. Boyd, R. Sarma, R. K. Lange, J. A. Endrizzi, J. B. Broderick and J. W. Peters, *Nature*, 2010, **465**, 248.
- 60 R. C. Driesener, B. R. Duffus, E. M. Shepard, I. R. Bruzas, K. S. Duschene, N. J. R. Coleman, A. P. G. Marrison, E. Salvadori, C. W. M. Kay, J. W. Peters, J. B. Broderick and P. L. Roach, *Biochemistry*, 2013, **52**, 8696.

- 61 J. M. Kuchenreuther, W. K. Myers, T. A. Stich, S. J. George, Y. NejatyJahromy, J. R. Swartz and R. D. Britt, *Science*, 2013, **342**, 472.
- 62 J. M. Kuchenreuther, W. K. Myers, D. L. M. Suess, T. A. Stich, V. Pelmeshnikov, S. A. Shiigi, S. P. Cramer, J. R. Swartz, R. D. Britt and S. J. George, *Science*, 2014, **343**, 424.
- 63 W. Lubitz, H. Ogata, O. Rüdiger and E. Reijerse, *Chem. Rev.*, 2014, **114**, 4081.
- 64 C. Tard and C. J. Pickett, *Chem. Rev.*, 2009, **109**, 2245.
- 65 G. Voordouw, W. R. Hagen, K. M. Krüse-Wolters, A. van Berkel-Arts and C. Veeger, *Eur. J. Biochem.*, 1987, **162**, 31.
- 66 M. C. Posewitz, P. W. King, S. L. Smolinski, R. Davis Smith II, A. R. Ginley, M. L. Ghirardi and M. Seibert, *Biochem. Soc. Trans.*, 2005, **33**, 102.
- 67 J. Meyer, *Cell. Mol. Life Sci.*, 2007, **64**, 1063.
- 68 S. E. McGlynn, S. S. Ruebush, A. Naumov, L. E. Nagy, A. Dubini, P. W. King, J. B. Broderick, M. C. Posewitz and J. W. Peters, *J. Biol. Inorg. Chem.*, 2007, **12**, 443.
- 69 X. Brazzolotto, J. K. Rubach, J. Gaillard, S. Gambarelli, F. M. Atta and M. Fontecave, *J. Biol. Chem.*, 2006, **281**, 769.
- 70 P. W. King, M. C. Posewitz, M. L. Ghirardi and M. Seibert, *J. Bacteriol.*, 2006, **188**, 2163.
- 71 J. K. Rubach, X. Brazzolotto, J. Gaillard and M. Fontecave, *FEBS Lett.*, 2005, **579**, 5055.
- 72 Y. Nicolet, J. K. Rubach, M. C. Posewitz, P. Amara, C. Mathevon, M. Atta, M. Fontecave, J. C. Fontecilla-Camps, *J. Biol. Chem.*, 2008, **283**, 18861.
- 73 S. E. McGlynn, E. M. Shepard, M. A. Winslow, A. V. Naumov, K. S. Duschene, M. C. Posewitz, W. E. Broderick, J. B. Broderick and J. W. Peters, *FEBS Lett.*, 2008, **582**, 2183.

- 74 I. Czech, A. Silakov, W. Lubitz and T. Happe, *FEBS Lett.*, 2010, **584**, 638.
- 75 I. Czech, S. Stripp, O. Sanganas, N. Leidel, T. Happe and M. Haumann, *FEBS Lett.*, 2011, **585**, 225.
- 76 E. M. Shepard, S. E. McGlynn, A. L. Bueling, C. S. Grady-Smith, S. J. George, M. A. Winslow, S. P. Cramer, J. W. Peters and J. B. Broderick, *Proc. Natl. Acad. Sci. USA*, 2010, **107**, 10448.
- 77 P. Berto, M. Di Valentin, L. Cendron, F. Vallese, M. Albertini, E. Salvadori, G. M. Giacometti, D. Carbonera and P. Costantini, *BBA-Bioenergetics*, 2012, **1817**, 2149.
- 78 G. Berggren, R. Garcia-Serres, X. Brazzolotto, M. Clemancey, S. Gambarelli, M. Atta, J. M. Latour, H. L., Hernández, S. Subramanian, M. K. Johnson and M. Fontecave, *J. Biol. Inorg. Chem.*, 2014, **19**, 75.
- 79 N. Joshi, E. M. Shepard, A. S. Byer, K. D. Swanson, J. B. Broderick and J. W. Peters, *FEBS Lett.*, 2012, **586**, 3939.
- 80 Y. Nicolet, P. Amara, J.-M. Mousesca and J. C. Fontecilla-Camps, *Proc. Natl. Acad. Sci. USA*, 2009, **106**, 14867.
- 81 E. M. Shepard, B. R. Duffus, S. J. George, S. E. McGlynn, M. R. Challand, K. D. Swanson, P. L. Roach, S. P. Cramer, J. W. Peters and J. B. Broderick, *J. Am. Chem. Soc.*, 2010, **132**, 9247.
- 82 R. C. Driesener, M. R. Challand, S. E. McGlynn, E. M. Shepard, E. S. Boyd, J. B. Broderick, J. W. Peters and P. L. Roach, *Angew. Chem. Int. Ed.*, 2010, **49**, 1687.
- 83 J. M. Kuchenreuther, S. J. George, C. S. Grady-Smith, S. P. Cramer, J. R. Swartz, *PLoS One*, 2011, **6**, 1.
- 84 M. Kriek, F. Martins, M. R. Challand, A. Croft and P. L. Roach, *Angew. Chem. Int. Ed.*, 2007, **46**, 9223.

- 85 Y. Nicolet, L. Martin, C. Tron and J. C. Fontecilla-Camps, *FEBS Lett.*, 2010, **584**, 4197.
- 86 C. Tron, M. V. Cherrier, P. Amara, L. Martin, F. Fauth, E. Fraga, M. Correard, M. Fontecave, Y. Nicolet and J. C. Fontecilla-Camps, *Eur. J. Inorg. Chem.*, 2011, 1121.
- 87 P. Dinis, D. L. M. Suess, S. J. Fox, J. E. Harmer, R. C. Driesener, L. De La Paz, J. R. Swartz, J. W. Essex, R. D. Britt and P. L. Roach, *Proc. Natl. Acad. Sci. USA*, 2015, **112**, 1362.
- 88 E. Pilet, Y. Nicolet, C. Mathevon, T. Douki, J. C. Fontecilla-Camps and M. Fontecave, *FEBS Lett.*, 2009, **583**, 506.
- 89 J. M. Kuchenreuther, R. D. Britt, J. R. Swartz, *PLoS One*, 2012, **7**, e45850.
- 90 F. Vallese, P. Berto, M. Ruzzene, L. Cendron, S. Sarno, E. De Rosa, G. M. Giacometti, P. Costantini, *J. Biol. Chem.*, 2012, **287**, 36544.
- 91 J. Esselborn, C. Lambertz, A. Adamska-Venkatesh, T. Simmons, G. Berggren, J. Noth, J. Siebel, A. Hemschemeier, V. Artero, E. Reijerse, M. Fontecave, W. Lubitz, and T. Happe, *Nat. Chem. Biol.*, 2013, **9**, 607.
- 92 H. S. Shafaat, O. Rüdiger, H. Ogata and W. Lubitz, *BBA-Bioenergetics*, 2013, **1827**, 986.
- 93 H. Ogata, Y. Mizoguchi, N. Mizuno, K. Miki, S. I. Adachi, N. Yasuoka, T. Yagi, O. Yamauchi, S. Hirota and Y. Higuchi, *J. Am. Chem. Soc.*, 2002, **124**, 11628.
- 94 C. Tard and C. J. Pickett, *Chem. Rev.*, 2009, **109**, 2245.
- 95 A. Volbeda, L. Martin, C. Cavazza, M. Matho, B. Faber, W. Roseboom, S. J. Albracht, E. Garcin, M. Rousset and J. Fontecilla-Camps, *J. Biol. Inorg. Chem.*, 2005, **10**, 239.
- 96 A. L. De Lacey, E. C. Hatchikian, A. Volbeda, M. Frey, J. C. Fontecilla-Camps and V. M. Fernandez, *J. Am. Chem. Soc.*, 1997, **119**, 7181.

- 97 A. Volbeda, P. Amara, C. Darnault, J. M. Mouesca, A. Parkin, M. M. Roessler, F. A. Armstrong and J. C. Fontecilla-Camps, *Proc. Natl. Acad. Sci. USA*, 2012, **109**, 5305.
- 98 M. Brecht, M. van Gastel, T. Buhrke, B. Friedrich and W. Lubitz, *J. Am. Chem. Soc.*, 2003, **125**, 13075.
- 99 S. Foerster, M. Gastel, M. Brecht and W. Lubitz, *J. Biol. Inorg. Chem.*, 2005, **10**, 51.
- 100 A. Böck, P. W. King, M. Blokesch and M. C. Posewitz, *Adv. Microb. Physiol.*, 2006, **51**, 1.
- 101 L. Forzi and R. G. Sawers, *Biometals*, 2007, **20**, 565.
- 102 L. Casalot and M. Rousset, *Trends Microbiol.*, 2001, **9**, 228.
- 103 A. Paschos, R. S. Glass and A. Böck, *FEBS Lett.*, 2001, **488**, 9.
- 104 S. Reissmann, E. Hochleitner, H. Wang, A. Paschos, F. Lottspeich, R. S. Glass and A. Böck, *Science*, 2003, **299**, 1067.
- 105 Y. Shomura and Y. Higuchi, *J. Biol. Chem.*, 2012, **287**, 28409.
- 106 C. Rosano, S. Zuccotti, M. Bucciantini, M. Stefani, G. Ramponi and M. Bolognesi, *J. Mol. Biol.*, 2002, **321**, 785.
- 107 S. Petkun, R. Shi, Y. Li, A. Asinas, C. Munger, L. Zhang, M. Waclawek, B. Soboh, R. G. Sawers and M. Cygler, *Structure*, 2011, **19**, 1773.
- 108 T. Tominaga, S. Watanabe, R. Matsumi, H. Atomi, T. Imanaka and K. Miki, *Acta Cryst. F*, 2012, **68**, 1153.
- 109 Y. Shomura, H. Komori, N. Miyabe, M. Tomiyama, N. Shibata and Y. Higuchi, *J. Mol. Biol.*, 2007, **372**, 1045.
- 110 S. Watanabe, R. Matsumi, T. Arai, H. Atomi, T. Imanaka and K. Miki, *Mol. Cell.*, 2007, **27**, 29.
- 111 W. Roseboom, M. Blokesch, A. Böck and S. P. J. Albracht, *FEBS Lett.*, 2005, **579**, 469.

- 112 L. Forzi, P. Hellwig, R. K. Thauer and R. G. Sawers, *FEBS Lett.*, 2007, **581**, 3317.
- 113 O. Lenz, I. Zebger, J. Hamann, P. Hildebrandt and B. Friedrich, *FEBS Lett.*, 2007, **581**, 3322.
- 114 I. Bürstel, P. Hummel, E. Siebert, N. Wisitruangsakul, I. Zebger, B. Friedrich and O. Lenz, *J. Biol. Chem.*, 2011, **286**, 44937.
- 115 B. Soboh, S. T. Stripp, E. Muhr, C. Granich, M. Braussemann, M. Herzberg, J. Heberle and R. G. Sawers, *FEBS Lett.*, 2012, **586**, 3882.
- 116 S. T. Stripp, B. Soboh, U. Lindenstraus, M. Braussemann, M. Herzberg, D. H. Nies, R. G. Sawers and J. Heberle, *Biochemistry*, 2013, **52**, 3289.
- 117 C. Beimgraben, K. Gutekunst, F. Opitz and J. Appel, *Appl. Env. Microbiol.*, 2014, **80**, 3776.
- 118 B. Soboh, S. T. Stripp, C. Bielak, U. Lindenstrauß, M. Braussemann, M. Javaid, M. Hallensleben, C. Granich, M. Herzberg, J. Heberle and R. G. Sawers, *FEBS Lett.*, 2013, **587**, 2512.
- 119 K. H. Chan, K. M. Lee and K. B. Wong, *PLoS One*, 2012, **7**, e32592.
- 120 W. Xia, H. Li, X. Yang, K. B. Wong and H. Sun, *J. Biol. Chem.*, 2012, **287**, 6753.
- 121 S. Watanabe, T. Arai, R. Matsumi, H. Atomi, T. Imanaka and K. Miki, *J. Mol. Biol.*, 2009, **394**, 448.
- 122 W. Xia, H. Li, K. H. Sze and H. Sun, *J. Am. Chem. Soc.*, 2009, **131**, 10031.
- 123 K. C. Chan Chung and D. B. Zamble, *J. Biol. Chem.*, 2011, **286**, 43081.
- 124 R. W. Herbst, I. Perovic, V. Martin-Diaconescu, K. O'Brien, P. T. Chivers, S. S. Pochapsky, T. C. Pochapsky and M. J. Maroney, *J. Am. Chem. Soc.*, 2010, **132**, 10338.
- 125 C. D. Douglas, T. T. Ngu, H. Kaluarachchi and D. B. Zamble, *Biochemistry*, 2013, **52**, 6030.

- 126 M. R. Leach, S. Sandal, H. Sun and D. B. Zamble, *Biochemistry*, 2005, **44**, 12229.
- 127 K. H. Chan, T. Li, C. O. Wong and K. B. Wong, *PLoS One*, 2012, **7**, e30547.
- 128 M. R. Leach, J. W. Zhang and D. B. Zamble, *J. Biol. Chem.*, 2007, **282**, 16177.
- 129 H. Kaluarachchi, D. E. K. Sutherland, A. Young, I. J. Pickering, M. J. Stillman and D. B. Zamble, *J. Am. Chem. Soc.*, 2009, **131**, 18489.
- 130 M. Fontecave and S. Ollagnier-de-Choudens, *Arch. Biochem. Biophys.*, 2008, **474**, 226.
- 131 L. Loiseau, C. Gerez, M. Bekker, S. Ollagnier-de Choudens, B. Py, Y. Sanakis, J. Teixeira de Mattos, M. Fontecave and F. Barras, *Proc. Natl. Acad. Sci. USA*, 2007, **104**, 13626.
- 132 C. Pinske and R. G. Sawers, *PLoS One*, 2012, **7**, e31755.
- 133 T. Schubert, O. Lenz, E. Krause, R. Volkmer and B. Friedrich, *Mol. Microbiol.*, 2007, **66**, 453.
- 134 S. Shima and U. Ermler, *Eur. J. Inorg. Chem.*, 2011, **2011**, 963.
- 135 C. Zirngibl, R. Hedderich and R. K. Thauer, *FEBS Lett.*, 1990, 261, 112.
- 136 C. Zirngibl, W. Van Dongen, B. Schworer, R. Von Bunau, M. Richter, A. Klein and R. K. Thauer, *Eur. J. Biochem.*, 1992, **208**, 511.
- 137 S. Shima, O. Pilak, S. Vogt, M. Schick, M. S. Stagni, W. Meyer-Klaucke, E. Warkentin, R. K. Thauer and U. Ermler, *Science*, 2008, **321**, 572.
- 138 O. Pilak, B. Mamat, S. Vogt, C. H. Hagemeyer, R. K. Thauer, S. Shima, C. Vonrhein, E. Warkentin and U. Ermler, *J. Mol. Biol.*, 2006, **358**, 798.
- 139 T. J. Lie, K. C. Costa, D. Pak, V. Sakesan and J. A. Leigh, *FEMS Microbiol. Lett.*, 2013, **343**, 156.
- 140 T. Fujishiro, H. Tamura, M. Schick, J. Kahnt, X. Xie, U. Ermler and S. Shima, *Angew. Chem. Int. Ed.*, 2013, **52**, 12555.

- 141 T. Fujishiro, U. Ermler and S. Shima, *FEBS Lett.*, 2014, **588**, 2789.
- 142 M. Schick, X. Xie, K. Ataka, J. Kahnt, U. Linne and S. Shima, *J. Am. Chem. Soc.*, 2012, **134**, 3271.
- 143 H. L. Drake and S. L. Daniel, *Res. Microbiol.*, 2004, **155**, 869.
- 144 J. Xia, J. F. Sinclair, T. O. Baldwin and P. A. Lindahl, *Biochemistry*, 1996, **35**, 1965.
- 145 T. C. Harrop, M. M. Olmstead and P. K. Mascharak, *Inorg. Chem.*, 2006, **45**, 3424.
- 146 R. R. Eady, *Chem. Rev.*, 1996, **96**, 3013.
- 147 B. Hinnemann and J. K. Norskov, *Phys. Chem. Chem. Phys.*, 2004, **6**, 843.
- 148 K. Schneider and A. Müller, in *Catalysts for Nitrogen Fixation*, eds. B. Smith, R. Richards and W. Newton, Springer Netherlands, 2004, pp. 281-307.
- 149 Y. Hu, C. C. Lee and M. W. Ribbe, *Dalton Trans.*, 2012, **41**, 1118.
- 150 C. C. Lee, Y. Hu and M. W. Ribbe, *Proc. Natl. Acad. Sci. USA*, 2009, **106**, 9209.
- 151 C. C. Lee, Y. Hu and M. W. Ribbe, *Science*, 2010, **329**, 642.
- 152 E. Krahn, B. Weiss, M. Kröckel, J. Groppe, G. Henkel, S. Cramer, A. Trautwein, K. Schneider and A. Müller, *J. Biol. Inorg. Chem.*, 2002, **7**, 37.
- 153 T. Herskovitz, B. A. Averill, R. H. Holm, J. A. Ibers, W. D. Phillips and J. F. Weiher, *Proc. Natl. Acad. Sci. USA*, 1972, **69**, 2437.
- 154 B. A. Averill, T. Herskovitz, R. H. Holm and J. A. Ibers, *J. Am. Chem. Soc.*, 1973, **95**, 3523.
- 155 L. Que, M. A. Bobrik, J. A. Ibers and R. H. Holm, *J. Am. Chem. Soc.*, 1974, **96**, 4168.
- 156 K. S. Hagen, D. W. Stephan and R. H. Holm, *Inorg. Chem.*, 1982, **21**, 3928.
- 157 P. Venkateswara Rao and R. H. Holm, *Chem. Rev.*, 2004, **104**, 527.
- 158 C. J. A. Daley and R. H. Holm, *J. Inorg. Biochem.*, 2003, **97**, 287.
- 159 R. H. Holm, *Pure Appl. Chem.*, 1998, **70**, 931.
- 160 M. A. Whitener, G. Peng and R. H. Holm, *Inorg. Chem.*, 1991, **30**, 2411.

- 161 T. Terada, T. Wakimoto, T. Nakamura, K. Hirabayashi, K. Tanaka, J. Li, T. Matsumoto and K. Tatsumi, *Chem. Asian J.*, 2012, **7**, 920.
- 162 D. L. Gerlach, D. Coucouvanis and N. Lehnert, *Eur. J. Inorg. Chem.*, 2013, 3883.
- 163 T. E. Wolff, J. M. Berg, C. Warrick, K. O. Hodgson, R. H. Holm and R. B. Frankel, *J. Am. Chem. Soc.*, 1978, **100**, 4630.
- 164 S. Ciurli, P. K. Ross, M. J. Scott, S. B. Yu and R. H. Holm, *J. Am. Chem. Soc.*, 1992, **114**, 5415.
- 165 R. Holm, *Adv. Inorg. Chem.*, 1992, **38**, 1.
- 166 R. Panda, C. P. Berlinguette, Y. Zhang and R. H. Holm, *J. Am. Chem. Soc.*, 2005, **127**, 11092.
- 167 Y. Zhang, J. L. Zuo, H. C. Zhou and R. H. Holm, *J. Am. Chem. Soc.*, 2002, **124**, 14292.
- 168 Y. Ohki, *Bull. Chem. Soc. Jpn.*, 2014, **87**, 1.
- 169 J. Schimpl, H. M. Petrilli and P. E. Blöchl, *J. Am. Chem. Soc.*, 2003, **125**, 15772.
- 170 H. Reihlen, A. Gruhl and G. V. Hessling, *J. Liebigs Ann. Chem.*, 1929, **472**, 268.
- 171 D. Seyferth, G. B. Womack, M. K. Gallagher, M. Cowie, B. W. Hames, J. P. Fackler and A. M. Mazany, *Organometallics*, 1987, **6**, 283.
- 172 A. Le Cloirec, S. C. Davies, D. J. Evans, D. L. Hughes, C. J. Pickett, S. P. Best and S. Borg, *Chem. Commun.*, 1999, 2285.
- 173 M. Schmidt, S. M. Contakes and T. B. Rauchfuss, *J. Am. Chem. Soc.*, 1999, **121**, 9736.
- 174 E. J. Lyon, I. P. Georgakaki, J. H. Reibenspies and M. Y. Darensbourg, *Angew. Chem. Int. Ed.*, 1999, **38**, 3178.

- 175 G. Berggren, A. Adamska, C. Lambertz, T. R. Simmons, J. Esselborn, M. Atta, S. Gambarelli, J. M. Mouesca, E. Reijerse, W. Lubitz, T. Happe, V. Artero and M. Fontecave, *Nature*, 2013, **499**, 66.
- 176 J. D. Lawrence, H. Li, T. B. Rauchfuss, M. Bénard and M.-M. Rohmer, *Angew. Chem. Int. Ed.*, 2001, **40**, 1768.
- 177 L.-C. Song, Z.-Y. Yang, H.-Z. Bian and Q.-M. Hu, *Organometallics*, 2004, **23**, 3082.
- 178 L.-C. Song, Z.-Y. Yang, H.-Z. Bian, Y. Liu, H.-T. Wang, X.-F. Liu and Q.-M. Hu, *Organometallics*, 2005, **24**, 6126.
- 179 J. F. Capon, F. Gloaguen, F. Y. Pétilion, P. Schollhammer and J. Talarmin, *Coord. Chem. Rev.*, 2009, **253**, 1476.
- 180 M. Razavet, S. C. Davies, D. L. Hughes and C. J. Pickett, *Chem. Commun.*, 2001, 847.
- 181 A. K. Justice, M. J. Nilges, T. B. Rauchfuss, S. R. Wilson, L. De Gioia and G. Zampella, *J. Am. Chem. Soc.*, 2008, **130**, 5293.
- 182 J. I. van der Vlugt, T. B. Rauchfuss, C. M. Whaley and S. R. Wilson, *J. Am. Chem. Soc.*, 2005, **127**, 16012.
- 183 C. Tard, X. Liu, S. K. Ibrahim, M. Bruschi, L. D. Gioia, S. C. Davies, X. Yang, L. S. Wang, G. Sawers and C. J. Pickett, *Nature*, 2005, **433**, 610.
- 184 E. S. Donovan, J. J. McCormick, G. S. Nichol and G. A. N. Felton, *Organometallics*, 2012, **31**, 8067.
- 185 F. Gloaguen, J. D. Lawrence and T. B. Rauchfuss, *J. Am. Chem. Soc.*, 2001, **123**, 9476.
- 186 C. Tard and C. J. Pickett, *Chem. Rev.*, 2009, **109**, 2245.
- 187 R. Zaffaroni, T. B. Rauchfuss, D. L. Gray, L. De Gioia and G. Zampella, *J. Am. Chem. Soc.*, 2012, **134**, 19260.

- 188 D. Chouffai, G. Zampella, J. F. Capon, L. D. Gioia, A. L. Goff, F. Y. Pétilion, P. Schollhammer and J. Talarmin, *Organometallics*, 2012, **31**, 1082.
- 189 S. Ezzaher, J. F. Capon, F. Gloaguen, F. Y. Pétilion, P. Schollhammer, J. Talarmin and N. Kervarec, *Inorg. Chem.*, 2009, **48**, 2.
- 190 M. Karnahl, S. Tschierlei, O. F. Erdem, S. Pullen, M. P. Santoni, E. J. Reijerse, W. Lubitz and S. Ott, *Dalton Trans.*, 2012, **41**, 12468.
- 191 M. E. Carroll, B. E. Barton, T. B. Rauchfuss and P. J. Carroll, *J. Am. Chem. Soc.*, 2012, **134**, 18843.
- 192 J. M. Camara and T. B. Rauchfuss, *Nat. Chem.*, 2012, **4**, 26.
- 193 C. H. Lai, J. H. Reibenspies and M. Y. Darensbourg, *Angew. Chem. Int. Ed.*, 1996, **35**, 2390.
- 194 S. Canaguier, V. Artero and M. Fontecave, *Dalton Trans.*, 2008, 315.
- 195 Z. Li, Y. Ohki and K. Tatsumi, *J. Am. Chem. Soc.* 2005, **127**, 8950.
- 196 T. R. Simmons, G. Berggren, M. Bacchi, M. Fontecave and V. Artero, *Coord. Chem. Rev.*, 2014, **270–271**, 127.
- 197 T. Naota, H. Takaya and S. I. Murahashi, *Chem. Rev.*, 1998, **98**, 2599.
- 198 T. Matsumoto, B. Kure and S. Ogo, *Chem. Lett.*, 2008, **37**, 970.
- 199 S. Ogo, R. Kabe, K. Uehara, B. Kure, T. Nishimura, S. C. Menon, R. Harada, S. Fukuzumi, Y. Higuchi, T. Ohhara, T. Tamada and R. Kuroki, *Science*, 2007, **316**, 585.
- 200 S. Ogo, K. Ichikawa, T. Kishima, T. Matsumoto, H. Nakai, K. Kusaka and T. Ohhara, *Science*, 2013, **339**, 682.
- 201 B. C. Manor and T. B. Rauchfuss, *J. Am. Chem. Soc.*, 2013, **135**, 11895.
- 202 A. R. Sadique, W. W. Brennessel and P. L. Holland, *Acta Cryst. C*, 2009, **65**, 174.
- 203 B. Hu, D. Chen and X. Hu, *Chem. Eur. J.*, 2014, **20**, 1677.

- 204 K. F. Kalz, A. Brinkmeier, S. Dechert, R. A. Mata and F. Meyer, *J. Am. Chem. Soc.*, 2014, **136**, 16626.
- 205 W. L. F. Armarego and C. L. L. Chai, Purification of laboratory chemicals, Butterworth-Heinemann, Amsterdam; London, 2003.
- 206 G. S. Girolami, T. B. Rauchfuss, and R. J. Angelici, Synthesis and Technique in Inorganic Chemistry: A laboratory manual, University Science Books, 1999.
- 207 S. K. Ibrahim, Ph.D. Thesis, University of Sussex, 1992.
- 208 J. Keeler and P. Wothers, Chemical Structure and reactivity: an integrated approach, Oxford University Press, Oxford, 2008.
- 209 Q. Hu, R. J. Noll, H. Li, A. Makarov, M. Hardman and R. G. Cooks, *J. Mass Spectrom.*, 2005, **40**, 430.
- 210 W. Clegg, Blake, A. J., Gould, R. O., Main, P., Crystal Structure Analysis: Principles and Practice, Oxford Science Publications, 2001.
- 211 K. M. Alenezi, Ph.D. Thesis, University of East Anglia, 2013.
- 212 L. R. Webster, Ph.D. Thesis, University of East Anglia, 2014.
- 213 A. C. Fisher, Electrode Dynamics, Oxford, 1996.
- 214 A. J. Bard and L. R. Faulkner, Electrochemical Methods: Fundamentals and Applications, John Wiley & Sons, 2001.
- 215 A. J. White, K. Drabble and C. W. Wharton, *Biochem. J.*, 1995, **306**, 843.
- 216 D. Sholl and J. Steckel, Density Functional Theory: A Practical Introduction, Wiley, 2009.
- 217 ElchSoft, Kleinromstedt, Germany.
- 218 E. J. Lyon, S. Shima, R. Boecher, R. K. Thauer, F. W. Grevels, E. Bill, W. Roseboom and S. P. J. Albracht, *J. Am. Chem. Soc.*, 2004, **126**, 14239.

- 219 S. Shima, E. J. Lyon, R. K. Thauer, B. Mienert and E. Bill, *J. Am. Chem. Soc.*, 2005, **127**, 10430.
- 220 A. M. Royer, T. B. Rauchfuss and S. R. Wilson, *Inorg. Chem.*, 2007, **47**, 395.
- 221 M. Korbas, S. Vogt, W. Meyer-Klaucke, E. Bill, E. J. Lyon, R. K. Thauer and S. Shima, *J. Biol. Chem.*, 2006, **281**, 30804.
- 222 F. A. Cotton and G. Wilkinson, *Advanced Inorganic Chemistry*, Wiley, New York, 1988.
- 223 Y. Guo, H. Wang, Y. Xiao, S. Vogt, R. K. Thauer, S. Shima, P. I. Volkers, T. B. Rauchfuss, V. Pelmeshnikov, D. A. Case, E. E. Alp, W. Sturhahn, Y. Yoda and S. P. Cramer, *Inorg. Chem.*, 2008, **47**, 3969.
- 224 A. M. Royer, T. B. Rauchfuss and D. L. Gray, *Organometallics*, 2009, **28**, 3618.
- 225 B. V. Obrist, D. Chen, A. Ahrens, V. Schünemann, R. Scopelliti and X. Hu, *Inorg. Chem.*, 2009, **48**, 3514.
- 226 X. Wang, Z. Li, X. Zeng, Q. Luo, D. J. Evans, C. J. Pickett and X. Liu, *Chem. Commun.*, 2008, 3555.
- 227 P. J. Turrell, J. A. Wright, J. N. T. Peck, V. S. Oganessian and C. J. Pickett, *Angew. Chem. Int. Ed.*, 2010, **49**, 7508.
- 228 L.-C. Song, Z. J. Xie, M.-M. Wang, G. Y. Zhao and H. B. Song, *Inorg. Chem.*, 2012, **51**, 7466.
- 229 D. Chen, R. Scopelliti and X. Hu, *Angew. Chem. Int. Ed.*, 2011, **50**, 5671.
- 230 D. Chen, R. Scopelliti and X. Hu, *Angew. Chem. Int. Ed.*, 2012, **51**, 1919.
- 231 B. Schworer, V. M. Fernandez, C. Zirngibl and R. K. Thauer, *Eur. J. Biochem.*, 1993, **212**, 255.
- 232 J. Schleucher, C. Griesinger, B. Schworer and R. K. Thauer, *Biochemistry*, 1994, **33**, 3986.

- 233 J. Schleucher, B. Schwoerer, R. K. Thauer and C. Griesinger, *J. Am. Chem. Soc.*, 1995, **117**, 2941.
- 234 P. M. Vignais, *Coord. Chem. Rev.*, 2005, **249**, 1677.
- 235 G. C. Hartmann, E. Santamaria, V. M. Fernandez, R. K. Thauer, *J. Biol. Inorg. Chem.*, 1996, **1**, 446–450.
- 236 D. W. Stephan, *Dalton Trans.*, 2009, 3129.
- 237 T. Hiromoto, E. Warkentin, J. Moll, U. Ermler and S. Shima, *Angew. Chem. Int. Ed.*, 2009, **48**, 6457.
- 238 X. Yang and M. B. Hall, *J. Am. Chem. Soc.*, 2008, **130**, 14036.
- 239 X. Yang and M. B. Hall, *J. Am. Chem. Soc.*, 2009, **131**, 10901.
- 240 A. Dey, *J. Am. Chem. Soc.*, 2010, **132**, 13892.
- 241 A. R. Finkelmann, H. M. Senn and M. Reiher, *Chem. Sci.*, 2014, **5**, 4474.
- 242 E. T. Tisza and B. Joos, *US Patent*, 1863676, 1932.
- 243 J. A. Bexrud, L. L. Schafer, *Dalton Trans.*, 2010, **39**, 361.
- 244 CrysAlisPro, Oxford Diffraction Ltd, 2010.
- 245 Z. Otwinowski and W. Minor, *Methods Enzymol.*, 1997, **276**, 307.
- 246 G. Chapuis, L. Palatinus, *J. Appl. Cryst.*, 2007, **40**, 786.
- 247 G. M. Sheldrick, *Acta Cryst. C*, 2008, **64**, 112.
- 248 A. Altomare, G. Cascarano, C. Giacovazzo, *J. Appl. Cryst.*, 1994, **27**, 435.
- 249 R. H. Holm, P. Kennepohl, E. I. Solomon, *Chem. Rev.*, 1996, **96**, 2239.
- 250 C. Goh, J. A. Weigel, R. H. Holm, *Inorg. Chem.*, 1994, **33**, 4861.
- 251 E. L. Bominaar, S. A. Borshch, J. J. Girerd, *J. Am. Chem. Soc.* 1994, **116**, 5362.
- 252 D. W. Stephan, G. C. Papaefthymiou, R. B. Frankel and R. H. Holm, *Inorg. Chem.*, 1983, **22**, 1550.

- 253 G. Christou, C. D. Garner, R. M. Miller, C. E. Johnson and J. D. Rush, *J. Chem. Soc., Dalton Trans.*, 1980, 2363.
- 254 M. J. Carney, G. C. Papaefthymiou, M. A. Whitener, K. Spartalian, R. B. Frankel, R. H. Holm, *Inorg. Chem.*, 1988, **27**, 346.
- 255 X. B. Wang, S. Niu, X. Yang, S. K. Ibrahim, C. J. Pickett, T. Ichiye and L. S. Wang, *J. Am. Chem. Soc.*, 2003, **125**, 14072.
- 256 C. H. Langford and H. B. Gray, *Ligand Substitution Processes*, Benjamin: New York, 1965.
- 257 R. A. Henderson, *Chem. Rev.*, 2005, **105**, 2365.
- 258 G. R. Dukes and R. H. Holm, *J. Am. Chem. Soc.*, 1975, **97**, 528.
- 259 R. A. Henderson and K. E. Oglieve, *J. Chem. Soc., Dalton Trans.*, 1993, 1467.
- 260 R. H. Holm, Phillips, W. D., Averill, B. A., Mayerle, J. J., Herskovitz, T., *J. Am. Chem. Soc.*, 1974, **96**, 2109.
- 261 V. R. Almeida, C. A. Gormal, K. L. C. Gronberg, R. A. Henderson, K. E. Oglieve and B. E. Smith, *Inorg. Chem. Acta*, 1999, **291**, 212.
- 262 A. J. Dunford, R. A. Henderson, *Chem. Commun.*, 2002, 360.
- 263 B. V. DePamphilis, B. A. Averill, T. Herskovitz, L. Que and R. H. Holm, *J. Am. Chem. Soc.*, 1974, **96**, 4159.
- 264 C. J. Pickett, *J. Chem. Soc., Chem. Commun.*, 1985, 323.
- 265 T. A. Scott, C. P. Berlinguette, R. H. Holm and H. C. Zhou, *Proc. Natl. Acad. Sci. USA*, 2005, **102**, 9741.
- 266 Y. J. Fu, X. Yang, X. B. Wang and L. S. Wang, *Inorg. Chem.*, 2004, **43**, 3647.
- 267 C. J. Pickett, K. A. Vincent, S. K. Ibrahim, C. A. Gormal, B. E. Smith, S. A. Fairhurst and S. P. Best, *Chem. Eur. J.*, 2004, **10**, 4770.
- 268 F. T. Al-Ani and C. J. Pickett, *J. Chem. Soc., Dalton Trans.*, 1988, 2329.

- 269 T. A. Scott and H. C. Zhou, *Angew. Chem. Int. Ed.*, 2004, **43**, 5628.
- 270 C. Goh, J. A. Weigel and R. H. Holm, *Inorg. Chem.*, 1994, **33**, 4861.
- 271 R. W. Johnson and R. H. Holm, *J. Am. Chem. Soc.*, 1978, **100**, 5338.
- 272 F. A. Armstrong, J. N. Butt, S. J. George, E. C. Hatchikian and A. J. Thomson, *FEBS Lett.*, 1989, **259**, 15.
- 273 S. J. George, Z. Cui, M. Razavet and C. J. Pickett, *Chem. Eur. J.*, 2002, **8**, 4037.
- 274 J. J. Mayerle, S. E. Denmark, B. V. DePamphilis, J. A. Ibers and R. H. Holm, *J. Am. Chem. Soc.*, 1975, **97**, 1032.
- 275 S. Zilberman, E. I. Stiefel, M. H. Cohen and R. Car, *Inorg. Chem.*, 2006, **45**, 5715.
- 276 C. Zhou and R. H. Holm, *Inorg. Chem.*, 1997, **36**, 4066.
- 277 M. E. Pandelia, H. Ogata and W. Lubitz, *ChemPhysChem*, 2010, **11**, 1127.
- 278 D. J. Darensbourg, W. Z. Lee, M. J. Adams and J. C. Yarbrough, *Eur. J. Inorg. Chem.*, 2001, 2811.
- 279 J. Jiang and S. A. Koch, *Angew. Chem. Int. Ed.*, 2001, **40**, 2629.
- 280 P. Excoffon, J. Laugier and B. Lamotte, *Inorg. Chem.*, 1991, **30**, 3075.
- 281 J. C. Fontecilla-Camps, personal communication 2015.
- 282 Y. Nicolet, A. Pagnier, L. Zeppieri, L. Martin, P. Amara and J. C. Fontecilla-Camps, *ChemBioChem*, 2015, **16**, 397.
- 283 C. Tard, Ph.D. Thesis, University of East Anglia, 2006.